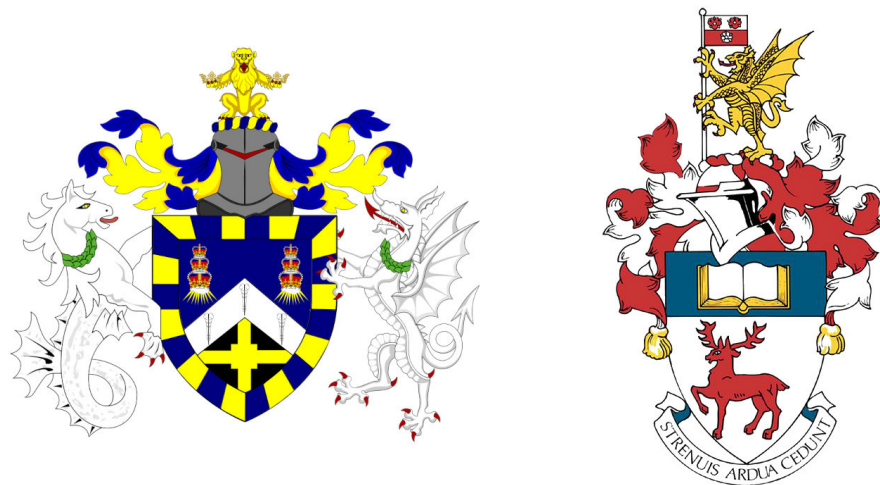


<sup>1</sup> ADVANCING NEUTRINO  
<sup>2</sup> DETECTION AND TRIGGERING IN  
<sup>3</sup> DUNE



<sup>5</sup> Francisco Martínez López

<sup>6</sup> Submitted in partial fulfillment of the requirements  
<sup>7</sup> of the Degree of Doctor of Philosophy

<sup>8</sup> School of Physical and Chemical Sciences  
<sup>9</sup> Queen Mary University of London

<sup>10</sup> School of Physics and Astronomy  
<sup>11</sup> University of Southampton

<sup>12</sup> December 2024



## <sup>13</sup> Statement of originality

- <sup>14</sup> I, Francisco Martínez López, confirm that the research included within this thesis is my  
<sup>15</sup> own work or that where it has been carried out in collaboration with, or supported by  
<sup>16</sup> others, that this is duly acknowledged below and my contribution indicated. Previously  
<sup>17</sup> published material is also acknowledged below.
- <sup>18</sup> I attest that I have exercised reasonable care to ensure that the work is original, and  
<sup>19</sup> does not to the best of my knowledge break any UK law, infringe any third party's  
<sup>20</sup> copyright or other Intellectual Property Right, or contain any confidential material.
- <sup>21</sup> I accept that the University has the right to use plagiarism detection software to check  
<sup>22</sup> the electronic version of the thesis.
- <sup>23</sup> I confirm that this thesis has not been previously submitted for the award of a degree  
<sup>24</sup> by this or any other university.
- <sup>25</sup> The copyright of this thesis rests with the author and no quotation from it or information  
<sup>26</sup> derived from it may be published without the prior written consent of the author.
- <sup>27</sup> Signature: [can be digital signature]
- <sup>28</sup> Date:
- <sup>29</sup> Details of collaboration and publications:  
<sup>30</sup> [insert details here if applicable]



# <sup>31</sup> Abstract

<sup>32</sup> Work in progress . . .



*¡Oh memoria, enemiga mortal de mi descanso!*

---

*El ingenioso hidalgo don Quijote de la Mancha*

MIGUEL DE CERVANTES SAAVEDRA



## <sup>33</sup> Acknowledgements

<sup>34</sup> Work in progress . . .



# <sup>35</sup> Contents

<sup>36</sup>	Statement of originality . . . . .	3
<sup>37</sup>	Abstract . . . . .	5
<sup>38</sup>	Acknowledgements . . . . .	9
<sup>39</sup>	<b>List of Figures</b>	<b>15</b>
<sup>40</sup>	<b>List of Tables</b>	<b>31</b>
<sup>41</sup>	<b>List of Abbreviations</b>	<b>33</b>
<sup>42</sup>	<b>1 Introduction</b>	<b>35</b>
<sup>43</sup>	<b>2 Neutrino physics</b>	<b>37</b>
<sup>44</sup>	2.1 Neutrinos in the SM . . . . .	37
<sup>45</sup>	2.2 Trouble in the neutrino sector . . . . .	41
<sup>46</sup>	2.2.1 The solar neutrino problem . . . . .	41
<sup>47</sup>	2.2.2 The atmospheric neutrino problem . . . . .	43
<sup>48</sup>	2.3 Massive neutrinos . . . . .	45
<sup>49</sup>	2.4 Neutrino oscillation formalism . . . . .	48
<sup>50</sup>	2.4.1 Oscillations in vacuum . . . . .	50
<sup>51</sup>	2.4.2 Oscillations in matter . . . . .	52
<sup>52</sup>	2.4.3 Current status of neutrino oscillations . . . . .	54
<sup>53</sup>	2.5 Open questions in the neutrino sector . . . . .	55
<sup>54</sup>	2.6 Neutrino interactions . . . . .	57

## CONTENTS

55	<b>3 The Deep Underground Neutrino Experiment</b>	59
56	3.1 Overview . . . . .	59
57	3.2 Physics goals of DUNE . . . . .	61
58	3.3 LBNF beamline . . . . .	63
59	3.4 Near Detector . . . . .	65
60	3.4.1 ND-LAr . . . . .	67
61	3.4.2 TMS/ND-GAr . . . . .	68
62	3.4.3 PRISM . . . . .	69
63	3.4.4 SAND . . . . .	70
64	3.5 A More Capable Near Detector . . . . .	70
65	3.5.1 Requirements . . . . .	71
66	3.5.2 Reference design . . . . .	71
67	3.5.3 R&D efforts . . . . .	74
68	3.6 Far Detector . . . . .	77
69	3.6.1 Horizontal Drift . . . . .	78
70	3.6.2 Vertical Drift . . . . .	80
71	3.6.3 FD Data Acquisition System . . . . .	82
72	<b>4 Matched Filter approach to induction wire Trigger Primitives</b>	85
73	4.1 Motivation . . . . .	85
74	4.2 Signal-to-noise ratio definition . . . . .	87
75	4.3 Low-pass FIR filter design . . . . .	89
76	4.4 Matched filters . . . . .	92
77	4.5 Using simulated samples . . . . .	98
78	4.5.1 Angular dependence . . . . .	104
79	4.5.2 Distortion and peak asymmetry . . . . .	106
80	4.5.3 Hit sensitivity . . . . .	109
81	<b>5 DM searches with neutrinos from the Sun</b>	119
82	5.1 Motivation . . . . .	119

## CONTENTS

83	5.2 Gravitational capture of DM by the Sun . . . . .	119
84	5.3 Neutrino flux from DM annihilations . . . . .	126
85	5.4 Computing limits from solar neutrino fluxes . . . . .	127
86	5.5 Example: Kaluza-Klein Dark Matter . . . . .	131
87	5.6 High energy DM neutrino signals . . . . .	135
88	5.6.1 DIS events . . . . .	137
89	5.6.2 Single proton QEL events . . . . .	142
90	5.6.3 Results . . . . .	145
91	5.7 Example: Leptophilic Dark Matter . . . . .	147
92	<b>6 Particle ID in GArSoft</b>	<b>153</b>
93	6.1 GArSoft . . . . .	154
94	6.1.1 Event generation . . . . .	154
95	6.1.2 Detector simulation . . . . .	155
96	6.1.3 Reconstruction . . . . .	156
97	6.2 $dE/dx$ measurement in the TPC . . . . .	158
98	6.2.1 Energy calibration . . . . .	160
99	6.2.2 Truncated $dE/dx$ mean . . . . .	170
100	6.2.3 Mean $dE/dx$ parametrisation . . . . .	173
101	6.2.4 Particle identification . . . . .	177
102	6.3 Muon and pion separation in the ECal and MuID . . . . .	177
103	6.3.1 Track-ECal matching . . . . .	180
104	6.3.2 Classification strategy . . . . .	185
105	6.3.3 Feature selection and importance . . . . .	188
106	6.3.4 Hyperparameter optimisation . . . . .	200
107	6.3.5 Probability calibration . . . . .	203
108	6.3.6 Performance . . . . .	205
109	6.4 ECal time-of-flight . . . . .	205
110	6.4.1 Arrival time estimations . . . . .	207

## CONTENTS

111	6.4.2 Proton and pion separation . . . . .	209
112	6.5 Charged pion decay in flight . . . . .	210
113	6.5.1 Track breakpoints . . . . .	212
114	6.6 Neutral particle identification . . . . .	219
115	6.6.1 ECal clustering . . . . .	219
116	6.6.2 $\pi^0$ reconstruction . . . . .	222
117	<b>7 Event selection in ND-GAr</b>	<b>225</b>
118	7.1 CAFs and CAFAna . . . . .	225
119	7.2 Event selection . . . . .	225
120	7.2.1 $\nu_\mu$ CC selection . . . . .	225
121	7.2.2 Charged pion multiplicity . . . . .	225
122	<b>8 Conclusions</b>	<b>227</b>
123	<b>A An appendix</b>	<b>229</b>
124	<b>Bibliography</b>	<b>231</b>

# <sup>125</sup> List of Figures

<sup>126</sup>	2.1	Solar neutrino fluxes for the solar model BS05(OP). . . . .	42
<sup>127</sup>	2.2	Zenith angle distributions for the selected $\nu_e$ and $\nu_\mu$ events in the SK detector. . . . .	44
<sup>128</sup>	2.3	$K^0 \rightleftharpoons \bar{K}^0$ mixing through $W^\pm$ exchange. . . . .	48
<sup>130</sup>	2.4	. . . . .	57
<sup>131</sup>	2.5	Schematic representation of a $\nu_\mu$ CCQE interaction with a neutron inside a nucleus. . . . .	58
<sup>133</sup>	3.1	Schematic diagram of the DUNE experiment and the LBNF beamline. .	60
<sup>134</sup>	3.2	Schematic longitudinal section of the LBNF beamline at Fermilab. . . .	63
<sup>135</sup>	3.3	Predicted neutrino fluxes at the FD in FHC mode and RHC mode. . . .	64
<sup>136</sup>	3.4	Representation of the ND hall in Phase II, showing the different subcomponents.	65
<sup>137</sup>	3.5	Schematic representation of the external components of ND-LAr, including the cryostat and the PRISM movable system and detailed drawing of one ArgonCube module. . . . .	66
<sup>139</sup>	3.6	Schematic view of the TMS detector, highlighting its main parts. . . . .	67
<sup>140</sup>	3.7	Cross section of the ND-GAr geometry, showing the HPgTPC, ECal and magnet. . . . .	68
<sup>143</sup>	3.8	Predicted beam muon neutrino flux at the ND location for different off-axis positions. . . . .	69
<sup>144</sup>	3.9	Diagram of the ALICE TPC, showing the two drift chambers, inner and outer field cages and readout chambers. . . . .	72

## LIST OF FIGURES

147	3.10 Diagram of the ALICE TPC, showing the two drift chambers, inner and outer field cages and readout chambers. . . . .	73
148		
149	3.11 Photographs of the TOAD pressure vessel at RHUL. . . . .	75
150		
151	3.12 Electron microscope image and schematic diagram of a GEM electrode. .	76
152		
153	3.13 Schematic diagram showing the operating principle of a LArTPC with wire readout. . . . .	77
154		
155	3.14 Proposed design for the FD-1 and FD-2 modules following the HD principle. .	78
156		
157	3.15 Schematic representation of an APA frames showing the U, V, X and G wires. . . . .	79
158		
159	3.16 A PDS module containing 24 X-ARAPUCAs and the location of the modules on the APAs. . . . .	80
160		
161	3.17 Proposed design for the FD-3 module following the VD principle. . . . .	81
162		
163	3.18 Schematic representation of the electrode strip configuration for a top and bottom CRU. . . . .	82
164		
165	3.19 Detailed diagram of the DUNE FD DAQ system. . . . .	83
166		
167	4.1 <i>Schematic representation of an APA. The black lines represent the APA steel frame. The green and magenta lines correspond to the direction of the U and V induction wires respectively. The blue lines indicate the direction of the X collection wires and the wire shielding G.</i> . . . . .	86
168		
169	4.2 <i>Left panel: Zoomed unfiltered waveform corresponding to channel 7840 from the ProtoDUNE-SP raw data capture felix-2020-07-17-21:31:44 (blue line). The green dashed lines mark the region <math>\pm 3\sigma_{raw}</math>. The resulting noise waveform is also shown (red line). Top right panel: ADC distribution for channel 7840, where the green shaded region represents <math>\pm \sigma_{raw}</math>. Bottom right panel: noise ADC distribution for channel 7840, where the green shaded region represents <math>\pm \sigma_{noise}</math>.</i> . . . . .	87
170		
171		
172		

## LIST OF FIGURES

173	4.3 <i>Left panel:</i> Zoomed filtered waveform corresponding to channel 7840 from the ProtoDUNE-SP raw data capture <i>felix-2020-07-17-21:31:44</i> (blue line). The filter used was the current implementation of the low-pass FIR filter in <i>dtp-firmware</i> . The green dashed lines mark the region $\pm 3\sigma_{\text{raw}}$ . The resulting noise waveform is also shown (red line). <i>Top right panel:</i> ADC distribution for channel 7840 after filtering, where the green shaded region represents $\pm \sigma_{\text{raw}}$ . <i>Bottom right panel:</i> noise ADC distribution for channel 7840 after filtering, where the green shaded region represents $\pm \sigma_{\text{noise}}$	89
181	4.4 Power spectrum in decibels for the current implementation of the low-pass FIR filter in <i>dtp-firmware</i> (blue line), compared to the response of an optimal filter obtained using the Parks-McClellan algorithm for the same pass-band (red line). Also for comparison I include the spectrum of the optimal filter when taking only the integer part of the coefficients (red dashed line).	90
187	4.5 Relative change in the S/N for the ProtoDUNE-SP raw data capture <i>felix-2020-07-17-21:31:44</i> , using different values of the cutoff frequency $f_c$ and the transition width $\delta f$ . The optimal Chebyshev filters were applied using just the integer part of the coefficients given by the Parks-McClellan algorithm.	91
192	4.6 Distribution of the relative change of the S/N on the different wire planes from the ProtoDUNE-SP raw data capture <i>felix-2020-07-17-21:31:44</i> after the optimal Chebyshev filter was applied. The filter was computed with the Parks-McClellan algorithm using a cutoff of $f_c = 0.068 \text{ ticks}^{-1}$ and a transition width $\delta f = 0.010 \text{ ticks}^{-1}$ .	92

## LIST OF FIGURES

197	4.7	<i>Left panel: Zoomed match filtered waveform corresponding to channel 7840 from the ProtoDUNE-SP raw data capture <code>felix-2020-07-17-21:31:44</code> (blue line). The filter used was directly extracted from the data, being the 32 values around the first peak in the original waveform. The green dashed lines mark the region <math>\pm 3\sigma_{\text{raw}}</math>. The resulting noise waveform is also shown (red line). Top right panel: ADC distribution for channel 7840 after match filtering, where the green shaded region represents <math>\pm \sigma_{\text{raw}}</math>. Bottom right panel: noise ADC distribution for channel 7840 after match filtering, where the green shaded region represents <math>\pm \sigma_{\text{noise}}</math> . . . . .</i>	93
206	4.8	<i>Relative improvement in the S/N for the raw data capture <code>felix-2020-07-17-21:31:44</code>, using the matched filter following the parametrisation in Eq. (4.17). The black crosses in both panels denote the location of the maximum ratio value.</i>	96
209	4.9	<i>Left panel: Optimal matched filter coefficients for the U (blue line) and V (red line) planes. The filters were computed with our parametrisation in Eq. (4.17) for the parameter values <math>\delta = 0.035</math>, <math>\sigma = 0.191</math> and <math>\delta = 0.018</math>, <math>\sigma = 0.191</math> respectively. Right panel: Distribution of the relative change of the S/N on the two induction wire planes from the ProtoDUNE-SP raw data capture <code>felix-2020-07-17-21:31:44</code> after their respective optimal matched filters were applied. . . . .</i>	99
216	4.10	<i>Left panel: distributions of the particles track length in the liquid argon for the generated <math>E_k = 100</math> MeV monoenergetic samples, electrons (blue), muons (red), protons (green) and neutral pions (purple). Right panel: distribution of the length of the longest photon in the neutral pion sample after the decay process <math>\pi^0 \rightarrow \gamma\gamma</math>. . . . .</i>	100

## LIST OF FIGURES

## LIST OF FIGURES

246	4.15 Selected consecutive waveforms corresponding to two monoenergetic $E_k =$	
247	100 MeV muon events, one is parallel to the APA and to the wires in	
248	the U plane (left panel) and the other is normal to the APA plane and	
249	perpendicular to the U plane wires (right panel). The solid lines represent	
250	the raw waveforms whereas the dashed lines correspond to the waveforms	
251	after the matched filter was applied. The waveforms on the left panel have	
252	been scaled by a factor of 0.15 to have similar amplitude to the ones on	
253	the right panel. . . . .	107
254	4.16 Left panel: peak asymmetry distribution for the case of the monoenergetic	
255	$E_k = 100$ MeV muon sample. Each value corresponds to a single bipolar	
256	signal peak from a channel in any event. The blue distribution represents	
257	the peaks on U plane channels, whereas the red corresponds to signal peaks	
258	in V wires. Right panel: relation between the mean peak asymmetry per	
259	event with the S/N for U channel waveforms from the $E_k = 100$ MeV	
260	muon sample. The top subplot shows the decimal logarithm of the mean	
261	S/N for the raw (red) and the matched filtered (blue) waveforms. The	
262	bottom subplot contains the mean S/N improvement ratio after the matched	
263	filter was applied. . . . .	108
264	4.17 Raw data display in the plane time (in firmware ticks) vs. offline channel	
265	number for an $E_k = 100$ MeV electron event. The produced true hits are	
266	superimposed (black boxes) as well as the hits comming from the standard	
267	hit finder chain (blue circles) and the hit finder using the matched filter	
268	(green triangles). . . . .	110

## LIST OF FIGURES

- 269 4.18 Dependence of the precision (blue), sensitivity (red) and  $F_1$  (green) scores  
270 on the threshold values used in the hit finder, for the FIR (left panel)  
271 and matched filter (right panel) cases. The results were obtained after  
272 matching the hits to the true hits in the case of the isotropic muon sample  
273 with kinetic energy in the range 5 to 100 MeV, taking only into account  
274 the induction plane channels. The points represent the mean value while  
275 the error bars indicate one standard deviation around that mean value. . . 112

276 4.19 Dependence of the averaged hit sensitivity on the kinetic energy of the  
277 events for the matched filter (blue) and standard (red) hits, for the case of  
278 the muon (left panel) and electron (right panel) samples, separated between  
279  $U$  (top plots) and  $V$  (bottom plots) induction wire planes. The top subplots  
280 contain the hit sensitivities for the two hit finder alternatives, while the  
281 bottom subplots show the ratio between the two. The horizontal lines sit at  
282 the mean value and represent the size of the energy bins, while the vertical  
283 error bars indicate one standard deviation around that mean value. . . . 114

284 4.20 Distributions of the hit sensitivity in the  $U$  (top panels) and  $V$  (bottom  
285 panels) planes versus the hit sensitivity in the  $X$  plane, both for the  
286 standard hits (left panels) and the matched filter hits (right panels), in the  
287 case of the electron sample and a threshold of 30 ADC. . . . . . . . . . 115

288 4.21 Top panels: standard residual plots of the hit sensitivities between the  $X$   
289 and  $U$  planes. Bottom panels: quantile-quantile plots of the hit sensitivity  
290 standard residuals between the  $X$  and  $U$  planes. In all cases, the left  
291 panel corresponds to the standard hits while the right panel represents the  
292 matched filter case, all from the electron sample with a 30 ADC threshold. 116

## LIST OF FIGURES

293	5.1	<i>Input solar parameters used in our capture rate computation as functions of the Sun's radius, from left to right: temperature (with respect to the temperature at the core), mass (in solar masses) and electron number density (with respect to the electron density at the core). All quantities shown correspond to the standard solar model BS2005-OP [1]. . . . .</i>	123
298	5.2	<i>Capture rates as a function of the DM mass for the DM-electron interactions (red lines), SD DM-nucleons interactions (green lines) and SI DM-nucleons interactions (blue lines). Solid lines represent the values computed in this work while the dashed lines are the one given in Ref. [2]. All the rates are shown for a choice of scattering cross section of <math>\sigma_i = 10^{-40} \text{ cm}^2</math>. . .</i>	124
303	5.3	<i>NuWro computed <math>\nu_\mu - {}^{40}\text{Ar}</math> charged-current scattering cross section as a function of the neutrino energy <math>E_\mu</math>. The black line shows to the total cross section, whereas the others correspond to the different contributions (in red quasi-elastic scattering, in green resonant pion exchange, in blue deep inelastic scattering and in purple meson exchange current). . . . .</i>	128
308	5.4	<i>Expected atmospheric neutrino flux as a function of the neutrino energy <math>E_\nu</math> at Homestake at solar minimum, taken from Ref. [3]. The blue solid (dashed) line correspond to muon neutrinos (antineutrinos) and the red solid (dashed) line correspond to electron neutrinos (antineutrinos). . . .</i>	130
312	5.5	Feynman diagrams for $B^1B^1$ annihilation into SM fermions. . . . .	132
313	5.6	Feynman diagrams for $B^1B^1$ annihilation into a Higgs boson pair. . . .	132
314	5.7	<i>Computed spectra of muon neutrinos at the DUNE FD site from <math>B^1</math> annihilations in the Sun for three different values of <math>M_{\text{LKP}}</math>, plotted in relative energy units for legibility. . . . .</i>	133

## LIST OF FIGURES

<p>317    5.8    <i>Projected 90% confidence level upper limit for DUNE (400 kT yr) on the</i>         318    <i>spin-dependent <math>B^1</math>-proton scattering cross section as a function of <math>M_{\text{LKP}}</math></i>         319    <i>(green dots). I also show the previous limits from IceCube [4] (blue line)</i>         320    <i>and Antares [5] (red line) on the LKP cross section. The shaded area</i>         321    <i>represents the disfavoured region (at 95% confidence level) on the mass of</i>         322    <i>the LKP from LHC data [6]. . . . .</i></p> <p>323    5.9    <i>Computed spectra of muon neutrinos at the DUNE FD site from <math>\tau^+\tau^-</math></i>         324    <i>(left panel) and <math>b\bar{b}</math> (right panel) annihilations in the Sun for the DM</i>         325    <i>masses <math>m_{\text{DM}} = 10 \text{ GeV}</math> (red line), <math>50 \text{ GeV}</math> (green line) and <math>100 \text{ GeV}</math></i>         326    <i>(blue line), plotted in relative energy units. . . . .</i></p> <p>327    5.10    <i>Distribution of the muon neutrino energies from the <math>\tau^+\tau^-</math> (left panel)</i>         328    <i>and <math>b\bar{b}</math> (right panel) annihilation channels, for <math>m_{\text{DM}} = 10 \text{ GeV}</math>, separated</i>         329    <i>by CC interaction type: QEL (blue), MEC (orange), RES (green) and</i>         330    <i>DIS (red). . . . .</i></p> <p>331    5.11    <i>Distributions of <math>\theta_\mu</math> (left panel), <math>\theta_j</math> (central panel) and <math>\theta_{\text{plane}}</math> (right panel)</i>         332    <i>for the <math>b\bar{b}</math> sample with <math>m_{\text{DM}} = 10 \text{ GeV}</math> (blue) and the atmospheric</i>         333    <i>background (red). . . . .</i></p> <p>334    5.12    <i>Left panel: signal efficiencies (blue lines) and background rejections (red</i>         335    <i>lines) for events passing the cuts <math>\theta &lt; \theta_{\text{cut}}</math> for the jet (solid lines) and</i>         336    <i>muon (dashed lines) angles. Right panel: signal efficiency (blue line) and</i>         337    <i>background rejection (red line) for events passing the cut <math>\theta_{\text{plane}} &lt; \theta_{\text{cut}}</math> for</i>         338    <i>the momentum conservation plane deviation. . . . .</i></p> <p>339    5.13    <i>Signal efficiencies for the <math>\tau^+\tau^-</math> (blue line) and <math>b\bar{b}</math> (red line) DIS samples</i>         340    <i>as functions of the DM mass, <math>m_{\text{DM}}</math>, obtained by applying the optimal</i>         341    <i>angular cuts <math>\theta_\mu &lt; 27^\circ</math>, <math>4^\circ &lt; \theta_j &lt; 26^\circ</math> and <math>\theta_{\text{plane}} &lt; 3.5^\circ</math>. . . . .</i></p> <p>342    5.14    <i>Distributions of <math>\cos \theta_\mu</math> (left panel), <math>\cos \theta_p</math> (central panel) and <math>\cos \theta_N</math></i>         343    <i>(right panel) for the <math>\tau^+\tau^-</math> QEL sample with <math>m_{\text{DM}} = 5 \text{ GeV}</math> (blue) and</i>         344    <i>the atmospheric background (red). . . . .</i></p>	<p>134</p> <p>135</p> <p>137</p> <p>138</p> <p>139</p> <p>141</p> <p>142</p>
--	--

## LIST OF FIGURES

345	5.15 Left panel: value of the loss function for the training sample (blue line) and accuracy for the validation sample (red line) versus the number of iterations for the MLP classifier training. Right panel: distributions of the predicted probabilities assigned by the MLP classifier to the test sample for the $\tau^+\tau^-$ QEL signal with $m_{\text{DM}} = 5$ GeV (blue) and the atmospheric background (red). . . . .	143
351	5.16 Signal efficiencies for the $\tau^+\tau^-$ (blue line) and $b\bar{b}$ (red line) single proton QEL samples as functions of the DM mass, $m_{\text{DM}}$ , obtained by requiring a minimum predicted probability from the MLP classifier of 0.97 in order to achieve a background rejection greater than 99.8%. . . . .	144
355	5.17 Projected 90% confidence level upper limit for DUNE (400 kT yr) on the spin-dependent DM-nucleon scattering cross section as a function of $m_{\text{DM}}$ , for the annihilation channels $\tau^+\tau^-$ (blue) and $b\bar{b}$ (red) separated by interaction type (up triangles denote DIS interactions whereas down triangles represent QEL interactions). I also show the previous limits from IceCube [7] (solid lines) and the projected sensitivities for Pingu [8] (dashed lines) and Hyper-Kamiokande [9] (dash-dotted lines), as well as the direct detection limits from PICASSO [10] (solid green line) and PICO-60 C <sub>3</sub> F <sub>8</sub> [11] (dashed green line). . . . .	146
364	5.18 Left panel: Projected 90% confidence level sensitivity of DUNE (400 kT yr) to the scale $\Lambda$ of an EFT containing only leptophilic DM axial-axial interactions (blue line). Right panel: . In both cases the corresponding limits from DarkSide-50 [12] (dotted green line) and XENON1T [13] (dashed red line) are also shown, together with the configurations for which the correct relic density is achieved (black line), all for the coupling values $c_A^e = 10^3$ and $c_A^\nu = 10^{-2}$ . . . . .	150

## LIST OF FIGURES

371    6.1 Distribution of the fraction of energy deposits with residual range less 372       than 20% of the total track length, and distribution of the ionisation per 373       unit length after removing the tracks with less than 30% of their energy 374       deposits in the last 20% of the track. . . . . 	162
375    6.2 Distribution of the reconstructed ionisation charge per unit length for 376       different reclustering values, and distribution of the median change in 377 $dQ/dx$ per track for the $N_{group} = 4$ reclustering. . . . . 	163
378    6.3 Distribution of the Geant4-simulated energy losses per unit length versus 379       residual range for the stopping proton sample. . . . . 	164
380    6.4 Fitted most probable $dQ/dx$ values for each $dE/dx$ bin, together with 381       best fit to the logarithmic calibration function. . . . . 	165
382    6.5 Fitted most probable $dQ/dx$ values for each $dE/dx$ bin for three different 383       ADC bit limits. . . . . 	167
384    6.6 Area normalised $dE/dx$ distributions for the true and the reconstructed 385       energy deposits in the stopping proton sample, both after applying the 386       calibration and the calibration and the normalisation correction. . . . . 	168
387    6.7 Fractional residuals between the true and the corrected $dE/dx$ means 388       and the 60% truncated means, and fractional residuals between the true 389       and the uncorrected, corrected and uncalibrated $dE/dx$ 60% truncated 390       means. . . . . 	170
391    6.8 Estimated values of the mean $dE/dx$ bias and resolution for the stopping 392       proton sample at different values of the truncation factor. . . . . 	171
393    6.9 Examples of the truncated mean $dE/dx$ LanGauss fits for various $\beta\gamma$ 394       bins, from a simulated FHC neutrino sample. . . . . 	174
395    6.10 Resulting one and two dimensional projections of the posterior probability 396       distributions of the ALEPH $\langle dE/dx \rangle$ parameters obtained by fitting the 397       60% truncated mean $dE/dx$ values from a FHC neutrino sample. . . . . 	175

## LIST OF FIGURES

398	6.11 Truncated mean $dE/dx$ obtained for the FHC neutrino sample as a function of the $\beta\gamma$ product, together with the fitted most probable values for each $\beta\gamma$ bin and the best fit obtained using the ALEPH parametrisation.	176
401	6.12 Distribution of the 60% truncated mean $dE/dx$ versus reconstructed momentum for the FHC neutrino sample. . . . .	177
403	6.13 Estimated values of the mean $dE/dx$ bias and resolution obtained for the true protons in a FHC neutrino sample. . . . .	178
405	6.14 True momentum distribution for the primary muon in $\nu_\mu$ CC $N\pi^\pm$ interactions inside the fiducial volume of ND-GAr, compared to the post FSI charged pion spectrum. . . . .	179
408	6.15 Distributions of energy deposits in the ECal for a muon and a charged pion with similar momenta. . . . .	180
410	6.16 Left panel: comparison between the precision (blue), sensitivity (yellow) and $F_1$ score (red) obtained for the default (horizontal lines) and new algorithms, both with the $\chi^2$ -based direction estimator (squares) and cheating the directions (circles), for different values of the $\chi^2$ cut. Right panel: comparison of the performance of the new algorithm when applying the cluster $t_0$ correction (squares) and when (circles). . . . .	182
416	6.17 Schematics of a possible option to deal with track-ECal associations in non-zero $t_0$ neutrino interaction events, trying to correct for the drift direction uncertainty in a cluster-by-cluster basis using the cluster time, $t_{cluster}$ . . . . .	184
420	6.18 Momentum distribution for the reconstructed muons (top panel) and charged pions (bottom panel) in a FHC neutrino sample, together with the fraction of them reaching the ECal (red) and MuID (blue). Each entry corresponds to a reconstructed track, backtracked to a true muon or pion which has not produced any other reconstructed track. . . . .	185

## LIST OF FIGURES

<p>425    6.19 Predicted truncated mean <math>dE/dx</math> versus momentum, for electrons, muons, 426    charged pions and protons, obtained using the ALEPH parametrisation. 427    The vertical dashed lines represent the boundaries of the six regions used 428    for the muon and pion classification training. . . . .</p> <p>429    6.20 Example ECal feature distributions for muons and charged pions in the 430    five different momentum ranges considered. . . . .</p> <p>431    6.21 Example MuID feature distributions for muons and charged pions in the 432    three different momentum ranges considered. . . . .</p> <p>433    6.22 Left panel: cumulative explained variance for the first three principal 434    components (top panel) and contribution of the different features to the 435    principal axes in feature space (bottom panel). Right panel: Shapley 436    (blue) and Gini (red) feature importances for the different input features. 437    Both figures correspond to the samples in the momentum range <math>0.3 \leq</math> 438    <math>p &lt; 0.8 \text{ GeV}/c</math>. . . . .</p> <p>439    6.23 Left panel: cumulative explained variance for the first three principal 440    components (top panel) and contribution of the different features to the 441    principal axes in feature space (bottom panel). Right panel: Shapley 442    (blue) and Gini (red) feature importances for the different input features. 443    Both figures correspond to the samples in the momentum range <math>0.8 \leq</math> 444    <math>p &lt; 1.5 \text{ GeV}/c</math>. . . . .</p> <p>445    6.24 Evolution of the SHAP importance for the top six most important features 446    across all five momentum ranges. . . . .</p> <p>447    6.25 Permutation importances for the ten most important features in the 448    different momentum ranges (from left to right, top to bottom, in increasing 449    momentum order). The bars indicate the effect that permutations of 450    each feature have on the purity (blue) and the sensitivity (yellow), the 451    translucent regions representing one standard deviation around the central 452    value. . . . .</p>	<p style="margin-right: 20px;">186</p> <p style="margin-right: 20px;">190</p> <p style="margin-right: 20px;">191</p> <p style="margin-right: 20px;">193</p> <p style="margin-right: 20px;">194</p> <p style="margin-right: 20px;">197</p> <p style="margin-right: 20px;">198</p>
---	--

## LIST OF FIGURES

453	6.26 Values of the precision and sensitivity obtained for 10000 BDT hyperparameter configurations, for the momentum regions I, III and V. . . . .	201
454		
455	6.27 Reliability diagrams for the BDT classifier used in the momentum range	
456	$0.3 \leq p < 0.8 \text{ GeV}/c$ , both for the original (blue circles) and calibrated	
457	(yellow squares) responses. For reference, the response of a perfectly	
458	calibrated classifier is also shown (black dashed line). . . . .	204
459		
460	6.28 Uncalibrated (left panel) and calibrated (right panel) predicted probabilities assigned by the BDT classifiers for true muons (blue) and charged pions	
461	(red) in the momentum range $0.3 \leq p < 0.8 \text{ GeV}/c$ . . . . .	205
462		
463	6.29 Schematic of the hit selection used for the ToF measurement. The grid represents the layers of the inner ECal, with coloured squares indicating	
464	the tiles with hits. Green squares indicate the selected hits. . . . .	206
465		
466	6.30 Particle velocity versus momentum measured with different ECal arrival time estimations. From left to right: earliest hit time, average hit time,	
467	and fitted hit time. In all cases the time resolution is $\Delta\tau = 0.1 \text{ ns}$ . . . . .	208
468		
469	6.31 Mass spectra for $p$ (blue) and $\pi^\pm$ (yellow) particles, using different ECal time resolution values (from top to bottom, in ascending order), and arrival time estimates. From left to right: earliest hit time, average hit time, and fitted hit time. The dashed lines indicate the true masses of	
470		
471	the particles. . . . .	210
472		
473	6.32 Efficiency (top panel) and purity (bottom panel) for the proton selection as a function of the momentum, for $\Delta\tau = 0.10 \text{ ns}$ . . . . .	211
474		
475	6.33 Distributions of the velocities measured by ToF with the inner ECal, for different momentum bins, in a FHC neutrino interaction sample. The	
476	Gaussian fits are performed around the maxima for each particle species.	212
477		

## LIST OF FIGURES

478	6.34 Left panel: number of non-decaying, decaying and decaying in the fiducial volume pions for a MC sample of 100000, $p = 500$ MeV/ $c$ isotropic positively charged pions inside the TPC. Right panel: event display for a positive pion decaying inside the fiducial volume, with a single reconstructed track for the pion and muon system. . . . .	213
483	6.35 Values of $\chi_k^2(FB)$ (top left panel), $F_k$ (top right panel), $D_k^{1/R}$ (bottom left panel) and $D_k^\phi$ (bottom right panel) versus position along the drift direction for a reconstructed track in a positive pion decay event. The vertical red dashed line indicates the true location of the decay point. . .	214
487	6.36 Fractional residual distributions of the true and reconstructed decay position along the drift coordinate, using the position of the maximum of $\chi_k^2(FB)$ (left panel) and $F_k$ (right panel) as estimates of the decay position. Also shown are double Gaussian fits to these points (red lines).	215
491	6.37 Distributions of the extreme values of $\chi_k^2(FB)$ (top left panel), $F_k$ (top right panel), $D_k^{1/R}$ (bottom left panel) and $D_k^\phi$ (bottom right panel) for non-decaying reconstructed pion tracks (blue) and tracks which include the decay inside the fiducial volume (red). . . . .	217
495	6.38 Left panel: distributions of the predicted probabilities assigned by the BDT classifier to a test sample of decaying pion+muon tracks (blue) and non-decaying pion tracks (red). Left: signal efficiency versus background acceptance (ROC curve) obtained from the BDT for the test sample. . .	218
499	6.39 Left panel: dependence of the decay position finding resolution on the true value of the decay angle for the $\chi_k^2(FB)$ (red) and $F_k$ (blue) methods. Right panel: signal efficiency (blue line) and background rejection (red line) from the BDT classifier versus true decay angle. . . . .	218

## LIST OF FIGURES

503	6.40 Mean values of the $F_1$ -score marginal distributions for the different	
504	free parameters of the new clustering algorithm, with the error bars	
505	representing one standard deviation around the mean. The $F_1$ -score	
506	values were computed for the 6561 possible parameter configurations	
507	using 1000 $\nu_\mu$ CC interaction events. . . . .	221
508	6.41 Left panel: distributions of the number of ECal clusters per photon from	
509	$\pi^0$ decays for the standard (red) and new (blue) clustering algorithms.	
510	Right panel: reconstructed invariant mass distributions for photon pairs	
511	from single $\pi^0$ events using the standard (red) and new (blue) ECal	
512	clustering algorithms. . . . .	223

# **513 List of Tables**

514	2.1	Values of $T_3$ and $Y/2$ assigned to the first generation of fermions. . . . .	39
515	2.2	Neutral current couplings. . . . .	40
516	2.3	Summary of neutrino oscillation parameters determined in the Neutrino	
517		Global Fit of 2020 [14]. . . . .	56
518	3.1	Summary of the two-phased plan for DUNE. . . . .	61
519	3.2	Exposure and time required to achieve the different physics milestones of	
520		the two phases. . . . .	62
521	4.1	<i>Characteristic parameters of the two monoenergetic muon events selected, relative to the U plane: projected angles in the <math>xz'</math> and <math>y'z'</math> planes, S/N values for the raw and filtered waveforms, mean improvement of the S/N and peak asymmetry.</i> . . . . .	107
525	6.1	Calibration parameters obtained from the fit of the ND-GAr simulated stopping proton sample to the calibration function, for different ADC limits. 167	
526	6.2	Momentum ranges and description of the PID approach assumed for the muon and pion classification task. . . . .	187
529	6.3	Optimal values of the hyperparameters used by the BDT, for each momentum range. . . . .	202
531	6.4	Performance metrics of the BDTs with optimal hyperparameters, for the different momentum ranges. . . . .	203

## LIST OF TABLES

533	6.5 Summary of parameters and sampled values used in the optimisation of	
534	the clustering algorithm. . . . .	221

535

## <sup>536</sup> List of Abbreviations

<b>ADC</b>	Analog to Digital Converter.
<b>ALEPH</b>	Apparatus for LEP PHysics.
<b>ALICE</b>	A Large Ion Collider Experiment.
<b>BDT</b>	Boosted Decision Tree.
<b>CC</b>	Charged Current.
<b>DM</b>	Dark Matter.
<b>DUNE</b>	Deep Underground Neutrino Experiment.
<b>ECal</b>	Electromagnetic Calorimeter.
<b>FD</b>	Far Detector.
<b>FHC</b>	Forward Horn Current.
<b>HPgTPC</b>	High Pressure gaseous Time Projection Chamber.
<b>LBL</b>	Long BaseLine.
<b>MuID</b>	Muon IDentification system.
<b>NC</b>	Neutral Current.
<b>ND</b>	Near Detector.
<b>ND-GAr</b>	Near Detector Gaseous Argon.
<b>ND-LAr</b>	Near Detector Liquid Argon.
<b>PDG</b>	Particle Data Group.
<b>RHC</b>	Reverse Horn Current.



<sup>537</sup> Chapter 1

<sup>538</sup> Introduction



539 Chapter 2

540 Neutrino physics

541        *Little particles of inspiration sleet through the universe all the time traveling  
542        through the densest matter in the same way that a neutrino passes through a  
543        candyfloss haystack, and most of them miss.*

544                          – Terry Pratchett, *Sourcery*

545        Ever since they were postulated in 1930 by Wolfgang Pauli to explain the continuous  
546         $\beta$  decay spectrum [15] and later found by F. Reines and C. Cowan at the Savannah  
547        River reactor in 1953 [16], neutrinos have had a special place among all other elementary  
548        particles. They provide a unique way to probe a wide range of quite different physics,  
549        from nuclear physics to cosmology, from astrophysics to colliders. Moreover, there is  
550        compelling evidence to believe that the study of neutrinos may be key to unveil different  
551        aspects of physics beyond the SM, difficult to test elsewhere.

552        In this Chapter, I will review the basics of neutrino physics, from its role within the  
553        SM to the main open questions related to the neutrino sector, paying special attention  
554        to the phenomenology of neutrino oscillations.

555 2.1 Neutrinos in the SM

556        The SM of fundamental interactions was initially proposed in 1967 by S. Glashow, S.  
557        Weinberg and A. Salam[17–19]. This theoretical framework describes the dynamics

## Chapter 2. Neutrino physics

of leptons and quarks, by introducing a collection of mediating gauge vector bosons and one scalar particle, known as the Higgs boson. It assumes that the local  $SU(3) \times SU(2)_L \times U(1)_Y$  gauge symmetry is an internal symmetry of the system, with  $SU(3)$  describing quantum chromodynamics, and  $SU(2)_L \times U(1)_Y$  being the gauge groups of the electroweak sector. For a detailed overview of the SM of electroweak interactions, see Ref. [20].

In the SM, neutrinos appear in three flavours, namely  $\nu_e$ ,  $\nu_\mu$ , and  $\nu_\tau$ . These are associated with the corresponding charged leptons,  $e$ ,  $\mu$ , and  $\tau$ . Neutrinos exist only as left-handed particles, grouped in doublets with the charged leptons, while the later come in both chirality states:

$$\begin{pmatrix} \nu_e \\ e_L^- \end{pmatrix}, \quad \begin{pmatrix} \nu_\mu \\ \mu_L^- \end{pmatrix}, \quad \begin{pmatrix} \nu_\tau \\ \tau_L^- \end{pmatrix}, \quad e_R^-, \quad \mu_R^-, \quad \tau_R^-. \quad (2.1)$$

Similarly, quarks also exist in both chirality states, and are grouped as:

$$\begin{pmatrix} u_L \\ d_L \end{pmatrix}, \quad \begin{pmatrix} s_L \\ c_L \end{pmatrix}, \quad \begin{pmatrix} t_L \\ b_L \end{pmatrix}, \quad u_R, \quad d_R, \quad s_R, \quad c_R, \quad t_R, \quad b_R. \quad (2.2)$$

The fact that there are no right-handed neutrino fields implies that neutrinos are strictly massless within the SM. This restriction follows from the experimental observation that all neutrinos produced via weak interactions are pure left-handed helicity states (and similarly antineutrinos are pure right-handed states). The hypothetical existence of right-handed neutrinos could be indirectly inferred from the observation of non-zero neutrino masses, nevertheless the existence of neutrino masses is not a sufficient condition for the existence of such fields.

Left and right-handed fermions transform differently under  $SU(2)_L \times U(1)_Y$  rotations, as the right-handed particles are singlets under  $SU(2)_L$ . Applying a local transformation, they change as:

$$\begin{aligned} \psi_L &\longrightarrow e^{-iY\beta(x)/2} e^{-iT_a\alpha_a(x)} \psi_L, \\ \psi_R &\longrightarrow e^{-iY\beta(x)/2} \psi_R, \end{aligned} \quad (2.3)$$

## 2.1. Neutrinos in the SM

**Table 2.1:** Values of  $T_3$  and  $Y/2$  assigned to the first generation of fermions.

	$e_L$	$\nu_e$	$e_R$	$u_L$	$d_L$	$u_R$	$d_R$
$T_3$	-1/2	1/2	0	1/2	-1/2	0	0
$Y/2$	-1/2	-1/2	-1	1/6	1/6	2/3	-1/3

579 where  $Y/2$  and  $T_a$  are the generators of  $SU(2)_L$  and  $U(1)_Y$ , respectively, and  $\beta(x)$  and  
580  $\alpha_a(x)$  are the parameters of the rotation.

581 The values of the quantum numbers  $Y/2$  and  $T_3$ , the third component of the weak  
582 isospin, have to be assigned to the different particles. The values of  $T_3$  follow from the  
583 commutation relations of the generators of  $SU(2)$ . After the spontaneous symmetry  
584 breaking  $SU(2)_L \times U(1)_Y \rightarrow U(1)_{EM}$ , one finds the relation which determines the electric  
585 charge:

$$Q = T_3 + \frac{Y}{2}, \quad (2.4)$$

586 Setting the electric charge to  $-1$  for electrons, we can find the values of the hypercharge  
587 for the rest of the fermions. The resulting values for the first generation of leptons and  
588 quarks are shown in Tab. 2.1.

589 It is clear that the free Lagrangian of the theory is not be invariant under the gauge  
590 transformations, as the kinetic terms contain derivatives. Therefore, to make it invariant,  
591 one needs to introduce a set of gauge bosons. They appear in the so-called covariant  
592 derivative, which replaces the common derivative and transforms in the same way as the  
593 fermion fields under local rotations. This constrain fixes completely the transformations  
594 of the spin-1 fields. For left and right-handed particles, the covariant derivatives are  
595 given by:

$$\begin{aligned} D_\mu \psi_L &= \left( \partial_\mu + ig' \frac{Y}{2} B_\mu + ig T_a W_\mu^a \right) \psi_L, \\ D_\mu \psi_R &= \left( \partial_\mu + ig' \frac{Y}{2} B_\mu \right) \psi_R, \end{aligned} \quad (2.5)$$

596 where  $W_\mu^i$ ,  $i = 1, 2, 3$  and  $B_\mu$  are the gauge bosons for the  $SU(2)_L$  and  $U(1)_Y$  factors,  
597 respectively, and  $g$  and  $g'$  are the corresponding gauge couplings. It can be shown that

## Chapter 2. Neutrino physics

**Table 2.2:** Neutral current couplings.

	$u$	$d$	$\nu_e$	$e$
$2v_f$	$1 - \frac{8}{3}\sin^2\theta_W$	$-1 + \frac{4}{3}\sin^2\theta_W$	1	$-1 + 4\sin^2\theta_W$
$2a_f$	1	-1	1	-1

598 these fields transform in the adjoint representation of the gauge group.

599 So far, the theory only contains massless particles, as adding bare mass terms to  
 600 the Lagrangian would spoil the gauge symmetry. Therefore, the mass terms need to  
 601 be induced by a spontaneous violation of the symmetries. In the SM, the responsible  
 602 for this is the Higgs mechanism. The Higgs doublet is coupled to the gauge bosons  
 603 through the covariant derivative, and to the fermions through the Yukawa couplings.  
 604 Upon spontaneous symmetry breaking, the vacuum expectation value of the Higgs field  
 605 generate the mass terms of the particles.

606 In order to obtain the physical intermediate vector boson states, we need to perform  
 607 the following redefinitions:

$$\begin{aligned} A_\mu &= \sin \theta_W W_\mu^3 + \cos \theta_W B_\mu, \\ Z_\mu &= \cos \theta_W W_\mu^3 - \sin \theta_W B_\mu, \\ W_\mu^\pm &= \frac{1}{\sqrt{2}} (W_\mu^1 \mp i W_\mu^2), \end{aligned} \tag{2.6}$$

608 where  $A_\mu$  is the photon field, and  $Z_\mu$  and  $W_\mu^\pm$  are the neutral and the charged weak  
 609 boson fields, respectively. The Weinberg angle,  $\theta_W$ , relates the weak coupling constants  
 610 and the electric charge:

$$e = g' \cos \theta_W = g \sin \theta_W. \tag{2.7}$$

611 At this point, the interacting part of the electroweak Lagrangian can be re-written  
 612 as the sum of three contributions: the electromagnetic (EM), charged-current (CC) and

## 2.2. Trouble in the neutrino sector

613 neutral-current (NC) components:

$$\begin{aligned}\mathcal{L}_{\text{EW}}^{\text{int}} &= \mathcal{L}_{\text{EM}} + \mathcal{L}_{\text{CC}} + \mathcal{L}_{\text{NC}} \\ &= -eA_\mu J_{\text{EM}}^\mu - \frac{g}{2\sqrt{2}}(W_\mu^+ J_{\text{CC}}^\mu + \text{h.c.}) - \frac{g}{2\cos\theta_W}Z_\mu J_{\text{NC}}^\mu,\end{aligned}\tag{2.8}$$

614 with the currents defined as:

$$\begin{aligned}J_{\text{EM}}^\mu &= \sum_f Q_f \bar{f} \gamma^\mu f, \\ J_{\text{CC}}^\mu &= \sum_\ell \bar{\nu}_\ell \gamma^\mu (1 - \gamma_5) \ell + \sum_f \bar{u}_f \gamma^\mu (1 - \gamma_5) d_f, \\ J_{\text{NC}}^\mu &= \sum_f \bar{f} \gamma^\mu (v_f - a_f \gamma_5) f,\end{aligned}\tag{2.9}$$

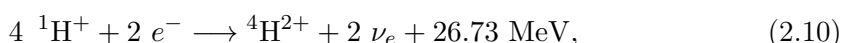
615 where  $f$  denotes any SM fermion,  $\ell$  and  $\nu_\ell$  a charged lepton and a neutrino of any flavour,  
616 and  $u_f$  and  $d_f$  an up-like and a down-like quarks of any flavour. For the NC case, the  
617 values of the  $v_f$  and  $a_f$  couplings are given in Tab. 2.2.

618 As seen in Eq. (5.8), in the electroweak theory neutrinos are coupled to the  $Z$  boson  
619 in a universal way. Therefore, by measuring the so-called invisible decay width of the  $Z$   
620 boson we have an estimate of the number of light (i.e. lighter than the  $Z$  boson) neutrino  
621 flavours. This number was measured by LEP in a combined analysis of  $e^+e^- \rightarrow \mu^+\mu^-$   
622 and  $e^+e^- \rightarrow \text{hadrons}$  to be  $N_\nu = 2.9840 \pm 0.0082$  [21].

## 623 2.2 Trouble in the neutrino sector

### 624 2.2.1 The solar neutrino problem

625 Neutrinos are produced everywhere in vast amounts. One of the most prominent sources  
626 of neutrinos in our vicinity is our Sun. The Sun is powered mainly by two nuclear fusion  
627 reactions, the p – p chain and the CNO cycle. In both cases, the overall reaction is:



## Chapter 2. Neutrino physics

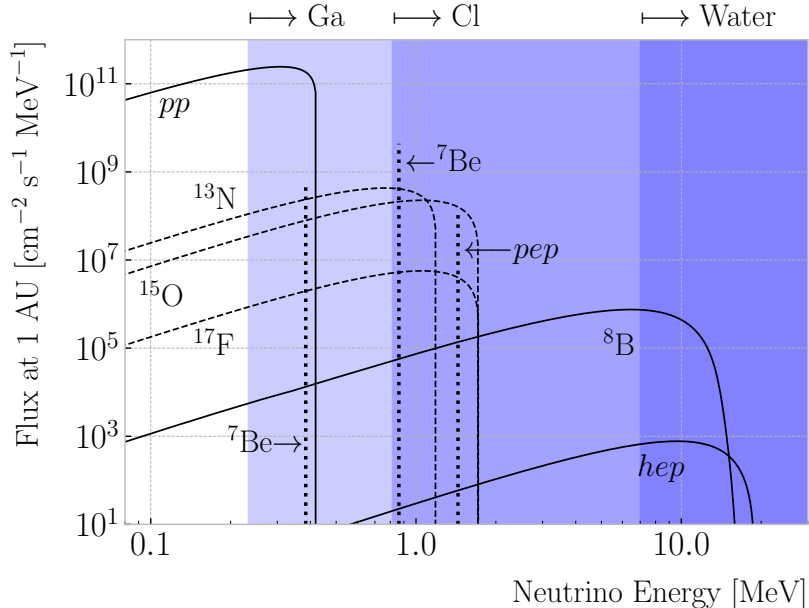


**Figure 2.1:** Solar neutrino fluxes for the solar model BS05(OP). The detection thresholds for Gallium, Chlorine and water-based experiments are also shown. Figure adapted from Ref. [1].

where part of the released energy is lost to the neutrinos. The electron neutrinos produced are often labelled after the processes that generate them. Figure 2.1 shows the solar neutrino flux as a function of the neutrino energy, broken down by the production process.

In the late 1960s, the Brookhaven Solar Neutrino Experiment, led by R. Davis, started data taking with the goal of measuring the solar neutrino flux [22]. The experiment used a tank containing  $380 \text{ m}^3$  of tetrachloroethene ( $\text{C}_2\text{Cl}_4$ ), a liquid commonly used in dry-cleaning, located 1.5 km underground in the Homestake mine, in Lead, South Dakota. The incoming neutrinos would get captured following the reaction:



therefore allowing to measure the neutrino flux by counting the  ${}^{37}\text{Ar}$  isotopes. The threshold for this reaction is 0.814 MeV, just below the 0.862 MeV line from the  ${}^7\text{Be}$  ground state transition.

## 2.2. Trouble in the neutrino sector

640 The results of the experiment were compared to the theoretical predictions made by  
641 J. Bahcall [23]. During its operation from 1968 to 2002, the experiment observed a solar  
642  $\nu_e$  flux that was approximately a third of the total prediction [24].

643 In the early 1990s, the SAGE [25] and GALLEX [26] experiments started operations.  
644 The detection principle used for both experiments was similar to that of the Homestake  
645 experiment, but using  $^{71}\text{Ga}$  instead of  $\text{C}_2\text{Cl}_4$ . With a detection threshold of 0.233 MeV,  
646 the Gallium-based experiments were able to observe the  $pp$  neutrino flux. Both  
647 experiments measured a solar electron neutrino flux that was a factor of two lower  
648 than the predictions, demonstrating that this deficit was energy-dependent.

649 In the early 2000s, the SNO experiment put an end to the solar neutrino puzzle  
650 [27, 28]. Thanks to its directionality capabilities, being a Cherenkov light detector, as  
651 well as to its heavy water target, SNO measured the total solar neutrino flux through  
652 the NC process:

$$\nu_\alpha + d \longrightarrow n + p + \nu_\alpha, \quad (2.12)$$

653 where  $\alpha = e, \mu, \tau$ . This measurement agreed with the solar model predictions. Then,  
654 measuring the CC reaction:

$$\nu_e + d \longrightarrow p + p + e^-, \quad (2.13)$$

655 they were able to establish that the  $\nu_\mu$  and  $\nu_\tau$  solar fluxes are in fact non-zero, revealing  
656 that electron neutrinos were transitioning into different flavours.

### 657 2.2.2 The atmospheric neutrino problem

658 When cosmic-rays interact with the atoms in the upper atmosphere, a plethora of  
659 hadrons, mainly  $\pi$  and  $K$  mesons, are produced. In particular, for the charged pions,  
660 we have the following decay chain dominates:

$$\begin{aligned} \pi^+ &\longrightarrow \mu^+ + \nu_\mu, \\ \mu^+ &\longrightarrow e^+ + \bar{\nu}_\mu + \nu_e, \end{aligned} \quad (2.14)$$

## Chapter 2. Neutrino physics

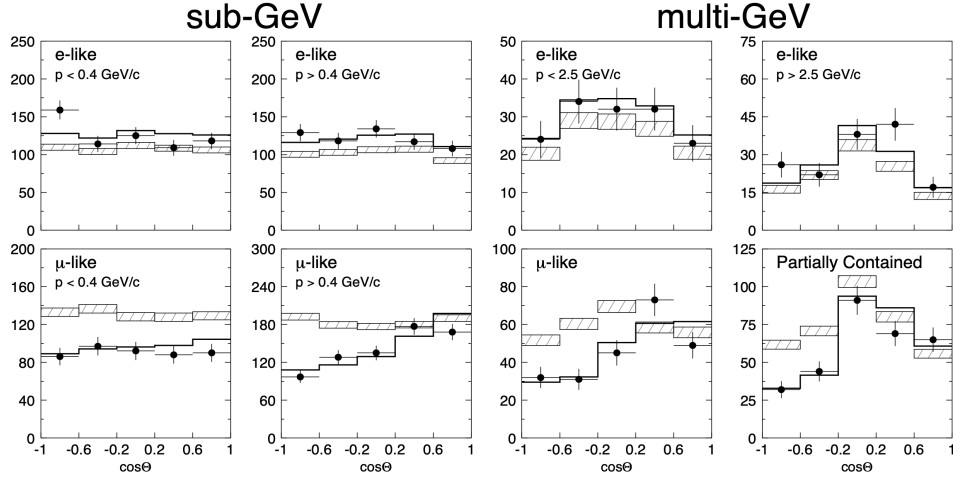


**Figure 2.2:** Zenith angle distributions for the selected  $\nu_e$  (top row) and  $\nu_\mu$  (bottom row) events in the SK detector. The hatched region corresponds to the expectation in the case of no oscillations, whereas the solid line indicates the best-fit in the case of  $\nu_\mu \rightarrow \nu_\tau$  oscillations. Figure taken from Ref. [34].

and similar for the antiparticles. For neutrino energies  $< 1$  GeV, the ratio:

$$\frac{N(\nu_\mu + \bar{\nu}_\mu)}{N(\nu_e + \bar{\nu}_e)}, \quad (2.15)$$

of produced neutrinos and antineutrinos is, in good approximation, equal to two [29].

During the 1980s, several proton decay experiments, like Kamiokande [30], IMB [31], MACRO [32], and Soudan-2 [33], measured the flux of atmospheric neutrinos. This was an important part of their research programme, as the atmospheric neutrinos constitute their main background. All these experiments reported an atmospheric neutrino ratio lower than the predictions.

A few years before the SNO discovery, in 1998, Super-Kamiokande (SK) collaboration measured the atmospheric  $\nu_e$  and  $\nu_\mu$  spectra as a function of the zenith angle [34]. Upward-going particles have negative zenith angle,  $\cos \Theta < 0$ , indicating that they entered from the bottom of the detector. These upward-going neutrinos had to travel through the Earth in order to reach the detector, allowing SK to probe a broad range of baselines. Figure 2.2 shows the reported distributions (black dots), compared to the no oscillations prediction (hatched region). This measurement confirmed that muon

### 2.3. Massive neutrinos

neutrinos transition to other flavours, and that this phenomenon depends both on the energy and the path length of the neutrino.

The SK and SNO findings provided definitive evidence for the existence of neutrino oscillations, and therefore non-zero neutrino masses. This constitutes one of the groundbreaking discoveries of modern physics and has acted as driving force for beyond the Standard Model (BSM) physics. The minimal extension of the SM we can do to address these phenomena is introducing different masses for at least two of the neutrinos. This way, we are left with three neutrino mass eigenstates  $\nu_1$ ,  $\nu_2$ , and  $\nu_3$ , with masses  $m_1$ ,  $m_2$ , and  $m_3$  respectively, which in general will not coincide with the flavour eigenstates,  $\nu_e$ ,  $\nu_\mu$ , and  $\nu_\tau$ .

## 2.3 Massive neutrinos

The existence of neutrino oscillations imply that neutrinos are massive particles. However, as we have seen before, within the SM neutrinos are massless, as they do not have a mass term in the Lagrangian. If one wants to give neutrinos a mass, the particle content of the SM needs to be expanded.

A way of generating massive neutrinos while maintaining gauge invariance is by introducing an arbitrary number of sterile neutrinos  $N_i$ ,  $i = 1, \dots, m$ . These allow for two different types of neutrino mass terms:

$$-\mathcal{L}_{M_\nu} = \sum_{i=1}^m \sum_{j=1}^3 M_D^{ij} \bar{N}_i \nu_{Lj} + \frac{1}{2} \sum_{i=1}^m \sum_{j=1}^m M_N^{ij} \bar{N}_i N_j^c + \text{h.c.}, \quad (2.16)$$

where  $M_D$  is a complex  $m \times 3$  matrix and  $M_N$  a complex and symmetric  $m \times m$  matrix. The first term, often referred to as the Dirac mass term, arises from the corresponding Yukawa interaction after the spontaneous electroweak symmetry breaking, similar to the other fermions. The second term, called the Majorana mass term, is allowed in the Lagrangian, as it is a singlet of the gauge group. However, it violates lepton number conservation by two units.

## Chapter 2. Neutrino physics

If one imposes lepton number symmetry conservation, the Majorana term must banish,  $M_N = 0$ . In this case, if  $m = 3$  we can identify the sterile neutrinos as the right-handed component of the neutrino field. The Dirac mass matrix can be diagonalised using two unitary matrices,  $V_R^\nu$  and  $V_L^\nu$ , as:

$$M_D = V_R^\nu \text{ diag}(m_1, m_2, m_3) V_L^{\nu\dagger}, \quad (2.17)$$

where  $m_i$ ,  $i = 1, 2, 3$  are the masses of the three neutrino mass eigenstates.

The neutrino mass term can be written in term of the resulting eigenstates as:

$$-\mathcal{L}_{M_\nu} = \sum_{i=1}^3 m_i \bar{\nu}_{Di} \nu_{Di}, \quad (2.18)$$

with:

$$\nu_{Di} = \left( V_L^{\nu\dagger} \nu_L \right)_i + \left( V_R^{\nu\dagger} N \right)_i. \quad (2.19)$$

In this scenario, both the low energy particle budget and the symmetries of the SM have to be modified. Moreover, the masses of the neutrinos are generated exclusively through the Higgs mechanism, which does not explain why they are much smaller than those of the charged leptons.

Going back to the general case, we can re-write Eq. (2.16) in matrix form as:

$$-\mathcal{L}_{M_\nu} = \frac{1}{2} (\bar{\nu}_L^c, \bar{N}) \begin{pmatrix} 0 & M_D^T \\ M_D & M_N \end{pmatrix} \begin{pmatrix} \nu_L \\ N^c \end{pmatrix} + \text{h.c.} = \bar{\nu}^c M_\nu \nu + \text{h.c.}, \quad (2.20)$$

with  $\nu = (\nu_L, N^c)^T$  being a  $(3+m)$ -dimensional vector grouping the active and the sterile neutrinos. The matrix  $M_\nu$ , which is a complex  $(3+m) \times (3+m)$  symmetric matrix, can be diagonalised by means of a unitary matrix  $V^\nu$ , yielding:

$$M_\nu = V^\nu \text{ diag}(m_1, m_2, \dots, m_{3+m}) V^{\nu T}. \quad (2.21)$$

## 2.3. Massive neutrinos

<sup>714</sup> Using this eigendecomposition, the neutrino mass term can be expressed as:

$$-\mathcal{L}_{M_\nu} = \frac{1}{2} \sum_{i=1}^{3+m} m_i \bar{\nu}_{Mi} \nu_{Mi}, \quad (2.22)$$

<sup>715</sup> where the states  $\nu_{Mi}$ , commonly referred to as Majorana neutrinos, are defined as:

$$\nu_{Mi} = \left( V^{\nu\dagger} \nu \right)_i + \left( V^{\nu\dagger} \nu \right)_i^c, \quad (2.23)$$

<sup>716</sup> in such a way that the Majorana condition,  $\nu_M^c = \nu_M$ , holds true.

<sup>717</sup> As a consequence of the Majorana condition, the neutrino and the antineutrino states  
<sup>718</sup> can be described in terms of a single field. As opposed to the charged leptons, which  
<sup>719</sup> need to be represented by a four-component or Dirac spinor, the Majorana neutrino is  
<sup>720</sup> described by a two-component or Weyl spinor.

<sup>721</sup> If the eigenvalues of the Majorana mass matrix,  $M_N$ , are much larger than the  
<sup>722</sup> electroweak symmetry breaking scale, the diagonalisation of  $M_\nu$  leads to 3 light and  $m$   
<sup>723</sup> heavy neutrino states:

$$-\mathcal{L}_{M_\nu} = \frac{1}{2} \bar{\nu}_l M_l \nu_l + \frac{1}{2} \bar{\nu}_h M_h \nu_h, \quad (2.24)$$

<sup>724</sup> where the two mass matrices are given by:

$$\begin{aligned} M_l &\simeq -V_l^T M_D^T M_N^{-1} M_D V_l, \\ M_h &\simeq V_h^T M_N V_h, \end{aligned} \quad (2.25)$$

<sup>725</sup> with  $V_l$  and  $V_h$  two unitary matrices.

<sup>726</sup> This scenario represents the so-called see-saw mechanism [35–39]. The name comes  
<sup>727</sup> from the fact that the masses of the heavy states are proportional to  $M_N$ , whereas for  
<sup>728</sup> the light states they are proportional to  $M_N^{-1}$ . While both the heavy and the light  
<sup>729</sup> neutrinos are Majorana particles, it can be shown that the heavy states are mainly  
<sup>730</sup> right-handed, whereas the light ones are mostly left-handed.

## Chapter 2. Neutrino physics

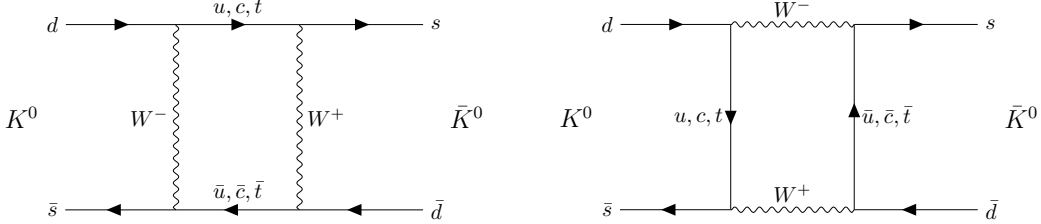


**Figure 2.3:**  $K^0 \rightleftharpoons \bar{K}^0$  mixing through  $W^\pm$  exchange.

### 731 2.4 Neutrino oscillation formalism

732 Neutrino oscillations were first proposed in 1958 by B. Pontecorvo [40], inspired by the  
 733 neutral kaon oscillation phenomenon [41]. Neutral kaons,  $K^0$  and  $\bar{K}^0$ , have opposite  
 734 strangeness ( $\pm 1$ ) and are produced in strong processes. It was observed that, when  
 735 having a beam initially pure of neutral kaons of one type, these would transition into  
 736 their antiparticles while propagating. Because the weak interaction does not conserve  
 737 strangeness, neutral kaons can change their identity via the processes shown in Fig. 2.3.

738 The mixing considered initially by Pontecorvo was between the neutrino and the  
 739 antineutrino states, as only one neutrino flavour was known at the time. After the  
 740 discovery of the muon neutrino, the mixing between flavours was also explored [42].

741 In the general case, we have 3 active and  $m$  sterile neutrinos, resulting in  $3 + m$   
 742 neutrino mass eigenstates. Working in the mass basis, the leptonic charged-current  
 743 Lagrangian can be written as:

$$-\mathcal{L}_{CC}^{lep} = \frac{g}{\sqrt{2}} (\bar{e}_L, \bar{\mu}_L, \bar{\tau}_L) \gamma^\mu U \begin{pmatrix} \nu_1 \\ \nu_2 \\ \vdots \\ \nu_{3+m} \end{pmatrix} W_\mu^+ + \text{h.c.}, \quad (2.26)$$

744 where  $U$  is a  $3 \times (3 + m)$  matrix which obeys  $UU^\dagger = I_{3 \times 3}$ , but in general will not be  
 745 unitary,  $U^\dagger U \neq I_{(3+m) \times (3+m)}$ .

746 The leptonic mixing matrix,  $U$ , establishes how the neutrino mass states couple to  
 747 the charged leptons. In general, a complex  $n \times n$  matrix can be fully specified by  $2n^2$  real  
 748 parameters. If the matrix is unitary, then the number of independent parameters reduces

## 2.4. Neutrino oscillation formalism

749 to  $n^2$ , as one has to impose  $n$  normalisation and  $n(n - 1)$  orthogonality constraints.  
 750 In our case, we can further reduce the number of parameters by performing a phase  
 751 redefinition of the charged lepton fields, without affecting the physics. This is not true  
 752 for the neutrinos. As they may be their own antiparticles, one is not allowed to remove  
 753 any physically relevant phases. If we consider  $n$  generations of leptons, the total number  
 754 of parameters in the mixing matrix is  $n^2 - n$ . Out of these, half of them are mixing  
 755 angles, while the other half are complex phase factors.

756 Considering the extended SM without any additional sterile neutrino states, the  
 757 resulting  $3 \times 3$  mixing matrix is unitary. This matrix, often called the Pontecorvo-Maki-  
 758 Nakagawa-Sakata (PMNS) matrix [43, 44], relates the set of active neutrinos and the  
 759 three mass eigenstates as:

$$|\nu_\alpha\rangle = \sum_{i=1}^3 U_{\alpha i}^* |\nu_i\rangle, \quad (2.27)$$

760 where the Greek index  $\alpha$  denotes the flavour  $\{e, \mu, \tau\}$  and the Latin index  $i$  the mass state  
 761  $\{1, 2, 3\}$ . This leptonic mixing matrix may be parametrized in terms of 6 parameters, 3  
 762 of which are mixing angles  $\theta_{12}$ ,  $\theta_{13}$  and  $\theta_{23}$ , one CP-violating phase  $\delta_{CP}$  and 2 Majorana  
 763 phases  $\alpha$  and  $\beta$ :

$$U = \begin{pmatrix} 1 & 0 & 0 \\ 0 & c_{23} & s_{23} \\ 0 & -s_{23} & c_{23} \end{pmatrix} \begin{pmatrix} c_{13} & 0 & s_{13} e^{-i\delta_{CP}} \\ 0 & 1 & 0 \\ -s_{13} e^{i\delta_{CP}} & 0 & c_{13} \end{pmatrix} \begin{pmatrix} c_{12} & s_{12} & 0 \\ -s_{12} & c_{12} & 0 \\ 0 & 0 & 1 \end{pmatrix} \begin{pmatrix} 1 & 0 & 0 \\ 0 & e^{i\alpha} & 0 \\ 0 & 0 & e^{i\beta} \end{pmatrix}, \quad (2.28)$$

764 where  $c_{ij} \equiv \cos \theta_{ij}$  and  $s_{ij} \equiv \sin \theta_{ij}$ . This matrix is analogous to the Cabibbo-Kobayashi-  
 765 Maskawa (CKM) matrix in the quark sector. If neutrinos are Dirac fermions, we can  
 766 drop the Majorana phases in the PMNS matrix, as in this case we can perform the  
 767 phase redefinitions. However, these phases play no role on the neutrino oscillation  
 768 phenomenology.

769 In the case that additional sterile neutrino states are present, the full leptonic mixing  
 770 matrix would not be unitary in general. For instance, in the see-saw scenario, the  $3 \times 3$   
 771 submatrix for the three light Majorana neutrinos is not unitary. However, the deviations  
 772 from unitarity are of the order  $\mathcal{O}(M_D/M_N)$ , and therefore expected to be negligible.

## Chapter 2. Neutrino physics

### 2.4.1 Oscillations in vacuum

Consider the case where a neutrino of flavour  $\alpha$  is produced at  $t = 0$ , and then it propagates through vacuum. Such a state will evolve in time according to the relation:

$$|\nu_\alpha(\vec{x}, t)\rangle = \sum_{i=1}^3 U_{\alpha i}^* e^{-i(E_i t - \vec{p}_i \cdot \vec{x})} |\nu_i(\vec{x} = \vec{0}, t = 0)\rangle, \quad (2.29)$$

in the plane wave approximation, as the mass eigenstates are also eigenstates of the free Hamiltonian.

This way, the probability for the neutrino to transition from flavour  $\alpha$  to flavour  $\beta$  will be given by:

$$\begin{aligned} P(\nu_\alpha \rightarrow \nu_\beta) &= |\langle \nu_\beta | \nu_\alpha(\vec{x}, t) \rangle|^2 = \left| \sum_{i=1}^3 \sum_{j=1}^3 U_{\alpha i}^* U_{\beta j} e^{-i(E_i t - \vec{p}_i \cdot \vec{x})} \langle \nu_j | \nu_i \rangle \right|^2 \\ &= \left| \sum_{i=1}^3 U_{\alpha i}^* U_{\beta i} e^{-i(E_i t - \vec{p}_i \cdot \vec{x})} \right|^2, \end{aligned} \quad (2.30)$$

where we have used the orthogonality relation  $\langle \nu_i | \nu_j \rangle = \delta_{ij}$ . A usual approximation to take at this point is to consider ultra-relativistic neutrinos, i.e.  $p_i \simeq E$ , so we can write the dispersion relations as:

$$E_i = \sqrt{p_i^2 + m_i^2} \approx E + \frac{m_i^2}{2E}. \quad (2.31)$$

In the end, assuming  $t \approx L$  where  $L$  is the distance between the production and the detection points, the probability for the  $\nu_\alpha \rightarrow \nu_\beta$  transition becomes:

$$\begin{aligned} P(\nu_\alpha \rightarrow \nu_\beta) &= \sum_{i,j} U_{\alpha i}^* U_{\beta i} U_{\alpha j} U_{\beta j}^* e^{-i \frac{\Delta m_{ij}^2}{2E} L} \\ &= \delta_{\alpha\beta} - 4 \sum_{i < j} \Re [U_{\alpha i}^* U_{\beta i} U_{\alpha j} U_{\beta j}^*] \sin^2 \left( \frac{\Delta m_{ij}^2}{4E} L \right) \\ &\quad + 2 \sum_{i < j} \Im [U_{\alpha i}^* U_{\beta i} U_{\alpha j} U_{\beta j}^*] \sin \left( \frac{\Delta m_{ij}^2}{2E} L \right), \end{aligned} \quad (2.32)$$

## 2.4. Neutrino oscillation formalism

785 where  $\Delta m_{ij}^2$  is the difference of the squared masses of the  $j$ th and  $i$ th neutrino mass  
 786 eigenvalues. At this point, it is usual to write the phase responsible for the oscillations  
 787 as:

$$\Delta_{ij} \equiv \frac{\Delta m_{ij}^2}{4E} L \simeq 1.27 \frac{\Delta m_{ij}^2}{(\text{eV}^2)} \frac{L}{(\text{km})} \frac{(\text{GeV})}{E}. \quad (2.33)$$

788 Notice that, in the case of antineutrinos, the only difference would be the sign of the  
 789 last term in the oscillation probability. As the process  $\bar{\nu}_\alpha \rightarrow \bar{\nu}_\beta$  is the CP-mirror image  
 790 of  $\nu_\alpha \rightarrow \nu_\beta$ , the differences between their oscillation probabilities would be a measure of  
 791 CP symmetry violation:

$$\begin{aligned} A_{CP}^{\alpha\beta} &= P(\nu_\alpha \rightarrow \nu_\beta) - P(\bar{\nu}_\alpha \rightarrow \bar{\nu}_\beta) \\ &= 4 \sum_{i < j} \Im \left[ U_{\alpha i}^* U_{\beta i} U_{\alpha j} U_{\beta j}^* \right] \sin 2\Delta_{ij}. \end{aligned} \quad (2.34)$$

792 Assuming that CPT invariance holds, then the following relation must be true:

$$P(\nu_\alpha \rightarrow \nu_\beta) = P(\bar{\nu}_\beta \rightarrow \bar{\nu}_\alpha), \quad (2.35)$$

793 as these two processes are related by the CPT symmetry. From the definition of probability,  
 794 we also must have:

$$\sum_\beta P(\nu_\alpha \rightarrow \nu_\beta) = \sum_\beta P(\bar{\nu}_\alpha \rightarrow \bar{\nu}_\beta) = 1, \quad (2.36)$$

795 where the sum includes all flavours, including  $\alpha$ . From these two constraints, one can  
 796 probe that:

$$A_{CP}^{\alpha\beta} = -A_{CP}^{\beta\alpha}, \quad (2.37)$$

797 and in particular:

$$A_{CP}^{\alpha\alpha} = 0. \quad (2.38)$$

798 A direct consequence of this last relation is that there are no observable CP-violating  
 799 effects in the so-called disappearance experiments. One needs to perform appearance  
 800 experiments, where the flavour detected is different from the original flavour, in order

## Chapter 2. Neutrino physics

801 to measure the CP asymmetry. Neutrino experiments often report the amount of CP-  
802 violation through the Jarlskog invariant. In terms of the parametrisation typically used  
803 to write the PMNS matrix, it is given by:

$$J = \frac{1}{8} \cos \theta_{13} \sin 2\theta_{12} \sin 2\theta_{13} \sin 2\theta_{23} \sin \delta_{CP}. \quad (2.39)$$

804 The Jarlskog invariant can be used to compare the amount of CP-violation in the lepton  
805 and the quark sectors, where  $J = 3.12^{+0.13}_{-0.12} \times 10^{-5}$  in the latter [45].

### 806 2.4.2 Oscillations in matter

807 When neutrinos propagate through matter, their oscillation can be affected in mainly  
808 two ways. First, neutrinos can inelastically scatter with nuclei, thus destroying the  
809 coherent propagation of their quantum state. Nevertheless, in most cases this effect is  
810 negligible (even in very dense mediums like the core of the Sun). Second, neutrinos can  
811 also experience coherent or forward scatterings, that can affect their oscillation but not  
812 lose the coherent propagation of the state.

813 The first proposed model to account for neutrino oscillations in matter was proposed  
814 by Mikhaev, Smirnov and Wolfenstein (MSW) [46]. It relies on the fact that, as the  
815 only charged lepton present in ordinary matter is the electron, electron neutrinos can  
816 undergo both charged and neutral-current interactions with matter whereas for muon  
817 and tau neutrinos just neutral currents are possible.

818 An illustrative way to introduce the MSW mechanism is by considering the two  
819 flavours case. It can be shown that the evolution of the two flavour eigenstates in vacuum  
820 is given by the following time-dependent Schrödinger equation:

$$i \frac{d}{dt} \begin{pmatrix} \nu_e \\ \nu_\mu \end{pmatrix} = H_V \begin{pmatrix} \nu_e \\ \nu_\mu \end{pmatrix}, \quad (2.40)$$

## 2.4. Neutrino oscillation formalism

821 with a vacuum Hamiltonian given by:

$$H_V = \frac{\Delta m^2}{4E} \begin{pmatrix} -\cos 2\theta & \sin 2\theta \\ \sin 2\theta & \cos 2\theta \end{pmatrix}, \quad (2.41)$$

822 where  $\Delta m^2$  is the mass splitting between the two neutrino states and  $\theta$  the only mixing  
 823 angle. For simplicity, I omit the terms of the Hamiltonian that are proportional to the  
 824 identity, as they do not affect the oscillation phenomenology.

825 The NC contribution to the matter potential is identical for all the flavours, and has  
 826 the form:

$$V_{\text{NC}} = -\frac{G_F}{\sqrt{2}} N_n(x), \quad (2.42)$$

827 where  $G_F$  is the Fermi constant and  $N_n(x)$  the local neutron density. Because it is  
 828 common to all flavours, I do not take it into account in the effective Hamiltonian, as it  
 829 would appear as a term proportional to the identity. The CC component only affects  
 830 the electron neutrino (and antineutrino). It can be written as:

$$V_{\text{CC}} = \pm \sqrt{2} G_F N_e(x), \quad (2.43)$$

831 with  $N_e(x)$  being the local electron density in the material. In the end, the effective  
 832 Hamiltonian which describes the propagation of the flavour eigenstates in matter only  
 833 contains an extra  $\nu_e - \nu_e$  element:

$$H_M = H_V + \begin{pmatrix} V_{\text{CC}} & 0 \\ 0 & 0 \end{pmatrix}. \quad (2.44)$$

834 The solution to the Schrödinger equation greatly simplifies if one considers the case  
 835 of a constant matter density. In that case, the effective Hamiltonian can be diagonalised,  
 836 obtaining the effective neutrino mass eigenstates in matter. It can be re-written in the  
 837 same form as the vacuum Hamiltonian:

$$H_M = \frac{\Delta m_m^2}{4E} \begin{pmatrix} -\cos 2\theta_m & \sin 2\theta_m \\ \sin 2\theta_m & \cos 2\theta_m \end{pmatrix}, \quad (2.45)$$

## Chapter 2. Neutrino physics

838 where the effective mass splitting and the effective mixing angle are given by:

$$\begin{aligned}\Delta m_m^2 &= \lambda \Delta m_m^2, \\ \sin 2\theta_m &= \frac{\sin 2\theta_m}{\lambda}\end{aligned}\tag{2.46}$$

839 with:

$$\begin{aligned}\lambda &= \sqrt{(\cos 2\theta - A)^2 + \sin^2 2\theta}, \\ A &= \pm \frac{2\sqrt{2}G_F N_e E}{\Delta m^2}.\end{aligned}\tag{2.47}$$

840 In terms of the effective matter oscillation parameters, the transition probability

841  $\nu_e \rightarrow \nu_\mu$  (in the two flavour approximation) reads:

$$P(\nu_e \rightarrow \nu_\mu) = \sin^2 2\theta_m \sin^2 \left( \frac{\Delta m_m^2}{2E} L \right)\tag{2.48}$$

842 From this last equation one can see that, when  $\cos 2\theta = A > 0$  the oscillations are

843 greatly enhanced. This effect is known as the MSW resonance. For the neutrinos, this

844 resonant condition is only satisfied if  $\Delta m^2 > 0$  (the opposite is true for antineutrinos).

845 This is can be exploited by long baseline experiments, which can gain sensitivity to the

846 neutrino mass hierarchy through matter effects.

### 847 2.4.3 Current status of neutrino oscillations

848 A wide range of neutrino experiments provide experimental input to the neutrino

849 oscillation framework, both using natural or synthetic neutrino sources. The results

850 from one of the neutrino global fit analyses, shown in Tab. 2.3 <sup>1</sup>, summarise well our

851 current understanding of the different oscillation parameters.

852 **Solar neutrino experiments** detect neutrinos produced in thermonuclear reactions

853 inside the Sun, mainly from the so-called *pp* chain and the CNO cycle. These neutrinos

854 have a typical energy in the range from 0.1 to 20 MeV. These experiments (Homestake

---

<sup>1</sup>These are the results reported during M. Tórtola's talk at Neutrino 2024 (see this link). I need to keep an eye and see if they publish these or other updated results in the near future.

## 2.5. Open questions in the neutrino sector

[47], GALLEX [26], SAGE [25], Borexino [48], Super-Kamiokande [49] and SNO [50]) provide the best sensitivities to  $\theta_{12}$  and  $\Delta m_{21}^2$ .

**Atmospheric neutrino experiments** detect the neutrino flux produced when cosmic rays scatter with particles in Earth's atmosphere. These collisions generate particle showers that eventually produce electron and muon neutrinos (and antineutrinos). Their energies range from few MeV to about  $10^9$  GeV. Experiments, like Super-Kamiokande [51] and IceCube [52] use atmospheric neutrinos to measure oscillations and are specially sensitive to  $\theta_{23}$  and  $\Delta m_{32}^2$ .

**Reactor neutrino experiments** look for the  $\bar{\nu}_e$  spectrum produced by nuclear reactors, with energies in the MeV scale. Depending on the distance to the source, long-baseline experiments like KamLAND [53] are sensitive to the solar mass splitting  $\Delta m_{21}^2$  whereas much shorter baseline experiment such as RENO [54] or DayaBay [55] measure  $\theta_{13}$  and  $\Delta m_{31}^2$ .

**Accelerator experiments** measure neutrino fluxes generated in particle accelerators. Usually mesons are produced in the accelerator to be focused into a beam, then some decay to muon neutrinos and the rest are absorbed by a target. Depending on the configuration one can obtain a beam made of mostly neutrinos or antineutrinos. The typical energies of these neutrinos are in the GeV range. Experiments such as NOvA [56], T2K [57], MINOS [58], OPERA [59] and K2K [60] (and in the future DUNE [61]) are primarily sensitive to  $\theta_{13}$ ,  $\theta_{23}$  and  $\Delta m_{32}^2$ . Also, in the coming years DUNE [61] and Hyper-Kamiokande [62] will be sensitive to  $\delta_{CP}$ .

## 2.5 Open questions in the neutrino sector

A crucial question that remains open these days, and is of vital importance for oscillation phenomena, is whether the mass eigenvalue  $\nu_3$  is the heaviest (what we call normal ordering) or the lightest (referred to as inverted ordering) of the mass eigenstates. In other words, this means that we do not know the sign of  $\Delta m_{32}^2$ , so we can either have  $m_1 < m_2 < m_3$  (NO) or  $m_3 < m_1 < m_2$  (IO).

## Chapter 2. Neutrino physics

**Table 2.3:** Summary of neutrino oscillation parameters determined in the Neutrino Global Fit of 2020 [14].

Parameter	Best fit $\pm 1\sigma$	$3\sigma$ range
$\Delta m_{21}^2$ [eV $^2 \times 10^{-5}$ ]	$7.55^{+0.22}_{-0.20}$	6.98 – 8.19
$ \Delta m_{31}^2 $ [eV $^2 \times 10^{-3}$ ] (NO)	$2.51^{+0.02}_{-0.03}$	2.43 – 2.58
$ \Delta m_{31}^2 $ [eV $^2 \times 10^{-3}$ ] (IO)	$2.41^{+0.03}_{-0.02}$	2.34 – 2.49
$\sin^2 \theta_{12}/10^{-1}$	$3.04 \pm 0.16$	2.57 – 3.55
$\sin^2 \theta_{23}/10^{-1}$ (NO)	$5.64^{+0.15}_{-0.21}$	4.23 – 6.04
$\sin^2 \theta_{23}/10^{-1}$ (IO)	$5.64^{+0.15}_{-0.18}$	4.27 – 6.03
$\sin^2 \theta_{13}/10^{-2}$ (NO)	$2.20^{+0.05}_{-0.06}$	2.03 – 2.38
$\sin^2 \theta_{13}/10^{-2}$ (IO)	$2.20^{+0.07}_{-0.04}$	2.04 – 2.38
$\delta_{CP}/\pi$ (NO)	$1.12^{+0.16}_{-0.12}$	0.76 – 2.00
$\delta_{CP}/\pi$ (IO)	$1.50^{+0.13}_{-0.14}$	1.11 – 1.87

882 Another big puzzle is related to the value of  $\delta_{CP}$ . Nowadays it is poorly constrained,  
 883 with all values between  $\pi$  and  $2\pi$  being consistent with data. A prospective measurement  
 884 different from  $\delta_{CP} = 0, \pi$  will predict CP-violation in the leptonic sector, and thus  
 885 contribute along with the one measured in the quark sector to the total amount of  
 886 CP-violation. Although it is true that these two contributions by themselves are not  
 887 enough to explain the matter anti-matter asymmetry in our universe, the amount of  
 888 CP-violation in the leptonic sector can be key to explain such imbalance.

889 Both of these questions, because of their nature, could be understood thanks to  
 890 future oscillation experiments.

891 Notwithstanding, there are other mysteries that can not be unveiled just by conducting  
 892 oscillation experiments, as certain quantities do not influence these phenomena. Among  
 893 these there is the question of the absolute values of the neutrino masses. Depending  
 894 on the value of the lightest of the neutrino masses we can have different mass spectra,  
 895 from hierarchical  $m_1 \ll m_2 < m_3$  (NO) or  $m_3 \ll m_1 < m_2$  (IO) to quasi-degenerate  
 896  $m_1 \simeq m_2 \simeq m_3$ .

897 Other open question concerns the nature itself of the neutrinos. If neutrinos are Dirac  
 898 particles then their mass term can be generated through the usual Higgs mechanism

## 2.6. Neutrino interactions

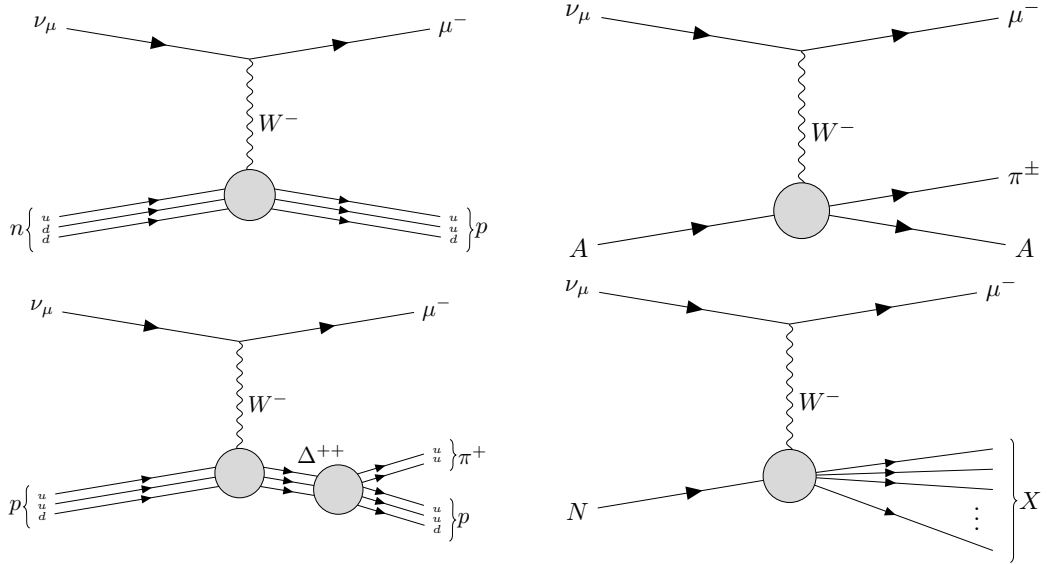


**Figure 2.4**

899 by adding right-handed neutrino fields. However, if they are Majorana particles and  
 900 therefore their own antiparticles, there is no need to add extra fields to have the mass  
 901 term in the Lagrangian. Experiments like SuperNEMO [63], SNO+ [64] and NEXT  
 902 [65], which search for neutrino-less double beta decay, will be able to determine whether  
 903 neutrinos are Dirac or Majorana.

904 **2.6 Neutrino interactions**

## Chapter 2. Neutrino physics

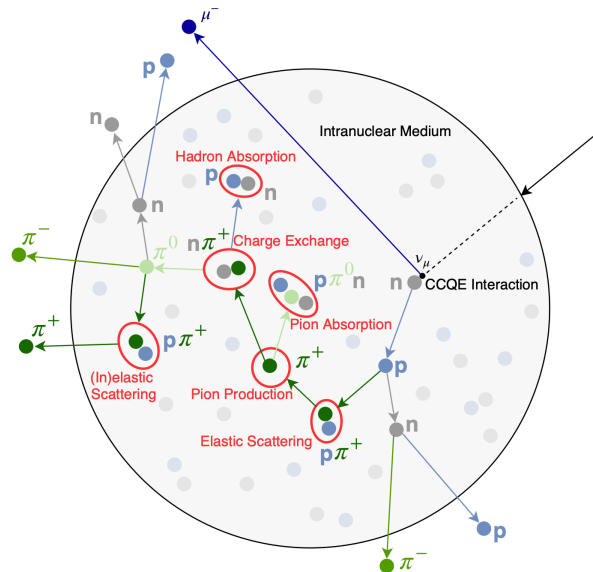


**Figure 2.5:** Schematic representation of a  $\nu_\mu$  CCQE interaction with a neutron inside a nucleus. The reaction produces a muon and a proton, which travel through the nuclear medium. The outgoing proton undergoes various kinds of hadronic FSIs on its way out. Figure taken from Ref. [66].

905 Chapter 3

906 The Deep Underground Neutrino  
907 Experiment

908 The Deep Underground Neutrino Experiment (DUNE) is a next generation long-baseline  
909 neutrino experiment [67]. It will aim to address several questions in neutrino physics,  
910 study neutrinos from astrophysical sources and search for beyond the standard model  
911 physics.

912 This chapter reviews the main goals of the DUNE experiment, the design of the far  
913 detector modules and their data acquisition (DAQ) system, and the role that the near  
914 detector plays in the physics program of DUNE.

915 3.1 Overview

916 The main physics goals of DUNE are:

- 917 • measure the neutrino mass hierarchy, the amount of CP violation in the leptonic  
918 sector and the  $\theta_{23}$  octant,
- 919 • detect rare low energy neutrino events, like neutrinos from supernova bursts, and
- 920 • search for proton decay and other beyond the standard model phenomena.

## Chapter 3. The Deep Underground Neutrino Experiment

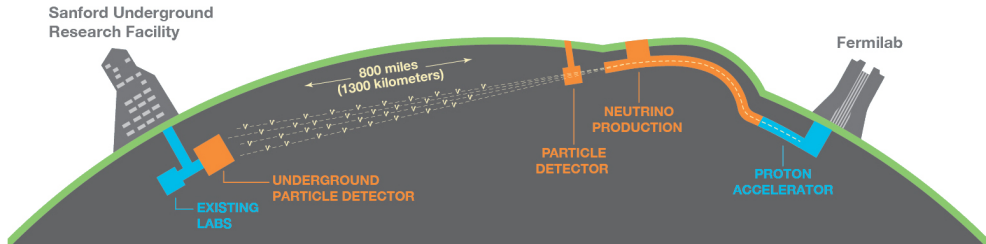


**Figure 3.1:** Schematic diagram of the DUNE experiment and the LBNF beamline [67].

The design of DUNE has been tailored with these goals in mind. It will consist of two neutrino detectors. A near detector (ND) complex will be placed at Fermilab, 574 m downstream of the neutrino production point, whereas a larger far detector (FD) will be built in the Sandford Underground Research Facility (SURF), South Dakota, approximately 1300 km away. Figure 3.1 shows a simplified view of the various components of DUNE (not to scale).

The beam neutrinos will be provided by the Long-Baseline Neutrino Facility (LBNF) beamline, the multi-megawatt wide-band neutrino beam planned for Fermilab. It will produce neutrinos travelling in the direction of SURF, with the capability to switch between neutrino and antineutrino mode.

Before arriving to the FD, the neutrino beam meets the ND complex, which serves as the experiment's control. The design of the DUNE ND is mainly driven by the needs of the oscillation physics program, as its main role is to measure the unoscillated neutrino energy spectra. From these we can predict the unoscillated spectra at the FD, which can be compared to the spectra measured at the FD to extract the oscillation parameters. Additionally, the ND has a physics programme of its own, including cross section measurements and BSM physics searches.

The technology chosen for the FD modules of DUNE is the liquid Argon time projection chamber (LArTPC). Its four modules will record neutrino interactions from the accelerator-produced beam arriving at predictable times. As it also aims at recording rare and low energy events, like supernovae and solar neutrinos, the FD requires trigger

## 3.2. Physics goals of DUNE

**Table 3.1:** Summary of the two-phased plan for DUNE. Adapted from Ref. [68].

Parameter	Phase I	Phase II	Benefit
FD mass	20 kt fiducial	40 kt fiducial	FD statistics
Beam power	up to 1.2 MW	2.4 MW	FD statistics
ND config.	ND-LAr, TMS, SAND	ND-LAr, ND-GAr, SAND	Systematic constraints

942 schemes which can deal with both kinds of physics, and also maximum uptime.

943 DUNE is planned to be built using a staged approach consisting on two phases,  
944 which are summarised in Tab. 3.1. Phase I consists of a FD with 50% of the total  
945 fiducial mass, a reduced version of the ND complex and a 1.2 MW proton beam. It will  
946 be sufficient to achieve some early physics goals, like the determination of the neutrino  
947 mass ordering. For its Phase II, DUNE will feature the full four FD modules, a more  
948 capable ND and a 2.4 MW proton beam. The physics milestones for the two phases are  
949 given in Tab. 3.2, in a staging scenario which assumes that Phase II is completed after  
950 6 years of operation.

951 A summary of the DUNE science program can be found in the DUNE FD Technical  
952 Design Report (TDR) Volume I [67]. For a detailed discussion on the two-phased  
953 approach the reader is referred to the DUNE Snowmass 2021 report [68].

## 954 3.2 Physics goals of DUNE

955 As noted in the literature (see for instance Ref. [14] for a review), the parameter space of  
956 the neutrino oscillation phenomena within the three-flavour picture is quite constrained  
957 by current experimental data. However, there are still crucial open questions, like the  
958 mass ordering, the value of  $\delta_{CP}$  or the  $\theta_{23}$  octant. One of the main goals of DUNE is to  
959 determine precisely the values of these parameters [69].

960 To address these questions DUNE can look to the subdominant oscillation channel  
961  $\nu_\mu \rightarrow \nu_e$  ( $\bar{\nu}_\mu \rightarrow \bar{\nu}_e$ ) and study the energy dependence of the  $\nu_e$  ( $\bar{\nu}_e$ ) appearance probability.  
962 When we focus on the antineutrino channel  $\bar{\nu}_\mu \rightarrow \bar{\nu}_e$  there is a change in the sign of  $\delta_{CP}$ ,  
963 thus introducing CP-violation. Moreover, due to the fact that there are no positrons in

### Chapter 3. The Deep Underground Neutrino Experiment

**Table 3.2:** Exposure and time required to achieve the different physics milestones of the two phases. The predictions assume a Phase II staging scenario where FD modules 3 and 4 are deployed in years 4 and 6 and both the beam and ND are upgraded after 6 years. Adapted from Ref. [68].

Stage	Physics milestone	Exposure (kt-MW-years)	Years (staged)
Phase I	$5\sigma$ MO ( $\delta_{CP} = -\pi/2$ )	16	1-2
	$5\sigma$ MO (100% of the $\delta_{CP}$ values)	66	3-5
	$3\sigma$ CPV ( $\delta_{CP} = -\pi/2$ )	100	4-6
Phase II	$5\sigma$ CPV ( $\delta_{CP} = -\pi/2$ )	334	7-8
	$\delta_{CP}$ resolution of 10 degrees ( $\delta_{CP} = 0$ )	400	8-9
	$5\sigma$ CPV (50% of the $\delta_{CP}$ values)	646	11
	$3\sigma$ CPV (75% of the $\delta_{CP}$ values)	936	14
	$\sin^2(2\theta_{13})$ resolution of 0.004	1079	16

964 the composition of Earth, there is a sign difference for the matter effect contribution  
 965 when looking to the antineutrino channel. This asymmetry is proportional to the baseline  
 966 length  $L$  and is sensitive to the sign of  $\Delta m_{31}^2$ , and thus to the neutrino mass ordering.

967 Another of the main physics goals of DUNE is the search for baryon-number violating  
 968 processes. Specifically, it will try to answer the question of whether protons are stable  
 969 or not. There is no symmetry argument that forbids protons from decaying, but its  
 970 apparent stability seems to suggest that baryon number is conserved [70]. However,  
 971 proton decay is a usual feature of grand-unified theories, where electromagnetic, weak  
 972 and strong interactions are unified above a certain energy scale [71].

973 As the energy deposition scale for this kind of searches is nearly the same as the one  
 974 for long-baseline neutrino oscillations, DUNE will be able to look for them. It has several  
 975 advantages over other experiments, such as excellent imaging and particle identification,  
 976 which can be translated to lower backgrounds.

977 The last of the main objectives of DUNE is the detection of neutrinos originated in  
 978 supernovae explosions, what is called a supernova neutrino burst (SNB). These neutrinos  
 979 carry with them information about the core-collapse process, from the progenitor to the  
 980 explosion and the remnant; but also may have information about new exotic physics. So  
 981 far, the only neutrino events ever recorded from such a process were a few dozens of  $\bar{\nu}_e$

### 3.3. LBNF beamline

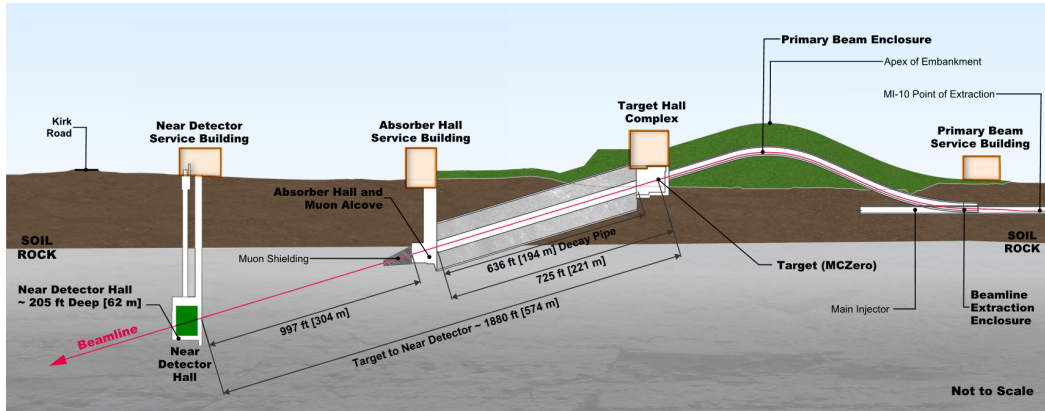


**Figure 3.2:** Schematic longitudinal section of the LBNF beamline at Fermilab (not to scale). Figure taken from Ref. [74].

982 events from the 1987A supernova located in the Magellanic Cloud, 50 kpc away from  
 983 Earth [72, 73].

984 DUNE aims to collect SNB events. Although these are quite rare, as the expected  
 985 supernovae explosion events are about one every few decades for our galaxy and  
 986 Andromeda, the long lifetime of the experiment (around a few decades as well) makes it  
 987 reasonable to expect some. Nowadays the main sensitivity to SNB of most experiments  
 988 is to the  $\bar{\nu}_e$  through inverse beta decay. One of the advantages of DUNE is its expected  
 989 sensitivity to  $\nu_e$ , since the dominant channel will be  $\nu_e$  CC scattering.

990 Moreover, due to the stringent requirements that the main physics goals set for  
 991 DUNE, it will allow also to perform searches for all kind of BSM physics. Among  
 992 others, DUNE will be able to look for: active-sterile neutrino mixing, non-unitarity of  
 993 the PMNS matrix, non-standard interactions, Lorentz and CPT violations, neutrino  
 994 trident production, light-mass DM, boosted DM and heavy neutral leptons. The reader  
 995 is referred to the DUNE FD TDR Volume II [69] for a full discussion of the physics  
 996 scope of DUNE.

### 997 3.3 LBNF beamline

998 The LBNF project is responsible for producing the neutrino beam for the DUNE detectors.  
 999 A detailed discussion of the LBNF program can be found in the DUNE/LBNF CDR

### Chapter 3. The Deep Underground Neutrino Experiment

1000 Volume III [74].

1001 A schematic diagram of the longitudinal section of the LBNF beamline is shown in  
 1002 Fig. 3.2. First, a beam of 60 – 120 GeV protons is extracted from the Fermilab Main  
 1003 Injector. This beam is aimed towards the target area, where it collides with a cylindrical  
 1004 graphite target to produce pions and kaons.

1005 The diffuse, secondary beam of particles is focused by a pair of magnetic horns.  
 1006 These select the positively charged particles when operated in Forward Horn Current  
 1007 (FHC) mode, or the negatively charged ones when the current is reversed, also known as  
 1008 Reverse Horn Current (RHC) mode. The focused secondary beam then enters a 194 m  
 1009 decay pipe where the pions and kaons will predominantly produce  $\mu^+\nu_\mu$  pairs when in  
 1010 FHC mode (or  $\mu^-\bar{\nu}_\mu$  in RHC mode).

1011 At the end of the decay pipe a hadron absorber removes the undecayed hadrons and  
 1012 muons from the beam, which reduces the  $\nu_e$  ( $\bar{\nu}_e$ ) and  $\bar{\nu}_\mu$  ( $\nu_\mu$ ) contamination coming  
 1013 from the  $\mu^+$  ( $\mu^-$ ) decays. The resulting neutrino flux at the FD is shown in Fig. 3.3,  
 1014 both for FHC (left) and RHC (right) modes. These predictions show the intrinsic  $(\bar{\nu})_e$   
 1015 contamination and wrong sign component from wrong sign and neutral meson decays,  
 1016 as well as muons decaying before reaching the absorber.

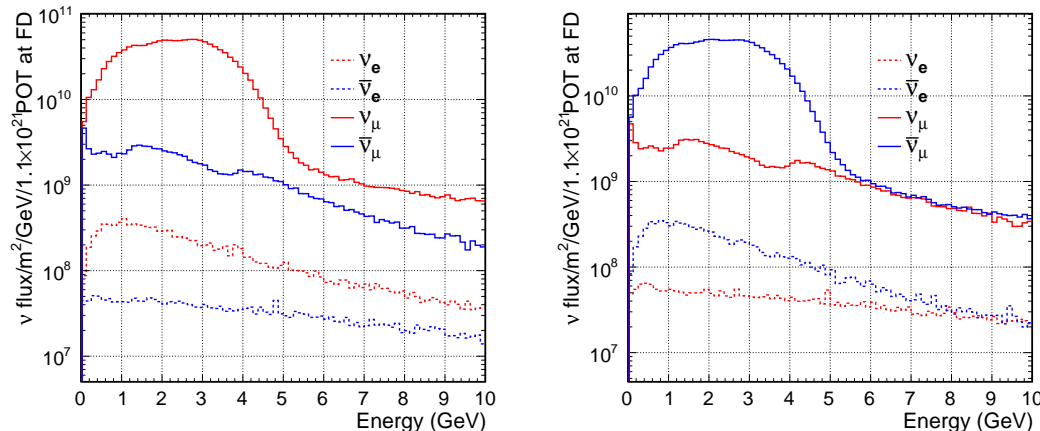


**Figure 3.3:** Predicted neutrino fluxes at the FD in FHC mode (left panel) and RHC mode (right panel). Figures taken from Ref. [69].

### 3.4. Near Detector

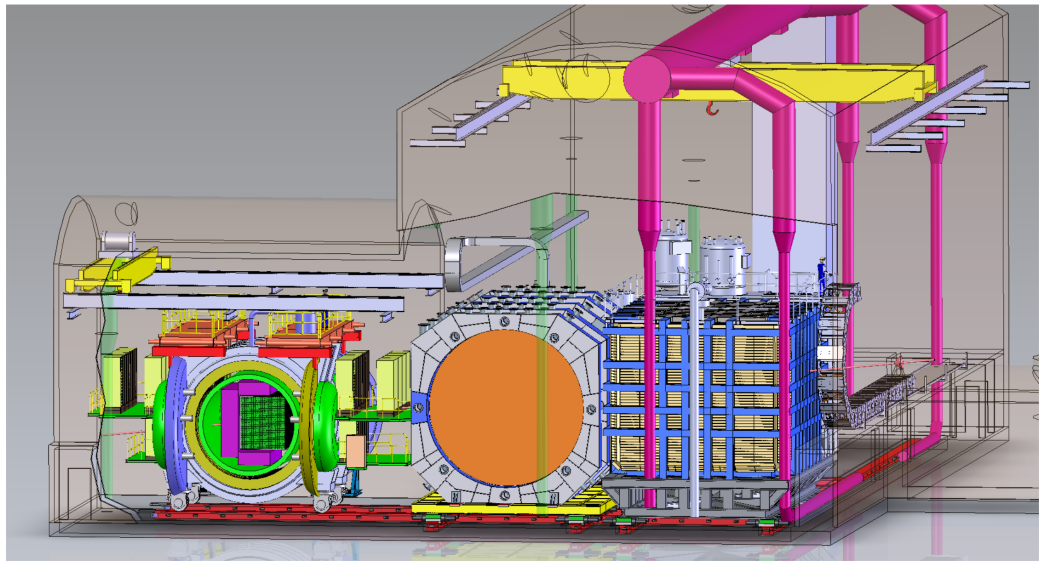


**Figure 3.4:** Representation of the ND hall in Phase II, showing the different subcomponents. From right to left, in the direction of the beam, we have ND-LAr, ND-GAr and SAND. Figure taken from Ref. [75].

## 1017 3.4 Near Detector

1018 To estimate the oscillation parameters we measure the neutrino energy spectra at the FD.  
1019 This reconstructed energy arises from a convolution of the neutrino flux, cross section,  
1020 detector response and the oscillation probability. Using theoretical and empirical models  
1021 to account for the other effects, one can extract the oscillation probability using the  
1022 measurement. However, these models have associated a number of uncertainties that  
1023 are then propagated to the oscillation parameters.

1024 One of the main roles of the ND is to measure the neutrino interaction rates before  
1025 the oscillation effects become relevant, i.e. close to the production point. By measuring  
1026 the  $\nu_\mu$  and  $\nu_e$  energy spectra, and that of their corresponding antineutrinos, at the ND  
1027 we can constrain the model uncertainties. A complete cancellation of the uncertainties  
1028 when taking the ratio between the FD and ND measurements is not possible, as that  
1029 would require both detectors to have identical designs and the neutrino fluxes to be  
1030 the same. Because of the distance, the flux probed by the FD will have a different  
1031 energy and flavour composition than that at the ND, as neutrinos oscillate and the beam

## Chapter 3. The Deep Underground Neutrino Experiment

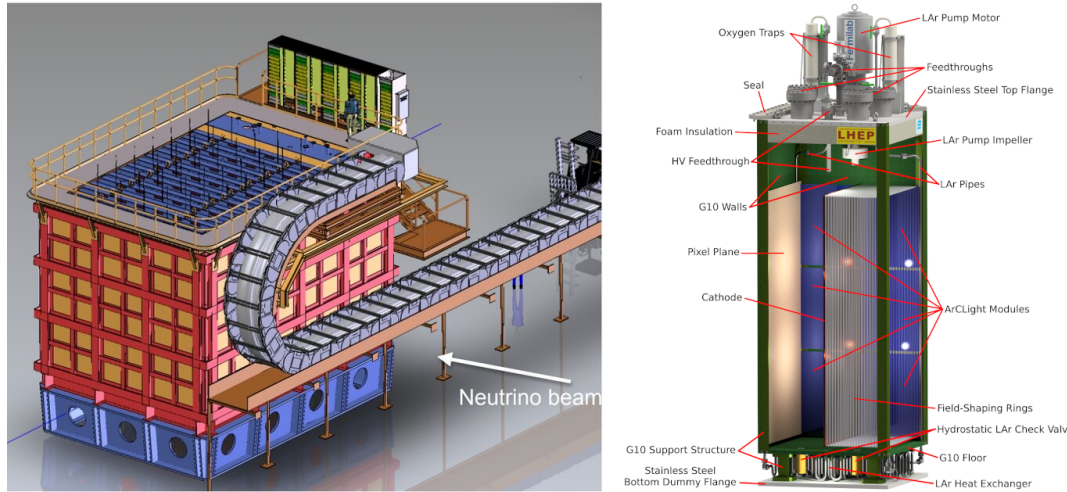


**Figure 3.5:** Schematic representation of the external components of ND-LAr, including the cryostat and the PRISM movable system (left) and detailed drawing of one ArgonCube module (right). Figure adapted from Ref. [67].

spreads. The differences in the flux also determine the design of the detectors, therefore the ND is limited in its capability to match the FD design.

Nevertheless, having a highly capable ND, DUNE can minimise the systematic uncertainties affecting the observed neutrino energy. The ND data can be used to tune the model parameters by comparison with the prediction. Then, one uses the tuned model to predict the unoscillated FD spectra. Comparing the prediction with the measured spectra it is possible to extract the oscillation parameters.

Additionally, the ND will have a physics program of its own. In particular, it will measure neutrino cross sections that will then be used to constrain the model used in the long-baseline oscillation analysis. It will also be used to search for BSM phenomena such as heavy neutral leptons, dark photons, millicharged particles, etc.

The DUNE ND can be divided in three main components, a LArTPC known as ND-LAr, a magnetised muon spectrometer, which will be the Temporary Muon Spectrometer (TMS) in Phase I and ND-GAr in Phase II, and the System for on-Axis Neutrino Detection (SAND). The layout of the Phase II DUNE ND can be seen in Fig. 3.4. The first two components of the ND will be able to move off-axis, in what is called the Precision Reaction-Independent Spectrum Measurement (PRISM) concept. More details

### 3.4. Near Detector

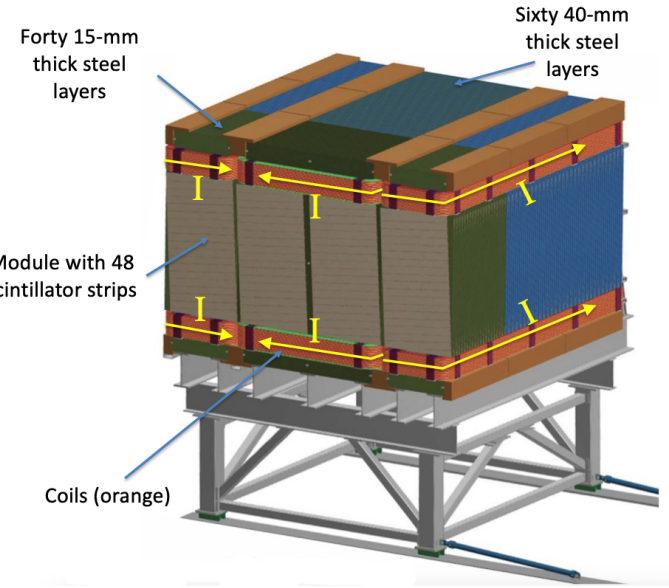


**Figure 3.6:** Schematic view of the TMS detector, highlighting its main parts. Figure adapted from Ref. [67].

1049 on the purpose and design of the ND can be found in the DUNE ND Conceptual Design  
 1050 Report (CDR) [75].

#### 1051 3.4.1 ND-LAr

1052 ND-LAr is a LArTPC, as the ND needs a LAr component to reduce cross section and  
 1053 detector systematic uncertainties in the oscillation analysis. However, its design differs  
 1054 significantly from those proposed for the FD modules. Because of the high event rates  
 1055 at the ND, approximately 55 neutrino interaction events per  $10 \mu\text{s}$  spill, ND-LAr will be  
 1056 built in a modular way. Each of the modules, based on the ArgonCube technology, is a  
 1057 fully instrumented, optically isolated TPC with a pixelated readout. The pixelisation  
 1058 allows for a fully 3D reconstruction and the optical isolation reduces the problems due  
 1059 to overlapping interactions. Figure 3.5 shows a representation of the external parts of  
 1060 ND-LAr (left) and a detailed diagram of an ArgonCube module (right).

1061 With a fiducial mass of 67 t and dimensions  $7 \text{ m} (\text{w}) \times 3 \text{ m} (\text{h}) \times 5 \text{ m} (\text{l})$ , ND-LAr  
 1062 will be able to provide high statistics and contain the hadronic systems from the beam  
 1063 neutrino interactions, but muons with a momentum higher than 0.7 GeV will exit the

## Chapter 3. The Deep Underground Neutrino Experiment

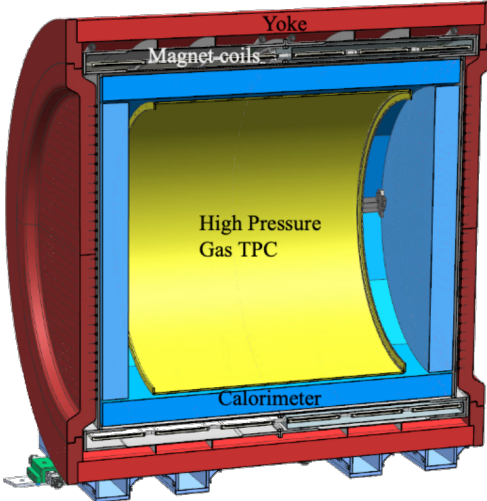


**Figure 3.7:** Cross section of the ND-GAr geometry, showing the HPgTPC, ECal and magnet. Figure adapted from Ref. [76].

1064 detector.

### 1065 3.4.2 TMS/ND-GAr

1066 To accurately estimate the neutrino energy, the momentum of the outgoing muons needs  
1067 to be determined. That is the reason why a muon spectrometer is needed downstream  
1068 of ND-LAr.

1069 In Phase I that role will be fulfilled by TMS. It is a magnetised sampling calorimeter,  
1070 with alternating steel and plastic scintillator layers. Figure 3.6 shows a schematic view  
1071 of the TMS detector. The magnetic field allows a precise measurement of the sign of the  
1072 muon, so one can distinguish between neutrino and antineutrino interactions.

1073 After the Phase II upgrade, TMS will be replaced with a more capable near detector.  
1074 The current technology considered is ND-GAr. This detector is a magnetised, high-  
1075 pressure GAr TPC (often denoted as HPgTPC) surrounded by an electromagnetic  
1076 calorimeter (ECal) and a muon tagger. A cross section of its geometry can be seen  
1077 in Fig. 3.7. ND-GAr will be able to measure the momenta of the outgoing muons  
1078 while also detect neutrino interactions inside the GAr volume. This allows ND-GAr  
1079 to constrain the systematic uncertainties even further, as it will be able to accurately

### 3.4. Near Detector

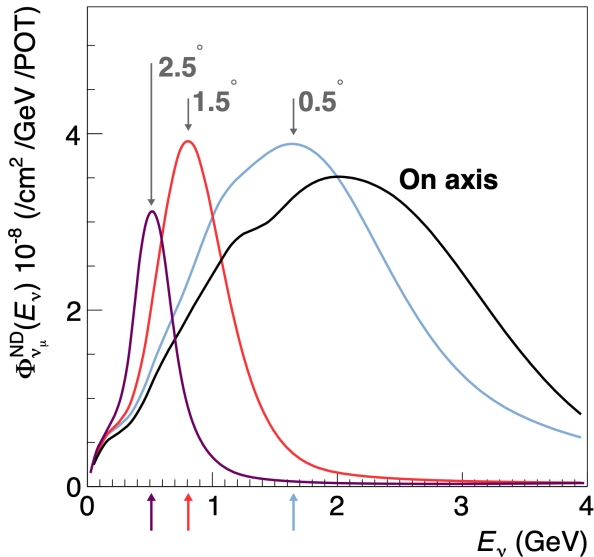


**Figure 3.8:** Predicted beam muon neutrino flux at the ND location for different off-axis positions. Figure taken from Ref. [75].

1080 measure neutrino interactions at low energies thanks to the lower tracking thresholds of  
 1081 GAr.

#### 1082 3.4.3 PRISM

1083 In general, the observed peak neutrino energy of a neutrino beam decreases as the  
 1084 observation angle with respect to the beam direction increases. This feature has been  
 1085 used in other long-baseline neutrino experiments, like T2K ( $2.5^\circ$  off-axis) and NOvA  
 1086 ( $0.8^\circ$  off-axis), to achieve narrower energy distributions. The DUNE PRISM concept  
 1087 exploits this effect using a movable ND. Within PRISM both ND-LAr and the muon  
 1088 spectrometer (TMS in Phase I and ND-GAr in Phase II) can be moved up to  $3.2^\circ$   
 1089 off-axis, equivalent to move the detectors 30.5 m laterally through the ND hall.

1090 This allows to record additional data samples with different energy compositions.  
 1091 Figure 3.8 compares the on-axis muon neutrino flux at the ND with the fluxes at different  
 1092 off-axis positions. As the off-axis position increases the neutrino flux becomes closer to  
 1093 a monoenergetic beam with a lower peak energy. These samples can be used to perform  
 1094 a data-driven determination of the relation between true and reconstructed neutrino

### Chapter 3. The Deep Underground Neutrino Experiment

1095 energy, to reduce the dependence on the interaction model. The off-axis samples are  
1096 linearly combined to produce a narrow Gaussian energy distribution centered on a target  
1097 true energy. From the combination coefficients one can build a sample of reconstructed  
1098 neutrino events that will determine the energy mapping.

1099 The PRISM samples will be used to form a flux at the ND location similar in shape  
1100 to the oscillated flux measured by the FD. This method can be used to extract the  
1101 oscillation parameters with minimal input from the neutrino interaction model.

#### 1102 3.4.4 SAND

1103 The role of SAND is to monitor the beam stability by measuring the on-axis neutrino  
1104 energy spectra. As the PRISM program requires that ND-LAr and its downstream  
1105 muon spectrometer spend about half of the time in off-axis positions, it is not possible  
1106 to monitor the stability with the movable detectors. Moreover, for the success of PRISM  
1107 it is essential to have a stable beam configuration, or, at least, a quick assessment and  
1108 modeling of the distortions.

1109 The SAND detector is magnetised, and features an inner low density tracker, a LAr  
1110 target with optical readout and surrounding sampling calorimeter.

### 1111 3.5 A More Capable Near Detector

1112 In DUNE Phase II, a more capable near detector is needed to achieve the ultimate physics  
1113 goals of the experiments. The current leading proposal for this detector is ND-GAr.  
1114 As mentioned previously, it will fulfill the role of TMS, measuring the momentum and  
1115 sign of the charged particles exiting ND-LAr. Additionally, it will be able to measure  
1116 neutrino interactions inside the HPgTPC, achieving lower energy thresholds than those  
1117 of the ND and FD LArTPCs. By doing so ND-GAr will allow to constrain the relevant  
1118 systematic uncertainties for the LBL analysis even further. A detailed discussion on the  
1119 requirements, design, performance and physics of ND-GAr can be found in the DUNE  
1120 ND CDR [75] and the ND-GAr white paper [77].

### 3.5. A More Capable Near Detector

#### 3.5.1 Requirements

The primary requirement for ND-GAr is to measure the momentum and charge of muons from  $\nu_\mu$  and  $\bar{\nu}_\mu$  CC interactions in ND-LAr, in order to measure their energy spectrum. To achieve the sensitivity to the neutrino oscillation parameters described in the DUNE FD TDR Volume II [69], ND-GAr should be able to constrain the muon energy within a 1% uncertainty or better. The main constraint will come from the calibration of the magnetic field, which will be performed using neutral kaon decays in the HPgTPC.

Another requirement for ND-GAr is the precise measurement of neutrino interactions on argon for the energies relevant to the neutrino oscillation program. The goal is to constrain the cross section systematic uncertainties in the regions of phase space that are not accessible to ND-LAr. This requires the kinematic acceptance for muons in ND-GAr to exceed that of ND-LAr, being comparable to the one observed in the FD.

ND-GAr should also be able to help establishing the relationship between true and reconstructed energy from neutrino interactions on argon with low thresholds, being sensitive to particles that are not observed or may be misidentified in ND-LAr. In particular, ND-GAr needs to have low tracking thresholds in order to measure the spectrum of pions and protons produced in final-state interactions (FSI). It also must be able to accurately measure the pion multiplicity in 1, 2 and 3 pions final states, to inform the pion mass correction in the LArTPCs.

#### 3.5.2 Reference design

The final design of ND-GAr is still under preparation. However, a preliminary baseline design was in place at the time of the ND CDR. This section summarises the main features of that design, as it is also the one used for the default geometry in our simulation. A DUNE Phase II white paper, discussing the different options under consideration for the ND-GAr design, is in progress.

## Chapter 3. The Deep Underground Neutrino Experiment

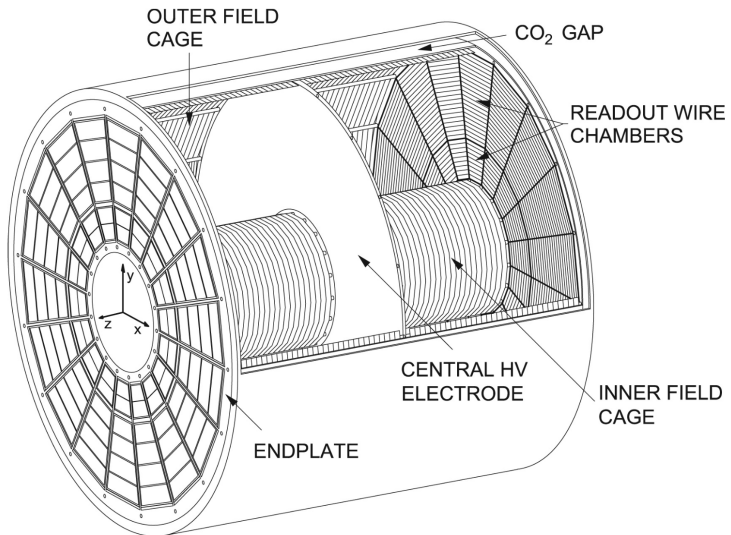


**Figure 3.9:** Diagram of the ALICE TPC, showing the two drift chambers, inner and outer field cages and readout chambers. Figure taken from Ref. [75].

### 1147 HPgTPC

1148 The reference design for the ND-GAr HPgTPC follow closely that of the ALICE TPC.  
 1149 It is a cylinder with a central high-voltage cathode, generating the electric field for  
 1150 the two drift volumes, with a maximum drift distance of 2.5 m each. The anodes will  
 1151 be instrumented with charge readout chambers. The original design repurposed the  
 1152 multi-wire proportional readout chambers (MWPCs) of ALICE, however some of the  
 1153 current R&D efforts focus on a gas electron multiplier (GEM) [78] option instead. Figure  
 1154 3.9 shows a schematic diagram of the ALICE TPC design. The basic ND-GAr geometry  
 1155 will resemble this, except for the inner field cage.

1156 It will use a 90:10 molar fraction Ar:CH<sub>4</sub> mixture at 10 bar. With this baseline gas  
 1157 mixture light collection is not possible, as the quenching gas absorbs most of the VUV  
 1158 photons. Additional R&D efforts are underway, to understand if different mixtures allow  
 1159 for the light signal to be used to provide a  $t_0$  while maintaining stable charge gain.

### 3.5. A More Capable Near Detector

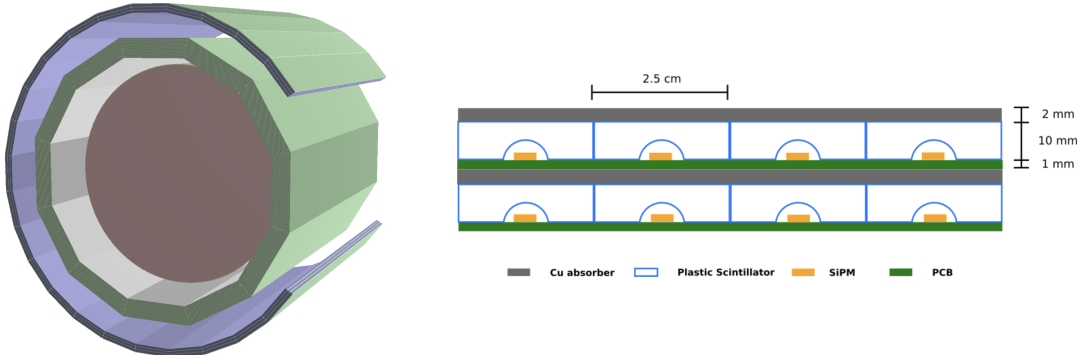


**Figure 3.10:** View of the 12-sided ECal barrel and outer muon tagger geometries (left) and layout of the ECal tile layers for the 2 mm Cu, 10 mm scintillator option (right). Figure adapted from Ref. [75].

#### 1160    ECal

1161    The main role of the ND-GAr ECal is the calorimetric measurement of the electron  
 1162    energies and the reconstruction of photons, in particular those from neutral pion decays.  
 1163    Also, the ECal is able to provide a  $t_0$  timestamp for neutrino interactions, by associating  
 1164    its activity to the tracks in the HPgTPC. The ECal will also be able to perform  
 1165    neutron reconstruction using time of flight and reject external backgrounds, thanks to  
 1166    its sub-nanosecond time resolution.

1167       The ECal design features three independent subdetectors, two end caps at each side  
 1168    and a barrel surrounding the HPgTPC. Each of the detectors is divided in modules,  
 1169    which combine alternating layers of plastic scintillator and absorber material readout  
 1170    by SiPMs. The inner scintillator layers consist of  $2.5 \times 2.5 \text{ cm}^2$  high-granularity tiles,  
 1171    whereas the outer ones are made out of 4 cm wide cross-strips spanning the whole  
 1172    module length. The current barrel geometry consists of 8 tile layers and 34 strip layers,  
 1173    while the end caps feature 6 and 36 respectively. The thickness of the scintillator layers  
 1174    is 7 mm and 5 mm for the Pb absorber layers. The 12-sided geometry of the ECal barrel  
 1175    (left) and the layout of the tile layers (left)<sup>1</sup> can be seen in Fig. 3.10.

---

<sup>1</sup>The figure shows the layout of the tile layers for a previous design with 2 mm Cu absorber and 10 mm plastic scintillator, as mentioned in the text the current choice is 5 mm Pb absorber and 7 mm scintillator.

## Chapter 3. The Deep Underground Neutrino Experiment

### **1176 Magnet**

1177 The ND-GAr magnet design, know as the Solenoid with Partial Yoke (SPY), consists of  
1178 two coupled solenoids with an iron return yoke. The idea behind the design is to have a  
1179 solenoid as thin as possible, as well as a return yoke mass distribution that minimises  
1180 the material budget between ND-LAr and ND-GAr. The magnet needs to provide a  
1181 0.5 T field in the direction perpendicular to the beam, parallel to the drift electric field.  
1182 It needs to host the pressure vessel and the surrounding ECal, which points to a inner  
1183 diameter of  $\sim 6.4$  m.

1184 The solenoid is a single layer coil, based on niobium titanium superconducting  
1185 Rutherford cable. The total length of the coil is 7.5 m. The bobbin will be split in four  
1186 segments grouped in pairs with two identical cryostats, connected in series. The iron  
1187 yoke features an aperture in the upstream side to allow the muons coming from ND-LAr.  
1188 Still, its material will be enough to reduce the magnetic field reaching SAND, and also  
1189 stop the charged pions produced inside the HPgTPC.

### **1190 Muon system**

1191 The design of the ND-GAr muon system is still in a preliminary stage. Its role is to  
1192 distinguish between muons and pions punching through the ECal. This is especially  
1193 important for wrong-sign determination, to separate these from neutral current events.

1194 In its current form, the muon system consists of three layers of longitudinal sampling  
1195 structures. It alternates 10 cm Fe absorber slabs with 2 cm plastic scintillator strips.  
1196 The transverse granularity required is still under study.

### **1197 3.5.3 R&D efforts**

1198 There are several ND-GAr-related prototypes, mostly focused on the TPC charge  
1199 readout and electronics. The priority is to test the full readout chain, in a high-pressure  
1200 environment, using a gas mixture with high argon fraction. A detailed summary of these  
1201 can be found in the DUNE Phase II white paper [76].

### 3.5. A More Capable Near Detector

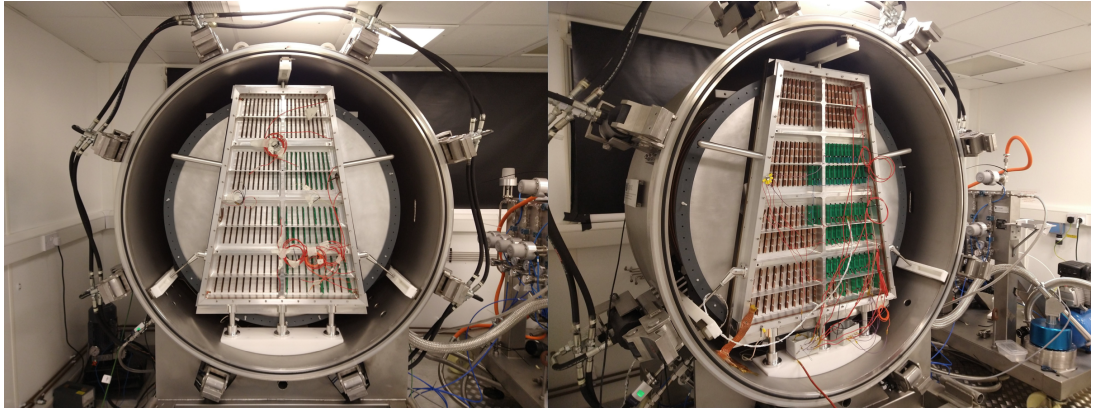


**Figure 3.11:** Photographs of the TOAD pressure vessel at RHUL. The TPC is mounted inside the vessel, and the OROC is supported by an aluminium frame. Figure taken from Ref. [79].

#### 1202 Multi-Wire Proportional Chambers

1203 As mentioned before, the original ND-GAr design repurposes the MWPCs of the ALICE  
1204 TPC, which became available after the recent upgrade [80]. These were operated using  
1205 a 90:10:5 Ne:CO<sub>2</sub>:N<sub>2</sub> gas mixture at 1 atm. Therefore, their performance needed to be  
1206 studied in an argon gas environment at high pressure.

1207 The Gas-argon Operation of ALICE TPC (GOAT) test stand tested the ALICE  
1208 readout chambers at high pressure. In particular, it used one of the previously operated  
1209 ALICE inner MWPCs, also known as IROCs, in a pressure vessel rated to 10 atm. It  
1210 measured the gas gain at various pressure points, voltages and gas mixtures.

1211 The Test stand of an Overpressure Argon Detector (TOAD) tested an ALICE outer  
1212 MWPC, also known as OROC, up to 5 atm. During its time at RHUL, it was used to  
1213 study the achievable gas gain of the OROC [79]. At the moment, it is being commissioned  
1214 at Fermilab for a full detector test of the readout electronics and the DAQ.

1215 Figure 3.11 shows the interior of the TOAD pressure vessel. The TPC is mounted  
1216 inside the vessel on three rails. The back of the OROC, supported by an aluminium  
1217 frame, can be seen at the front.

## Chapter 3. The Deep Underground Neutrino Experiment

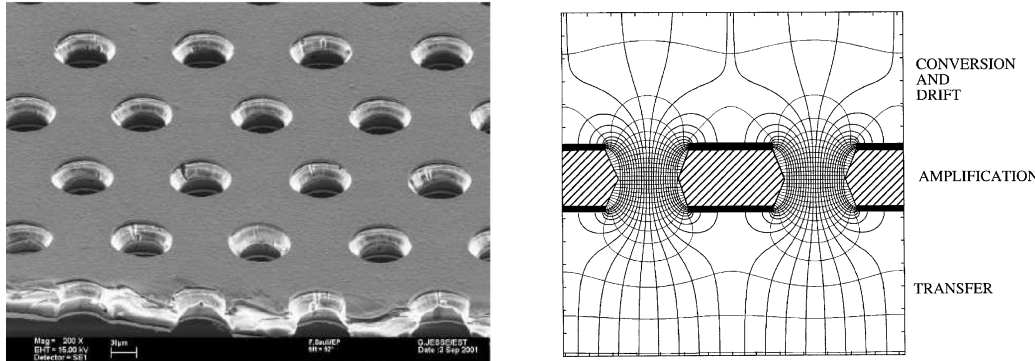


**Figure 3.12:** Left panel: electron microscope image of a  $50\ \mu\text{m}$  thick GEM electrode, with hole pitch and diameter of  $140$  and  $70\ \mu\text{m}$ , respectively. Right panel: Schematics of a GEM electrode cross section, showing the electric field lines around the holes. Figures taken from Ref. [81].

### 1218 Gas Electron Multiplier

1219 An alternative to the MWPC option is the use of GEMs. These are a type of micro-patter  
1220 detector, where the ionisation electrons passing through the holes in the GEM layers  
1221 are accelerated by a high intensity electric field. The acceleration causes the electrons  
1222 to ionise the medium, resulting in an avalanche which increase the signal exponentially  
1223 [78]. GEMs are used in numerous experiments that need a high spatial resolution, like  
1224 ALICE [82] and CMS [83] after their upgrades.

1225 Figure 3.12 (left panel) shows an electron microscope picture of a  $50\ \mu\text{m}$  thick GEM  
1226 electrode, with a pitch between neighbouring holes of  $140\ \mu\text{m}$  and a hole diameter of  
1227  $70\ \mu\text{m}$ . A schematic representation of the cross section of a GEM layer is shown in Fig.  
1228 3.12 (left panel).

1229 The Gaseous Argon T0 (GAT0<sup>2</sup>) prototype studies the use of thick GEMs made out  
1230 of glass to achieve optical imaging of the primary ionisation. Using a 10 atm pressure  
1231 vessel, the goal is to study different argon-based mixtures that allow for a precise  $t_0$   
1232 determination.

1233 The GEM Over-pressurized with Reference Gases (GORG<sup>3</sup>) test stand is currently  
1234 testing a GEM-based charge readout, using a triple-GEM stack.

<sup>2</sup>Spanish for cat.

<sup>3</sup>Persian for wolf.

### 3.6. Far Detector

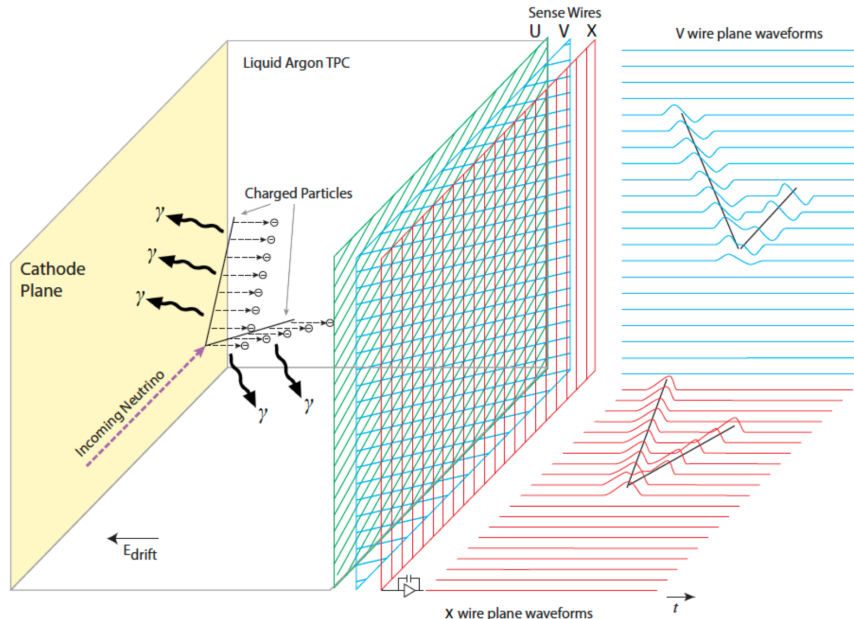


**Figure 3.13:** Schematic diagram showing the operating principle of a LArTPC with wire readout. Figure taken from Ref. [67].

## 3.6 Far Detector

The DUNE FD complex will sit 1300 km away from the beam target and 1.5 km underground at SURF, South Dakota. Two caverns will host the four FD modules, two of them per cavern, each embedded in cryostats of dimensions 18.9 m (w)  $\times$  17.8 m (h)  $\times$  65.8 m (l). A central, smaller cavern will host the cryogenic system.

Three out of the four modules will be liquid argon (LAr) time projection chamber detectors, often refer to as LArTPCs, with a LAr fiducial mass of at least 10 kt each. The first and second FD modules, FD-1 and FD-2, will use a Horizontal Drift (HD) technology, whereas the third module, FD-3, will have a Vertical Drift (VD) direction. The technology for the fourth module is still to be decided,

For each event, with energies ranging from a few MeV to several GeV, these detectors collect both the scintillation light and the ionisation electrons created when the charged particles produced in neutrino-nucleus interactions ionise the argon nuclei. In both HD and VD designs the characteristic 128 nm scintillation light of argon is collected by a photon detection system (PDS). This light will indicate the time at which electrons

## Chapter 3. The Deep Underground Neutrino Experiment

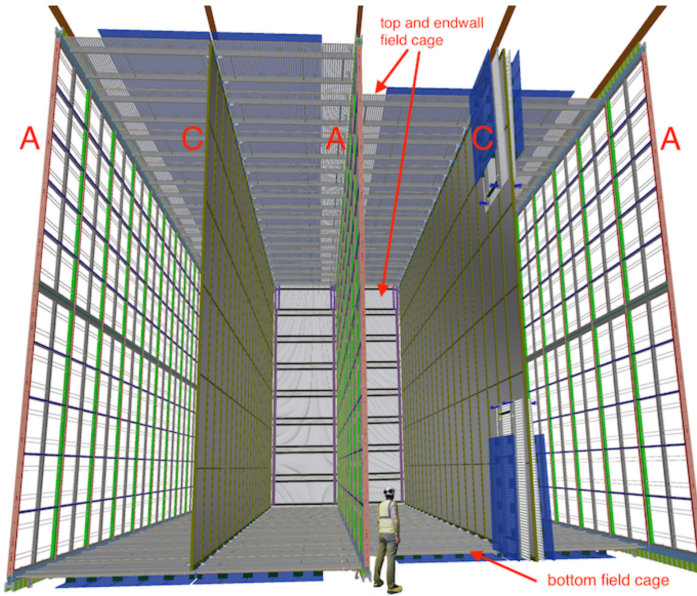


**Figure 3.14:** Proposed design for the FD-1 and FD-2 modules following the HD principle. Figure taken from Ref. [67].

1250 start to drift, thus enabling reconstruction over the drift coordinate when compared  
1251 to the time when the first ionisation electron arrives to the anode. Reconstruction of  
1252 the topology in the transverse direction is achieved using the charge readout. Fig. 3.13  
1253 illustrates the detection principle described, for the case of a HD detector with a wire  
1254 readout.

### 1255 3.6.1 Horizontal Drift

1256 The HD design the ionisation electrons produced as charged particles traverse the LAr  
1257 drift horizontally towards the anode planes, due to the effect of an electric field. These  
1258 anode planes are made out of three layers of wire readout. This design, previously  
1259 known as single-phase (SP), was tested by the ProtoDUNE-SP detector at CERN. The  
1260 prototype collected data from a hadron beam and cosmic rays, providing high-quality  
1261 data sets for calibration and performance studies.

1262 Each FD HD detector module is divided in four drift regions, with a maximum drift  
1263 length of 3.5 m, by alternating anode and cathode walls. The surrounding field cage  
1264 ensures the uniformity of the 500 V/cm horizontal electric field across the drift volumes.

### 3.6. Far Detector

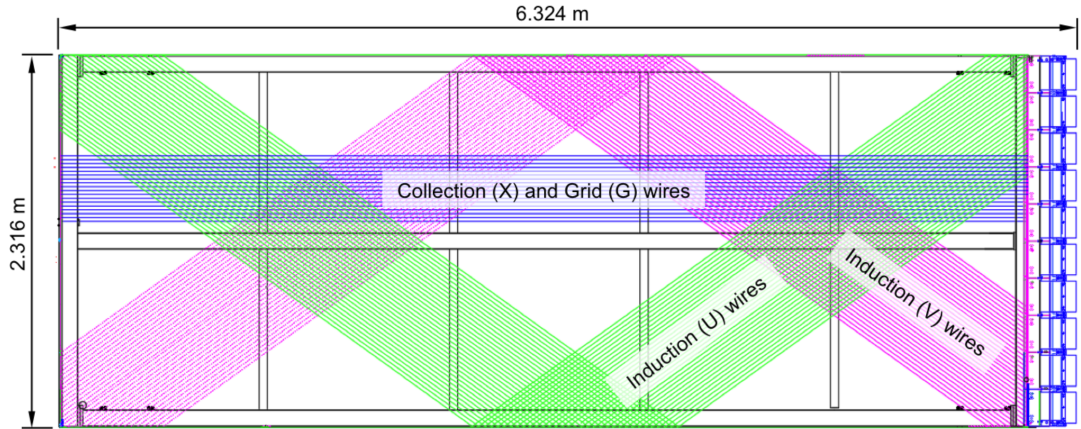


**Figure 3.15:** Schematic representation of an APA. The black lines represent the APA steel frame. The green and magenta lines correspond to the direction of the U and V induction wires respectively. The blue lines indicate the direction of the X collection wires and the wire shielding G. Figure taken from Ref. [67].

1265 The three anode walls, which constitute the charge readout of the detector, are built by  
 1266 stacking anode plane assemblies (APAs), 2 high times 25 wide. The design of the HD  
 1267 modules is shown in Fig. 3.14.

1268 Each APA is made of 2560 active wires arranged in three layers, plus an extra grid  
 1269 layer, wrapped around a metal frame. The two induction wire planes, U and V, sit at  
 1270  $\pm 35.7^\circ$  to the vertical on each side of the APA. The collection and shielding plane wires,  
 1271 X and G, run parallel to the vertical direction. The ionisation electrons drift past the  
 1272 induction planes, generating bipolar signals on those wires, and are collected by the  
 1273 collection plane, producing a monopolar positive signal. The spacing between the wires  
 1274 is  $\sim 5$  mm, and it defines the spatial resolution of the APA.

1275 The front-end readout electronics, or cold electronics as they are immerse in the LAr,  
 1276 are attached to the top of the up APAs and the bottom of the down APAs. Mounted on  
 1277 the front-end mother boards we have a series of ASICs that digitize the signals from the  
 1278 collection and induction planes. Each wire signal goes to a charge-sensitive amplifier,  
 1279 then there is a pulse-shaping circuit and this is followed by the analogue-to-digital  
 1280 converter. This part of the process happens inside the LAr to minimise the number of  
 1281 cables penetrating the cryostat. The digitised signals come out finally via a series of

## Chapter 3. The Deep Underground Neutrino Experiment

1282 high-speed serial links to the warm interface boards (WIBs), from where the data is sent  
1283 to the back-end DAQ through optical fibers.

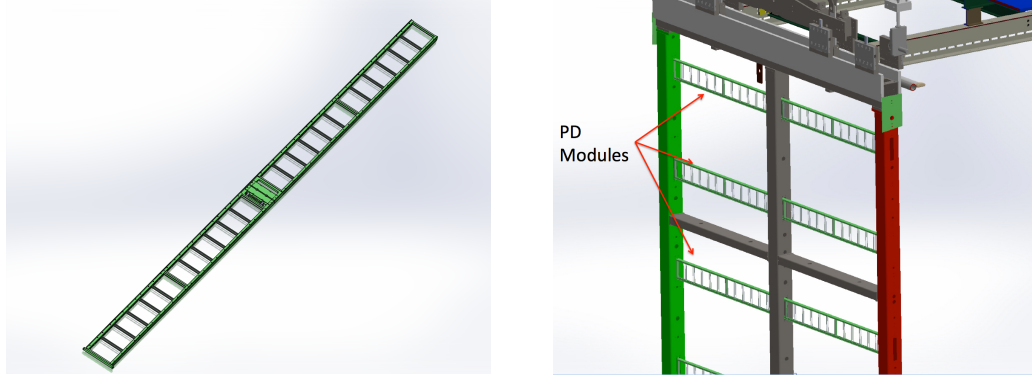


**Figure 3.16:** A PDS module containing 24 X-ARAPUCAs (left) and the location of the modules on the APAs (right). Figure taken from Ref. [67].

1284 The PDS uses modules of X-ARAPUCA devices, mounted on the APA frames  
1285 between the wire planes. Each X-ARAPUCA consists of layers of dichroic filter and  
1286 wavelength-shifter. They shift the VUV scintillation light into the visible spectrum,  
1287 sending then the visible photons to silicon photomultiplier (SiPM) devices. The PDS  
1288 modules are 209 cm × 12 cm × 2 cm bars, containing 24 X-ARAPUCAs. There are 10  
1289 of these PDS modules per APA. Fig. 3.16 shows a PDS module (left) and the placement  
1290 of the modules on the APAs (right).

### 1291 3.6.2 Vertical Drift

1292 In the VD case the ionisation electrons will drift vertically until they meet a printed  
1293 circuit board-based (PCB) readout plane. It is based on the original dual-phase (DP)  
1294 design deployed at CERN, known as ProtoDUNE-DP, used a vertical drift design with  
1295 an additional amplification of the ionization electrons using a gaseous argon (GAr) layer  
1296 above the liquid phase. The VD module incorporates the positive features of the DP  
1297 design without the complications of having the LAr-GAr interface.

1298 The current design of the FD VD module counts with two drift chambers with a  
1299 maximum drift distance of 6.5 cm. A cathode plane splits the detector volume along the  
1300 drift direction while the two anode planes are connected to the bottom and top walls

### 3.6. Far Detector

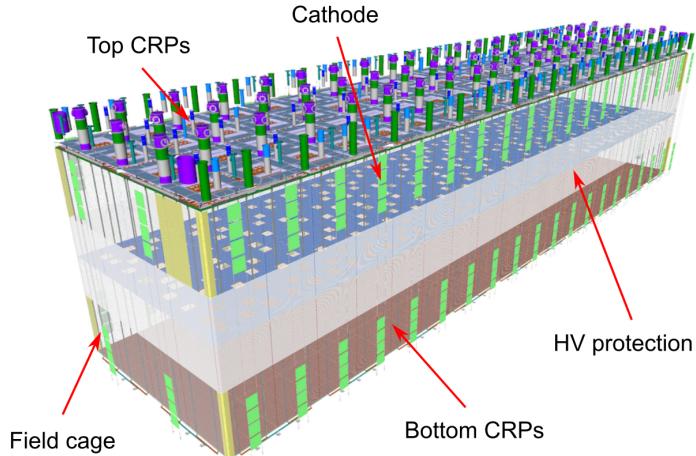


**Figure 3.17:** Proposed design for the FD-3 module following the VD principle. Figure adapted from Ref. [84].

of the detector. The layout of the VD module is shown in Fig. 3.17. Compared with the HD design, the VD option offers a slightly larger instrumented volume and a more cost-effective solution for the charge readout.

As in the HD design, each drift volume features a 500 V/cm electric field and a field cage that ensures its uniformity. The anode planes are arrays of  $3.4\text{ m} \times 3\text{ m}$  charge-readout planes (CRPs). These are formed by a pair of charge-readout units (CRUs), which are built from two double-sided perforated PCBs, with their perforations aligned. The perforations allow the drift electrons to pass between the layers.

The PCB face opposite to the cathode has a copper guard plane which acts as shielding, while its reverse face is etched with electrode strips forming the first induction plane. The outer PCB has electrode strips on both faces, the ones facing the inner PCB form the second induction plane while the outermost ones form the collection plane. Fig. 3.18 shows the layout of the electrode strips for the top (left) and bottom (right) CRUs. The magenta and blue lines represent the first and second induction planes respectively, and the green lines correspond to the collection plane.

The PDS in the VD module will use the same X-ARAPUCA technology developed for the HD design. The plan is to place the PDS modules on the cryostat walls and on

## Chapter 3. The Deep Underground Neutrino Experiment

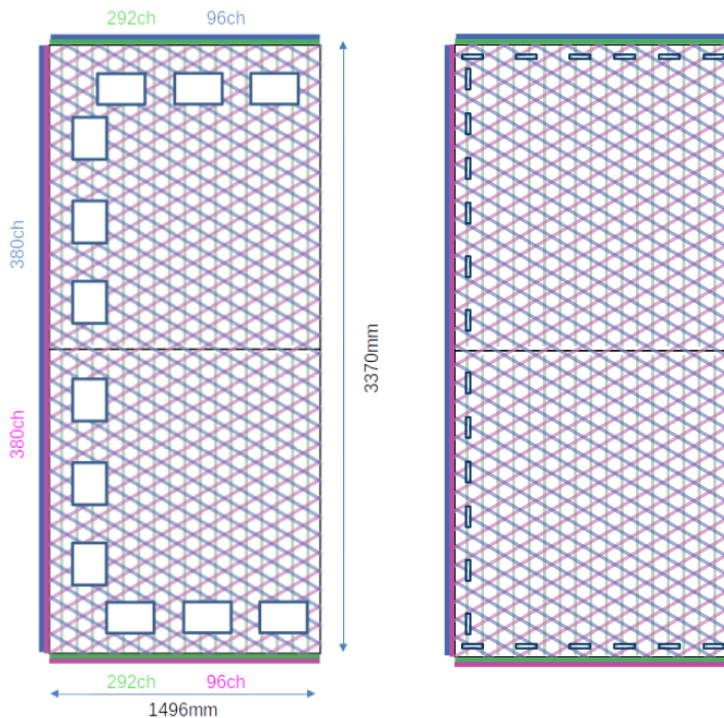


**Figure 3.18:** Schematic representation of the electrode strip configuration for a top (left) and bottom (right) CRU. Figure taken from Ref. [84].

the cathode, in order to maximise the photon yield.

### 3.6.3 FD Data Acquisition System

The data acquisition (DAQ) system receives, processes and stores data from the detector modules. In the case of DUNE the DAQ architecture is designed to work for all FD modules interchangeably, except some aspects of the upstream part which may depend on the specific module technology.

The enormous sample rate and the number of channels in TPC and PD readouts will produce a very large volume of data. These pose really strong requirements and challenges to the DUNE FD DAQ architecture. It will be required to read out data of the order of ten thousand or more channels at rates of a few MHz. To cope with the huge data volume, segmented readouts and compression algorithms are used to reduce the data rate to manageable levels.

The DAQ system of the DUNE FD is composed of five different subsystems. The

### 3.6. Far Detector

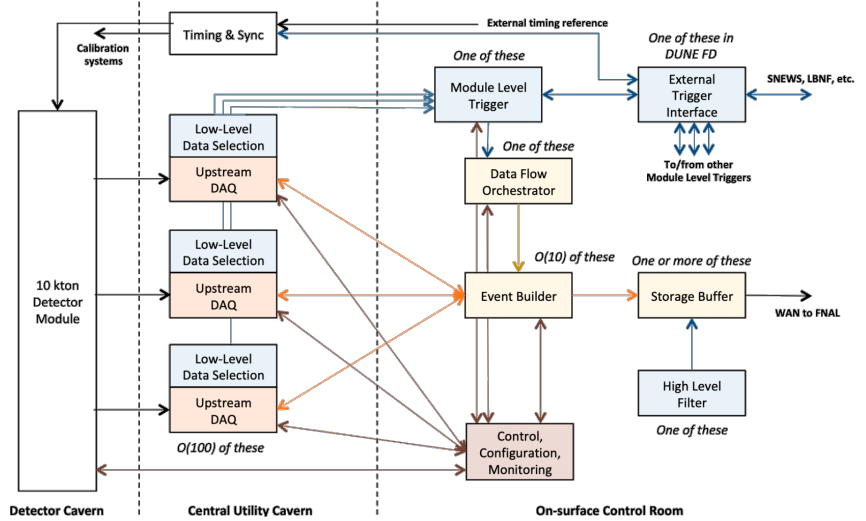


**Figure 3.19:** Detailed diagram of the DUNE FD DAQ system. Figure taken from Ref. [85].

1331 first one is the upstream DAQ, which receives the raw data from the detector, buffers it  
 1332 and perform some low-level pre-processing. The minimally processed data is then fed  
 1333 into a hierarchical data selection system, which then performs a module level trigger  
 1334 decision. In case of a positive decision a trigger command is produced and executed by  
 1335 the data flow orchestrator, located in the back-end (BE) DAQ subsystem. Subsequently  
 1336 the DAQ BE retrieves the relevant data from the buffers located in the upstream DAQ,  
 1337 adds all the data into a cohesive record and saves it to permanent storage. Watching  
 1338 over all the other subsystems we also have the control, configuration and monitoring  
 1339 subsystem and the time and synchronization subsystem. Figure 3.19 shows a schematic  
 1340 diagram of the DAQ system, showing the different subsystems and their relations.

1341 A notorious challenge for the DUNE DAQ system comes from its broad physics  
 1342 goals. We must be prepared to process events spanning a wide range of time windows  
 1343 (from 5 ms in the case of beam and cosmic neutrinos and nucleon decay to 100 s in the  
 1344 case of SNBs) and therefore this requires a continuous readout of the detector modules.  
 1345 Moreover, because of the off-beam measurements we need to ensure the capabilities  
 1346 of online data processing and self-triggering. Having this into account, together with  
 1347 the technical constraints, the DUNE FD DAQ faces a series of challenges: it needs to

### **Chapter 3. The Deep Underground Neutrino Experiment**

- 1348 be fault tolerant and redundant to reduce downtime, accommodate new components
- 1349 while it keeps serving the operational modules, have large upstream buffers to handle
- 1350 SNB physics, be able to support a wide range of readout windows and last reduce the
- 1351 throughput of data to permanent storage to be at most 30 PB/year.

1352 Chapter 4

1353 Matched Filter approach to  
1354 induction wire Trigger Primitives

1355 4.1 Motivation

1356 The filter implemented in the firmware of the upstream DUNE FD DAQ is a 32nd-order  
1357 low-pass finite impulse-response (FIR) filter. The output of such filter for a discrete  
1358 system can be written as:

$$y[i] = \sum_{j=0}^N h[j]x[i-j], \quad (4.1)$$

1359 where  $N$  is the order of the filter,  $y$  is the output sequence,  $x$  is the input sequence and  $h$   
1360 is the set of coefficients of the filter. The current implementation within `dtp-firmware`  
1361 [86] uses a set of 16 non-zero integer coefficients.

1362 Filtering is a vital step in the hit finder chain. It helps to suppress the noise and  
1363 enhance the signal peaks with respect to the noiseless baseline. A good filtering strategy  
1364 allows us to use lower thresholds when forming the trigger primitives (TPs) and thus  
1365 increasing the sensitivity of our detector to low energy physics events. In such events,  
1366 the hits produced by the ionisation electrons tend to have lower amplitudes than those  
1367 of interest to the baseline physics programme of the DUNE experiment.

1368 This is particularly important for the induction planes. In general, signal peaks in

## Chapter 4. Matched Filter approach to induction wire Trigger Primitives

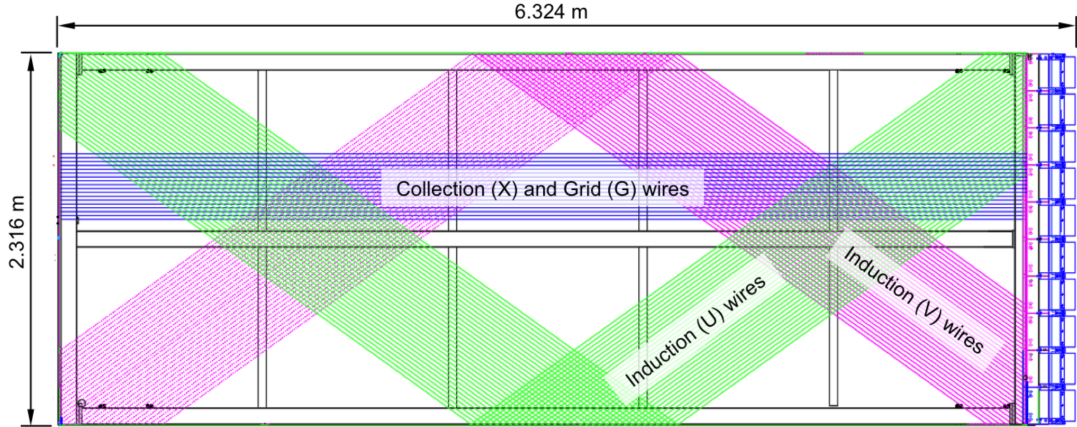


**Figure 4.1:** Schematic representation of an APA. The black lines represent the APA steel frame. The green and magenta lines correspond to the direction of the U and V induction wires respectively. The blue lines indicate the direction of the X collection wires and the wire shielding G.

1369 the induction wires have smaller amplitude than the ones in the induction plane. This,  
 1370 together with the fact that the pulse shapes are bipolar, reduces our capacity to detect  
 1371 the hits on these channels. The inefficiency of detecting TPs in the induction planes  
 1372 (denoted as U and V planes) lead trigger algorithms to focus mainly on the TPs from  
 1373 the collection plane (so-called X plane). As a result, the possibility of making trigger  
 1374 decisions based on the coincidence of TPs across the three wire planes remains nowadays  
 1375 unexploited in DUNE. Fig. 4.1 shows a schematic view of an anode plane assembly  
 1376 (APA), with the different wire plane orientations highlighted.

1377 A possible improvement of the current hit finder chain could require optimising  
 1378 the existing or choosing a new filter implementation. A filter strategy which improves  
 1379 the induction signals may be able to enhance the detection efficiency of TPs from the  
 1380 induction planes and ideally make it comparable to that of the collection plane.

1381 The goal is to implement a better finite-impulse response filter design and to evaluate  
 1382 its performance relative to the current filter. To do so, we need to take into account the  
 1383 limitations of the firmware: the FIR filter shall have maximum 32 coefficients (so-called  
 1384 taps) whose values are 12-bit unsigned integers. Although it is technically possible to  
 1385 include non-integer coefficients, it would be a technical challenge as we have 40 FIR

## 4.2. Signal-to-noise ratio definition

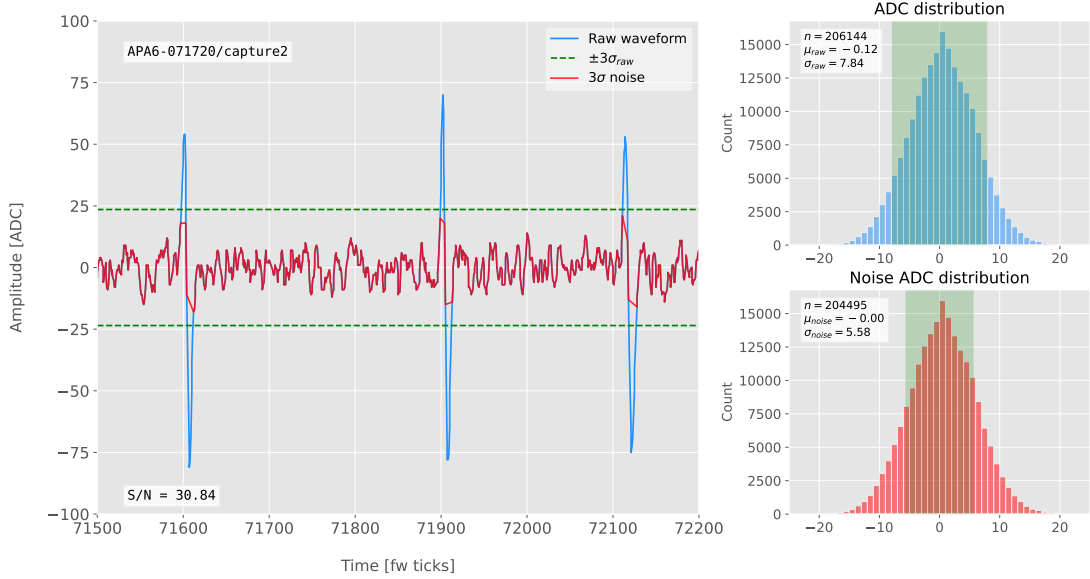


**Figure 4.2:** Left panel: Zoomed unfiltered waveform corresponding to channel 7840 from the ProtoDUNE-SP raw data capture `felix-2020-07-17-21:31:44` (blue line). The green dashed lines mark the region  $\pm 3\sigma_{\text{raw}}$ . The resulting noise waveform is also shown (red line). Top right panel: ADC distribution for channel 7840, where the green shaded region represents  $\pm \sigma_{\text{raw}}$ . Bottom right panel: noise ADC distribution for channel 7840, where the green shaded region represents  $\pm \sigma_{\text{noise}}$ .

1386 instances per APA, as there are 4 FIR per optical link and 10 optical links per APA.  
 1387 With these restrictions, the task is to provide a set of 32 coefficients which yield an  
 1388 optimal filter performance for the induction wires.

1389 **4.2 Signal-to-noise ratio definition**

1390 I introduce the signal to noise ratio (S/N) as a measure of the FIR filter performance  
 1391 and demonstrate how to extract its value for a set of ProtoDUNE-SP data. The S/N  
 1392 metrics allow us to compare different filter implementations and serve as a basis for more  
 1393 detailed studies presented later in this document. Specifically, I use the ADC capture  
 1394 `felix-2020-07-17-21:31:44` (data capture taken for firmware validation purposes). I  
 1395 defined S/N as the height of the signal peaks relative to the size of the noise peaks.  
 1396 To quantify this quantity channel by channel one first need to estimate the standard  
 1397 deviation of the ADC data for each channel,  $\sigma_{\text{ADC}}$ . Then, I define the corresponding

## Chapter 4. Matched Filter approach to induction wire Trigger Primitives

1398 noise waveform to be the ADC values in the range  $\pm 3\sigma_{ADC}$ . From this new noise data  
1399 one can estimate again the mean and standard deviation,  $\mu_{noise}$  and  $\sigma_{noise}$ , so I can  
1400 write the S/N for any given channel as:

$$S/N = \frac{\max [ADC] - \mu_{noise}}{\sigma_{noise}}, \quad (4.2)$$

1401 where  $\max [ADC]$  is simply the maximum ADC value found in the corresponding channel.

1402 One can apply this definition of the S/N with a waveform from one of the channels  
1403 of the data capture<sup>1</sup>. Fig. 4.2 shows a zoomed region of the waveform corresponding to  
1404 channel 7840 (blue line), where one can clearly see three signal peaks and continuous  
1405 additive noise (we actually see 6 peaks, 3 positive and 3 negative, but, because by design  
1406 for induction channels the expected signal pulse shapes are bipolar, I treat them as a  
1407 collection of 3 individual signal peaks). I estimated the standard deviation of this raw  
1408 waveform to be  $\sigma_{raw} = 7.84$  ADC, so I am able to define the noise waveform (red line)  
1409 as the ADC values in the range  $\pm 23.52$  ADC. This way one obtains  $\mu_{noise} = 0$  and  
1410  $\sigma_{noise} = 5.58$  ADC, which gives  $S/N = 30.84$ .

1411 We can repeat this calculation now for the corresponding filtered waveform (using the  
1412 current firmware FIR filter). In Fig. 4.3 I plotted the same time window for the filtered  
1413 waveform from channel 7840 (blue line). In this case, the standard deviation of the  
1414 waveform is larger than before, giving  $\sigma_{raw} = 10.99$  ADC. The resulting noise waveform  
1415 (red line) results from selection the ADC values in the range  $\pm 32.91$  ADC, giving now  
1416  $\mu_{noise} = -0.47$  ADC and  $\sigma_{noise} = 7.03$  ADC. Finally, one obtains  $S/N = 24.68$ . Notice  
1417 that the value of S/N decreases after the filtering. Clearly, one can see that the noise  
1418 baseline has increased by a factor of 1.35 when we applied the FIR filter and at the same  
1419 time the amplitude of the signal peaks has remained almost unchanged, leading to this  
1420 poorer S/N value.

---

<sup>1</sup>All the original work was done within the `dtp-simulation` package [87], which offers a variety of tools to read raw data and emulate the TPG block (pedestal subtraction, filtering and hit finder). However, the results shown in this report were re-worked later using the C++ based `dtpemulator` package [88]. Its main purpose is the emulation of the TPG block and, in the same way as its predecessor, it has been cross-checked against the current firmware implementation.

### 4.3. Low-pass FIR filter design

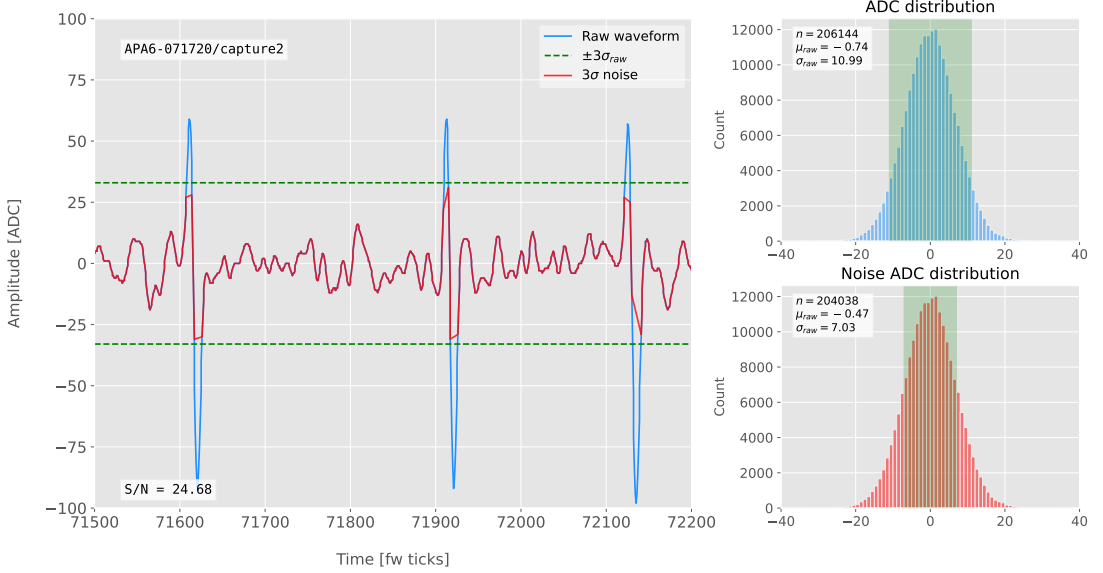


**Figure 4.3:** Left panel: Zoomed filtered waveform corresponding to channel 7840 from the ProtoDUNE-SP raw data capture `felix-2020-07-17-21:31:44` (blue line). The filter used was the current implementation of the low-pass FIR filter in `dtp-firmware`. The green dashed lines mark the region  $\pm 3\sigma_{\text{raw}}$ . The resulting noise waveform is also shown (red line). Top right panel: ADC distribution for channel 7840 after filtering, where the green shaded region represents  $\pm \sigma_{\text{raw}}$ . Bottom right panel: noise ADC distribution for channel 7840 after filtering, where the green shaded region represents  $\pm \sigma_{\text{noise}}$

## 4.3 Low-pass FIR filter design

In general, when one uses a method to optimize the frequency response of a digital filter, such as the Parks-McClellan algorithm, one finds a set of  $N$  real coefficients that give the best response for the specified pass-band and order of the filter [89].

In our case, as the sampling frequency is defined as  $1 \text{ ticks}^{-1}$ , the Nyquist frequency will simply be  $1/2 \text{ ticks}^{-1}$ . The current implementation of the filter seems to have as pass-band the range  $[0, 0.1] \text{ ticks}^{-1}$ . This can be seen in Fig. 4.4, where I show the power spectrum, in decibels, of such filter implementation (blue solid line). For instance, the Park-McClellan algorithm finds the optimal Chebyshev FIR filter taking as input the boundaries of the target pass-band and stop-band, which can be written in the form:

$$\left\{ \begin{array}{l} [0, f_c] \\ [f_c + \delta f, f_N] \end{array} \right. , \quad (4.3)$$

## Chapter 4. Matched Filter approach to induction wire Trigger Primitives

where  $f_c$  is the cut-off frequency,  $\delta f$  is the transition width and  $f_N$  is the aforementioned Nyquist frequency. A similar behaviour to the one in the current filter can be obtained by setting  $f_c = 0$  and  $\delta f = 0.1 \text{ ticks}^{-1}$ . The response of the resulting filter is also shown in Fig. 4.4 (blue solid line). Notice that the suppression of the stop-band is enhanced for this optimal filter. For comparison I included the power response of the filter obtained by taking the integer part of the coefficients resulting from the Parks-McClellan method (red dashed line). One can see that it does not suppress that much the stop-band, in a similar way to the current implementation of the filter.

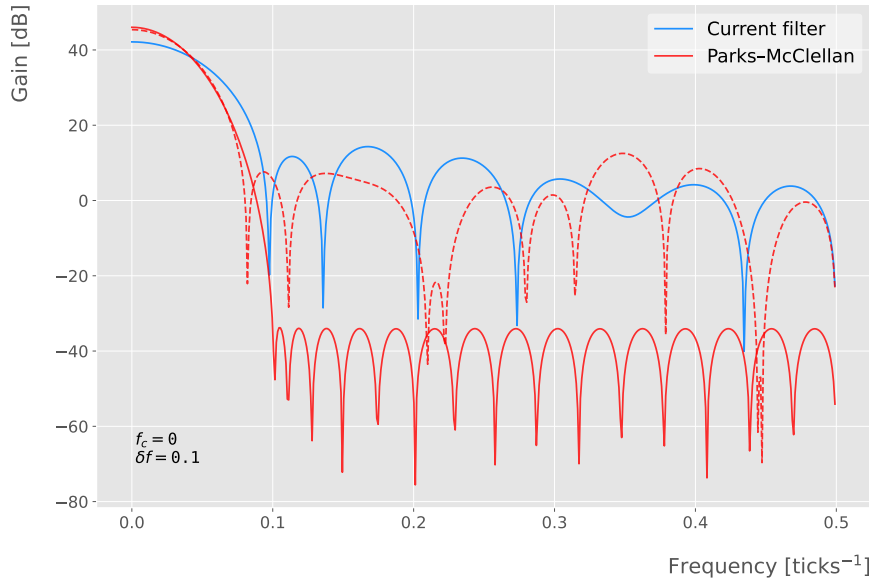


**Figure 4.4:** Power spectrum in decibels for the current implementation of the low-pass FIR filter in `dtp-firmware` (blue line), compared to the response of an optimal filter obtained using the Parks-McClellan algorithm for the same pass-band (red line). Also for comparison I include the spectrum of the optimal filter when taking only the integer part of the coefficients (red dashed line).

At this point, I tried to improve the performance of the FIR filter using the Parks-McClellan method, i.e. maximize the overall S/N, using the available data captures. I did so by varying the values of the two quantities that parametrize the pass-band and stop-band, the cut-off frequency  $f_c$  and the transition width  $\delta f$ .

Fig. 4.5 shows the average relative change in the S/N (i.e. the ratio between the value of the S/N after and before the filtering) for capture `felix-2020-07-17-21:31:44`,

### 4.3. Low-pass FIR filter design

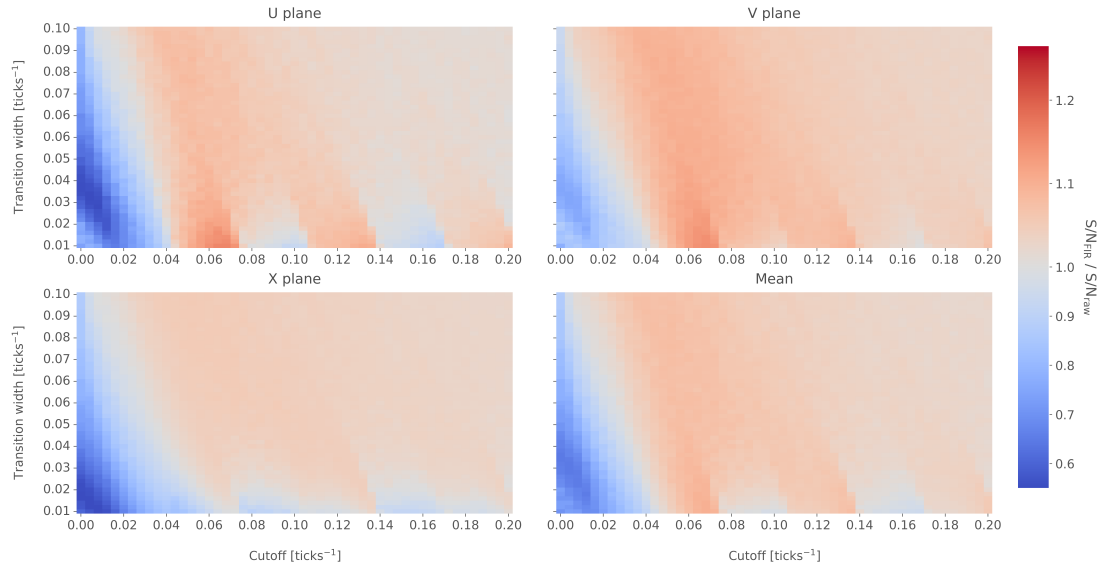


**Figure 4.5:** Relative change in the S/N for the ProtoDUNE-SP raw data capture `felix-2020-07-17-21:31:44`, using different values of the cutoff frequency  $f_c$  and the transition width  $\delta f$ . The optimal Chebyshev filters were applied using just the integer part of the coefficients given by the Parks-McClellan algorithm.

when using filters designed with the Parks-McClellan algorithm for the specified values of the cut-off frequency  $f_c$  and the transition width  $\delta f$ , restricted to integer values for the filter coefficients. One can clearly distinguish different regions where we get an improvement of up to a factor of 1.35 for the U plane. For large values of  $f_c + \delta f$  the ratio tends to 1, as expected (in that limit the width of the stop-band goes to 0, meaning that no frequencies are filtered out and thus the waveform remains the same).

Using the configuration which gives the best mean performance for the three planes (see bottom right panel of Fig. 4.5), i.e.  $f_c = 0.068 \text{ ticks}^{-1}$  and  $\delta f = 0.010 \text{ ticks}^{-1}$ , we can see how such filter affects the different channels. Fig. 4.6 shows the distribution of the S/N improvement values for all the channels in the raw ADC capture `felix-2020-07-17-21:31:44`, separated by wire plane, after the optimal Chebyshev filter was applied. One can see that there is a clear improvement for both U and V induction wire planes, obtaining a mean change of 1.25 and 1.30 for them respectively. However, in the case of the collection plane X the mean of this distribution is roughly 1, meaning that a good fraction of channels in that plane get a slightly worse S/N after the

## Chapter 4. Matched Filter approach to induction wire Trigger Primitives

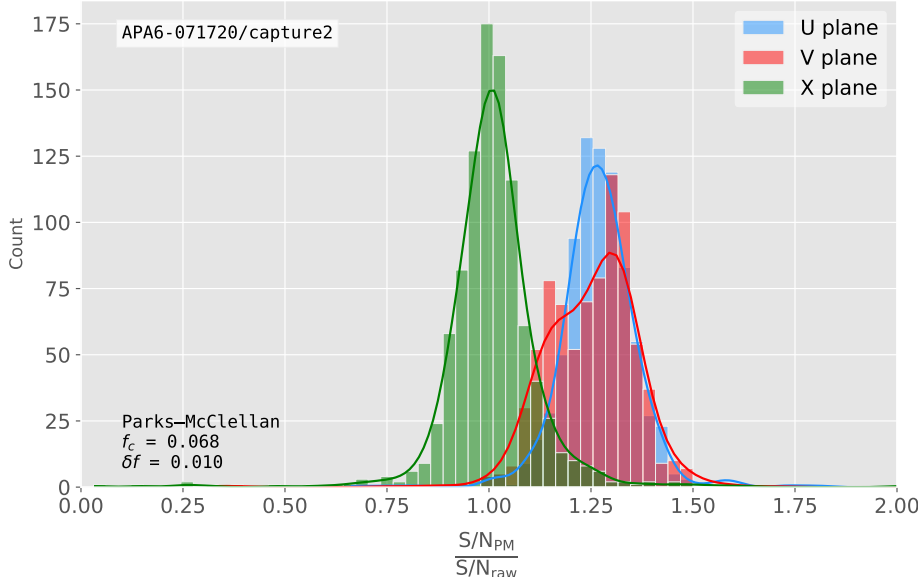


**Figure 4.6:** Distribution of the relative change of the S/N on the different wire planes from the ProtoDUNE-SP raw data capture *felix-2020-07-17-21:31:44* after the optimal Chebyshev filter was applied. The filter was computed with the Parks-McClellan algorithm using a cutoff of  $f_c = 0.068 \text{ ticks}^{-1}$  and a transition width  $\delta f = 0.010 \text{ ticks}^{-1}$ .

filter is applied. In any case, this is not a big issue as the S/N for collection channels is usually much higher than the one for induction channels.

The results I obtained optimising the low pass filter with the Parks-McClellan method are promising. Nonetheless, the improvement found is rather marginal so I wondered if there could be an alternative approach to the filtering problem which yields better outputs. At this point, I found a possible alternative in matched filters. By construction, this kind of filters offer the best improvement on the S/N.

## 4.4 Matched filters

In the context of signal processing, a matched filter is the optimal linear filter for maximising the signal-to-noise ratio (S/N) in the presence of additive noise, obtained by convolving a conjugated time-reversed known template with an unknown signal to detect the presence of the template in the signal [90].

Given a known signal sequence  $s(t)$  and another (a priori unknown) noise sequence

#### 4.4. Matched filters

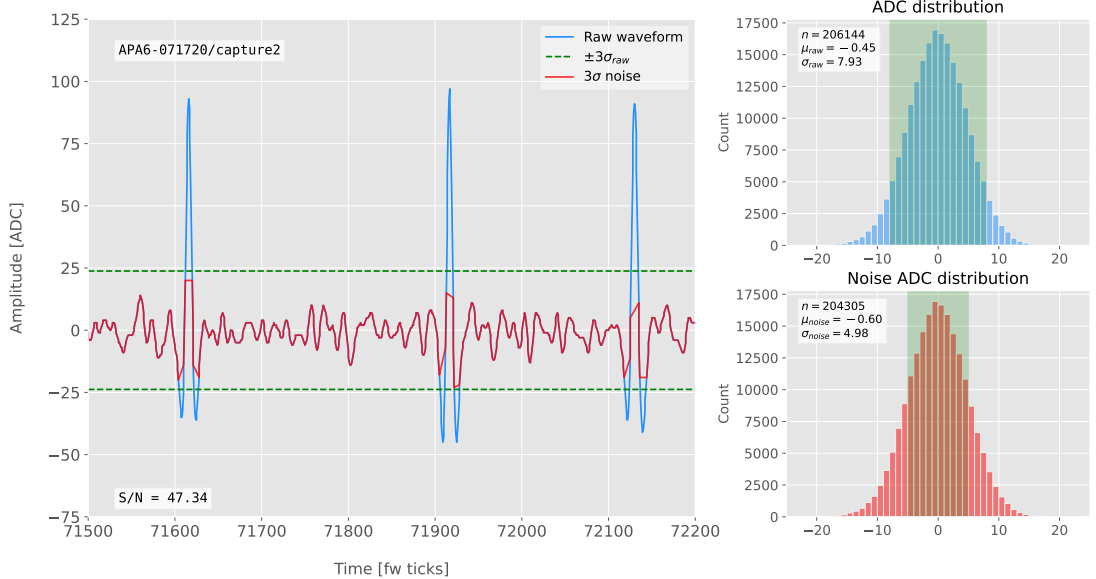


**Figure 4.7:** Left panel: Zoomed match filtered waveform corresponding to channel 7840 from the ProtoDUNE-SP raw data capture felix-2020-07-17-21:31:44 (blue line). The filter used was directly extracted from the data, being the 32 values around the first peak in the original waveform. The green dashed lines mark the region  $\pm 3\sigma_{\text{raw}}$ . The resulting noise waveform is also shown (red line). Top right panel: ADC distribution for channel 7840 after match filtering, where the green shaded region represents  $\pm \sigma_{\text{raw}}$ . Bottom right panel: noise ADC distribution for channel 7840 after match filtering, where the green shaded region represents  $\pm \sigma_{\text{noise}}$

1473  $n(t)$ , the input signal can be written as:

$$x(t) = s(t) + n(t). \quad (4.4)$$

1474 Now, considering a linear time-invariant filter, whose impulse-response function I  
1475 will refer to as  $h(t)$ , one can write the output signal as:

$$\begin{aligned} y(t) &= x(t) * h(t) \\ &= (s(t) + n(t)) * h(t) \\ &= y_s(t) + y_n(t), \end{aligned} \quad (4.5)$$

1476 where  $y_s(t)$  and  $y_n(t)$  are simply the outputs of the filter due to the signal and the noise  
1477 components respectively.

## Chapter 4. Matched Filter approach to induction wire Trigger Primitives

1478 The goal of the matched filter is to detect the presence of the signal  $s(t)$  in the input  
 1479 sample  $x(t)$  at a certain time  $t_0$ , which effectively means we need to maximise the S/N.  
 1480 This way, what one wants is to have a filter which gives a much bigger output when the  
 1481 known signal is present than when it is not. Putting it in other words, the instantaneous  
 1482 power of the signal output  $y_s(t)$  should be much larger than the average power of the  
 1483 noise output  $y_n(t)$  at some time  $t_0$ .

1484 For the case of the filtered signal, one can easily re-write it as an inverse Fourier  
 1485 transform:

$$y_s(t) = \frac{1}{2\pi} \int_{-\infty}^{\infty} d\omega H(\omega)S(\omega)e^{i\omega t}, \quad (4.6)$$

1486 where  $H(\omega)$  and  $S(\omega)$  are the Fourier transforms of the impulse-response function (i.e.  
 1487 the transfer function of the filter) and of the input signal, respectively.

1488 Now focusing on the noise, we can use the Wiener-Khinchin theorem [91] to write  
 1489 the mean power of the noise after filtering as:

$$E|y_n(t)|^2 = \frac{1}{2\pi} \int_{-\infty}^{\infty} d\omega |H(\omega)|^2 S_n(\omega), \quad (4.7)$$

1490 where  $S_n(\omega)$  is the power spectral density of the noise.

1491 Having these, one can write the instantaneous S/N at time  $t_0$  as:

$$\begin{aligned} \left( \frac{S}{N} \right)_{t_0} &= \frac{|y_s|^2}{E|y_n(t)|^2} \\ &= \frac{1}{2\pi} \frac{\left| \int_{-\infty}^{\infty} d\omega H(\omega)S(\omega)e^{i\omega t_0} \right|^2}{\int_{-\infty}^{\infty} d\omega |H(\omega)|^2 S_n(\omega)}. \end{aligned} \quad (4.8)$$

1492 Once we have this expression, we need to find the upper limit of it to determine what  
 1493 would be the optimal choice for the transfer function. One can use the Cauchy-Schwarz  
 1494 inequality, which in the present case takes the form:

$$\left| \int_{-\infty}^{\infty} dx f(x)g(x) \right|^2 \leq \int_{-\infty}^{\infty} dx |f(x)|^2 + \int_{-\infty}^{\infty} dx |g(x)|^2, \quad (4.9)$$

#### 4.4. Matched filters

for any two analytical functions  $f(x)$  and  $g(x)$ . One can prove that making the choice:

$$\begin{aligned} f(x) &= H(\omega) \sqrt{S_n(\omega)} e^{i\omega t_0}, \\ g(x) &= \frac{S(\omega)}{\sqrt{S_n(\omega)}}, \end{aligned} \quad (4.10)$$

leads to the following upper bound for the S/N:

$$\left( \frac{S}{N} \right)_{t_0} \leq \frac{1}{2\pi} \int_{-\infty}^{\infty} d\omega \frac{|S(\omega)|^2}{S_n(\omega)}. \quad (4.11)$$

From Eqs. (4.8), (4.9) and (4.10) one can also derive the form of the transfer function such that the upper bound is exactly reached [92]:

$$H(\omega) \propto \frac{S^*(\omega) e^{-i\omega t_0}}{S_n(\omega)}. \quad (4.12)$$

From this last expression we can clearly see the way the matched filter acts. As the transfer function is proportional to the Fourier transform of the signal it will try to only pick the frequencies present in the signal [93].

The matched filter transfer function can be greatly simplified if the input noise is Gaussian. In that case, the power spectral density of the noise is a constant, so it can be re-absorbed in the overall normalisation of the transfer function. Moreover, considering that the input signal is a real function, one can simply set  $S^*(\omega) = S(-\omega)$ , which gives:

$$H(\omega) \propto S(-\omega) e^{-i\omega t_0}. \quad (4.13)$$

For a discrete signal, one can think of the input and impulse-response sequences as vectors of  $\mathbb{R}^N$ . Then, the matched filter tries to maximise the inner product of the signal and the filter while minimising the output due to the noise by choosing a filter vector orthogonal to the later. In the case of additive noise, that leads to the impulse-response vector:

$$h = \frac{1}{\sqrt{s^\dagger R_n^{-1} s}} R_n^{-1} s, \quad (4.14)$$

## Chapter 4. Matched Filter approach to induction wire Trigger Primitives

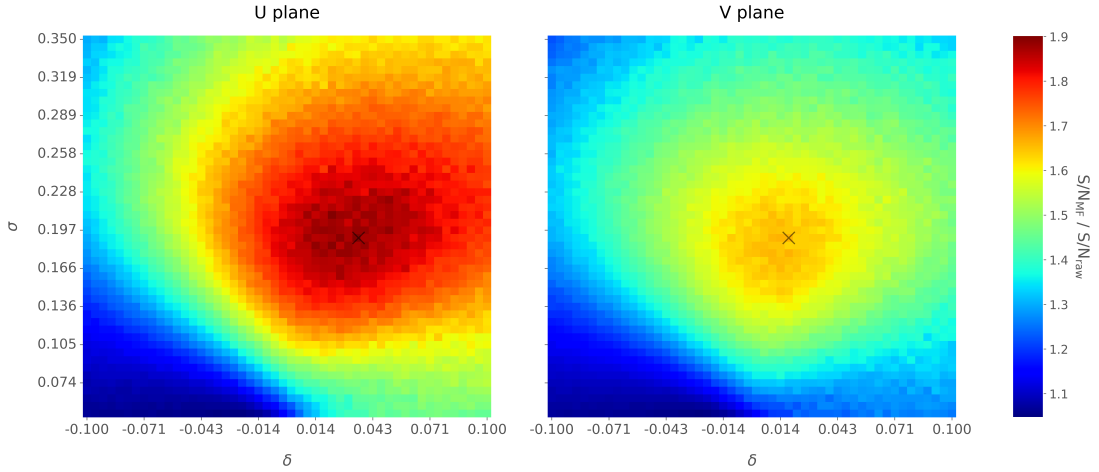


**Figure 4.8:** Relative improvement in the S/N for the raw data capture `felix-2020-07-17-21:31:44`, using the matched filter following the parametrisation in Eq. (4.17). The black crosses in both panels denote the location of the maximum ratio value.

1511 where  $s$  is a reversed signal template sequence of length  $N$  equal to the order of the filter  
 1512 and  $R_n$  is the covariance matrix associated with the noise sequence  $n$ . For the Gaussian  
 1513 noise case, the covariance matrix is simply the unit matrix, so the above expression  
 1514 simplifies again to:

$$h = \frac{s}{|s|}. \quad (4.15)$$

1515 For this first stage of the study, I use a definition of the S/N per channel given by:

$$\text{S/N} = \frac{\max [ADC] - \mu_{noise}}{\sigma_{noise}}, \quad (4.16)$$

1516 where the subscript *noise* refers to a subset of the data obtained by only taking into  
 1517 account waveform values within a  $\pm 3\sigma$  range around the mean of the data and  $\max [ADC]$   
 1518 is the maximum of the original waveform. This definition is further discussed in App.  
 1519 4.2, where I also show examples of its application to raw data and to a waveform filtered  
 1520 with the current low-pass FIR filter.

1521 To test whether this choice of filter is appropriate one needs to choose a signal  
 1522 template. As an example of how a matched filter would affect our signal, I simply took  
 1523 the filter coefficients to be the 32 ADC values around a signal peak present in the data.

#### 4.4. Matched filters

1524 In Fig. 4.7 (left panel) I plotted a zoomed region for channel 7840 in the raw data capture  
1525 `felix-2020-07-17-21:31:44`, after applying the matched filter described before (blue  
1526 line). When compared to the raw and FIR filtered case (see App. 4.2), after applying  
1527 the match filter the standard deviation of the noise waveform (red line) decreases and at  
1528 the same time the signal peaks are enhanced. This leads to an improvement of the S/N  
1529 by a factor of 1.92 when compared to the raw waveform.

1530 In order to obtain the matched filter that is more suitable for our data, I explored  
1531 different configurations of signal templates. In order to perform this exploration, I  
1532 parametrised the signal using the bipolar function:

$$f(x) = -A(x + \delta) e^{-x^2/\sigma^2}, \quad (4.17)$$

1533 where the parameter  $\delta$  controls the asymmetry between the positive and negative peaks  
1534 and  $\sigma$  controls their width. The amplitude parameter  $A$  is set such that it keeps the  
1535 height of the biggest peak to be less than 200 ADC in absolute value.

1536 As this parametrisation is only adequate for bipolar signals I will focus exclusively  
1537 on the induction channels. Also, the optimal configurations I found for the U and V  
1538 plane will be kept separate, i.e. I will have two sets of coefficients that will be applied to  
1539 either the U and V planes of wires. I do so as I found this was the choice giving the  
1540 best performance. Even so, as I will discuss, the differences are not very pronounced. In  
1541 case it is not technically possible to separate channels in the firmware according to the  
1542 wire plane they come from and use different sets of filter coefficients for them, we can  
1543 just find a common unique set of coefficients. In such case, I do not expect our results  
1544 to change dramatically.

1545 In Fig. 4.8 I present the results of our parameter scan, for channels in the induction  
1546 planes U (left panel) and V (right panel). For each configuration of  $\sigma$  and  $\delta$  the resulting  
1547 matched filter was applied to all channels in the corresponding plane within the data  
1548 capture `felix-2020-07-17-21:31:44`, the S/N improvement was computed with respect  
1549 to the raw waveforms and then the S/N mean value was kept as a score for such filter.

## Chapter 4. Matched Filter approach to induction wire Trigger Primitives

1550 One can see that the improvement obtained for the U plane is in general higher than the  
1551 one for the V plane. In any case, I got substantially higher ratios than the ones obtained  
1552 for the low-pass FIR filters. For the optimal configurations I attained improvements up  
1553 to a factor of 1.85 for the U plane and 1.65 for the V plane.

1554 The sets of optimal matched filter coefficients were obtained for the parameters  
1555  $\delta = 0.035$ ,  $\sigma = 0.191$  for the U plane and  $\delta = 0.018$ ,  $\sigma = 0.191$  for the V plane. I  
1556 show these two sets of coefficients in Fig. 4.9 (left panel). Also in Fig. 4.9 (right  
1557 panel) I plot the distribution of the S/N improvement after the optimal match filters  
1558 for the U and V were applied to the corresponding channels in the raw data capture  
1559 `felix-2020-07-17-21:31:44`. As mentioned before, the mean improvement achieved  
1560 for the U plane channels is slightly bigger than the one for the V channels. Note, however,  
1561 that the spread of the distribution for the V plane is also smaller than the one for the U  
1562 plane.

1563 I also performed a similar scan for the case of a low-pass FIR filter using the Parks-  
1564 McClellan algorithm. In that case, the parameters to check were the cutoff frequency  
1565 and the transition width of the filter. A summary of the results is given in App. 4.3.

1566 Overall, one can see that the improvements on the S/N are much more significant in  
1567 the case of the matched filter than it is for the low-pass FIR filters. The analysis of this  
1568 and other raw data captures from ProtoDUNE-SP suggest that matched filters increase  
1569 the S/N of induction channels by a factor of 1.5 more than the optimal low-pass FIR  
1570 filters.

1571 Although these results are by themselves great points in favour of the matched  
1572 filter, more studies are needed to completely assess the robustness of this approach. I  
1573 proceeded then to test the matched filter with simulated data samples.

### 1574 4.5 Using simulated samples

1575 In order to further test the matched filter, the next step was to generate and process  
1576 data samples using *LArSoft* [94]. In this way, one can control the particle content of

## 4.5. Using simulated samples

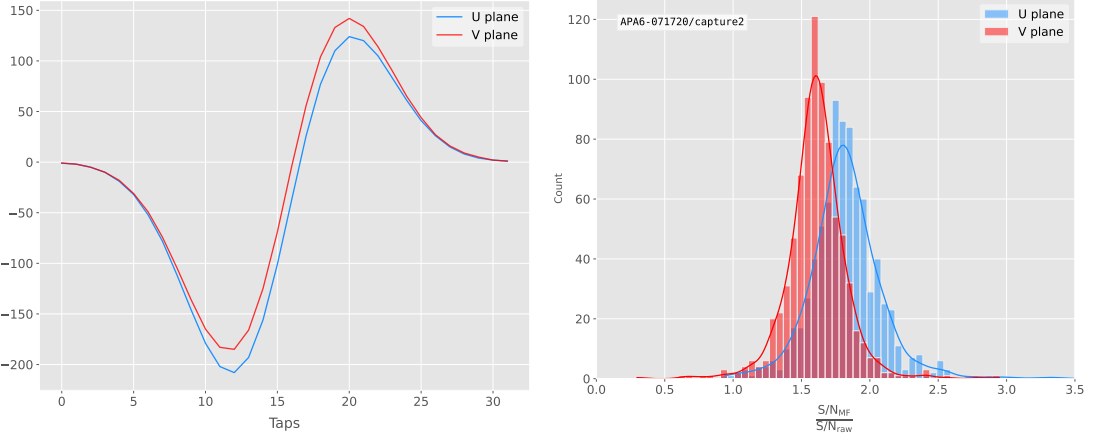


**Figure 4.9:** Left panel: Optimal matched filter coefficients for the  $U$  (blue line) and  $V$  (red line) planes. The filters were computed with our parametrisation in Eq. (4.17) for the parameter values  $\delta = 0.035$ ,  $\sigma = 0.191$  and  $\delta = 0.018$ ,  $\sigma = 0.191$  respectively. Right panel: Distribution of the relative change of the  $S/N$  on the two induction wire planes from the ProtoDUNE-SP raw data capture *felix-2020-07-17-21:31:44* after their respective optimal matched filters were applied.

1577 the samples, the orientation of the tracks and their energy, and therefore see how the  
1578 matched filter behaves in various situations.

1579 To begin with, I prepared different monoenergetic and isotropic samples containing  
1580 a single particle per event. Each sample contains a different particle species, namely  
1581 electrons, muons, protons and neutral pions all with a kinetic energy of  $E_k = 100$  MeV.  
1582 I chose these because of the fairly different topologies they generate in the liquid argon,  
1583 ranging from shower-like to track-like. The procedure I followed to generate the samples  
1584 and process them is discussed in detail in App. ??.

1585 These were generated with the single particle gun and the Geant4 stage of the  
1586 *LArSoft* simulation [94] was performed with the standard configuration for the DUNE  
1587 FD 10kt module.

1588 For simplicity, I restricted the particles to start drifting in a single TPC volume  
1589 (in this case TPC 0), so I can focus exclusively on the signals coming from one APA.  
1590 The chosen kinetic energy for all the particles in my first trial is  $E_k = 100$  MeV, so a  
1591 necessary check is to see if all our tracks will be typically contained in one TPC volume.  
1592 Fig. 4.10 (left panel) shows the distributions of the track lengths in the liquid argon

## Chapter 4. Matched Filter approach to induction wire Trigger Primitives

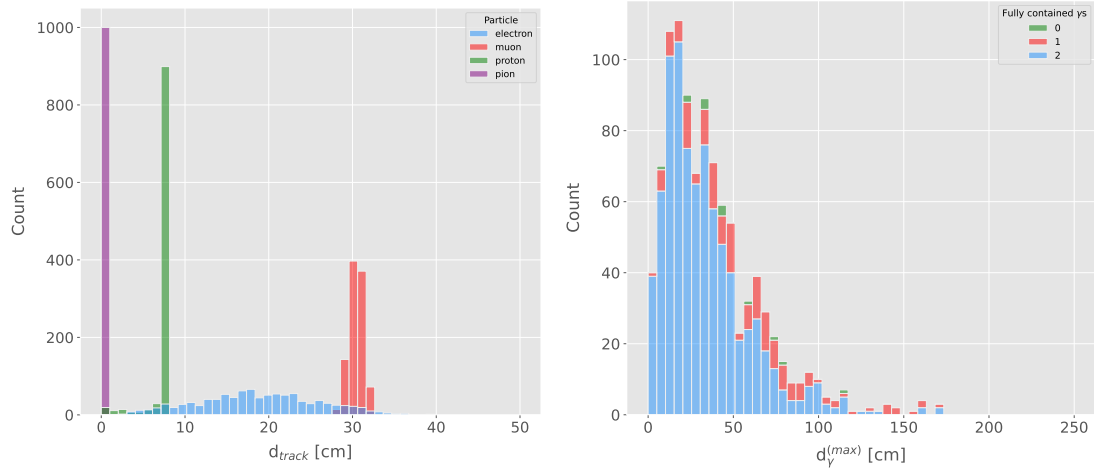


**Figure 4.10:** Left panel: distributions of the particles track length in the liquid argon for the generated  $E_k = 100$  MeV monoenergetic samples, electrons (blue), muons (red), protons (green) and neutral pions (purple). Right panel: distribution of the length of the longest photon in the neutral pion sample after the decay process  $\pi^0 \rightarrow \gamma\gamma$ .

of all generated particles with  $E_k = 100$  MeV. One can see that, in the case of the track-like particles (i.e. muons and protons), their length distributions are quite sharp and centered at relatively low distances (30 and 8 cm, respectively). For electrons, the distribution is quite broad but it does not extend past  $\sim 30$  cm. The case of neutral pions can be misleading, as they decay promptly the track length associated with the true Monte Carlo particle is always  $< 1$  cm. In Fig. 4.10 (right panel) I show the effective length distribution of the longest photon after the pion decays as  $\pi^0 \rightarrow \gamma\gamma$ , highlighting the number of fully contained photons in the TPC volume per event (either zero, one or both). One can see that the vast majority of events has both photons contained and that just a negligible number of them has none of them contained in the TPC volume. In any case, for the sake of caution, I will only keep the pion events with both photons contained.

Once I have prepared a sample at the Geant4 level, I need to process it through the detector simulation. In order to make adequate estimations of the noise levels and run the filtering and hit finder as I did with the ProtoDUNE data, one needs to turn off the default zero-suppression of the waveforms produced by the simulation. At this first stage I am only concerned with the waveforms with the noise added, so I keep the noise

## 4.5. Using simulated samples

addition option as true in the configuration. However, for studies related to the hit finder performance one will also need to store the noiseless waveforms in order to retrieve the truth information of the hits. I will discuss this approach next.

After the detector simulation stage, one needs to extract the no zero-suppressed noisy waveforms, along with their offline channel numbers, and store them in a certain format to be analysed later. To reduce the amount of data that will go for processing, I used the information from the Geant4 step of the simulation to select only the active channels, i.e. the channels where some ionisation electrons arrive. Moreover, as said previously, I only extract the waveforms from APA 0 and exclusively the ones coming from induction channels. The resulting ROOT file contains a tree with two branches, one containing the waveforms for each event and channel and the other with the corresponding offline channel numbers.

Finally, to extract the truth values for the orientation of the tracks and the energies of the particles I used a modified analysis module. This gives a ROOT file with a single tree, containing several branches with different information such as the components of the initial momentum of the particles, initial and final  $xyz$  location, track length, etc.

For the analysis of the resulting waveforms and truth values I used a custom set of Python libraries (available at [??]). Among other functionalities, these enable the user to read the ROOT files, export the raw data as pandas objects, apply the filters and compute the S/N of both the raw and filtered signals. So far, the default configuration for the filtering uses the set of optimal matched filter coefficients that I found using the ProtoDUNE data samples.

Additionally, for the analysis of the samples it was necessary to use two different reference frames, to study separately the signals coming from the U and V induction wire planes. As I am focussing on a single APA, the U and V wires have a different orientation in the  $yz$  plane. In the case of U wires, these are tilted  $35.7^\circ$  clockwise from the vertical ( $y$  direction), whereas the V wires are at the same angle but in the counter clockwise direction. Because of this, the best option is to deal with two new coordinate systems rotated by  $\pm 35.7^\circ$  along the  $x$  axis, so the new  $y'$  and  $y''$  directions are aligned with the

## Chapter 4. Matched Filter approach to induction wire Trigger Primitives

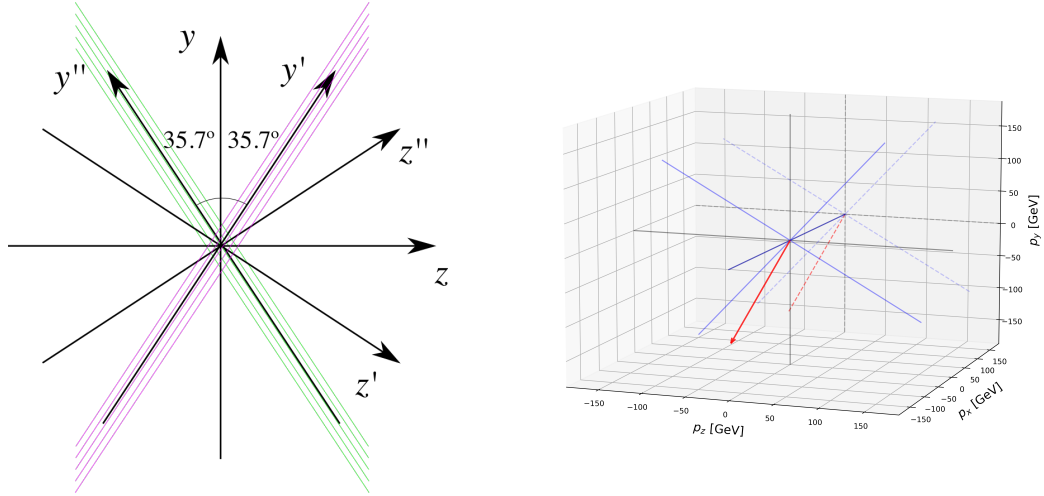


**Figure 4.11:** Left panel: schematic representation of the two new rotated reference frames used in this analysis (denoted as prime and double prime), viewed from the  $yz$  plane. The magenta stack of lines represent the wires in the  $U$  plane, whereas the green lines correspond to the wires in the  $V$  plane. Right panel: 3D representation of the momentum of one of the generated monoenergetic muons (red arrow) in the original reference frame (black lines), along with the new reference frame used for the  $U$  plane waveforms (blue lines). In the  $yz$  plane I added the projection of these three.

1639 U and V induction wires. Fig. 4.11 (left panel) shows a schematic representation of  
 1640 the original reference frame together with the two rotated ones (denoted by primed and  
 1641 double primed). This way, one can easily understand how parallel was a track to the  
 1642 wires in the two induction planes. Fig. 4.11 (right panel) shows a 3D representation of  
 1643 the momentum of a track (red arrow) in the original reference frame (black lines), along  
 1644 with the new reference frame for U wires (blue lines). I added the projection in the  $yz$   
 1645 plane of this three, to show the usefulness of the new reference frame to tell whether a  
 1646 track is parallel or normal to the wires in the induction plane.

1647 Fig. 4.12 shows the distribution of the average S/N improvement per event when one  
 1648 applies the optimal matched filters. I produced separate distributions for the channels  
 1649 in the U (red) and V (blue) induction wire planes. Notice that the S/N distributions  
 1650 for the track-like particles, i.e. muons (top left panel) and protons (bottom left panel),  
 1651 have significantly larger mean values than the distributions of the shower like particles,  
 1652 i.e. electrons (top right panel) and neutral pions (bottom right panel). An important

## 4.5. Using simulated samples

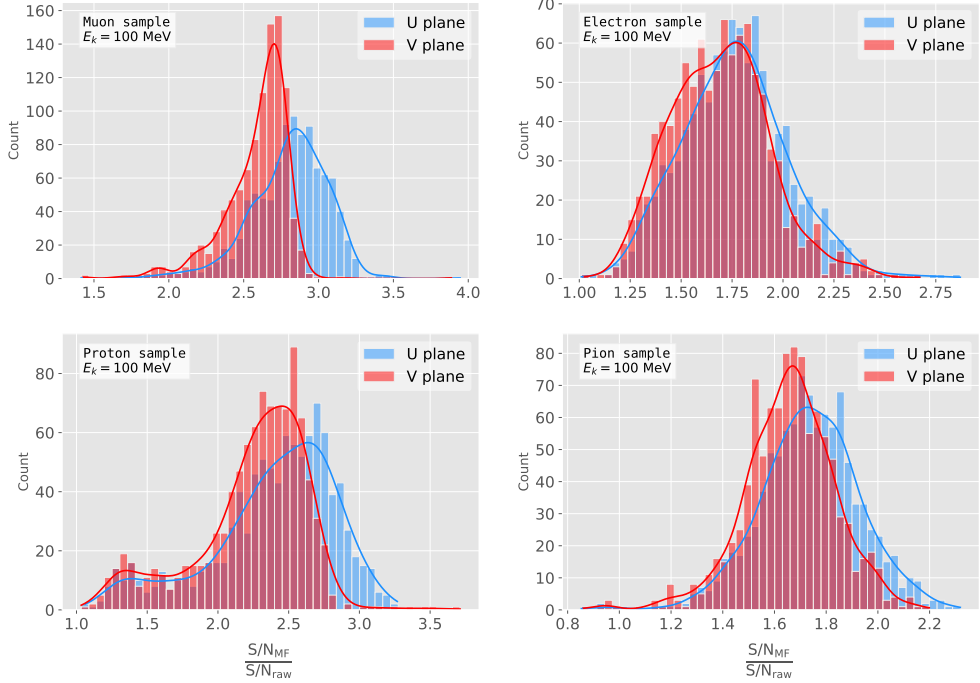


**Figure 4.12:** Distributions of the mean  $S/N$  improvement per event for the corresponding sample after applying the matched filters. Here I separated the change in the U plane (blue) and the V plane (red) channels. From top left to the right: muon, electron, proton and neutral pion. All the events have a fixed kinetic energy of  $E_k = 100 \text{ MeV}$ .

difference between these results and the ones seen before for ProtoDUNE data is that, overall, the improvements that I get for simulated data are bigger. This could be due either to the default noise model used in the *LArSoft* simulation or to the simulated hits having higher energy than the ones in the recorded data. Nonetheless, the concluding message is that the previously optimised matched filters give an overall significant improvement of the S/N for the different samples.

About the convention I followed for the plots and results, in the case of the raw and filtered S/N of each event in the sample I simply took the average of the quantities over all the active channels in the event. That is, if a certain event has  $N_{chan}$  active channels these two quantities are computed as:

$$(S/N_{fir})_{event} = \frac{\sum_{i=0}^{N_{chan}} (S/N_{fir})_i}{N_{chan}},$$

$$(S/N_{raw})_{event} = \frac{\sum_{i=0}^{N_{chan}} (S/N_{raw})_i}{N_{chan}}.$$
(4.18)

## Chapter 4. Matched Filter approach to induction wire Trigger Primitives

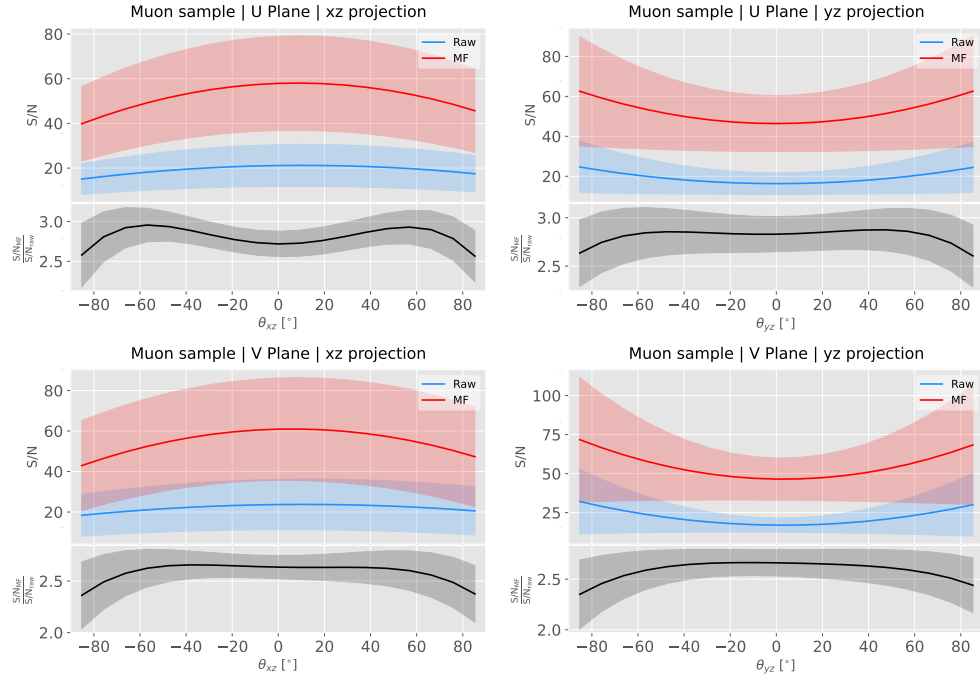


**Figure 4.13:** Angular dependence of the mean S/N and the S/N improvement, for the different monoenergetic samples considered (from top to bottom: electrons, muons, protons and neutral pions). The two columns on the left represent the values for the U plane waveforms. The top subplots show the mean S/N for raw (green) and filtered (red) waveforms whereas the bottom subplots depict the averaged S/N improvement (black).

1663 However, for the ratio of the raw and filtered S/N (what I called the S/N improvement)  
 1664 per event I am not just taking the ratio of the previous two quantities but computing  
 1665 the average of the individual ratios per channel in the event:

$$\left( \frac{S/N_{\text{fir}}}{S/N_{\text{raw}}} \right)_{\text{event}} = \frac{\sum_{i=0}^{N_{\text{chan}}} \left( \frac{S/N_{\text{fir}}}{S/N_{\text{raw}}} \right)_i}{N_{\text{chan}}}, \quad (4.19)$$

1666 and so:

$$\left( \frac{S/N_{\text{fir}}}{S/N_{\text{raw}}} \right)_{\text{event}} \neq \frac{(S/N_{\text{fir}})_{\text{event}}}{(S/N_{\text{raw}})_{\text{event}}}. \quad (4.20)$$

### 1667 4.5.1 Angular dependence

1668 Having these monoenergetic samples, one can also study the angular dependence of the  
 1669 performance of the matched filter. This is an important point, as it is a well established  
 1670 fact that for certain configurations (an extreme case configuration being signals normal

## 4.5. Using simulated samples

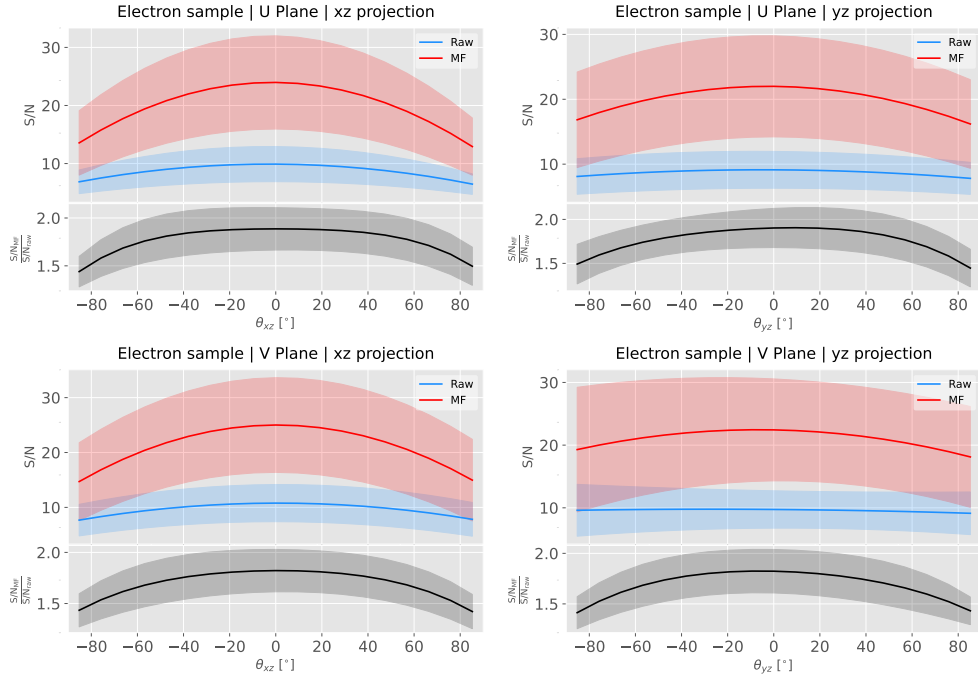


**Figure 4.14:** Angular dependence of the mean S/N and the S/N improvement, for the different monoenergetic samples considered (from top to bottom: electrons, muons, protons and neutral pions). The two columns on the left represent the values for the U plane waveforms. The top subplots show the mean S/N for raw (green) and filtered (red) waveforms whereas the bottom subplots depict the averaged S/N improvement (black).

to the wire plane and perpendicular to the induction wires at the same time) the S/N is much lower than average as the corresponding waveforms are severely distorted. In this sense, I am interested to see how the matched filter behaves for these cases and how the S/N improvement on those compare to the average.

Fig. 4.13 shows the angular dependence of the S/N for the monoenergetic  $E_k = 100$  MeV isotropic muons, for the different induction wire planes and projections. The angles for each event are given by the components of the initial value of the momentum of the particles, taking the angles of the projections on the  $xz$  and  $yz$  planes with respect to the  $z$  axis (more accurately, one needs to compute these angles twice for each event, a pair for the  $xy'z'$  coordinate system and the other for the  $xy''z''$ ). The top row shows the dependence on the angles corresponding to the U plane, i.e.  $\theta_{xz'}$  and  $\theta_{y'z'}$ , whereas the bottom row shows the angular dependence viewed from the V plane,  $\theta_{xz''}$  and  $\theta_{y''z''}$ . In each plot, the top subplot represents the mean values of the S/N for the raw (blue) and

## Chapter 4. Matched Filter approach to induction wire Trigger Primitives

1684 matched filtered (red) signals, and the bottom subplot the averaged S/N improvement  
1685 (black). The solid lines represent the mean value obtained for the corresponding angular  
1686 value, whereas the semitransparent bands represent one standard deviation around the  
1687 mean at each point.

1688 As expected, the S/N is in general higher when tracks are parallel to the APA (i.e.  
1689  $\theta_{xz} \sim 0$ ) and lower when it is normal to the plane ( $\theta_{xz} \sim \pm 90^\circ$ ). In the same way, tracks  
1690 parallel to the wires ( $\theta_{yz} \sim \pm 90^\circ$ ) tend to have higher S/N than those perpendicular to  
1691 these ( $\theta_{yz} \sim \pm 0$ ).

1692 Fig. 4.14 shows the corresponding angular dependence information for the  $E_k =$   
1693 100 MeV electrons sample. Notice that, in this case, the S/N behaviour discussed above  
1694 does not hold. A possible explanation can be that, because most hits in these events  
1695 are produced by the secondary particles generated in the EM shower, the signal peaks  
1696 whose S/N ratios were computed do not correspond to the directional information of  
1697 the primary electron.

### 1698 4.5.2 Distortion and peak asymmetry

1699 As a little case of study, I selected two of the simulated  $E_k = 100$  MeV monoenergetic  
1700 muon events. With respect to the U induction plane, one is parallel to the APA (low  
1701  $\theta_{xz'}$ ) and to the wires (high  $\theta_{y'z'}$ ) and the other is normal to the APA plane (high  $\theta_{xz'}$ )  
1702 and perpendicular to the wires (low  $\theta_{y'z'}$ ). As expected from the results on the angular  
1703 dependence discussed above, the former has a higher S/N (before and after the filtering)  
1704 when compared to the latter. An interesting thing to notice about these two samples  
1705 is that, even though one has a much bigger S/N than the other, it is the one with the  
1706 smallest S/N the one that got the biggest averaged S/N improvement. In Table 4.1  
1707 I included all the relevant parameters of these two  $E_k = 100$  MeV muon events I am  
1708 considering, namely, the angles with respect to the  $xy'z'$  reference frame, the values of  
1709 the S/N, the S/N improvement and also the so-called peak asymmetry  $\Delta_{peak}$  that I will  
1710 discuss next.

1711 One can try to understand better what is going on with these two events by looking

## 4.5. Using simulated samples

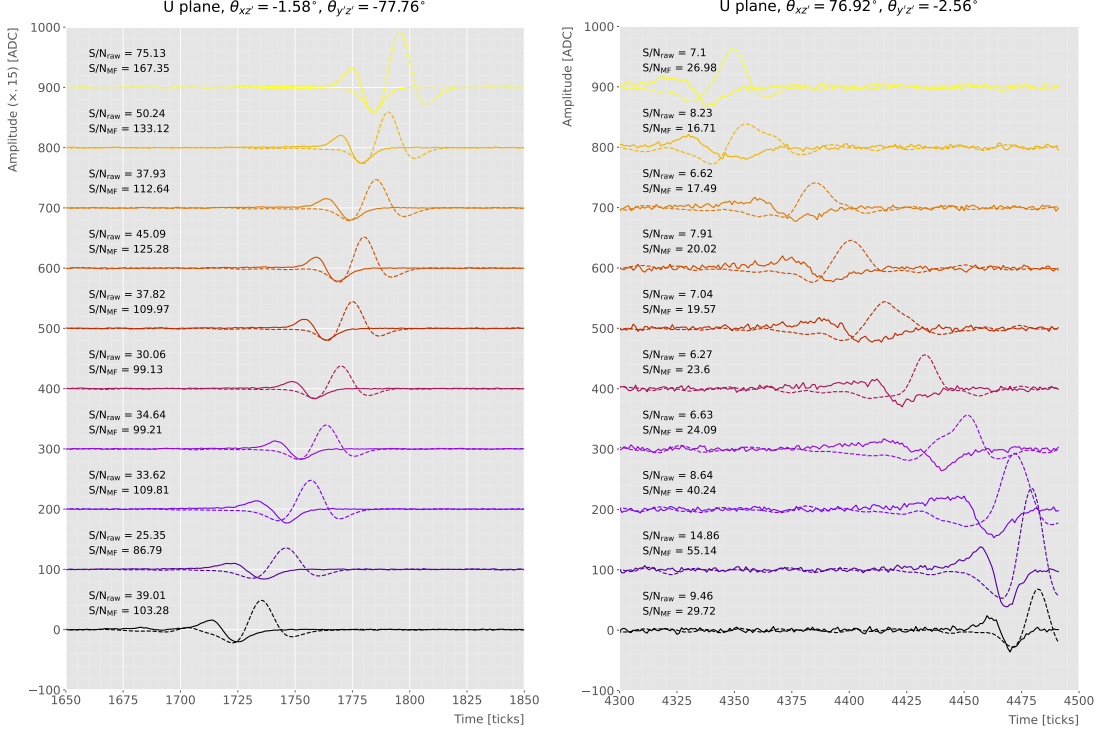


**Figure 4.15:** Selected consecutive waveforms corresponding to two monoenergetic  $E_k = 100$  MeV muon events, one is parallel to the APA and to the wires in the U plane (left panel) and the other is normal to the APA plane and perpendicular to the U plane wires (right panel). The solid lines represent the raw waveforms whereas the dashed lines correspond to the waveforms after the matched filter was applied. The waveforms on the left panel have been scaled by a factor of 0.15 to have similar amplitude to the ones on the right panel.

**Table 4.1:** Characteristic parameters of the two monoenergetic muon events selected, relative to the U plane: projected angles in the  $xz'$  and  $yz'$  planes, S/N values for the raw and filtered waveforms, mean improvement of the S/N and peak asymmetry.

	$\theta_{xz'}$ ( $^\circ$ )	$\theta_{yz'}$ ( $^\circ$ )	S/N <sub>raw</sub>	S/N <sub>MF</sub>	$\frac{S/N_{MF}}{S/N_{raw}}$	$\Delta_{peak}$ (ADC)
High ("parallel")	-1.58	-77.76	41.65	112.44	2.83	-35.73
Low ("normal")	76.92	-2.56	8.07	25.46	3.12	-10.38

at the raw and filtered data from some of their active channels. Fig. 4.15 shows a selection of consecutive raw and filtered U plane waveforms from the event with high S/N (left panel) and the one with low S/N (right panel). Notice that to show both collections of waveforms at a similar scale I had to apply a factor of 0.15 to the waveforms with high S/N. Additionally, next to each waveform I included the values of the raw and matched filtered S/N for the corresponding channel. The first thing to notice in this plot

## Chapter 4. Matched Filter approach to induction wire Trigger Primitives

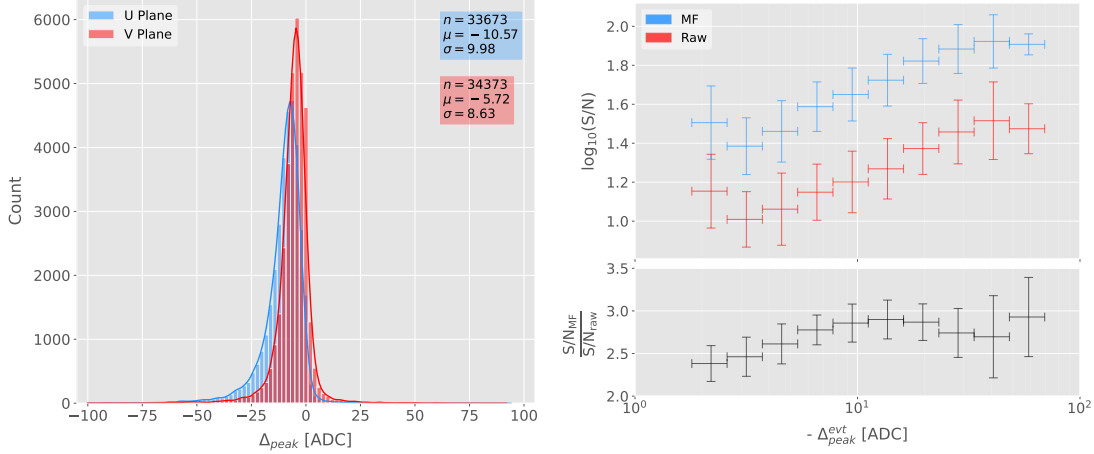


**Figure 4.16:** Left panel: peak asymmetry distribution for the case of the monoenergetic  $E_k = 100$  MeV muon sample. Each value corresponds to a single bipolar signal peak from a channel in any event. The blue distribution represents the peaks on U plane channels, whereas the red corresponds to signal peaks in V wires. Right panel: relation between the mean peak asymmetry per event with the S/N for U channel waveforms from the  $E_k = 100$  MeV muon sample. The top subplot shows the decimal logarithm of the mean S/N for the raw (red) and the matched filtered (blue) waveforms. The bottom subplot contains the mean S/N improvement ratio after the matched filter was applied.

is that the amplitude of the signal peaks from the normal track have a much smaller  
 amplitude, and also appear quite distorted when compared to the others. On the other  
 hand, although the matched filtered S/N is still smaller, the relative improvement is  
 bigger than in the parallel case.

A way I found to quantify the difference between the shapes within these two events  
 is their different peak asymmetry. One can define the peak asymmetry as the (signed)  
 difference between the positive and the negative peaks of the bipolar shape, i.e.:

$$\Delta_{peak} \equiv h_+ - h_-, \quad (4.21)$$

where both heights  $h_+$  and  $h_-$  are positive defined. Fig. 4.16 (left panel) shows the distribution of this peak asymmetry for all the waveforms corresponding to channels in the U (blue) and V (red) planes for the monoenergetic muon sample. One can see that these distributions are clearly shifted to negative values (with mean values  $\mu_\Delta^U = -10.57$  ADC and  $\mu_\Delta^V = -5.72$  ADC respectively). It is interesting to notice

## 4.5. Using simulated samples

that the peak asymmetry value of the sample with high S/N sits at the left tail of the distribution whereas the corresponding value of the sample with low S/N lies around the mean.

Now, one can try to correlate the peak asymmetry with the S/N and the S/N change per event. Fig. 4.16 (right panel) shows the result of comparing (minus) the mean peak asymmetry per event to the averaged raw (red) and matched filtered (blue) S/N per event (top subplot). The horizontal lines sit at the mean value obtained in the fit and represent the width of the  $-\Delta_{peak}$  bins used, while the vertical lines indicate one standard deviation around that mean value. Notice that, when taking decimal logarithm on both, there is an approximate linear relation between these quantities, except for peak asymmetry values bigger than  $-5$  ADC where the S/N remains constant.

Also, in the bottom subplot of Fig. 4.16 (right panel) I show the relation between the peak asymmetry and the mean S/N improvement. In this case, one see that there is a maximum at  $\Delta_{peak} \sim -10$  ADC. As mentioned previously, this is also the value of the mean of the peak asymmetry distribution. In fact, it is expected that our filter favours the signal peaks with the most common values of the peak asymmetry, as this was one of the features I target in our filter coefficient optimisation through the parameter  $\delta$ .

These results suggest that events with poorer values of the mean S/N, usually associated to non-favourable track orientations, tend to have smaller values of the mean peak asymmetry (in absolute value). Nonetheless, because our matched filters have been optimised to account for these asymmetries, the improvement on the S/N for these events is sizeable if not better than the one for events which already had a high S/N.

### 4.5.3 Hit sensitivity

One of the advantages of the matched filter, directly related to increasing the S/N, is the capability of picking hits that before fell below the threshold. For instance, Fig. 4.17 shows the raw ADC data from an example event (electron,  $E_k = 100$  MeV) with the produced true hits superimposed (black boxes), together with the hits produced by the standard hit finder chain (blue circles), i.e. using the current FIR filter, and the hits

## Chapter 4. Matched Filter approach to induction wire Trigger Primitives

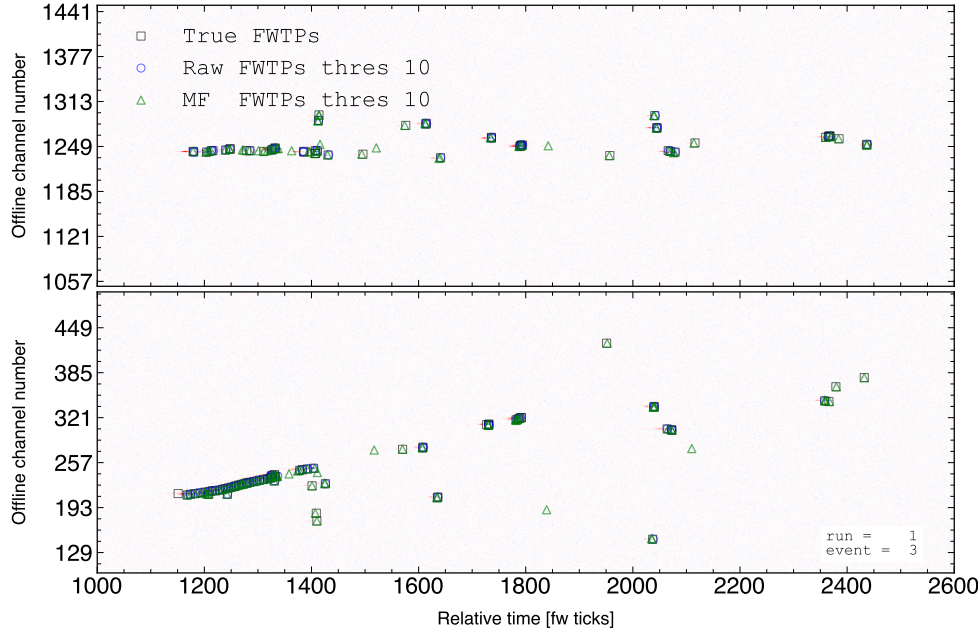


**Figure 4.17:** Raw data display in the plane time (in firmware ticks) vs. offline channel number for an  $E_k = 100$  MeV electron event. The produced true hits are superimposed (black boxes) as well as the hits coming from the standard hit finder chain (blue circles) and the hit finder using the matched filter (green triangles).

1758 obtained using the matched filters (green triangles). Both the standard and the matched  
 1759 filter hit finders were run with a threshold of 10 ADC. Notice that the standard hits  
 1760 match well the true ones at the initial part of the event (where we have a track-like  
 1761 object), but they miss most of the hits produced by the EM shower at later times. On  
 1762 the other hand, the hits produced with the matched filter have a better agreement with  
 1763 the true hits even for the more diffuse shower activity.

1764 Notwithstanding that now I get more hits with this combination of matched filter  
 1765 and low threshold as a results of the enhancement of the signal peaks relative to the  
 1766 noise level, it is also true that I pick some spurious hits not related to any real activity  
 1767 if one lowers the thresholds too much. Therefore, some optimisation of the threshold is  
 1768 needed. Basically one will need to make a trade-off between precision and sensitivity.

1769 Having this in mind, I tried to compare the produced hits one gets from the standard  
 1770 hit finder and the ones resulting from applying the matched filter with the true hits.  
 1771 By running the hit finders on our samples with different values of the threshold one

## 4.5. Using simulated samples

1772 can understand, for instance, how low one can set the threshold without getting mostly  
1773 spurious hits and then evaluate the gains obtained from this.

1774 Because now I am also interested in seeing how the hit sensitivity changes with the  
1775 energy, I prepared new isotropic samples with the same types of particles as before  
1776 (muons, electrons, protons and neutral pions) but with a flat kinetic energy distribution  
1777 ranging from 5 to 100 MeV.

1778 In order to estimate the hit sensitivity, given a certain sample, one needs to recover  
1779 the set of true hits to be able to compare these with the ones produced. To do so,  
1780 a modification in the procedure I was using to extract the raw waveforms is needed.  
1781 For this kind of study I run the detector simulation in two steps, first I produce the  
1782 waveforms without noise and extract them in the same format I used for the raw data,  
1783 then the noise is added and the noisy waveforms are then written to a file as well.

1784 To have a better comparison between the true hits and the ones produced from  
1785 the raw waveforms after applying the two filters, I applied also the FIR filter and the  
1786 matched filters to the noiseless waveforms and then I run the hit finder with a minimal  
1787 threshold (in this case I used 1 ADC) on these noiseless filtered waveforms. In this way  
1788 I generated two sets of true hits, I will refer to them as standard true hits (with the  
1789 current/default FIR filter) and matched filter true hits respectively. This allows a more  
1790 precise matching between the different groups of hits produced, as it will account for  
1791 any delays and distortions introduced by the FIR and the matched filters.

1792 In the case of the raw waveforms (with noise), I run the hit finder on them, with  
1793 different values of the threshold, after applying either the FIR or the matched filters. I  
1794 will name them simply standard hits and matched filter hits respectively. Then, I match  
1795 the generated hits to the true hits (the standard hits with the standard true hits and  
1796 the matched filter hits with the matched filter true hits). The matching is performed by  
1797 comparing the channel number and the timestamp of the hits. To count as a match,  
1798 I require that all hits with the same channel number and timestamp have overlapping  
1799 hit windows, i.e. the time windows between their hit end and hit start times need to  
1800 overlap. If more than one hit in one of the groups have hit overlap with the same hit in

## Chapter 4. Matched Filter approach to induction wire Trigger Primitives

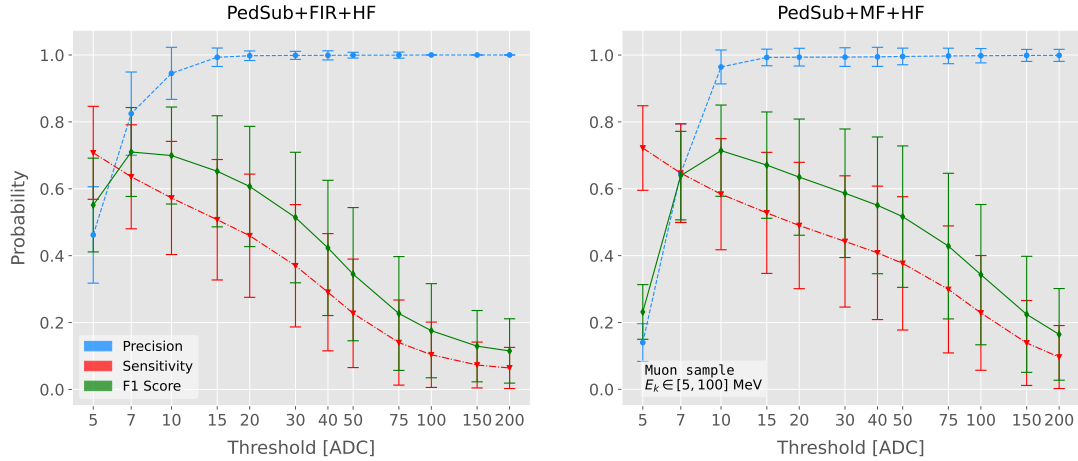


**Figure 4.18:** Dependence of the precision (blue), sensitivity (red) and  $F_1$  (green) scores on the threshold values used in the hit finder, for the FIR (left panel) and matched filter (right panel) cases. The results were obtained after matching the hits to the true hits in the case of the isotropic muon sample with kinetic energy in the range 5 to 100 MeV, taking only into account the induction plane channels. The points represent the mean value while the error bars indicate one standard deviation around that mean value.

1801 the other group I only count the hit with closer hit peak time value.

1802 The generation of the samples, the procedure to produce the standard hits (with the  
1803 default FIR filter) and matched filter hits and the matching of these with the true hits  
1804 is described in detail in App. ??.

1805 To quantify the performance of the two hit finder approaches, I use a classical method  
1806 from statistical classification known as confusion matrix [95]. This is basically a way of  
1807 sorting the outputs of a binary classifier, considering the true values of the classification  
1808 and the predicted values. It divides the outputs in four categories: true positive (TP,  
1809 both true and predicted values are 1), false negative (FN, true value is 1 but predicted  
1810 is 0), false positive (FP, true value is 0 but predicted is 1) and true negative (TN, both  
1811 true and predicted values are 0)).

1812 The contents of the confusion matrix allow us to compute other derived scores to  
1813 judge the performance of our classifiers. In this study, I will make use of three of these  
1814 metrics, namely the precision or positive predictive value:

$$\text{PPV} = \frac{\text{TP}}{\text{TP} + \text{FP}}, \quad (4.22)$$

## 4.5. Using simulated samples

1815 the sensitivity or true positive rate:

$$\text{TPR} = \frac{\text{TP}}{\text{TP} + \text{FN}}, \quad (4.23)$$

1816 and the  $F_1$  score [96]:

$$F_1 = \frac{2\text{TP}}{2\text{TP} + \text{FP} + \text{FN}}, \quad (4.24)$$

1817 which is the harmonic mean of the precision and the sensitivity.

1818 In our specific case I am not going to make use of the true negative value, as its  
1819 definition in this context can be ambiguous because one does not have clear instances in  
1820 the classification process. This way, I will only count the number of true positives as the  
1821 total amount of hits I can match between true and raw populations, the number of false  
1822 negatives will be the number of missing true hits and the false positive the number of  
1823 hits which do not match any true hit.

1824 In Fig. 4.18 I show the precision (blue), sensitivity (red) and  $F_1$  (green) scores I  
1825 obtained for different values of the threshold used in the hit finder for the case of the  
1826 muon sample. Because the matched filters are only applied to induction channels, I only  
1827 consider here hits coming from the U and V planes. The panel on the left corresponds  
1828 to the scores I got when I ran the hit finder on the FIR filtered waveforms, whereas the  
1829 right panel contains the scores for the matched filter case. The points are centered at  
1830 the threshold value used and represent the mean value obtained for each score using all  
1831 the generated events, while the error bars indicate one standard deviation around the  
1832 mean value.

1833 One can see that the precision for the matched filter case is lower when the thresholds  
1834 are very low, as the noise baseline is slightly amplified, but then rises to high values  
1835 quicker than for the FIR case. The other difference one can spot is that the sensitivity  
1836 in the FIR case starts dropping faster at around the same threshold values where the  
1837 precision stabilizes around 1, while in contrast for the matched filter this rapid decrease  
1838 starts at higher threshold values. A similar scan for the same thresholds was performed  
1839 for the electron sample in the same energy range, yielding similar results.

## Chapter 4. Matched Filter approach to induction wire Trigger Primitives

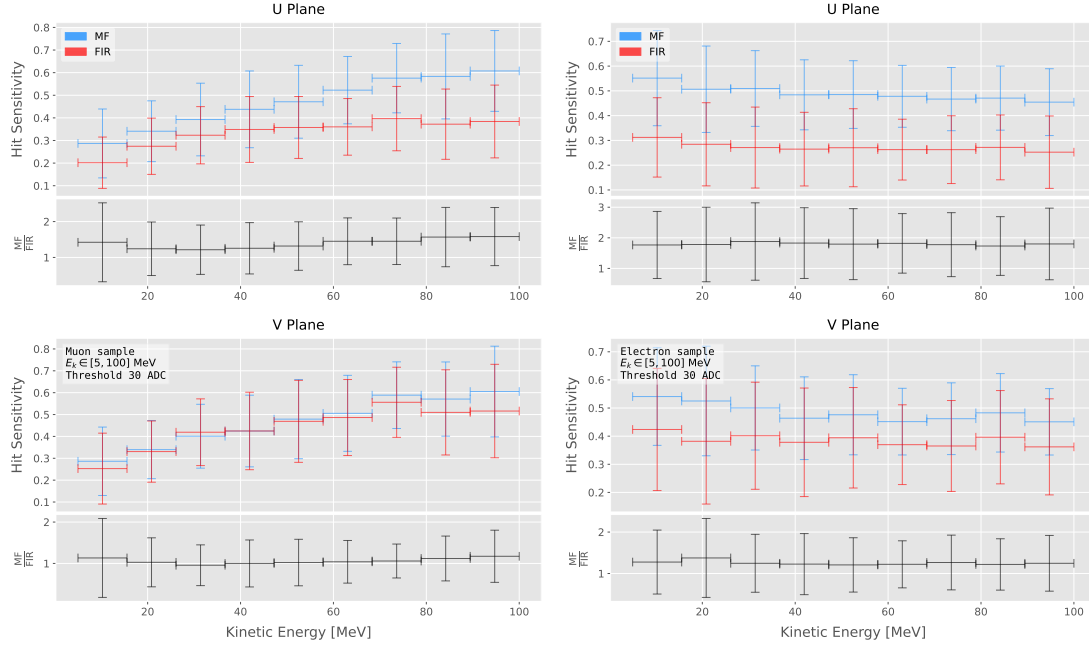


**Figure 4.19:** Dependence of the averaged hit sensitivity on the kinetic energy of the events for the matched filter (blue) and standard (red) hits, for the case of the muon (left panel) and electron (right panel) samples, separated between U (top plots) and V (bottom plots) induction wire planes. The top subplots contain the hit sensitivities for the two hit finder alternatives, while the bottom subplots show the ratio between the two. The horizontal lines sit at the mean value and represent the size of the energy bins, while the vertical error bars indicate one standard deviation around that mean value.

1840 In Fig. 4.19 I show the averaged hit sensitivity versus the kinetic energy of the  
 1841 events, both for the matched filter hits (blue) and the standard hits (red). The left  
 1842 panel corresponds to the muon sample, whereas the one on the right corresponds to the  
 1843 electron sample, both with kinetic energies between 5 and 100 MeV. In each panel the  
 1844 top plot corresponds to hits in the U plane, while the bottom plot contains the same  
 1845 information for the V plane. Each plot contains two subplots, the one on the top shows  
 1846 the hit sensitivity values for the matched filter and standard hits separate, while the  
 1847 bottom subplot depicts the ratio between the matched filter and standard sensitivities.  
 1848 The horizontal lines are placed at the mean value obtained in the fit and represent the  
 1849 width of the  $E_k$  bins used, while the vertical error bars indicate one standard deviation  
 1850 around that mean value. In both cases the threshold used was 30 ADC, as I required  
 1851 the precision to be higher than 0.99 for both matched filter and standard cases.

## 4.5. Using simulated samples

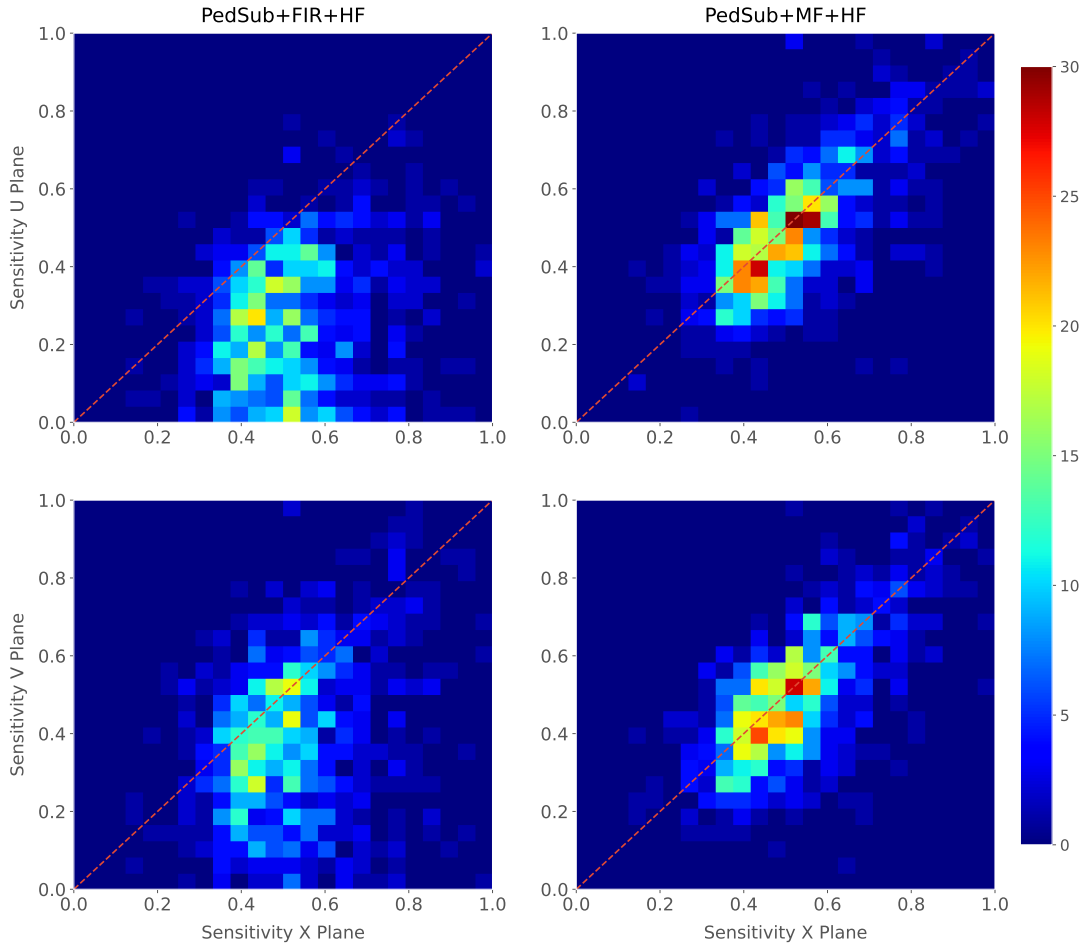


**Figure 4.20:** Distributions of the hit sensitivity in the U (top panels) and V (bottom panels) planes versus the hit sensitivity in the X plane, both for the standard hits (left panels) and the matched filter hits (right panels), in the case of the electron sample and a threshold of 30 ADC.

1852 One can see that, in general, the improvements are better for the U than for the V  
 1853 plane. While for the U channels I achieved a mean improvement of 50% and 80% for  
 1854 muons and electrons respectively, the improvement in the V plane is stalled at 10% and  
 1855 25%. Nevertheless, if I look at the sensitivities for the matched filter hits in both planes  
 1856 one can see these have similar mean values for each energy bin, while on the contrary  
 1857 for the standard hits the sensitivity remains relatively high for the V plane. This way, it  
 1858 looks there was a less significant gain because the hit sensitivity was already high.

1859 Another interesting observation is the different behaviors for muons and electrons.  
 1860 While hit sensitivity for muons grows significantly with energy, in the case of electrons

## Chapter 4. Matched Filter approach to induction wire Trigger Primitives

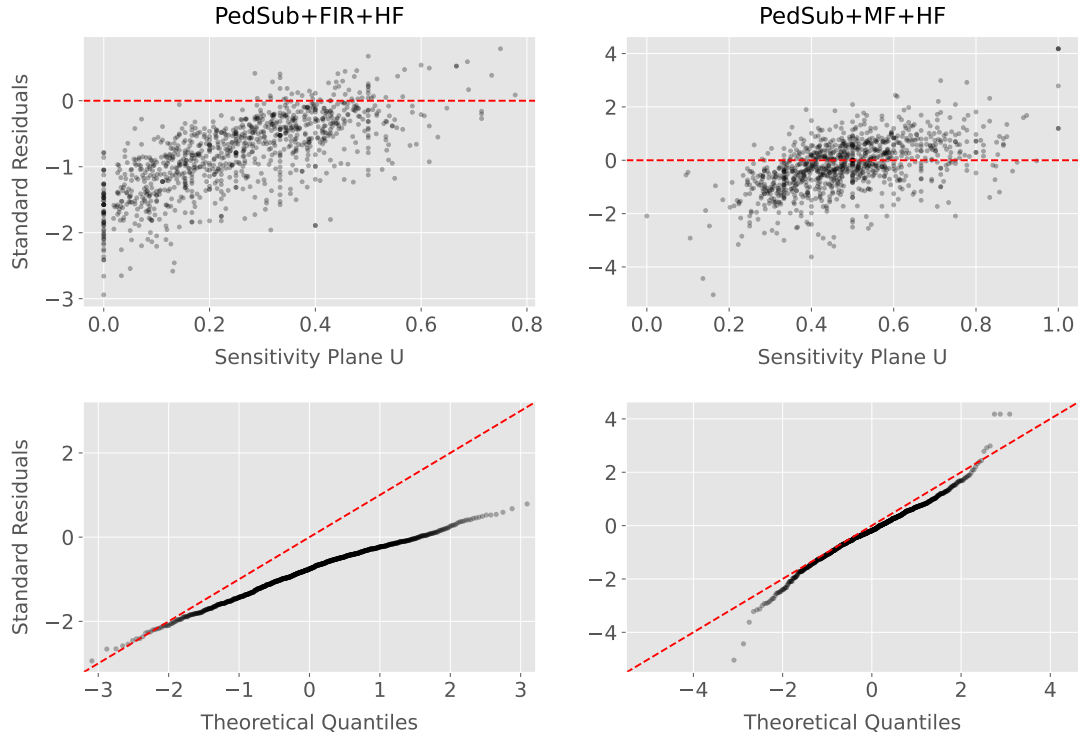


**Figure 4.21:** Top panels: standard residual plots of the hit sensitivities between the  $X$  and  $U$  planes. Bottom panels: quantile-quantile plots of the hit sensitivity standard residuals between the  $X$  and  $U$  planes. In all cases, the left panel corresponds to the standard hits while the right panel represents the matched filter case, all from the electron sample with a 30 ADC threshold.

1861 this slightly decreases the higher the kinetic energy of the event is. In any case, when it  
 1862 comes to the improvement on the sensitivities, this remains almost constant in all cases.

1863 Furthermore, we can look at how the concurrence of hits between the different wire  
 1864 planes has changed. For any given event, I expect to have a similar number of hits in the  
 1865 three planes. As the ionisation electrons need to cross the  $U$  and  $V$  planes prior to reach  
 1866 the collection plane  $X$  they will induce current in those wire planes. A way to check the  
 1867 concurrence of hits across planes is looking at the relation between the hit sensitivities  
 1868 for each individual event. One cannot expect the sensitivities to be exactly equal across  
 1869 planes, but ideally they should be normally distributed around the diagonal.

1870 Fig. 4.20 shows the hit sensitivity in the  $U$  (top panels) and  $V$  (bottom panels)  
 1871 planes versus the hit sensitivity in the  $X$  plane, for the case of the standard hits (left  
 1872 panels) and the matched filter hits (right panels). All plots were generated for the

## 4.5. Using simulated samples

1873 electron sample and a threshold of 30 ADC. From these one can see a clear trend,  
1874 when I use the standard hit finder chain the sensitivities in the induction planes are  
1875 systematically lower than the hit sensitivity in the X plane, i.e. most of the points sit  
1876 below the diagonal (red dashed line). In contrast, when the matched filters are applied,  
1877 the majority of the events are distributed around the diagonal. This points out that the  
1878 concurrence of hits across planes has improved.

1879 To exemplify the improvement I obtained, one can consider the residuals of the hit  
1880 sensitivities for the X and U planes. Assuming the diagonal hypothesis, i.e. given a  
1881 dataset of the form  $(x, y)$  for any  $x$  I take the predicted  $y$  value to be equal to the value  
1882 of  $x$ , I can compute the standard residuals for the hit sensitivities in U given the ones for  
1883 X. In Fig. 4.21 (top panels) I show these standard residuals against the corresponding  
1884 values of the hit sensitivity in the U plane, for our electron sample with kinetic energy  
1885 between 5 and 100 MeV. If I compare the scatter points in the case of the standard  
1886 hits (left panel) and the matched filter hits (right panel), I see that the residuals of the  
1887 standard hit finder case follow a certain pattern and their mean deviates from 0.

1888 To see clearly if the residuals are normally distributed, in Fig. 4.21 (bottom panels)  
1889 I plot the corresponding quantile-quantile plot for both the standard (left panel) and  
1890 matched filter (right panel) standard residuals. One can clearly see that the points for  
1891 the standard case follow a strongly non-linear pattern, suggesting that the residuals  
1892 do not follow a normal distribution. In contrast, for the matched filter hits the points  
1893 conform to a roughly linear path, implying that in this case the normality condition is  
1894 fulfilled.

1895 All these results hint at the fact that the concurrence of hits across the wire planes  
1896 can be strengthened by applying the matched filters.



1897 **Chapter 5**

1898 **DM searches with neutrinos from  
1899 the Sun**

1900 **5.1 Motivation**

1901 The idea of detecting neutrino signals coming from the Sun’s core to probe DM is not new.  
1902 The main focus of these searches has usually been high-energy neutrinos originated from  
1903 DM annihilations into heavy particles [97–100], although recent studies have proposed  
1904 to look at the low-energy neutrino flux arising from the decay of light mesons at rest in  
1905 the Sun [101–104] previously thought undetectable.

1906 In this chapter I try to demonstrate the capability of DUNE to constrain different  
1907 DM scenarios. I used the neutrino fluxes arising from DM annihilations in the core  
1908 of the Sun to compute the projected limits that DUNE would be able to set on the  
1909 annihilation rates in the Sun and the DM scattering cross sections.

1910 **5.2 Gravitational capture of DM by the Sun**

1911 The Sun and the centre of the Earth are possible sources of DM annihilations, specially  
1912 interesting because of their proximity. Their gravitational attraction ensured the capture  
1913 of DM from the local halo through repeated scatterings of DM particles crossing them.

## Chapter 5. DM searches with neutrinos from the Sun

1914 Only neutrinos produced from DM annihilations can escape the dense interior of these  
1915 objects. Therefore, neutrino telescopes are the most useful experimental layouts to  
1916 pursue DM searches from their cores.

1917 The neutrino flux from DM annihilations inside the Sun depends on the DM capture  
1918 rate, which is proportional to the DM scattering cross section, and the annihilation rate,  
1919 which is proportional to the velocity-averaged DM annihilation cross-section. The total  
1920 number of DM particles inside the Sun follows the Boltzmann equation [101]:

$$\frac{dN_{DM}}{dt} = C_{\odot} - A_{\odot} N_{DM}^2, \quad (5.1)$$

1921 where  $C_{\odot}$  and  $A_{\odot}$  are the total Sun DM capture and annihilation rates respectively.  
1922 In this expression I neglected the evaporation term, proportional to  $N_{DM}$ , which only  
1923 contribute for  $m_{DM} \lesssim 4$  GeV [105]. As the current threshold of neutrino telescopes  
1924 is a few GeV, this region falls below the probed range but can be important in future  
1925 low-energy projects.

1926 This equation has an equilibrium solution:

$$N_{DM}^{eq} = \sqrt{\frac{C_{\odot}}{A_{\odot}}}, \quad (5.2)$$

1927 which represents the amount of DM inside the Sun if the capture and annihilation have  
1928 reached equilibrium. As the Sun is approximately 4.6 Gyr old, it is usually assumed that  
1929 equilibrium has been achieved. Therefore, the anomalous neutrino flux from the Sun  
1930 would only depend on the DM scattering cross section, enabling us to set limits on this  
1931 quantity. If one does not assume equilibrium, some assumptions on the DM annihilation  
1932 cross section are necessary to extract predictions from neutrino signals.

1933 Here, I am going to consider three possible scenarios for the DM interactions: DM  
1934 scattering off electrons, spin-dependent (SD) and spin-independent interactions off nuclei.  
1935 For the case of these last two, the cross sections will be given in terms of the SD and  
1936 SI elastic scattering DM cross section off protons (assuming that DM interactions off

## 5.2. Gravitational capture of DM by the Sun

1937 protons and neutrons are identical),  $\sigma_p^{\text{SD}}$  and  $\sigma_p^{\text{SI}}$ , as [2, 101]:

$$\sigma_i^{\text{SD}} = \left( \frac{\tilde{\mu}_{A_i}}{\tilde{\mu}_p} \right)^2 \frac{4(J_i + 1)}{3J_i} |\langle S_{p,i} \rangle + \langle S_{n,i} \rangle|^2 \sigma_p^{\text{SD}}, \quad (5.3)$$

$$\sigma_i^{\text{SI}} = \left( \frac{\tilde{\mu}_{A_i}}{\tilde{\mu}_p} \right)^2 A_i^2 \sigma_p^{\text{SI}}, \quad (5.4)$$

1938 where  $\tilde{\mu}_{A_i}$  is the reduced mass of the DM-nucleus  $i$  system,  $\tilde{\mu}_p$  is the reduced mass of  
1939 the DM-proton system,  $A_i$  and  $J_i$  the mass number and total angular momentum of  
1940 nucleus  $i$  and  $\langle S_{p,i} \rangle$  and  $\langle S_{n,i} \rangle$  the expectation value of the spins of protons and neutrons  
1941 averaged over all nucleons, respectively (see Ref. [106] for a review on spin expectation  
1942 values).

1943 Since the Sun is mainly composed of Hydrogen, the capture of DM from the halo  
1944 is expected to occur mainly through spin-dependent scattering. However, since the  
1945 spin-independent cross section is proportional to the square of the atomic mass, heavy  
1946 elements can contribute to the capture rate (even though they constitute less than 2%  
1947 of the mass of the Sun). Heavy elements can also contribute to the spin-dependent cross  
1948 section if the DM has also momentum-dependent interactions.

1949 DM particles can get captured by the Sun if after repeated scatterings off solar  
1950 targets their final velocity is lower than the escape velocity of the Sun. In the limit of  
1951 weak cross sections, this capture rate can be approximately written as [2]:

$$C_{\odot}^{\text{weak}} = \sum_i \int_0^{R_{\odot}} dr 4\pi r^2 \int_0^{\infty} du_{\chi} \frac{\rho_{\chi}}{m_{\chi}} \frac{f_{v_{\odot}}(u_{\chi})}{u_{\chi}} \omega(r) \int_0^{v_e(r)} dv R_i^-(\omega \rightarrow v) |F_i(q)|^2, \quad (5.5)$$

1952 where the summation extends over all possible nuclear targets. In this expression,  $R_{\odot}$   
1953 is the radius of the Sun,  $\rho_{\chi}$  is the local DM density,  $m_{\chi}$  the mass of the DM particle,  
1954  $f_{v_{\odot}}(u_{\chi})$  the DM velocity distribution seen from the Sun's reference frame,  $R_i^-(\omega \rightarrow v)$   
1955 is the differential rate at which a DM particle with velocity  $v$  scatters a solar target of  
1956 mass  $m_i$  to end up with a velocity  $\omega$  and  $|F_i(q)|$  is the nuclear form factor of target  $i$ .

1957 The differential scattering rate takes a rather simple form when considering velocity-

## Chapter 5. DM searches with neutrinos from the Sun

<sup>1958</sup> independent and isotropic cross sections. In that case, this quantity is given by [2, 107]:

$$R_i^-(\omega \rightarrow v) = \frac{2}{\sqrt{\pi}} \frac{\mu_{i,+}^2}{\mu_i} \frac{v}{\omega} n_i(r) \sigma_i \left[ \chi(-\alpha_-, \alpha_+) + \chi(-\beta_-, \beta_+) e^{\mu_i(\omega^2 - v^2)/u_i^2(r)} \right], \quad (5.6)$$

<sup>1959</sup> where  $\mu_i$  is the ratio between the DM mass and the mass of target  $i$ ,  $\mu_{i,\pm}$  is defined as:

$$\mu_{i,\pm} \equiv \frac{\mu_i \pm 1}{2}, \quad (5.7)$$

<sup>1960</sup>  $n_i(r)$  is the density profile of target  $i$  in the solar medium,  $u_i(r)$  is the most probable

<sup>1961</sup> velocity of target  $i$  given by:

$$u_i(r) = \sqrt{\frac{2T_\odot(r)}{m_i}}, \quad (5.8)$$

<sup>1962</sup> where  $T_\odot(r)$  is the temperature of the Sun, the quantities  $\alpha_\pm$  and  $\beta_\pm$  are defined as:

$$\alpha_\pm \equiv \frac{\mu_{i,+}v \pm \mu_{i,-}\omega}{u_i(r)}, \quad (5.9)$$

$$\beta_\pm \equiv \frac{\mu_{i,-}v \pm \mu_{i,+}\omega}{u_i(r)}, \quad (5.10)$$

<sup>1963</sup> and the function  $\chi(a, b)$  is a Gaussian integral of the form:

$$\chi(a, b) \equiv \int_a^b dx e^{-x^2}. \quad (5.11)$$

<sup>1964</sup> Finally, if one assumes the DM halo velocity distribution in the galactic rest frame

<sup>1965</sup> to be a Maxwell-Boltzmann distribution, one can write the halo velocity distribution for

<sup>1966</sup> an observer moving at the speed of the Sun with respect to the DM rest frame as:

$$f_{v_\odot}(u_\chi) = \sqrt{\frac{3}{2\pi}} \frac{u_\chi}{v_\odot v_d} \left( e^{-\frac{3(u_\chi - v_\odot)^2}{2v_d^2}} - e^{-\frac{3(u_\chi + v_\odot)^2}{2v_d^2}} \right), \quad (5.12)$$

<sup>1967</sup> where:

$$\omega^2 = u_\chi + v_e(r)^2, \quad (5.13)$$

<sup>1968</sup> is the DM velocity squared,  $v_\odot$  the relative velocity of the Sun from the DM rest frame

## 5.2. Gravitational capture of DM by the Sun

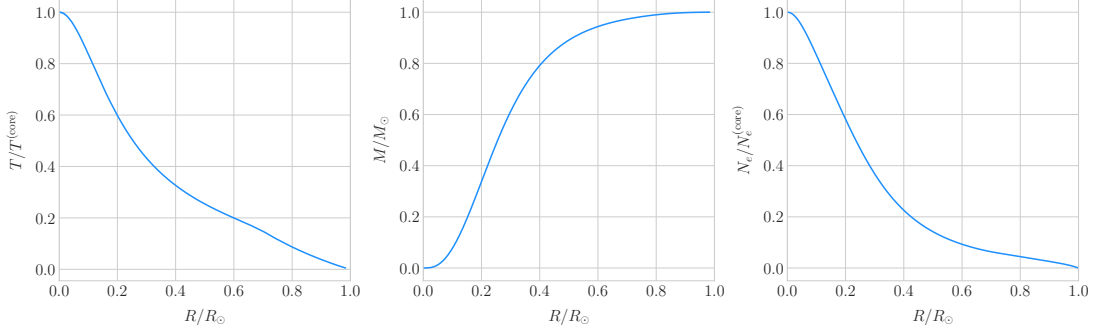


**Figure 5.1:** Input solar parameters used in our capture rate computation as functions of the Sun's radius, from left to right: temperature (with respect to the temperature at the core), mass (in solar masses) and electron number density (with respect to the electron density at the core). All quantities shown correspond to the standard solar model BS2005-OP [1].

1969 and  $v_d \simeq \sqrt{3/2}v_\odot$  the velocity dispersion.

1970 For the case of strong scattering cross section, Eq. (5.5) ceases to be valid, as it  
 1971 escalates indefinitely with the cross section. In that limit, the capture rate saturates to  
 1972 the case where the probability of interaction is equal to one, which can be written as:

$$C_\odot^{\text{geom}} = \pi R_\odot^2 \left( \frac{\rho_\chi}{m_\chi} \right) \langle v \rangle \left( 1 + \frac{3}{2} \frac{v_e^2(R_\odot)}{v_d^2} \right) \xi(v_\odot, v_d), \quad (5.14)$$

1973 where  $v_d = \sqrt{8/3\pi}v_d$  is the mean velocity in the DM rest frame and the factor  $\xi(v_\odot, v_d)$   
 1974 accounts for the suppression due to the motion of the Sun:

$$\xi(v_\odot, v_d) = \frac{v_d^2 e^{-\frac{3v_\odot^2}{2v_d^2}} + \sqrt{\frac{\pi}{6}} \frac{v_d}{v_\odot} (v_d^2 + 3v_e^2(R_\odot) + 3v_\odot^2) \text{Erf} \left( \sqrt{\frac{3}{2}} \frac{v_\odot}{v_d} \right)}{2v_d^2 + 3v_e^2(R_\odot)}. \quad (5.15)$$

1975 Having these into account, one can write the total capture rate as a combination of  
 1976 both contributions, allowing a smooth transition between the two, as:

$$C_\odot = C_\odot^{\text{weak}} \left( 1 - e^{C_\odot^{\text{geom}}/C_\odot^{\text{weak}}} \right). \quad (5.16)$$

1977 I computed the capture rate from Eq. (5.16) in the case of interactions with  
 1978 electrons. To do so, I used the standard solar model BS2005-OP [1]. Fig. 5.1 shows the

## Chapter 5. DM searches with neutrinos from the Sun

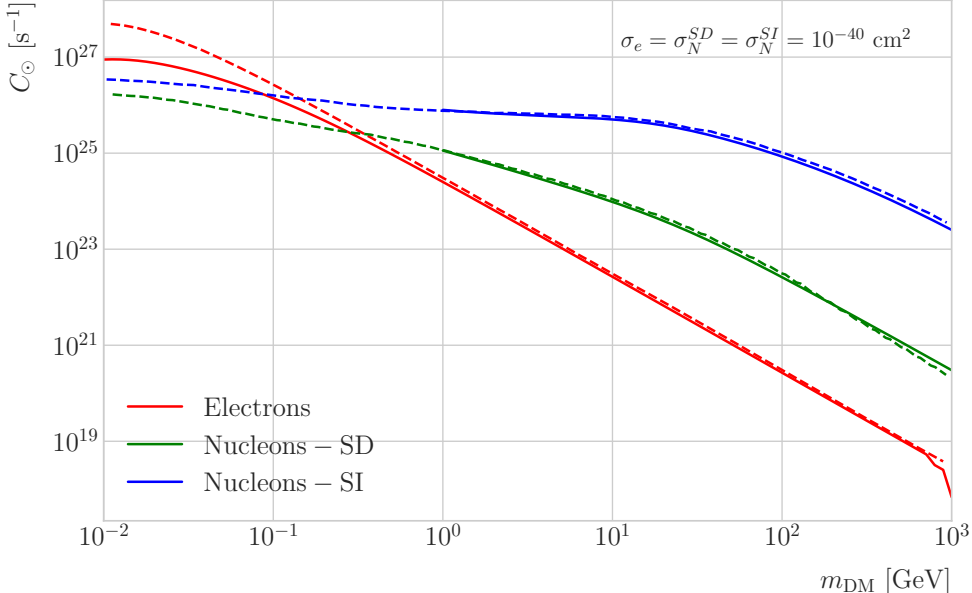


**Figure 5.2:** Capture rates as a function of the DM mass for the DM-electron interactions (red lines), SD DM-nucleons interactions (green lines) and SI DM-nucleons interactions (blue lines). Solid lines represent the values computed in this work while the dashed lines are the one given in Ref. [2]. All the rates are shown for a choice of scattering cross section of  $\sigma_i = 10^{-40} \text{ cm}^2$ .

1979 three parameters from the solar model that are needed for the computation, the solar

1980 temperature (left panel), mass (central panel) and electron density (right panel) profiles.

1981 For the case of the interactions off nuclei, the computations are more convoluted

1982 as one needs to add up the contributions of the different most abundant nuclei in

1983 the Sun. Also, in contrast to the electron scenario where the form factor is trivially

1984  $|F_e(q)|^2 = 1$ , for any nucleus  $i$  one would need to consider some appropriate nuclear

1985 density distribution (either a Gaussian approximation, a Woods-Saxon distribution, etc)

1986 which would complicate the calculations even further.

1987 That is the reason why, at this stage of our study, I decided to take an alternative

1988 approach to the computation of the DM-nucleus capture rates. I used the **DarkSUSY**

1989 software, that allows us to compute these quantities performing a full numerical

1990 integration over the momentum transfer of the form factors. The default standard

1991 solar model used by **DarkSUSY** is BP2000<sup>1</sup> [108].

---

<sup>1</sup>This is what they say in their manual, but I fear it is somewhat outdated. It appears to me this

## 5.2. Gravitational capture of DM by the Sun

1992 In Fig. 5.2 I show the results I obtained for the capture rates, for the case of  
 1993 interactions off electrons (red solid line), SD (green solid line) and SI (blue solid line)  
 1994 interactions of nucleons. In all cases I used a value of the scattering cross sections of  
 1995  $\sigma_i = 10^{-40} \text{ cm}^2$ . Note here one of the limitations of the **DarkSUSY** approach, one can  
 1996 not extend the computation below  $m_{\text{DM}} = 1 \text{ GeV}$ . Nevertheless, this is not something  
 1997 to worry about in this case, as I will discuss next. As a comparison, I added also the  
 1998 values computed in Ref. [2] (same color scheme, dashed lines). One can see there is good  
 1999 agreement between these and the **DarkSUSY** computation of the SD and SI interactions  
 2000 for  $m_{\text{DM}} \geq 1 \text{ GeV}$ . In this regime their computations also matches quite well our  
 2001 result for the electron capture rate. However, these start to differ significantly below  
 2002  $m_{\text{DM}} = 1 \text{ GeV}$ , being their estimate up to a factor of 5 bigger than ours for low masses.

2003 Let us comment briefly about the assumption I made before about not including  
 2004 an evaporation term in the Boltzmann equation. If I include this term in the equation  
 2005 (which will be proportional to the number of DM particles) the equilibrium solution  
 2006 takes the form:

$$N_{\text{DM}}^{eq} = \sqrt{\frac{C_{\odot}}{A_{\odot}}} \frac{1}{\kappa + \frac{1}{2} E_{\odot} \tau_{eq}}, \quad (5.17)$$

2007 where  $E_{\odot}$  is the total evaporation rate,  $\tau_{eq}$  is the equilibrium time in the absence of  
 2008 evaporation:

$$\tau_{eq} = \frac{1}{\sqrt{C_{\odot} A_{\odot}}}, \quad (5.18)$$

2009 and  $\kappa$  is defined as:

$$\kappa \equiv \sqrt{1 + \left( \frac{E_{\odot} \tau_{eq}}{2} \right)^2}. \quad (5.19)$$

2010 Now, it is easy to proof that in case evaporation dominates  $\kappa \gg 1$  and therefore:

$$N_{\text{DM}}^{eq} \simeq \frac{C_{\odot}}{E_{\odot}}. \quad (5.20)$$

2011 In contrast, if evaporation is irrelevant  $\kappa \simeq 1$  and one recovers Eq. (5.2).

---

model is relatively old and do not see why they are not using others like [1]. Maybe one can double-check in the code to make sure.

## Chapter 5. DM searches with neutrinos from the Sun

2012 In this way, one can define the evaporation mass as the mass for which the number  
2013 of DM particles in equilibrium approaches Eq. (5.20) at 10% level:

$$\left| N_{DM}^{eq}(m_{\text{evap}}) - \frac{C_{\odot}(m_{\text{evap}})}{E_{\odot}(m_{\text{evap}})} \right| = 0.1 N_{DM}^{eq}(m_{\text{evap}}). \quad (5.21)$$

2014 This can be regarded as the minimum testable mass one can reach using the annihilation  
2015 products of the DM in the Sun.

2016 It was reported in Ref. [2] that, in the case of both SD and SI DM interactions  
2017 off nuclei, this value ranges from 2 to 4 GeV depending on the specific scattering  
2018 cross section value, compatible with the usual assumptions in the literature. What is  
2019 interesting is the case of the electron capture. It was found that, when one applies a  
2020 cutoff in the velocity distribution of the DM trapped in the Sun slightly below the escape  
2021 velocity, the evaporation mass for the DM-electron interaction decreases remarkably. For  
2022 a moderate choice of  $v_c(r) = 0.9v_e(r)$  one gets an evaporation mass of around 200 to  
2023 600 MeV. This possibility opens a region of the parameter space that could be tested  
2024 with neutrino detectors.

### 2025 5.3 Neutrino flux from DM annihilations

2026 When WIMPs annihilate inside the Sun a flux of high-energy neutrinos is expected from  
2027 heavy quarks, gauge bosons and  $\tau^+\tau^-$  final states, which decay before losing energy in  
2028 the dense solar medium, as they will produce a continuum spectra up to  $E_{\nu} \sim m_{\chi}$  (in  
2029 the case of direct annihilation to neutrinos one would have a line at  $E_{\nu} = m_{\chi}$ ) [102].  
2030 This kind of signal has been extensively studied in the literature, allowing to put strong  
2031 limits on the SD WIMP-proton cross section for large  $m_{\chi}$ . However, the number of  
2032 high-energy neutrinos per WIMP annihilation is small and the spectrum depends on the  
2033 unknown final state. Moreover, background rejection is easier for large  $m_{\chi}$  but neutrinos  
2034 with  $E_{\nu} \gtrsim 100$  GeV are significantly attenuated by interactions in the Sun.

2035 Nevertheless, most WIMP annihilation final states eventually produce a low-energy  
2036 neutrino spectrum. In this case one does not just consider the more massive final states

## 5.4. Computing limits from solar neutrino fluxes

2037 but also annihilations into  $e^+e^-$ ,  $\mu^+\mu^-$  and light quarks [101]. In particular, light  
 2038 mesons would be produced and stopped in the dense medium, thus decaying at rest and  
 2039 producing a monoenergetic neutrino signal. The decay-at-rest of kaons will produce  
 2040 a  $E_\nu = 236$  MeV  $\nu_\mu$  while in the case of pions one would have a  $E_\nu = 29.8$  MeV  $\nu_\mu$ .  
 2041 In practice only  $K^+$  and  $\pi^+$  contribute to these signals, as  $K^-$  and  $\pi^-$  are usually  
 2042 Coulomb-captured in an atomic orbit and get absorbed by the nucleus. There is also a  
 2043 low-energy neutrino signal coming from muon decays, which are produced in kaon or  
 2044 pion decays, leptonic decays of other hadrons and heavy leptons or even directly from  
 2045 WIMP annihilations, which can decay at rest and contribute to the previous low-energy  
 2046 neutrino flux with a well known spectrum below 52.8 MeV.

2047 These monoenergetic MeV neutrinos were previously considered undetectable but,  
 2048 due to the large yield, the known spectra and the modern advances in the detector  
 2049 technology, these low-energy neutrino flux can be a good probe of the SD WIMP-proton  
 2050 cross-section in standard solar WIMP capture scenario, as it is sensitive to low WIMP  
 2051 masses and insensitive to the particular final state. A good place to look for these signals  
 2052 are next-generation neutrino experiments such as DUNE.

## 2053 5.4 Computing limits from solar neutrino fluxes

2054 In order to use the neutrino fluxes from DM annihilations in the Sun, the first thing I  
 2055 need to do is to determine the expected number of atmospheric background events, for  
 2056 a given exposure, after directionality selection has been applied. I can write this number  
 2057 as:

$$N_B = \eta_B \int d\Omega \int_{E_{min}}^{E_{max}} dE_\nu \frac{d^2\Phi_{atm}^\mu}{dE_\nu d\Omega} \times \left( A_{eff}^{(\mu)}(E_\nu) T \right), \quad (5.22)$$

2058 where  $\eta_B$  is the background efficiency,  $E_{min}$  and  $E_{max}$  the minimum and maximum  
 2059 energies to integrate over,  $d^2\Phi_{atm}^\mu/dE_\nu d\Omega$  the differential flux of atmospheric muon  
 2060 neutrinos,  $A_{eff}^{(\mu)}$  is the effective area of DUNE to muon neutrinos and  $T$  is the exposure  
 2061 time. The effective area can be expressed as the product of the neutrino-nucleus scattering  
 2062 cross section and the number of nuclei in the fiducial volume of the detector. This way

## Chapter 5. DM searches with neutrinos from the Sun

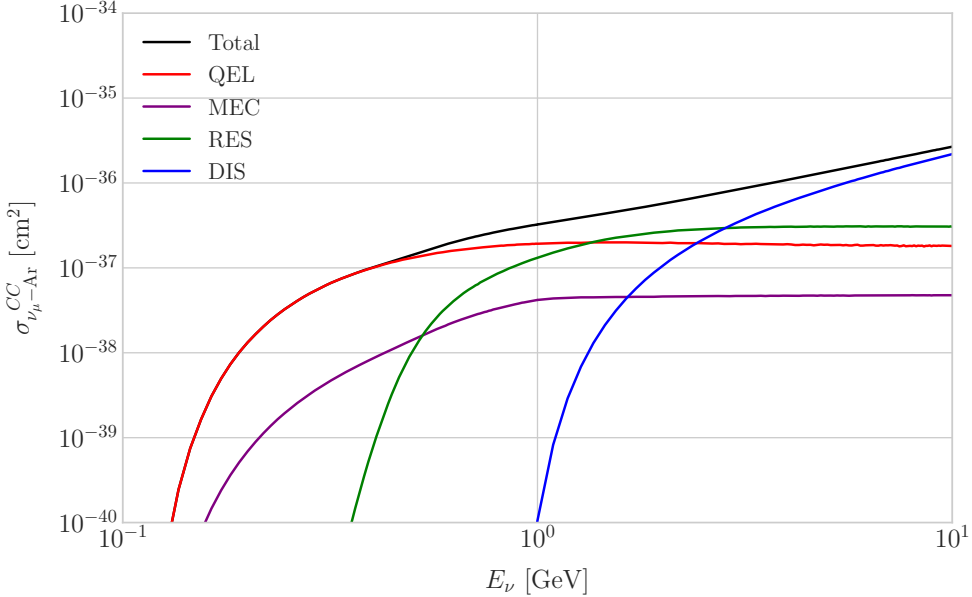


**Figure 5.3:** *NuWro* computed  $\nu_\mu - {}^{40}\text{Ar}$  charged-current scattering cross section as a function of the neutrino energy  $E_\mu$ . The black line shows to the total cross section, whereas the others correspond to the different contributions (in red quasi-elastic scattering, in green resonant pion exchange, in blue deep inelastic scattering and in purple meson exchange current).

2063 for DUNE I can write:

$$A_{eff}^{(\mu)}(E_\nu) = (6.0 \times 10^{-10} \text{ m}^2) \left( \frac{\sigma_{\nu-\text{Ar}}^{(\mu)}(E_\nu)}{10^{-38} \text{ cm}^2} \right) \left( \frac{M_{target}}{40 \text{ kT}} \right), \quad (5.23)$$

2064 where  $\sigma_{\nu-\text{Ar}}^{(\mu)}$  is the  $\nu_\mu - {}^{40}\text{Ar}$  charged-current scattering cross section. In Fig. 5.3 I  
 2065 show the computed value of this cross section as a function of the neutrino energy  $E_\nu$ ,  
 2066 in the range of interest both for the atmospheric background and signal events. It was  
 2067 computed using the NuWro Monte Carlo neutrino event generator [109], including the  
 2068 charged-current contributions of the quasi-elastic scattering (red line), resonant pion  
 2069 exchange (green line), deep inelastic scattering (blue line) and meson exchange current  
 2070 (purple line).

2071 The background rejection will depend on the resolution of the detector and the  
 2072 selection one applies on the events. A geometry argument can be used to estimate  
 2073 the maximum background rejection one can achieve in this case, considering one can

## 5.4. Computing limits from solar neutrino fluxes

2074 efficiently discriminate all events coming from a direction different from that of the  
 2075 Sun. In that case, the optimal background efficiency will simply be the relative angular  
 2076 coverage of the Sun. Taking the angular diameter of the Sun as seen from the Earth to  
 2077 be  $0.5^\circ$ , I have:

$$\eta_B^{(opt)} \approx \frac{\pi \left(\frac{0.5}{2}\right)^2}{360 \times 180} \simeq 3.03 \times 10^{-6}. \quad (5.24)$$

2078 This value will give a very optimistic estimate of the number of background events.  
 2079 However, it can be regarded as an lower limit, as it represents the best case scenario.

2080 In Fig. 5.4 I show the fluxes of atmospheric neutrinos at the Homestake mine during  
 2081 solar minimum, taken from Ref. [3]. The values are averaged over the two angular  
 2082 directions. In blue I have the flux of muon neutrinos while in red I indicate the flux  
 2083 of electron neutrinos. Additionally, the dashed lines correspond to both antineutrino  
 2084 species.

2085 Using these values for the muon neutrino and the corresponding total CC cross  
 2086 section, one can compute the number of expected background events by integrating over  
 2087 the given energy range (as in this case the angular integral is trivial). As for the energy  
 2088 range to integrate over, I choose the range for DUNE specified in [69],  $E_{min} = 10^{-1}$  GeV  
 2089 and  $E_{max} = 10$  GeV. Taking all these into account, I found the number of background  
 2090 events to be:

$$N_B \simeq \eta_B \times (3.827 \times 10^4) \times \left( \frac{\text{exposure}}{400 \text{ kT yr}} \right). \quad (5.25)$$

2091 In order to estimate the sensitivity of DUNE to this kind signal, one can consider a  
 2092 hypothetical data set where the number of observed neutrinos is taken to be the expected  
 2093 number of background events rounded to the nearest integer,  $N_{obs} = \text{round}(N_B)$  [110].  
 2094 Now, if I assume that the number of signal and background events seen by DUNE are  
 2095 given by Poisson distributions with means equal to the expected number of signal and  
 2096 background events,  $N_S$  and  $N_B$ , one can denote by  $N_S^{90}$  to the number of expected  
 2097 signal events such that the probability of having an experimental run with a number of  
 2098 events greater than  $N_{obs}$  is 90%. This number can be obtained as the numerical solution

## Chapter 5. DM searches with neutrinos from the Sun

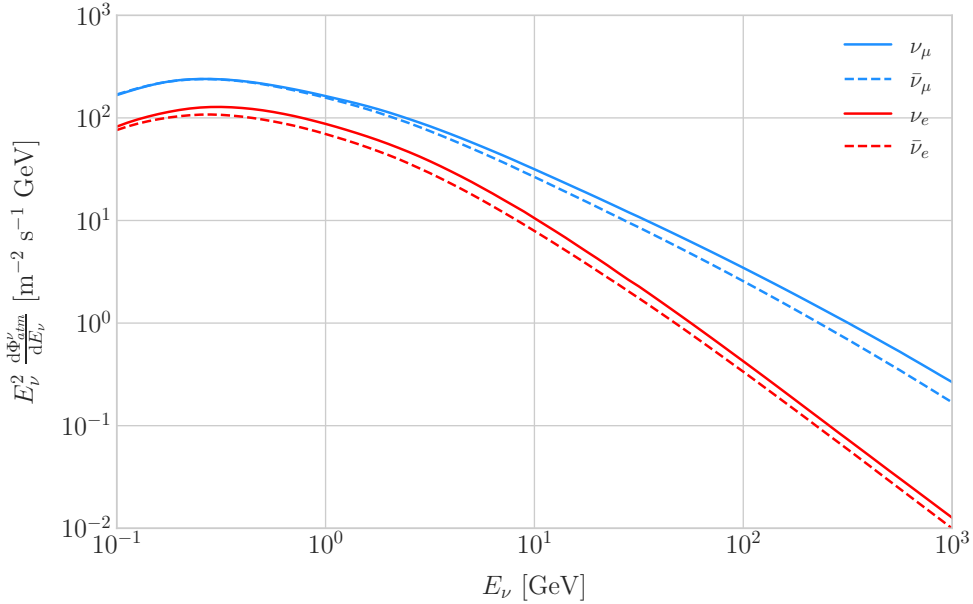


**Figure 5.4:** Expected atmospheric neutrino flux as a function of the neutrino energy  $E_\nu$  at Homestake at solar minimum, taken from Ref. [3]. The blue solid (dashed) line correspond to muon neutrinos (antineutrinos) and the red solid (dashed) line correspond to electron neutrinos (antineutrinos).

2099 to the equation:

$$1 - \frac{\Gamma(N_{obs} + 1, N_S^{90} + N_B)}{N_{obs}!} = 0.9, \quad (5.26)$$

2100 where  $\Gamma(x, y)$  is the upper incomplete gamma function.

2101 The number of signal events is related to the neutrino flux from DM annihilations in  
2102 a similar way as the background events to the atmospheric neutrino flux. In this case I  
2103 have:

$$N_S = \eta_S \Gamma_A^{eq} \int_{z_{min}}^{z_{max}} dz \frac{dN_\nu}{dAdN_Adz} \times (A_{eff}^\mu(z)T), \quad (5.27)$$

2104 where  $\eta_S$  is the signal efficiency,  $\Gamma_A^{eq}$  is the total annihilation rate of DM particles at  
2105 equilibrium,  $\Gamma_A^{eq} = A_\odot (N_{DM}^{eq})^2$ ,  $z_{min}$  and  $z_{max}$  the minimum and maximum relative  
2106 energies to integrate over (in such a way that  $z_{min,max} \leq E_{min,max}/m_{DM}$  for each  $m_{DM}$ )  
2107 and  $dN_\nu/dAdN_Adz$  the muon neutrino flux per DM annihilation in the Sun.

2108 Knowing  $N_S^{90}$  one can use the relation in Eq. (5.27) to obtain  $\Gamma_A^{eq,90}$  for different  
2109 values of the DM mass. From there I can directly translate those values into the

## 5.5. Example: Kaluza-Klein Dark Matter

upper limits for DUNE on the DM scattering cross sections, for a given exposure. The relation between the annihilation rate and the DM-nucleon cross section comes from the equilibrium condition through the solar DM capture rate. The details of the evolution of the number of DM particles inside the Sun and the computation of the capture rates are discussed in App. 5.2.

### 5.5 Example: Kaluza-Klein Dark Matter

Even though there are plenty of BSM theories which provide viable dark matter candidates, Kaluza-Klein type of models [111, 112] within the universal extra dimensions (UED) paradigm naturally predict the existence of a massive, stable particle that can play the role of the dark matter. In the UED scenario all the SM fields can propagate in one or more compact extra dimensions [113], as opposed to the idea of brane worlds [114, 115], where just gravity can propagate in the bulk while SM particles live at fixed points.

Furthermore, in UED there is no violation of the translational invariance along the extra dimensions, thus leading to degenerate KK modes masses and also the conservation of the KK number in the effective four dimensional theory. At loop level, radiative corrections and boundary terms shift the masses of the KK modes and break KK number conservation into a KK parity. As a result, this theory only contains interactions between an even number of odd KK modes and therefore the lightest among the first KK excitations will be stable. This particle is usually denoted as the lightest Kaluza-Klein particle (LKP) and its mass is proportional to  $1/R$ , being  $R$  the size of the extra dimension.

A viable DM candidate needs to be electrically neutral and non-baryonic, therefore good candidates among the first Kaluza-Klein excitations would be the KK neutral gauge bosons and the KK neutrinos [116]. Another possible candidate is the first KK excitation of the graviton, which receives negligible radiate contributions and therefore has a mass almost equal to  $1/R$ , but it has been shown that the lightest eigenstate from

## Chapter 5. DM searches with neutrinos from the Sun

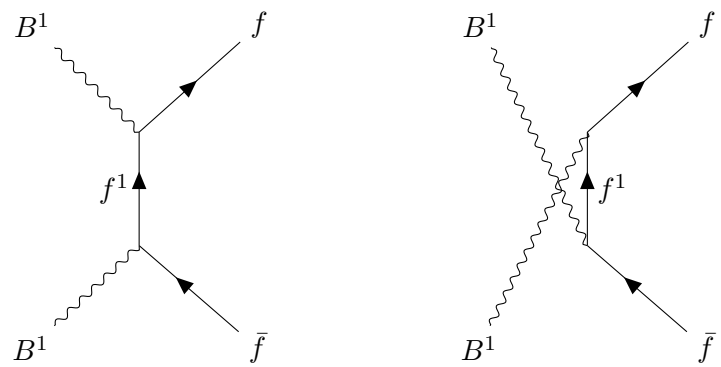


**Figure 5.5:** Feynman diagrams for  $B^1 B^1$  annihilation into SM fermions.

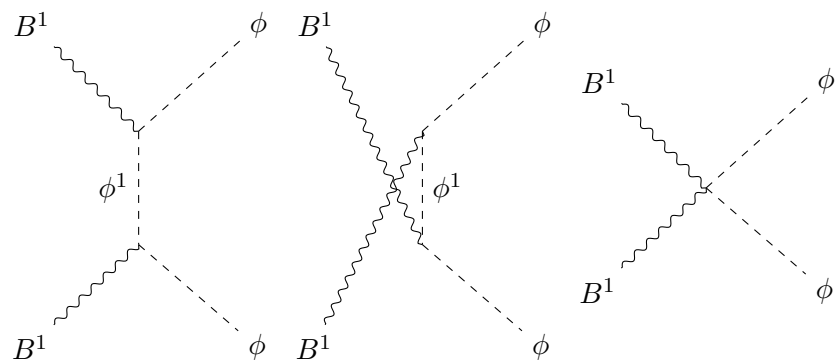


**Figure 5.6:** Feynman diagrams for  $B^1 B^1$  annihilation into a Higgs boson pair.

## 5.5. Example: Kaluza-Klein Dark Matter

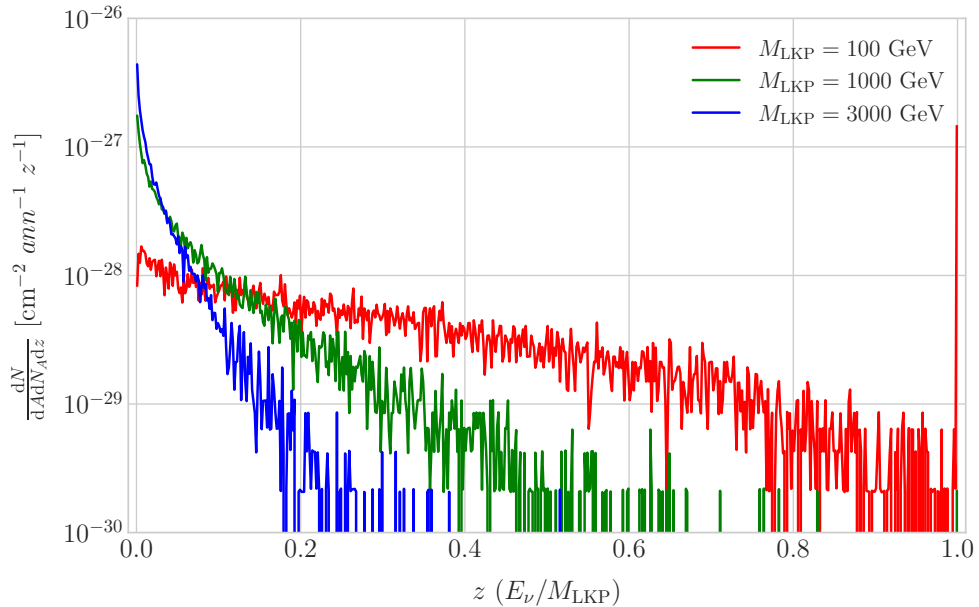


**Figure 5.7:** Computed spectra of muon neutrinos at the DUNE FD site from  $B^1$  annihilations in the Sun for three different values of  $M_{\text{LKP}}$ , plotted in relative energy units for legibility.

the mixing of the gauge mass states  $(B^1, W_3^1)$  would be lighter, as  $B^1$  and  $W_3^1$  receive negative radiative corrections [117]. It is also understood that, when these corrections become sizeable, the eigenstates become approximately pure  $B^1$  and  $W_3^1$  states as the Weinberg mixing angle grows small with the KK number [117]. In that case, the LKP can be well-approximated as being entirely  $B^1$ .

I need to compute the neutrino flux produced by the annihilations of the LKP in the core of the Sun, taking into account their propagation in the solar medium, as well as neutrino oscillations. To this end I used `WimpSim` [118, 119] to generate one million annihilation events in the Sun over a time span of four years and propagate them to the DUNE FD location ( $44^\circ 20' \text{ N}, 103^\circ 45' \text{ W}$ ), for different values of  $M_{\text{LKP}}$ . In Fig. 5.7 I show the obtained muon neutrino spectra arriving to the detector from LKP annihilations in the Sun, per unit area and per annihilation, plotted in relative energy units for different values of the mass. As one could expect the spectra get steeper the higher is the mass, due to the absorption of high-energy neutrinos in the solar medium. Also, one can see the peak at  $z = 1$  due to the direct annihilation into

## Chapter 5. DM searches with neutrinos from the Sun

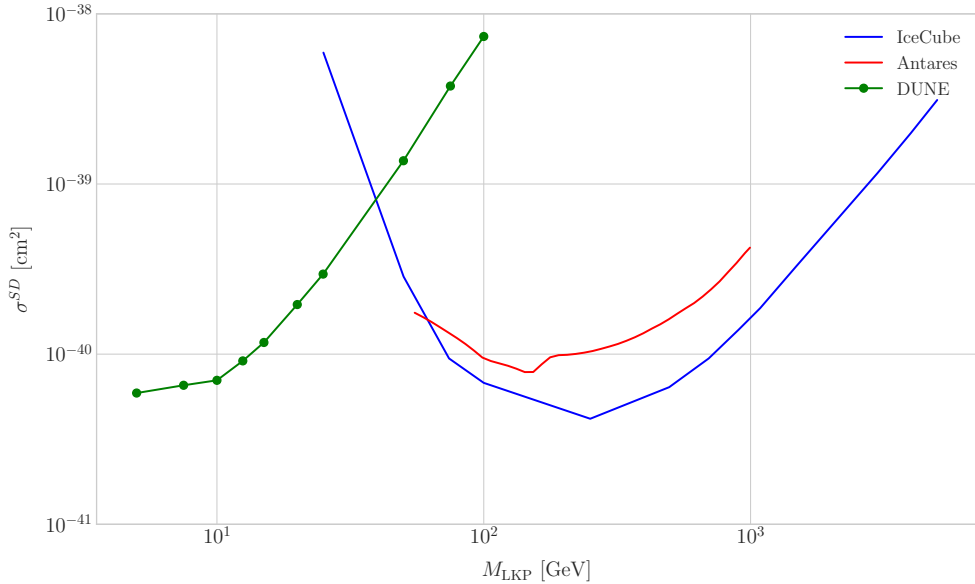


**Figure 5.8:** Projected 90% confidence level upper limit for DUNE (400 kT yr) on the spin-dependent  $B^1$ -proton scattering cross section as a function of  $M_{\text{LKP}}$  (green dots). I also show the previous limits from IceCube [4] (blue line) and Antares [5] (red line) on the LKP cross section. The shaded area represents the disfavoured region (at 95% confidence level) on the mass of the LKP from LHC data [6].

2152 neutrinos  $\chi\chi \rightarrow \nu\bar{\nu}$ .

2153 Now, one can estimate the sensitivity of DUNE to this particular model by using  
 2154 the methods I previously discussed. To begin with, I will use the optimistic estimation  
 2155 of the background efficiency in Eq. (5.24) to get our upper bound. Using it, one can  
 2156 directly compute the number of expected background events to be  $N_B = 0.1101$  for an  
 2157 exposure of 400 kT yr. Then, Eq. (5.26) give us a value of  $N_S^{90} = 2.20$  for the 90%  
 2158 exclusion number of expected signal events. By using the NuWro generated cross sections  
 2159 and the computed neutrino fluxes from  $B^1$  annihilations in the Sun I can estimate the  
 2160 limits on the SD and SI DM-nucleus cross section using the relation in Eq. (5.2) and  
 2161 the capture rates I computed with DarkSUSY.

2162 In Fig. 5.8 I show the projected sensitive for DUNE on the spin-dependent  $B^1$ -proton  
 2163 scattering cross section versus the mass of the DM particle, for a exposure of 400 kT yr  
 2164 (green dots). I also include the previous results from IceCube [4] (blue line) and Antares  
 2165 [5] (red line). The shaded area represents the disfavoured region from combined searches

## 5.6. High energy DM neutrino signals

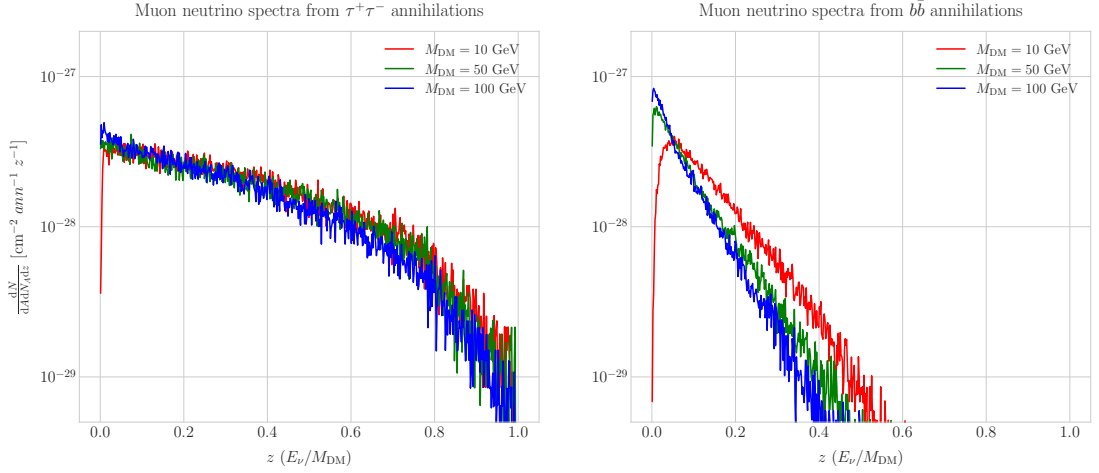


**Figure 5.9:** Computed spectra of muon neutrinos at the DUNE FD site from  $\tau^+\tau^-$  (left panel) and  $b\bar{b}$  (right panel) annihilations in the Sun for the DM masses  $m_{\text{DM}} = 10$  GeV (red line), 50 GeV (green line) and 100 GeV (blue line), plotted in relative energy units.

2166 for UED by ATLAS and CMS [6].

2167 From the experimental point of view, this estimation lacked a detailed simulation of  
 2168 the detector response and thus this must be consider as a mere optimistic sensitivity  
 2169 computation. However, it shows the potential of DUNE to constrain this kind of exotic  
 2170 scenarios, showing the region where it will be in a position to compete with other  
 2171 neutrino telescopes. A more detailed analysis is needed if I am to make a realistic  
 2172 estimation. Even though the region of the parameter space where DUNE would be  
 2173 sensitive to this particular model is quite constrained by collider searches [6] and other  
 2174 rare decay measurements [120, 121], it still constitutes an alternative indirect probe.

## 2175 5.6 High energy DM neutrino signals

2176 To have better estimates on the capability of the DUNE FD to constrain the parameter  
 2177 space of DM using solar neutrino fluxes, I need to start accounting for the detector  
 2178 resolution effects and the topologies of the different signatures. As a starting point, I  
 2179 will focus on specific annihilation channels. For the case of DUNE, the relevant ones  
 2180 are mainly the hard channels  $\tau^+\tau^-$  and  $\nu\bar{\nu}$  and the soft channel  $b\bar{b}$ . These are the open  
 2181 annihilation channels for relatively low mass WIMPs that will actually give neutrino

## Chapter 5. DM searches with neutrinos from the Sun

2182 fluxes. Other channels, like  $W^+W^-$  and  $ZZ$ , are open for more massive WIMPs, but  
2183 those will produce usually a higher energy neutrino flux that will be out of reach for  
2184 DUNE (usually the maximum neutrino energy is taken to be  $E_{max} = 10$  GeV).

2185 In Fig. 5.9 I show the `WimpSim` [118, 119] generated muon neutrino spectra at the  
2186 DUNE FD location ( $44^\circ 20' N, 103^\circ 45' W$ ) from  $\tau^+\tau^-$  (left panel) and  $b\bar{b}$  (right panel)  
2187 annihilations in the core of the Sun, for different DM masses. Here, one can clearly see  
2188 the meaning of the previous distinction between hard and soft channels. For the same  
2189 DM mass value, the muon neutrino spectrum from the  $\tau^+\tau^-$  channel is more flat and  
2190 reaches higher energies than the one from the  $b\bar{b}$  channel, which drops faster.

2191 In this case, I prepared two sets of files, one for  $\tau^+\tau^-$  and the other for  $b\bar{b}$ , for DM  
2192 masses in the range from 5 to 100 GeV (actually for  $b\bar{b}$  the first mass point I took is  
2193 7.5 GeV, as a WIMP with  $m_{DM} = 5$  GeV can not kinematically self annihilate into  $b\bar{b}$ ).  
2194 Then, I prepared the `WimpSim` output fluxes in a specific way to use them as inputs to  
2195 `NuWro`, which simulates the neutrino interaction with the argon.

2196 Because `WimpSim` outputs an event list together with the fluxes, I can use the former  
2197 to generate the events. The direction of these is given in terms of the azimuth and  
2198 altitude angles viewed from the specified location, so first I need to convert these into the  
2199 DUNE FD coordinates. Once I have done it, each event can be processed with `NuWro`.  
2200 To increase the number of samples and optimise the computation time, I generate 100  
2201 interactions (i.e. `NuWro` events) for each `WimpSim` event<sup>2</sup>. I restrict the event generation  
2202 to charged current interactions, but I allow all the different contributions to the CC  
2203 cross section, i.e. quasielastic scattering (QEL), meson exchange current process (MEC),  
2204 resonant pion production (RES) and deep inelastic scattering (DIS). I just take into  
2205 account the CC contribution because I am only interested in final states with charged  
2206 leptons, as we have better chances of reconstructing the kinematics of CC events.

2207 For the atmospheric fluxes I follow a similar procedure, only that this time I do not  
2208 have a set of events but the fluxes binned in azimuth and altitude angles. This way, I

---

<sup>2</sup>This also solves a problem related with the generation of the neutrino interactions in `NuWro`, as if you only produce one event each time you launch `NuWro` it will always produce an interaction of the dominant interaction type for that particular energy.

## 5.6. High energy DM neutrino signals

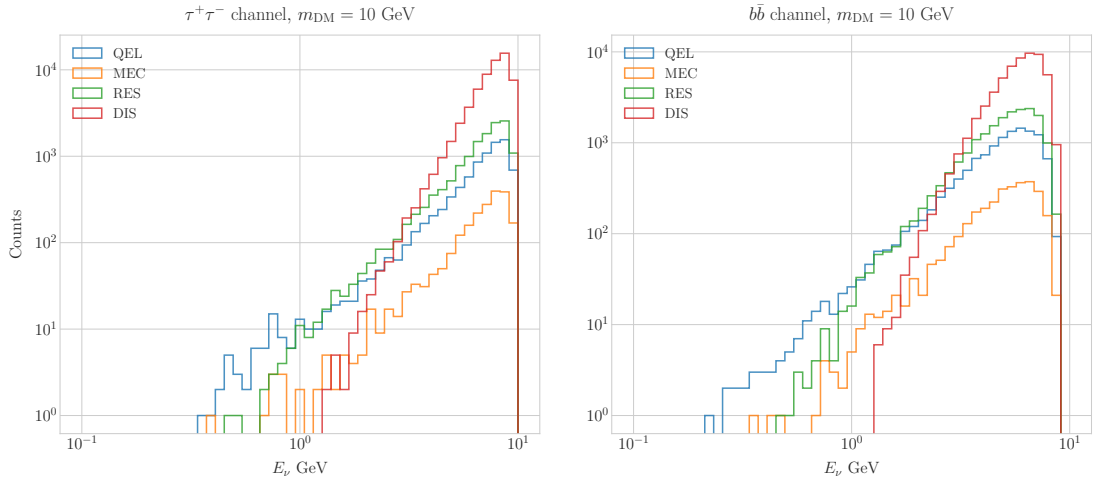


**Figure 5.10:** Distribution of the muon neutrino energies from the  $\tau^+\tau^-$  (left panel) and  $b\bar{b}$  (right panel) annihilation channels, for  $m_{\text{DM}} = 10 \text{ GeV}$ , separated by CC interaction type: QEL (blue), MEC (orange), RES (green) and DIS (red).

transform these to DUNE coordinates and process the fluxes for each bin separated with  
 NuWro.

At this point, I have two sets of events with different energies and final states.  
 In Fig. 5.10 one can see the distribution of the muon neutrino energies for the case  
 $m_{\text{DM}} = 10 \text{ GeV}$ , both for the  $\tau^+\tau^-$  (left panel) and  $b\bar{b}$  (right panel) channels, separated  
 by interaction. One can clearly see that there are different energy regimes where the  
 primary interaction type is different. This leads to a plurality of event topologies,  
 therefore making it difficult to implement a general approach to the selection of events  
 in detriment of the background. As a way to proceed, I decided to split our samples,  
 based on the different interaction modes and contents of the final state, into a CC DIS  
 sample and a single proton CC QEL sample.

### 5.6.1 DIS events

To begin with, I consider the high energy part of the spectrum. In this region DIS events  
 dominate, i.e. interactions of the form  $\nu_\mu + q_d(\bar{q}_u) \rightarrow \mu^- + q_u(\bar{q}_d)$ . Therefore, our final  
 estates will contain a muon and a hadronic jet from the fragmentation of the outgoing  
 quark. As all these events have  $E_\nu \gtrsim 1 \text{ GeV}$  the momentum transfer to the remnant

## Chapter 5. DM searches with neutrinos from the Sun

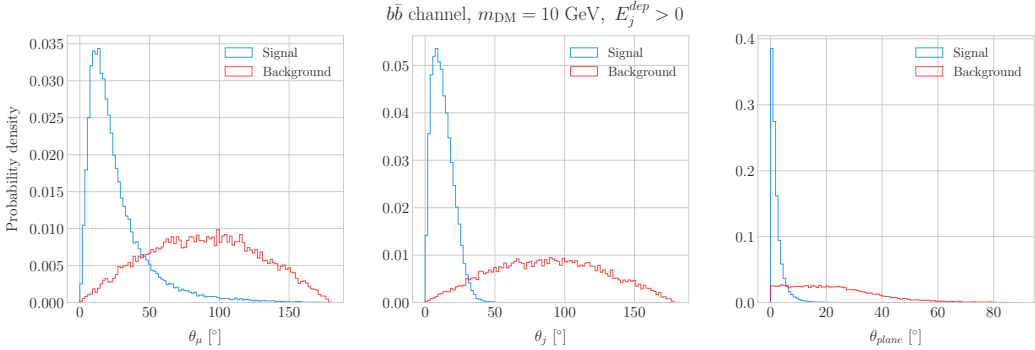


**Figure 5.11:** Distributions of  $\theta_\mu$  (left panel),  $\theta_j$  (central panel) and  $\theta_{\text{plane}}$  (right panel) for the  $b\bar{b}$  sample with  $m_{\text{DM}} = 10$  GeV (blue) and the atmospheric background (red).

nucleus is negligible, for this reason the neutrino energy can be effectively reconstructed just taking into account the momenta of the muon and the jet. This technique was successfully used in Ref. [122] to select monoenergetic DM solar neutrino events from  $\nu\bar{\nu}$  annihilation channels.

Using momentum conservation one sees that the plane generated by the momenta of the muon and the jet needs to also contain the momentum of the neutrino. As we are interested in neutrinos coming from the Sun, the momentum of the neutrino can be regarded as known beforehand. This will allow us to define the angle of the outgoing muon and jet with respect to the incoming neutrino. Moreover, one can also use that information to reject poorly reconstructed jets, checking for deviations of these from the momentum conservation plane.

To account for the limited angular resolution of the detector, I smeared the momenta of the muons and hadrons. In a liquid argon TPC muons are expected to be tracked with high precision, therefore I take the associated angular resolution to be  $1^\circ$ . In the case of jets, it is expected that for the hadrons dominating the cascade a detector like DUNE has an angular resolution between  $1^\circ$  to  $5^\circ$  [69], so I take the latter, more conservative, estimate.

As a first selection step, I will just take into account particles with kinetic energies above the detection threshold of DUNE. For muons and photons the specified threshold energy is 30 MeV, for charged pions 100 MeV and for other hadrons 50 MeV [69]. This

## 5.6. High energy DM neutrino signals

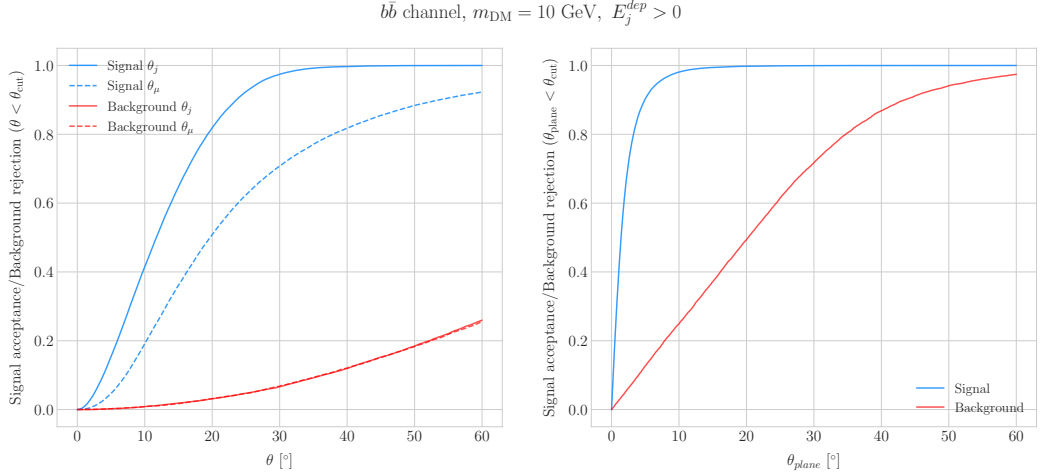


**Figure 5.12:** Left panel: signal efficiencies (blue lines) and background rejections (red lines) for events passing the cuts  $\theta < \theta_{cut}$  for the jet (solid lines) and muon (dashed lines) angles. Right panel: signal efficiency (blue line) and background rejection (red line) for events passing the cut  $\theta_{plane} < \theta_{cut}$  for the momentum conservation plane deviation.

way, if the outgoing muon in a certain event has an energy lower than the required threshold I will drop such event. For the case of hadrons and photons, I will only require to have at least one particle above the energy threshold, so then one can compute the jet momentum using the (smeared) momenta of the  $N$  particles above threshold as:

$$\vec{p}_j = \sum_{i=1}^N \vec{p}_i. \quad (5.28)$$

Additionally, I will also define an estimation of the deposited hadronic energy as:

$$E_j^{dep} = m_{^{39}\text{Ar}} - m_{^{40}\text{Ar}} + \sum_{i=1}^N \sqrt{|\vec{p}_i|^2 + m_i^2}. \quad (5.29)$$

This quantity is useful to select events with enough hadronic visible energy in the detector. For events where most of the hadronic energy is scattered across plenty of hadrons with individual energies below the detection threshold, this estimation will give  $E_j^{dep} \leq 0$ . In these cases it could be expected that the jet momentum is poorly reconstructed, and therefore I require events to pass the cut  $E_j^{dep} > 0$ .

For the events I can compute the angles for the muon and jet with respect to the

## Chapter 5. DM searches with neutrinos from the Sun

2256 incoming neutrino as:

$$\cos \theta_\mu = \hat{p}_\nu \cdot \hat{p}_\mu, \quad (5.30)$$

$$\cos \theta_j = \hat{p}_\nu \cdot \hat{p}_j, \quad (5.31)$$

2257 and the deviation from the momentum conservation plane as:

$$\sin \theta_{plane} = \left| \frac{\hat{p}_\mu \times \hat{p}_\nu}{|\hat{p}_\mu \times \hat{p}_\nu|} \cdot \hat{p}_j \right|. \quad (5.32)$$

2258 In Fig. 5.11 I show some distributions of these quantities for the case of the  $b\bar{b}$  sample  
2259 with  $m_{DM} = 10$  GeV (blue histograms) and for the atmospheric backgrounds (red).  
2260 In order to select the atmospheric events I followed the same criteria as for the signal  
2261 events. However, because in the signal case I used the true direction of the neutrino  
2262 as input, as it should be that of the Sun at that time and therefore known, in the  
2263 atmospheric case I used a set of solar positions as our ansatz for the neutrino direction.  
2264 From the distributions, one can see that the muon and the jet for the signal events are  
2265 predominantly forward and also that the deviations from the momentum conservation  
2266 plane are peaked at zero, as one should expect.

2267 Now, I can start applying cuts to maximise our signal selection efficiency while at  
2268 the same time I try to minimise the amount of atmospheric background events passing  
2269 the selection. To this end, I will need to find some lower and upper cuts for  $\theta_j$  and  
2270  $\theta_\mu$  and an upper bound for  $\theta_{plane}$ . In Fig. 5.12 I show how upper bound cuts in the  
2271 different angular variables affect the signal efficiency (blue lines) and the background  
2272 rejection (red lines). Notice that the signal efficiency behaves in a quite different way  
2273 when I apply cuts in the jet and the muon angles. On the contrary, the cuts on both  
2274 variables have a similar effect on the background rejection.

2275 In order to obtain the optimal set of cuts, I perform a multidimensional scan. I  
2276 do this separately for the  $\tau^+\tau^-$  and the  $b\bar{b}$  samples. For each case, I scan the possible  
2277 cuts for each mass point and then I take the mean value of the signal efficiency for

## 5.6. High energy DM neutrino signals

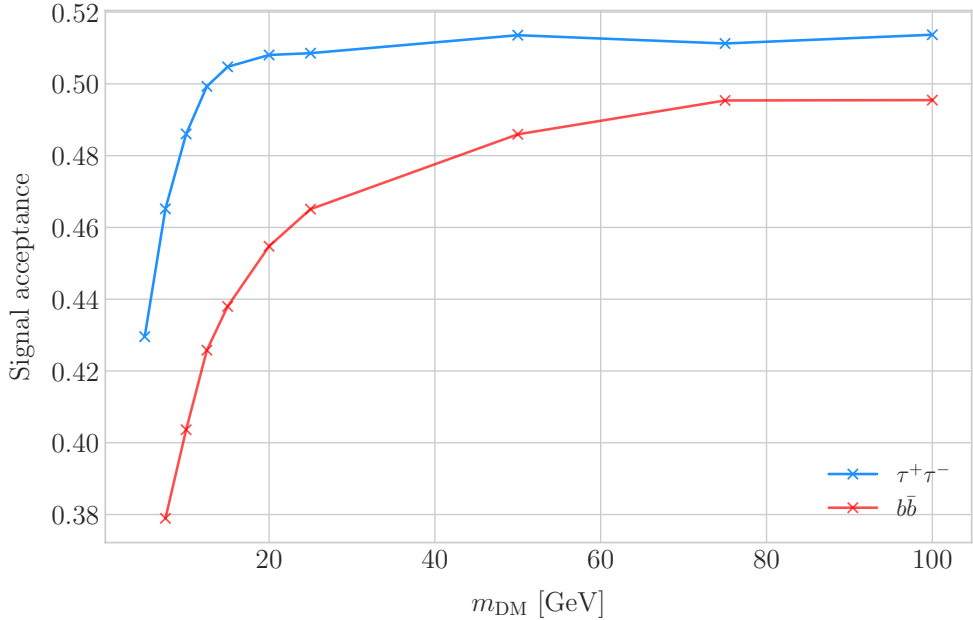


**Figure 5.13:** Signal efficiencies for the  $\tau^+\tau^-$  (blue line) and  $b\bar{b}$  (red line) DIS samples as functions of the DM mass,  $m_{\text{DM}}$ , obtained by applying the optimal angular cuts  $\theta_\mu < 27^\circ$ ,  $4^\circ < \theta_j < 26^\circ$  and  $\theta_{\text{plane}} < 3.5^\circ$ .

each configuration, to get the mean efficiency for each set of cuts. I do a similar scan for the atmospheric sample independently. Then, I take the sets of cuts such that the background rejection achieved is greater than 99.8% and search for the one which maximises the  $\tau^+\tau^-$  and  $b\bar{b}$  sample mean efficiencies. I found that with the cuts  $\theta_\mu < 27^\circ$ ,  $4^\circ < \theta_j < 26^\circ$  and  $\theta_{\text{plane}} < 3.5^\circ$  I get a background rejection of 99.80% while achieving a 49.40% and 44.92% mean signal efficiencies for the  $\tau^+\tau^-$  and  $b\bar{b}$  signals respectively.

In Fig. 5.13 I show the signal efficiencies as a function of the DM mass for the  $\tau^+\tau^-$  (blue line) and the  $b\bar{b}$  (red line) DIS events, after applying the cuts discussed above, as well as the energy threshold and hadronic visible energy selections. One can see that the efficiency grows with the mass, as annihilations of more massive DM particles will produce a neutrino spectrum centered at higher energies, where DIS events dominate. Notice also that the efficiency is higher for the  $\tau^+\tau^-$  case at every mass point, as in general this channel produces neutrinos at higher energies than the corresponding  $b\bar{b}$  channel.

## Chapter 5. DM searches with neutrinos from the Sun

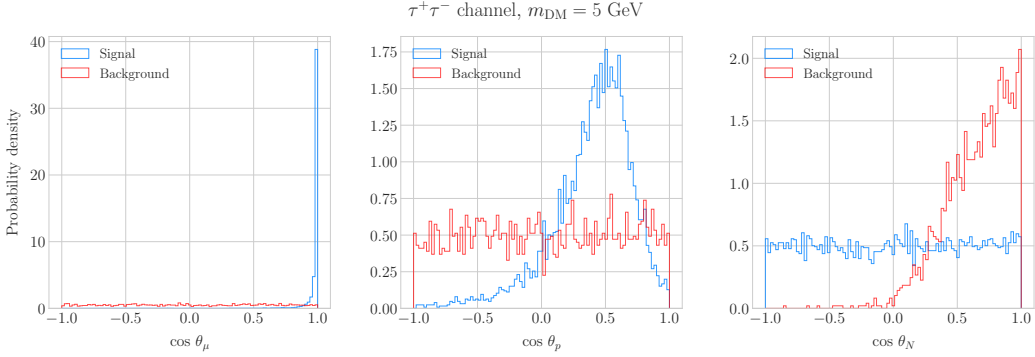


**Figure 5.14:** Distributions of  $\cos \theta_\mu$  (left panel),  $\cos \theta_p$  (central panel) and  $\cos \theta_N$  (right panel) for the  $\tau^+\tau^-$  QEL sample with  $m_{\text{DM}} = 5 \text{ GeV}$  (blue) and the atmospheric background (red).

### 2292 5.6.2 Single proton QEL events

2293 Now, one can try to explore the low energy tail of the neutrino energy distributions. This  
 2294 regime is dominated by the QEL interactions, i.e. events of the type  $\nu_\mu + n \rightarrow \mu^- + p$ .  
 2295 In this case, as the typical energies are  $E_\nu \lesssim 1 \text{ GeV}$ , the momentum transfer to the  
 2296 remnant nucleus is sizeable. Therefore, I can not make the approximation I did before  
 2297 and assume that the momentum of the muon and the proton will give an adequate  
 2298 estimation of the reconstructed neutrino energy.

2299 In any case, as before, I can take the direction of the incoming neutrino as known.  
 2300 That way, one can estimate the energy of the neutrino as:

$$E_\nu^{reco} = E_\mu + E_p + m_{^{39}\text{Ar}} - m_{^{40}\text{Ar}}, \quad (5.33)$$

2301 and using momentum conservation I can write the momentum of the remnant nucleus  
 2302 as:

$$\vec{p}_N = \hat{p}_\nu (E_\mu + E_p + m_{^{39}\text{Ar}} - m_{^{40}\text{Ar}}) - \vec{p}_\mu - \vec{p}_p. \quad (5.34)$$

2303 As in the previous case, I need to drop the events where the muon or the proton fall  
 2304 below the kinetic energy detection threshold [69]. Also, I again apply a smearing to the  
 2305 momenta of the particles, a 1% for muons and 5% for protons.

2306 Having done that, one can compute the following angular variables for our selected

## 5.6. High energy DM neutrino signals

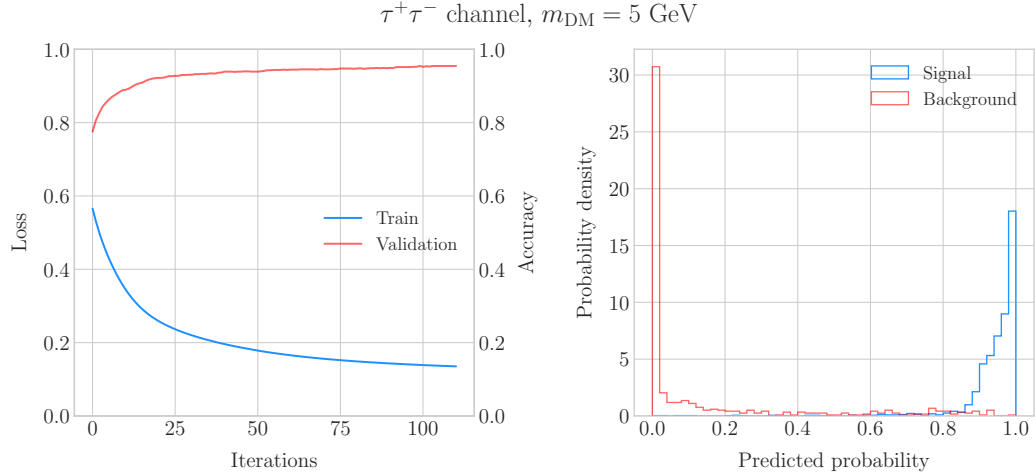


**Figure 5.15:** Left panel: value of the loss function for the training sample (blue line) and accuracy for the validation sample (red line) versus the number of iterations for the MLP classifier training. Right panel: distributions of the predicted probabilities assigned by the MLP classifier to the test sample for the  $\tau^+\tau^-$  QEL signal with  $m_{\text{DM}} = 5 \text{ GeV}$  (blue) and the atmospheric background (red).

2307 events:

$$\cos \theta_\mu = \hat{p}_\nu \cdot \hat{p}_\mu, \quad (5.35)$$

$$\cos \theta_p = \hat{p}_\nu \cdot \hat{p}_p, \quad (5.36)$$

$$\cos \theta_N = \hat{p}_\nu \cdot \hat{p}_N. \quad (5.37)$$

2308 Fig. 5.14 shows the distributions of these angular variables for the  $\tau^+\tau^-$  QEL  
 2309 sample with  $m_{\text{DM}} = 5 \text{ GeV}$  (blue) and the atmospheric background (red). Again, for  
 2310 the atmospheric events I used a random solar position as the ansatz for the incoming  
 2311 neutrino direction. Notice that now, opposed to the DIS case where the signal had very  
 2312 sharp distributions for the variables considered, the shapes of the angular distributions  
 2313 for signal and background are not that much different.

2314 This effectively means that the usual approach of applying simple angular cuts would  
 2315 not work as well as in the previous situation. Therefore, as a possible solution, I tried to  
 2316 use a multilayer perceptron (MLP) classifier to separate between signal and background  
 2317 events. Thus, the power of the hypothesis test will serve as an estimate of the signal

## Chapter 5. DM searches with neutrinos from the Sun

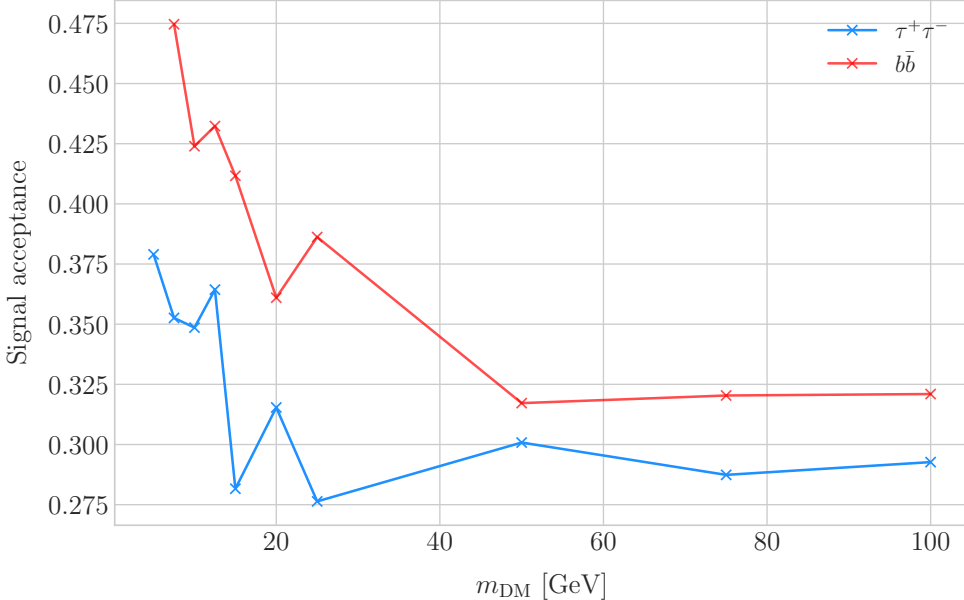


**Figure 5.16:** Signal efficiencies for the  $\tau^+\tau^-$  (blue line) and  $b\bar{b}$  (red line) single proton QEL samples as functions of the DM mass,  $m_{\text{DM}}$ , obtained by requiring a minimum predicted probability from the MLP classifier of 0.97 in order to achieve a background rejection greater than 99.8%.

efficiency, and in the same way one can take the size of the test to be our background rejection.

For each DM mass value and channel, as well as for the background sample, I divide our events into training, validation and test samples. The input variables for the classifier were the reconstructed neutrino energy from Eq. (5.33) and the angular variables defined in Eqs. (5.35 - 5.37). I used the MLP classifier implemented in `scikit-learn` [123], with a total of five hidden layers, the rectified linear unit activation function and adaptive learning rate. In order to account for fluctuations due to artifacts in the training process I repeated the training a thousand times for each sample, redefining each time the training, validation and test subsets, so one can take as our signal efficiency and background rejection the mean values of the powers and sizes of the tests.

The results of one of these training processes for the  $\tau^+\tau^-$  QEL signal with  $m_{\text{DM}} = 5$  GeV is shown in Fig. 5.15. On the left panel I show the loss function values (blue) and accuracy (red) at each iteration for the training and the validation samples respectively.

## 5.6. High energy DM neutrino signals

2332 The training stops either when the maximum number of iterations is reached (1000 in  
2333 this case) or when the accuracy for the validation sample reaches a certain tolerance  
2334 (I chose  $10^{-4}$  as our tolerance). On the right panel I have the distributions for the  
2335 predicted probability by the model, separated in true signal (blue) and background  
2336 (red) events, for the test sample. One can see that both populations are well separated,  
2337 obtaining a power of 44.97% and a size of 0.17% when I require a predicted probability  
2338 greater than 0.97.

2339 Applying this criteria for each sample, I obtain the mean signal efficiencies shown in  
2340 Fig. 5.16. Notice that the efficiencies for the channel  $\tau^+\tau^-$  (blue line) are consistently  
2341 lower than the ones for the  $b\bar{b}$  channel (red line). This can be due to the fact that, for  
2342 each DM mass point, the neutrino spectrum coming from the  $b\bar{b}$  annihilation channel is  
2343 centered at lower energies when compared to the  $\tau^+\tau^-$  spectrum. This directly translates  
2344 into more low energy neutrinos undergoing QEL interactions, which give signals that  
2345 can be easily separated from the atmospheric background. This explanation also help us  
2346 understand why in both cases the signal acceptance drops when the DM mass increases.  
2347 In all cases, the background rejection took values between 99.8% to 99.9%. I will assume  
2348 a 99.8% background rejection value in all cases to keep our estimation conservative.

### 2349 5.6.3 Results

2350 In order to estimate the DM-nucleon cross section sensitivities in the present case I need  
2351 again to compute the expected number of background events. As I am now separating  
2352 events by interaction type Eq. (5.25) does not hold anymore, as in that case I integrated  
2353 over the total neutrino-argon cross section. In this instance, the expected background  
2354 events for DIS events is approximately given by:

$$N_B^{DIS} \simeq \eta_B^{DIS} \times (4.655 \times 10^3) \times \left( \frac{\text{exposure}}{400 \text{ kT yr}} \right), \quad (5.38)$$

## Chapter 5. DM searches with neutrinos from the Sun

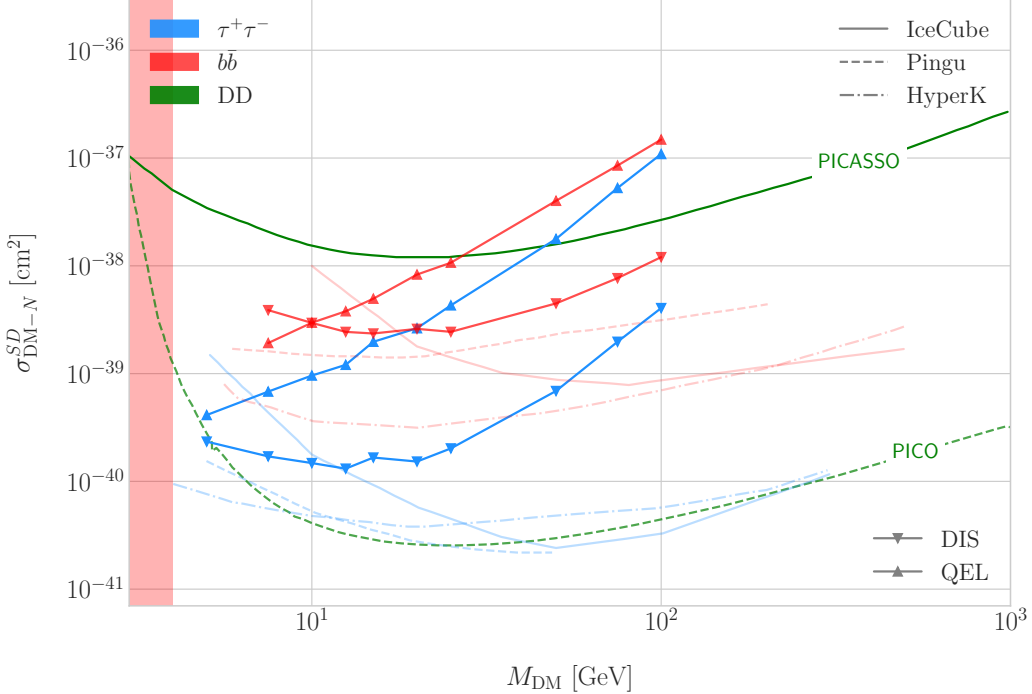


**Figure 5.17:** Projected 90% confidence level upper limit for DUNE (400 kT yr) on the spin-dependent DM-nucleon scattering cross section as a function of  $m_{\text{DM}}$ , for the annihilation channels  $\tau^+\tau^-$  (blue) and  $b\bar{b}$  (red) separated by interaction type (up triangles denote DIS interactions whereas down triangles represent QEL interactions). I also show the previous limits from IceCube [7] (solid lines) and the projected sensitivities for Pingu [8] (dashed lines) and Hyper-Kamiokande [9] (dash-dotted lines), as well as the direct detection limits from PICASSO [10] (solid green line) and PICO-60 C<sub>3</sub>F<sub>8</sub> [11] (dashed green line).

2355 whereas for QEL events we have:

$$N_B^{QEL} \simeq \eta_B^{QEL} \times (2.248 \times 10^4) \times \left( \frac{\text{exposure}}{400 \text{ kT yr}} \right). \quad (5.39)$$

2356 Now, using these together with Eqs. (5.26) and (5.27) one can obtain the 90% C.L.  
 2357 upper limit on the total annihilation rate at equilibrium for both kind of events. Then,  
 2358 applying the computed DM-nucleons capture rates I can translate these into limits on  
 2359 the DM-nucleon cross section by means of Eqs. (5.2), (5.5) and (5.6).

2360 Fig. 5.17 shows the obtained limits on the SD DM-nucleon cross section for DUNE,  
 2361 using the DIS (up triangles) and QEL (down triangles) events both for the  $\tau^+\tau^-$  (blue)  
 2362 and the  $b\bar{b}$  (red) samples, for an exposure of 400 kT yr. I also include the corresponding

## 5.7. Example: Leptophilic Dark Matter

2363 current limits from IceCube [7] (solid lines), as well as the projected sensitivities of  
2364 Pingu [8] (dashed lines) and Hyper-Kamiokande [9] (dash-dotted lines). For comparison,  
2365 I also show the reported direct detection limits from PICASSO [10] (solid green line)  
2366 and PICO-60 C<sub>3</sub>F<sub>8</sub> [11] (dashed green line).

2367 Notice that, for most of the mass range, the limits one can set by using the DIS  
2368 events are stronger than those of the QEL interactions, except for the low mass part  
2369 of both the  $\tau^+\tau^-$  and the  $b\bar{b}$  curves where the QEL events dominate. In general, the  
2370 expected sensitivity of DUNE for DM masses  $\lesssim 25$  GeV surpasses the stronger current  
2371 indirect limits. However, experiments like Hyper-Kamiokande are foreseen to have an  
2372 overall better sensitivity in this kind of searches, as they have a bigger active volume  
2373 and accept a broader energy range.

2374 A pending question is what happens when we add the RES and MEC charged-current  
2375 interaction contributions. In that case it would probably be more convenient to split  
2376 the samples by final state interaction topologies. Also, another necessary improvement  
2377 would be adding a full detector simulation and reconstructions. This will also require  
2378 considering the effect of poorly reconstructed events or final states containing neutral  
2379 particles such that they mimic the desired topology at the reconstruction level.

## 2380 5.7 Example: Leptophilic Dark Matter

2381 In general, the capture rate of DM particles by the Sun via interactions with electrons is  
2382 several orders of magnitude smaller than the capture via DM-nucleus scattering. Thus,  
2383 it would be sub-leading even when nucleon capture is loop suppressed. As I showed in  
2384 Fig. 5.2, the capture rate via scattering off electrons only surpasses the capture rates  
2385 via DM-nucleons interactions for DM masses  $\lesssim 100 - 500$  MeV.

2386 However, if one considers a model where DM-nucleon interactions are forbidden even  
2387 at loop level, then electron interactions will be the sole contributor to DM capture in  
2388 the Sun. One can describe such scenario where the DM particles couple to leptons but  
2389 not to the quark sector using effective operators.

## Chapter 5. DM searches with neutrinos from the Sun

2390 In general, assuming that the DM particle is a Dirac fermion, the dimension six  
 2391 operators describing the interaction between two DM particles and two leptons can be  
 2392 written as:

$$\mathcal{L}_{eff} = G \sum_i (\bar{\chi} \Gamma_\chi^i \chi) (\bar{\ell} \Gamma_\ell^i \ell), \quad (5.40)$$

2393 where  $G = 1/\Lambda^2$  is the effective coupling strength,  $\Lambda$  the cut-off of the effective field  
 2394 theory and  $\ell$  denotes any lepton. In principle, one should consider all the possible  
 2395 Lorentz structures  $\Gamma_f^i$  in order to have a complete set of effective operators.

2396 However, some combinations will induce interactions with nucleons at loop level.  
 2397 As we are specifically interested in interactions which forbid any communication with  
 2398 the quark sector, I will not consider those [124]. In addition, some of the effective  
 2399 operators give rise to velocity-suppressed scattering cross sections between DM particles  
 2400 and leptons. I will also neglect those, as the suppression goes with the square of the DM  
 2401 halo velocity which in units of the speed of light is  $\sim 10^{-6}$ .

2402 This way, the only Lorentz tensor structure that do not induce interactions with  
 2403 quarks at loop level and gives a contribution to the scattering cross section that is not  
 2404 velocity suppress is the axial-axial interaction. The effective Lagrangian is then given  
 2405 by:

$$\mathcal{L}_{eff} = \frac{c_A^\chi c_A^\ell}{\Lambda^2} (\bar{\chi} \gamma^\mu \gamma^5 \chi) (\bar{\ell} \gamma_\mu \gamma^5 \ell), \quad (5.41)$$

2406 where  $c_A^\chi$  and  $c_A^\ell$  are the couplings for the different species. As the DM coupling appears  
 2407 as a common factor for any lepton choice, I will redefine the corresponding coupling  $c_A^\ell$   
 2408 to absorb  $c_A^\chi$ . Also, for simplicity, I will assume that the couplings between the DM  
 2409 particles and the leptons are flavour independent, i.e. I have just two couplings,  $c_A^e$  for  
 2410 charged leptons and  $c_A^v$  for neutrinos.

2411 In the case of a scalar DM particle, the lowest order effective interaction with  
 2412 leptons happens through a dimension five operator, generating scalar and pseudoscalar  
 2413 interactions. However, the former induces interactions with quarks at two loop level  
 2414 whereas the latter gives a velocity suppressed scattering cross section.

2415 From the effective Lagrangian in Eq. (5.41) it can be shown that the axial-axial

## 5.7. Example: Leptophilic Dark Matter

2416 contribution to the scattering cross section for the fermionic DM and a charged lepton  
2417 is given by:

$$\sigma_{\text{DM}-e}^{AA} = 3(c_A^e)^2 \frac{m_e^2}{\pi \Lambda^4}. \quad (5.42)$$

2418 If the DM interacts exclusively with fermions, then the only annihilation channels  
2419 that will give us a measurable neutrino flux coming out of the Sun are  $\tau^+\tau^-$  and  $\nu\bar{\nu}$ . The  
2420 former channel, already explored previously in the more mainstream scenario of the DM  
2421 capture via scattering off nucleons, is open only for  $m_{\text{DM}} > m_\tau \simeq 1776.86 \pm 0.12$  MeV  
2422 [125], a mass region where the solar DM capture by electrons is at least one order of  
2423 magnitude smaller than the capture via interactions with nucleons. On the contrary, the  
2424 latter allows us to explore a region where the capture rate via scattering off electrons  
2425 dominates over the rest.

2426 One downside of focusing in such low mass range is that it falls below the usual  
2427 limit of  $m_{\text{evap}} \sim 4$  GeV usually explored in the literature. The pretext to explore this  
2428 region is the result discussed previously reported in Ref. [2], where DM evaporation in  
2429 the Sun for the case of capture via electron scattering could be negligible for masses  
2430 as low as  $m_{\text{evap}} \sim 200$  MeV. This result is quite sensitive to the high velocity tail of  
2431 the DM velocity distribution in equilibrium inside the Sun, and therefore full numerical  
2432 simulations would be needed to assess the impact of this effect. However, this falls out of  
2433 the scope of our work.

2434 In this case, as I have a specific realisation of the interaction between the DM  
2435 and leptons, one can estimate the relic density of our DM for different values of the  
2436 couplings and the effective field theory scale  $\Lambda$ . The first step to do so is compute the  
2437 self-annihilation cross section. Because I consider cold relics, at the freeze-out time our  
2438 DM particles were non-relativistic and so one can expand the annihilation cross section  
2439 in terms of the relative velocity  $v$  between two annihilating DM particles as [126]:

$$\sigma_{\text{ann}}^{AA}|v| \approx \frac{1}{2\pi\Lambda^4} \sum_\ell \left(c_A^\ell\right)^2 m_\chi^2 \sqrt{1 - \frac{m_\ell^2}{m_\chi^2} \left[ \frac{m_\ell^2}{m_\chi^2} + \frac{1}{12} \left(2 - \frac{m_\ell^2}{m_\chi^2}\right) v^2 \right]}, \quad (5.43)$$

## Chapter 5. DM searches with neutrinos from the Sun

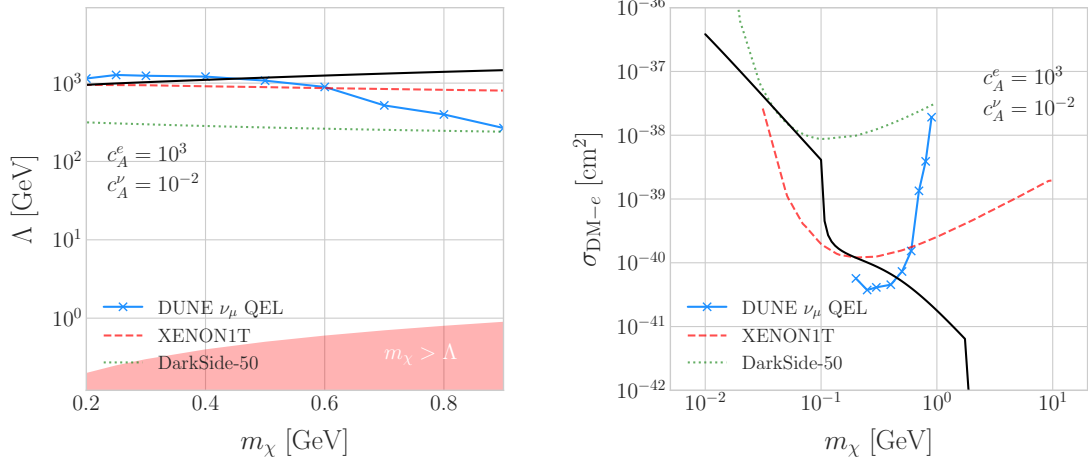


**Figure 5.18:** Left panel: Projected 90% confidence level sensitivity of DUNE (400 kT yr) to the scale  $\Lambda$  of an EFT containing only leptophilic DM axial-axial interactions (blue line). Right panel: . In both cases the corresponding limits from DarkSide-50 [12] (dotted green line) and XENON1T [13] (dashed red line) are also shown, together with the configurations for which the correct relic density is achieved (black line), all for the coupling values  $c_A^e = 10^3$  and  $c_A^\nu = 10^{-2}$ .

where the sum includes all the possible lepton final states with mass  $m_\ell$ .  
 Solving the Boltzmann equation for the evolution of the DM density gives as a solution a relic density of:

$$\Omega_\chi h^2 \approx \frac{(1.04 \times 10^9) x_F}{M_{Pl} \sqrt{g_*} (a + 3b/x_F)}, \quad (5.44)$$

where  $x_F = m_\chi/T_F$  being  $T_F$  the freeze-out temperature,  $g_*$  the number of relativistic degrees of freedom at freeze-out and  $a$  and  $b$  the terms in the annihilation cross section expansion  $\sigma_{ann}|v| \approx a + bv^2 + \mathcal{O}(v^4)$ . Using the current best fit for the relic DM density  $\Omega_\chi h^2 = 0.1198 \pm 0.0012$  [127] one can use these relations to compute the required effective theory scale  $\Lambda$  at which the correct density is achieved for any combinations of  $m_\chi$  and  $c_A^\ell$ .

As discussed before, in the low DM mass region QEL interactions dominate. Moreover, if I focus on direct annihilation to neutrinos, the energy of the muon neutrino flux is known as it must be equal to the mass of the DM particle,  $E_\nu = m_\chi$ . That way, now I do not need to use Eq. (5.33) in order to estimate the momentum transfer to the

## 5.7. Example: Leptophilic Dark Matter

2453 remnant nucleus, I can simply take:

$$\vec{p}_N = \hat{p}_\nu m_\chi - \vec{p}_\mu - \vec{p}_p. \quad (5.45)$$

2454 To estimate the signal efficiency and background rejection for this case I used again  
2455 the MLP classifier from `scikit-learn`, using the same specifications as before. The  
2456 only difference now is that I add also the reconstructed neutrino energy as one of the  
2457 features to train the classifier with, because the characteristic monoenergetic flux for  
2458 each  $m_\chi$  value will help to distinguish between signal and background events.

2459 In this case, for masses below  $\sim 500$  MeV I obtain a signal efficiency close to unity  
2460 while keeping a background rejection of 99.9%. For bigger values of the mass, the signal  
2461 efficiency drops significantly if I require to keep the background acceptance under 0.01%.  
2462 However, because this kind of search is dominated by the background, sacrificing the  
2463 signal acceptance to keep the background rejection to a minimum enhances the reach  
2464 of the analysis. This way, for DM masses of the order of  $m_\chi \sim 1$  GeV I end up with  
2465 efficiencies as low as 1%.

2466 Now, estimating the number of background events using Eq. (5.39) one can go on  
2467 and apply Eqs. (5.26) and (5.27) together with Eq. (5.42) to derive the sensitivity of  
2468 DUNE to this kind of model. Fig. 5.18 (left panel) shows the potential reach of DUNE  
2469 to constrain the EFT scale  $\Lambda$  this model containing only leptophilic DM axial-axial  
2470 interactions (blue line), for a choice of couplings  $c_A^e = 10^3$  and  $c_A^\nu = 10^{-2}$ . I also included  
2471 the current limits on the DM-electron scattering cross section from DarkSide-50 [12]  
2472 (dotted green line) and XENON1T [13] (dashed red line), reworked with Eq. (5.42) to  
2473 show their implications for the EFT scale. The values of  $\Lambda$  for which the correct DM relic  
2474 density value is achieved for each mass are also shown (black line). This tells us that,  
2475 for that specific choice of couplings, DUNE would be sensitive to DM configurations  
2476 allowed by the relic density constraint up to a mass of  $m_\chi \sim 400$  MeV.

2477 In Fig. 5.18 (right panel) I show the same upper limits but for the DM-electron  
2478 scattering cross section. From this view one can see that DUNE would be able to

## Chapter 5. DM searches with neutrinos from the Sun

2479 offer complementary information to the low energy DM-electron interaction searches  
2480 performed by direct detection experiments, in a slightly higher mass range.

2481 With the present example, although it focuses on a very specific realisation of the DM  
2482 interactions, I show the potential of DUNE to constrain exotic DM scenarios. Thanks  
2483 to its low backgrounds and superb angular resolution DUNE will be able to help with  
2484 the systematic searches for dark sectors physics.

2485 Chapter 6

2486 Particle ID in GArSoft

2487 ND-GAr is a magnetised, high-pressure gaseous argon TPC (HPgTPC), surrounded by  
2488 an electromagnetic calorimeter (ECal) and a muon detector (commonly refer to as  $\mu$ ID).  
2489 A detailed discussion on the requirements, design, performance and physics of ND-GAr  
2490 can be found in the DUNE ND CDR [75] and the ND-GAr whitepaper (cite).

2491 In DUNE Phase II ND-GAr will fulfill the role of TMS, measuring the momentum  
2492 and sign of the charged particles exiting ND-LAr. Additionally, it will be able to measure  
2493 neutrino interactions inside the HPgTPC, achieving lower energy thresholds than those  
2494 of the ND and FD LArTPCs. By doing so ND-GAr will allow to constrain the relevant  
2495 systematic uncertainties for the LBL analysis even further.

2496 The goal of the present chapter is to review the requirements that the physics program  
2497 of DUNE impose on ND-GAr, present the current status of its design and describe the  
2498 GArSoft package, its simulation and reconstruction software.

2499 As decided during the DUNE Phase II workshop in June 2023 [reference], we want  
2500 to build ND-GAr physics case by showing:

- 2501 • That ND-GAr can constrain systematic uncertainties that ND-LAr might miss.
- 2502 • The impact on the neutrino oscillation results if such systematic uncertainties are  
2503 missed.
- 2504 • That ND-GAr is necessary to reach DUNE's main physics goals.

## Chapter 6. Particle ID in GArSoft

2505        This way, the design of ND-GAr will be physics driven.

2506        In order to study the effects of final state interactions (FSI) in CC interactions,

2507        ND-GAr should be able to measure the spectrum of protons and charged pions at low

2508        energies. ND-GAr also needs to be able to measure the pion multiplicity, specially for

2509        energies above 100 MeV as at these energies the pions shower in the LAr, to inform the

2510        pion mass correction in the ND and FD LArTPCs.

2511        In order to correctly identify electrons, muons, pions, kaons and protons ND-GAr

2512        can use a combination of:  $dE/dx$  measurements in the HPgTPC,  $E_{ECAL}/p$  using the

2513        ECAL total energy and the momentum obtained from magnetic spectroscopy in the

2514        HPgTPC and penetration information through the ECAL and muon tagger.

### 2515      6.1    GArSoft

2516      GArSoft is a software package developed for the simulation and reconstruction of events

2517      in ND-GAr. It is inspired by the LArSoft toolkit used for the simulation of LArTPC

2518      experiments, like the DUNE FD modules. It is based on `art`, the framework for event

2519      processing in particle physics experiments [128]. Other of its main dependencies are

2520      `ROOT`, `NuTools`, `GENIE` and `Geant4`. It allows the user to run all the steps of a generation-

2521      simulation-reconstruction workflow using FHiCL configuration files.

#### 2522      6.1.1   Event generation

2523      The standard generator FHiCLs in GArSoft run the event generation and particle

2524      propagation simulation (i.e. Geant4) in the same job by default. However, it is possible

2525      to split them up if needed. The current version of GArSoft provides five different event

2526      generators, each of them producing `simb::MCTruth` products defined in `NuTools`. The

2527      available modules are:

- 2528      • `SingleGen`: particle gun generator. It produces the specified particles with a given
- 2529      distribution of momenta, initial positions and angles.

## 6.1. GArSoft

- 2530     • **TextGen**: text file generator. The input file must follow the `hepevt` format<sup>1</sup>, the  
2531         module simply copies this to `simb::MCTruth` data products.
- 2532     • **GENIEGen**: GENIE neutrino event generator. The module runs the neutrino-nucleus  
2533         interaction generator using the options specified in the driver FHiCL file (flux file,  
2534         flavour composition, number of interactions per event,  $t_0$  distribution, ...). Current  
2535         default version is `v3_04_00`.
- 2536     • **RadioGen**: radiological generator. It produces a set list of particles to model  
2537         radiological decays. Not tested.
- 2538     • **CRYGen**: cosmic ray generator. The module runs the CRY event generator with a  
2539         configuration specified in the FHiCL file (latitude and altitude of detector, energy  
2540         threshold, ...). Not tested.

2541         The module **GArG4** searches for all the generated `simb::MCTruth` data products, using  
2542         them as inputs to the Geant4 simulation with the specified detector geometry. A constant  
2543         0.5 T magnetic field along the drift coordinate is assumed. The main outputs of this step  
2544         are `simb::MCParticle` objects for the generated Geant4 particles, `gar::EnergyDeposit`  
2545         data products for the energy deposits in the HPgTPC and `gar::CaloDeposit` data  
2546         products for the energy deposits in the ECal and muon system.

### 2547 6.1.2 Detector simulation

2548         The standard detector simulation step in GArSoft is all run with a single FHiCL, but  
2549         the different modules can be run independently as well. First the `IonizationReadout`  
2550         module simulates the charge readout of the HPgTPC, and later the `SiPMReadout` module  
2551         runs twice, once for the ECal and then for the muon system, with different configurations.

---

<sup>1</sup>In brief, each event contains at least two lines. The first line contains two entries, the event number and the number of particles in the event. Each following line contains 15 entries to describe each particle. The entries are: status code, pdg code for the particle, entry of the first mother for this particle, entry of the second mother for this particle, entry of the first daughter for this particle, entry of the second daughter for this particle, x component of the particle momentum, y component of the particle momentum, z component of the particle momentum, energy of the particle, mass of the particle, x component of the particle initial position, y component of the particle initial position, z component of the particle initial position and time of the particle production.

## Chapter 6. Particle ID in GArSoft

2552        The `IonizationAndScintillation` module collects all the `gar::EnergyDeposit`  
2553    data products, to compute the equivalent number of ionization electrons for each energy  
2554    deposit. The `ElectronDriftAlg` module simulates the electron diffusion numerically  
2555    both in the longitudinal and transverse directions and applies an electron lifetime  
2556    correction factor. The induced charge on the nearest and neighbouring readout pads  
2557    is modeled using the provided pad response functions. The digitisation of the data is  
2558    then simulated with the `TPCReadoutSimAlg` module. By default, the ADC sampling  
2559    rate used is 50.505 MHz. The resulting raw waveforms for each channel are stored with  
2560    zero-suppression, in order to save memory and CPU time. The algorithms keep blocks  
2561    of ADC values above a certain threshold, plus some adjustable additional early and late  
2562    tick counts. The results of these three steps are `gar::raw::RawDigit` data products.

2563        For the ECal and the muon system the `SiPMReadout` module calls either the  
2564    `ECALReadoutSimStandardAlg` or `MuIDReadoutSimStandardAlg` modules. These take  
2565    all the `gar::CaloDeposit` data products in the corresponding detector and do the  
2566    digitisation depending on whether the hit was in a tile or strip layer. They include single  
2567    photon statistics, electronic noise, SiPM saturation and time smearing. The resulting  
2568    objects are `gar::raw::CaloRawDigit` data products.

### 2569    6.1.3 Reconstruction

2570        The reconstruction in GArSoft is also run as a single job by default. It first runs the hit  
2571    finding, clustering, track fitting and vertex identification in the HPgTPC, followed by  
2572    the hit finding and clustering in the ECal and muon system. After those it produces the  
2573    associations between the associations between the tracks and the ECal clusters.

2574        Focusing first on the HPgTPC reconstruction, the `CompressedHitFinder` module  
2575    takes the zero-suppressed ADCs from the `gar::raw::RawDigit` data products. The  
2576    reconstructed hits largely correspond to the above threshold blocks, however the hit  
2577    finder identifies waveforms with more than one maximum, diving them in multiple hits  
2578    if they dip below a certain threshold. The data products produced are of the form  
2579    `gar::rec::Hit`. These are the inputs to the clustering of hits in the `TPCHitCluster`

## 6.1. GArSoft

2580 module. Hits close in space and time are merged, and the resulting centroids are found.  
2581 This module outputs `gar::rec::TPCClusters` objects and associations to the input  
2582 hits.

2583 The following step prior to the track fitting is pattern recognition. The module  
2584 called `tpcvechitfinder2` uses the `gar::rec::TPCClusters` data products to find track  
2585 segments, typically called vector hits. They are identified by performing linear 2D fits  
2586 to the positions of the clusters in a 10 cm radius, one fit for each coordinate pair. A  
2587 3D fit defines the line segment of the vector hit, using as independent variable the one  
2588 whose sum of (absolute value) slopes in the 2D fits is the smallest. The clusters are  
2589 merged to a given vector hit if they are less than 2 cm away from the line segment. The  
2590 outputs are `gar::rec::VecHit` data products, as well as associations to the clusters. The  
2591 `tpcpatrec2` module takes the `gar::rec::VecHit` objects to form the track candidates.  
2592 The vector hits are merged together if their direction matches, their centers are within  
2593 60 cm and their direction vectors point roughly to their respective centers. Once  
2594 the clusters of vector hits are formed they are used to make a first estimation of the  
2595 track parameters, simply taking three clusters along the track. The module produces  
2596 `gar::rec::Track` data products and associations between these tracks and the clusters  
2597 and vector hits.

2598 The track is fitted by means of a Kalman filter in the `tpctrackfit2` module, using  
2599 the position along the drift direction as the independent variable. Two different fits are  
2600 performed per track, a forward and a backwards fit, each starting from one of the track  
2601 ends. The Kalman filter state vector ( $y, z, R, \phi, \tan\lambda$ ) is estimated at each point along  
2602 the track using a Bayesian update. The track parameters reported in the forward and  
2603 backwards fits are the ones computed at the opposite end where the fit started. The  
2604 main outputs of the track fit are the `gar::rec::Track` objects. Additionally, the module  
2605 stores the fitted 3D positions along the track in the `gar::rec::TrackTrajectory` data  
2606 products and the total charge and step sizes for each point also get stored in the form of  
2607 `gar::rec::TrackIonization` objects.

2608 After the tracking step, the `vertexfinder1` module looks at the reconstructed

## Chapter 6. Particle ID in GArSoft

2609    `gar::rec::Track` products, creating vertex candidates with the track ends that are  
2610    within 12 cm of each other. The vertices are then fitted using linear extrapolations from  
2611    the different track ends associated. The results are `gar::rec::Vertex` data products,  
2612    and associations to the tracks and corresponding track ends.

2613    For the ECal and muon tagger, the `SiPMHitFinder` module runs twice with different  
2614    configurations, adapted to the particular capabilities of both. The module simply takes  
2615    the `gar::raw::CaloRawDigit` products, applies a calibration factor to convert the ADC  
2616    counts to MeV and for the strip layer hits it calculates the position along the strip using  
2617    the times recorded of both SiPMs. This module produces `gar::rec::CaloHit` data  
2618    products. Next, these objects are used as inputs to the `CaloClustering` module. It  
2619    merges the hits based on a simple nearest neighbours (NN) algorithm. For the resulting  
2620    clusters it also computes the total energy and position of the centroid. The results are  
2621    stored as `gar::rec::Cluster` data products, with associations to the hits.

2622    The last step in the reconstruction is associating the reconstructed tracks in the  
2623    HPgTPC to the clusters formed in the ECal and muon system. The `TPCECALAssociation`  
2624    module checks first the position of the track end points, considering only the points  
2625    that are at least 215 cm away from the cathode or have a radial distance to the center  
2626    greater than 230 cm. The candidates are propagated up to the radial position, in the  
2627    case of clusters in the barrel, or the drift coordinate position, for the end cap cluster, of  
2628    the different clusters in the collection using the track parameters computed at the end  
2629    point. The end point is associated to the cluster if certain proximity criteria are met.  
2630    This module creates associations between the tracks, the end points and the clusters.  
2631    The criteria for the associations are slightly different for the ECal and the muon tagger.

## 2632    6.2 **dE/dx measurement in the TPC**

2633    Among the parameters extracted from the track fitting, ionisation is particularly useful  
2634    for particle identification, as it is a function of the particle velocity. Although for the  
2635    case of relativistic particles this dependence is not very strong, measuring the track on

## 6.2. $dE/dx$ measurement in the TPC

2636 a large number of points may allow us to estimate the amount of ionisation accuratel.  
 2637 This, paired with a measurement of the momentum, may allow us to identify the particle  
 2638 type.

2639 The first calculation of the energy loss per unit length of relativistic particles using a  
 2640 quantum-mechanical treatment is due to Bethe [129]. Using this approach, the mean  
 2641 ionisation rate of a charged particle traveling through a material medium is (using  
 2642 natural units  $G = \hbar = c = 1$ ):

$$\left\langle \frac{dE}{dx} \right\rangle = \frac{4\pi Ne^4}{m_e \beta^2} z^2 \left( \log \frac{2m_e \beta^2 \gamma^2}{I} - \beta^2 \right), \quad (6.1)$$

2643 where  $N$  is the number density of electrons in the medium,  $e$  the elementary charge,  $m_e$   
 2644 is the electron mass,  $z$  the charge of the particle in units of  $e$ ,  $\beta$  is the velocity of the  
 2645 particle,  $\gamma = (1 - \beta^2)^{-1}$  and  $I$  denotes the effective ionisation potential averaged over  
 2646 all electrons. This relation is known as the Bethe-Bloch formula.

2647 From Eq. (6.1) one can see that the ionisation loss does not depend explicitly on  
 2648 the mass of the charged particle, that for non-relativistic velocities it falls as  $\beta^{-2}$ , then  
 2649 goes through a minimum and increases as the logarithm of  $\gamma$ . This behaviour at high  
 2650 velocities is commonly known as the relativistic rise. The physical origin of this effect  
 2651 is partly due to the fact that the transverse electromagnetic field of the particle is  
 2652 proportional to  $\gamma$ , therefore as it increases so does the cross section.

2653 It was later understood that the relativistic rise could not grow indefinitely with  $\gamma$ .  
 2654 A way to add this feature in the Bethe-Bloch formula is by introducing the so-called  
 2655 density effect term. It accounts for the polarisation effect of the atoms in the medium,  
 2656 which effectively shield the electromagnetic field of the charged particle halting any  
 2657 further increase of the energy loss [130]. Denoting the correction as  $\delta(\beta)$ , one can rewrite  
 2658 Eq. (6.1) as:

$$\left\langle \frac{dE}{dx} \right\rangle = \frac{4\pi Ne^4}{m_e \beta^2} z^2 \left( \log \frac{2m_e \beta^2 \gamma^2}{I} - \beta^2 - \frac{\delta(\beta)}{2} \right). \quad (6.2)$$

2659 In general, the form of  $\delta(\beta)$  depends on the medium and its state of aggregation,  
 2660 involving the usage of tabulated parameters and implicit relations [131].

## Chapter 6. Particle ID in GArSoft

2661 Another standard method to compute the amount of ionisation a charged particle  
2662 produces is the so-called photo-absorption ionisation (PAI) model proposed by Allison  
2663 and Cobb [132]. Within their approach, the mean ionisation is evaluated using a  
2664 semiclassical calculation in which one characterises the continuum material medium by  
2665 means of a complex dielectric constant  $\varepsilon(k, \omega)$ . However, in order to model the dielectric  
2666 constant they rely on the quantum-mechanical picture of photon absorption and collision.  
2667 Therefore, in the PAI model the computation of the ionisation loss involves a numerical  
2668 integration of the measured photo-absorption cross-section for the relevant material.

2669 In a particle physics experiment, the typical way of determining the energy loss  
2670 per unit length as a function of the particle velocity is studying identified particles  
2671 over a range of momenta. Once we have established this relation we can use it for  
2672 other, unknown particles. In this sense, it makes sense to have a regular mathematical  
2673 expression for this relation that one can use.

2674 It happens that neither the Bethe-Bloch theory nor the PAI model from Allison and  
2675 Cobb offer a close mathematical form for the ionisation curve. This is the reason why a  
2676 full parametrisation of the ionisation curves can be useful. A parametrisation originally  
2677 proposed for the ALEPH TPC [133] and later used by the ALICE TPC [134] group that  
2678 manages to capture the features of the ionisation energy loss is:

$$f(\beta\gamma) = \frac{P_1}{\beta^{P_4}} \left( P_2 - \beta^{P_4} - \log \left[ P_3 + \frac{1}{(\beta\gamma)^{P_5}} \right] \right), \quad (6.3)$$

2679 where  $P_i$  are five free parameters. Hereafter, we will refer to Eq. (6.3) as the ALEPH  
2680  $dE/dx$  parametrisation.

### 2681 6.2.1 Energy calibration

2682 In order to obtain the amount of energy loss by a charged particle due to ionisation  
2683 in our TPC we need to determine the conversion between the charge deposited in our  
2684 readout planes and the actual energy depositions. This procedure is known as energy  
2685 calibration.

## 6.2. $dE/dx$ measurement in the TPC

2686 In a general, the first step of the calibration involves a non-uniformity correction,  
2687 to make sure that the detector response is uniform throughout the TPC. These are  
2688 typically divided into three categories, non-uniformities in the transverse  $YZ$  plane,  
2689 non-uniformities along the drift direction  $X$  and variations of the detector response  
2690 over time (would not apply to us as the detector is not built yet). These would correct  
2691 for effects such as electron diffusion and attenuation, space charge effects or channel  
2692 misconfiguration. However, because at the moment I am only interested in making sure  
2693 we recover a sensible result from our simulation, I will not apply uniformity corrections  
2694 to our charge deposits.

2695 Other effects, like electron-ion recombination or ADC saturation, lead to a non-linear  
2696 relation between the observed charge and the deposited energy in the detector, with the  
2697 observed readout charge saturating at high ionisation energies. In this case, because we  
2698 are dealing with gaseous argon and therefore recombination is not as important as in  
2699 liquid, we do not simulate recombination effects in the TPC. Even so, the simulation of  
2700 the electronic response will still introduce charge saturation, and one needs to correct  
2701 for it in order to obtain the exact amount of energy loss due to ionisation.

2702 By default, the track fitting algorithm in GArSoft provides a `TrackIonization`  
2703 object associated to each reconstructed track. It contains two collections of charge  
2704 deposits, one for each fitting direction, consisting on pairs of charge values ( $dQ$ , in ADC)  
2705 and step sizes ( $dx$ , in cm).

2706 In order to estimate the ionisation loss in the ND-GAr TPC, I have used an MC  
2707 sample consisting of single, isotropic protons propagating in the TPC. The starting points  
2708 of the protons were sampled inside a  $50 \times 50 \times 25$  cm box centered at  $(100, -150, 1250)$ ,  
2709 and their momenta are uniformly distributed in the range  $0.25 - 1.75$  GeV. I ran the  
2710 simulated sample through GArSoft's default detector simulation and reconstruction, and  
2711 then a custom analyser module that extracts the ionisation data together with other  
2712 reconstructed track information from the Kalman fit.

2713 For studying the energy loss of the protons I select the reconstructed tracks that  
2714 range out (i.e. slow down to rest) inside the TPC. A characteristic feature of the energy

## Chapter 6. Particle ID in GArSoft

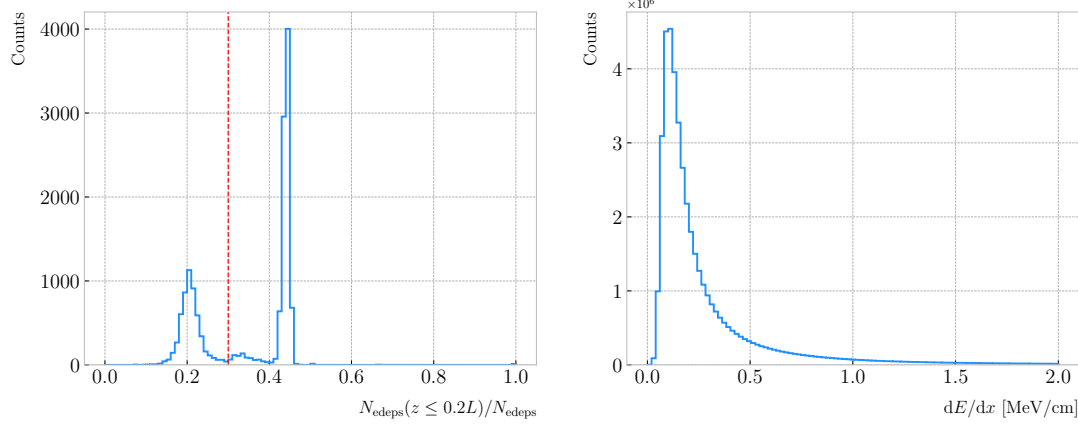


**Figure 6.1:** Left panel: distribution of the fraction of Geant4-level energy deposits per track with residual range less than 20% of the total track length, for the isotropic proton sample. Right panel: distribution of the ionisation per unit length of the energy deposits in the proton sample after removing the tracks with less than 30% of their energy deposits in the last 20% of the track.

loss profile of any stopping ionising particle is the so-called Bragg peak, a pronounced peak that occurs immediately before the particle comes to rest. From Eq. (6.1) we can see that this behaviour is expected, as the energy loss for non-relativistic particles is inversely proportional to  $\beta^2$ . In data, a way of identifying the Bragg peak, and thus select the stopping particles, is checking the number of energy deposits towards the end of the track. In this case, I count the fraction of the Geant4 simulated energy deposits with a residual range value (the distance from a given energy deposit to the last deposit in the track trajectory) less than a 20% of the corresponding track length<sup>2</sup>. The distribution of this fraction of energy deposits for our proton sample is shown in Fig. 6.1 (left panel). We can clearly see two well separated peaks in this distribution, one centered at 0.2 and another, narrower, one centered at a higher value. The first one corresponds to non-stopping protons, as in that case the number of energy deposits towards the end of the track is uniformly distributed due to the absence of the Bragg peak. In that way, I apply a cut in this distribution, requiring that at least 30% of the simulated energy deposits sit in the last 20% of the tracks, to ensure that the Bragg

<sup>2</sup>As we are applying this selection at the Geant4 level we could have simply selected the stopping protons using the `EndProcess` labels from the simulation. However, the Bragg peak identification method displayed here could serve as a starting point for a selection of stopping protons in real data.

## 6.2. $dE/dx$ measurement in the TPC

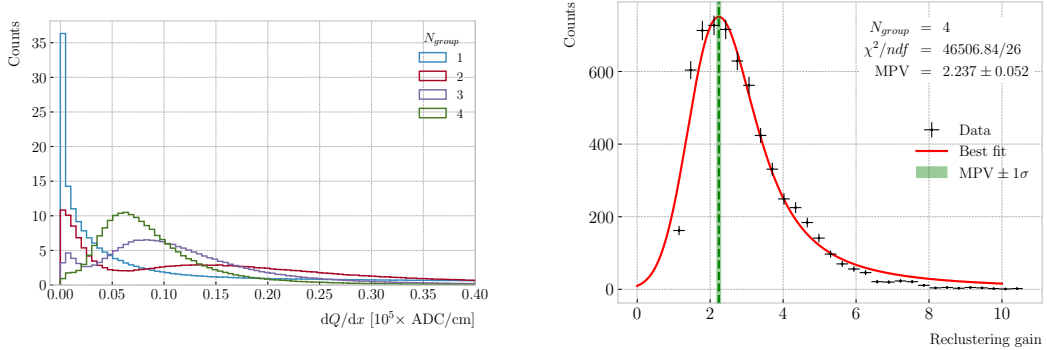


**Figure 6.2:** Left panel: distribution of the reconstructed ionisation charge per unit length for our MC stopping proton sample. The different colors indicate how many consecutive  $dQ/dx$  pairs were grouped together. Right panel: distribution of the median change in  $dQ/dx$  per track after  $N_{group} = 4$  clusters were reclustered together.

2730 peak is present.

2731 Figure 6.1 (right panel) shows the distribution of the energy loss per unit length for  
 2732 the Geant4 simulated energy deposits of the selected stopping protons. We can see that  
 2733 it follows the expected shape of a Landau distribution, which describes the fluctuations of  
 2734 the ionisation energy losses [135]. This distribution has a characteristic asymmetric PDF,  
 2735 with a long right tail that translates into a high probability for high-energy ionisation  
 2736 losses. The origin of these fluctuations is mainly the possibility of transferring a high  
 2737 enough energy to an electron, so it becomes a ionising particle itself.

2738 Now, from the point of view of the reconstruction, the objects that we have available  
 2739 to extract the ionisation information for the different reconstructed tracks are the  
 2740 collections of  $dQ$  and  $dx$  pairs, as stated before. The  $dQ$  values come from adding up  
 2741 the amplitude of all the reconstructed hits in a cluster, which is the input object to the  
 2742 Kalman fit.

2743 Figure 6.2 (left panel) shows the distribution of the ionisation charge deposits  
 2744 per unit length for the track in the stopping proton sample (blue line). As one can  
 2745 notice, this distribution does not resemble the expected shape of the Landau PDF. This  
 2746 distribution peaks sharply at 0 and has a heavy tailed behaviour. Notice, however, how  
 2747 the distribution changes its shape as we group together  $N_{group}$  consecutive charge deposit  
 2748 pairs (red, purple and green lines). The distribution in the  $N_{group} = 4$  case already has

## Chapter 6. Particle ID in GArSoft

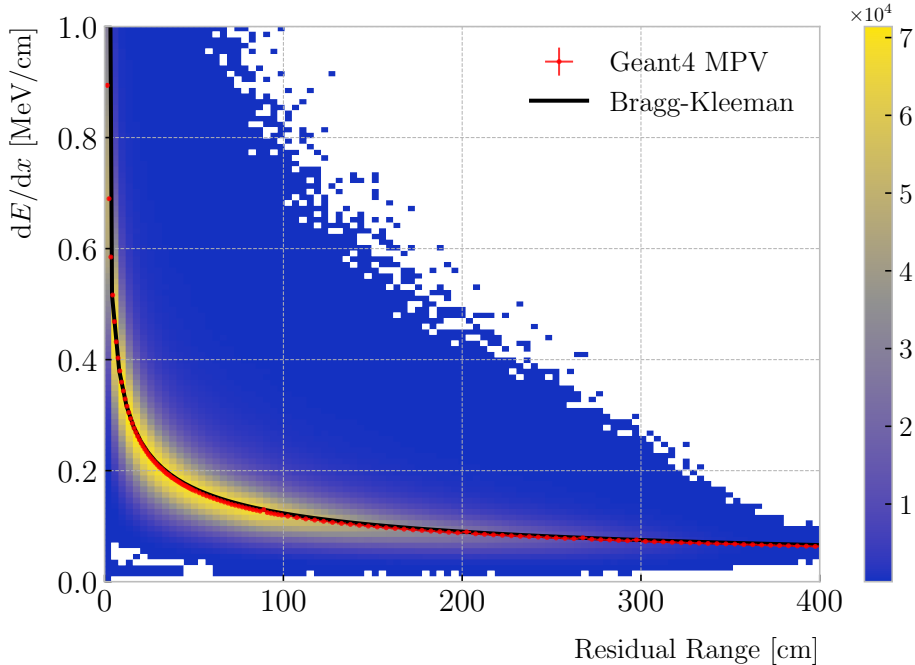


**Figure 6.3:** Distribution of the Geant4-simulated energy losses per unit length versus residual range for the stopping proton sample. The overlaid points represent the fitted most probable value of the  $dE/dx$  distribution in each residual range bin, whereas the curve is their best fit to the Bragg-Kleeman formula from Eq. (6.4).

2749 a shape which resembles that of the Geant4-level ionisation per unit length, so I will  
 2750 proceed using this amount of reclustering for the reconstruction-level depositions.

2751 An extra factor I need to account for, when reclustering is applied, is how the overall  
 2752  $dQ/dx$  per track changes. To do so, we can look at the ratio between the median  $dQ/dx$   
 2753 after and before the reclustering. Figure 6.2 (right panel) shows the median enhancement  
 2754 in  $dQ/dx$  per track for the stopping proton sample in the case  $N_{group} = 4$ . Fitting a  
 2755 Landau distribution convolved with a Gaussian<sup>3</sup>, I estimate the most probable value of  
 2756 this ratio to be  $G_{group} = 2.24 \pm 0.05$ .

2757 At this point, I am left with determining the conversion between the charge deposits  
 2758 per unit length  $dQ/dx$  and the energy deposits per unit length  $dE/dx$ . To this end, we  
 2759 need a way of comparing the two. I can use the residual range  $z$  to get a prediction of

---

<sup>3</sup>In the literature, this distribution is often referred to as Landau+Gaussian or langau. In the following, I will use LanGauss to refer to such PDF.

## 6.2. $dE/dx$ measurement in the TPC

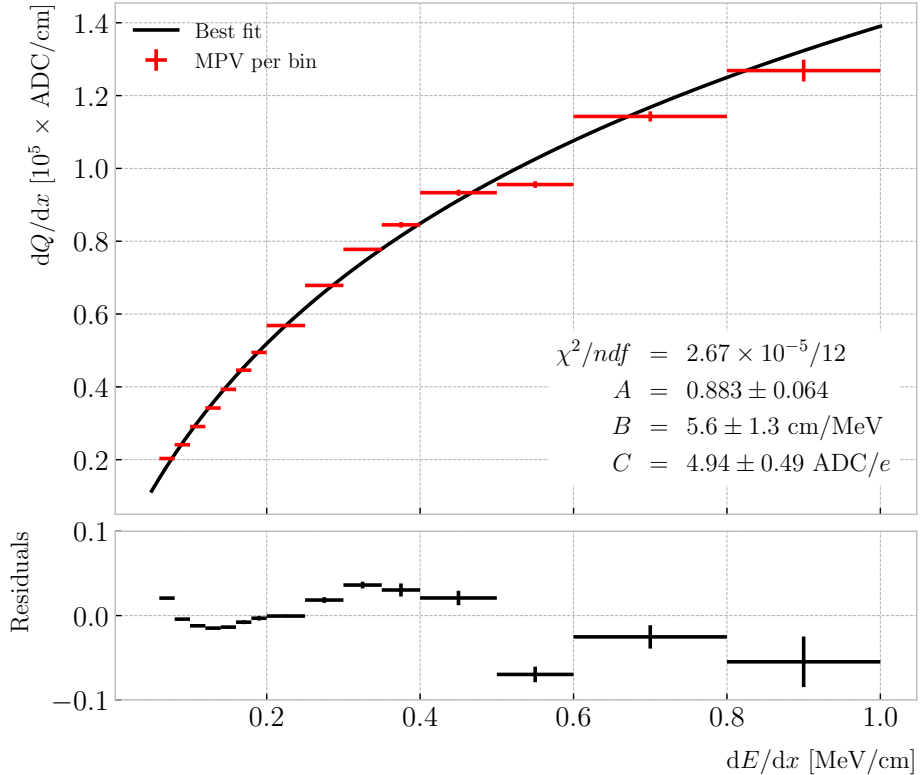


**Figure 6.4:** Fitted most probable  $dQ/dx$  values for each  $dE/dx$  bin (red points), obtained from the stopping proton sample. The overlaid curve (black line) represents the best fit to the logarithmic calibration function from Eq. (6.5).

2760 the most probable  $dE/dx$  by using the following empirical parametrisation [136]:

$$\frac{dE}{dx}(z) = \frac{z^{\frac{1}{p}-1}}{p\Lambda^{\frac{1}{p}}}, \quad (6.4)$$

2761 which is quoted in the literature as the Bragg-Kleeman formula. In order to obtain the  
2762  $p$  and  $\Lambda$  parameters I perform a fit using the energy losses and the residual ranges given  
2763 by the Geant4 stage of our proton sample.

2764 Within our simulation, the residual range is sampled with a maximum size of  
2765 5 mm. Therefore, to perform the fit to the Bragg-Kleeman formula, we can use a  
2766 fine-grained residual range binning. For each of the residual range bins I extract the  
2767  $dE/dx$  distribution and fit it to a LanGauss distribution, to obtain the value of the  
2768 most probable  $dE/dx$  in the bin together with a statistical uncertainty. I then fit Eq.

## Chapter 6. Particle ID in GArSoft

(6.4) to these most probable values and the centres of the residual range bins. This procedure is depicted in Fig. 6.3, where I show the distribution of the energy loss per unit length versus the residual range, together with the most probable  $dE/dx$  values and their uncertainty in each bin (red points) and the curve with the best fit of the Bragg-Kleeman relation to those values (black line). The best fit is obtained for the parameter values  $p = 1.8192 \pm 0.0005$  and  $\Lambda = 0.3497 \pm 0.0008 \text{ cm}/\text{MeV}^p$ <sup>4</sup>.

Having an analytical expression that relates the residual range to  $dE/dx$ , I can take our reconstruction-level residual ranges from the stopping proton sample and compute the most probable energy loss associated.

In order to parametrise the charge saturation, we can use the following logarithmic function inspired by the modified box model for recombination:

$$\frac{dE}{dx} = \frac{e^{\frac{dQ}{dx}B\frac{W_{ion}}{G_{group}C}} - A}{B}, \quad (6.5)$$

where  $A$  and  $B$  are the calibration parameters we need to determine,  $W_{ion}$  is the average energy to produce an electron-ion pair,  $G_{group}$  is the gain from the reclustering discussed above and  $C$  is the calibration constant to convert number of electrons to ADC counts, commonly refer to as gain (also to be obtained in the fit). In this case, I use a value for the electron-ion production energy of  $W_{ion} = 26.4 \text{ eV}$  [137]. This value, used in our simulation as well, was measured for gaseous argon in normal conditions, and therefore should be checked in the future to describe correctly the high-pressure argon-CH<sub>4</sub> mixture of ND-GAr.

For the calibration fit I follow a procedure similar to the previous one for Eq. (6.4). Binning the  $dE/dx$  range, I fit a LanGauss distribution to the corresponding  $dQ/dx$  distribution to obtain the most probable value. The resulting data points (red bars) are shown in Fig. 6.4 (top panel), the horizontal error bars depict the width of the  $dE/dx$  bin whereas the vertical bars represent the error associated to the most probable value estimation. A fit to the logarithmic function in Eq. (6.5) is also shown (black line).

---

<sup>4</sup>These strange units for  $\Lambda$  come from dimensional analysis, just to keep the Bragg-Kleeman formula (6.4) consistent.

## 6.2. $dE/dx$ measurement in the TPC

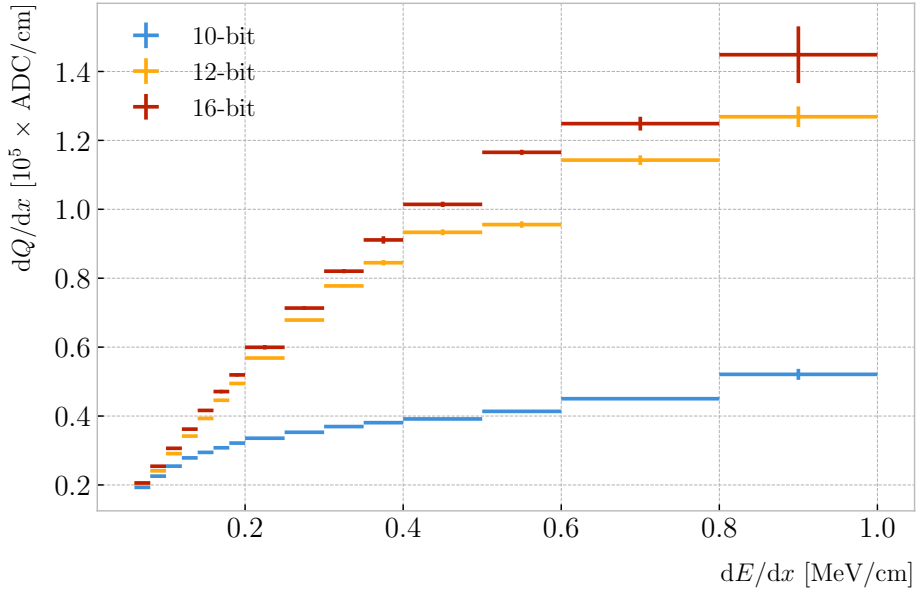


**Figure 6.5:** Fitted most probable  $dQ/dx$  values for each  $dE/dx$  bin for three different ADC bit limits, 10 (blue points), 12 (default, yellow points) and 16-bit (red points).

**Table 6.1:** Calibration parameters obtained from the fit of the ND-GAr simulated stopping proton sample to the calibration function from Eq. (6.5). The fits were performed for the 10, 12, and 16-bit ADC limits.

	$\chi^2/ndf$	Best fit $\pm 1\sigma$		
		$A$	$B$ (cm/MeV)	$C$ (ADC/e)
10-bit	$1.83 \times 10^{-6}/12$	$-9.3 \pm 3.9$	$270 \pm 69$	$27.1 \pm 5.4$
12-bit	$2.67 \times 10^{-5}/12$	$0.883 \pm 0.064$	$5.6 \pm 1.3$	$4.94 \pm 0.49$
16-bit	$1.44 \times 10^{-5}/12$	$0.949 \pm 0.024$	$3.53 \pm 0.58$	$4.52 \pm 0.29$

2794 For this I weighted the data points using the inverse of their relative error, obtaining  
 2795 a reduced chi-square value of  $\chi^2/ndf = 2.22 \times 10^{-6}$ . The best fit parameters I found  
 2796 from this fit are  $A = 0.883 \pm 0.064$ ,  $B = 5.6 \pm 1.3$  cm/MeV and  $C = 4.94 \pm 0.49$  ADC/e.  
 2797 Figure 6.4 (bottom panel) shows the residuals between the data points and the fit.

2798 The value for the gain I obtained from the fit is in reasonable agreement with our  
 2799 expectation. This value is set in GArSoft to 5 ADC/e by default.

2800 One interesting thing to check is what induces this non-linear relation between charge  
 2801 and energy. The only effects that modify the amount of electrons reaching the readout  
 2802 planes in the simulation are the transverse diffusion and the finite electron lifetime.

## Chapter 6. Particle ID in GArSoft

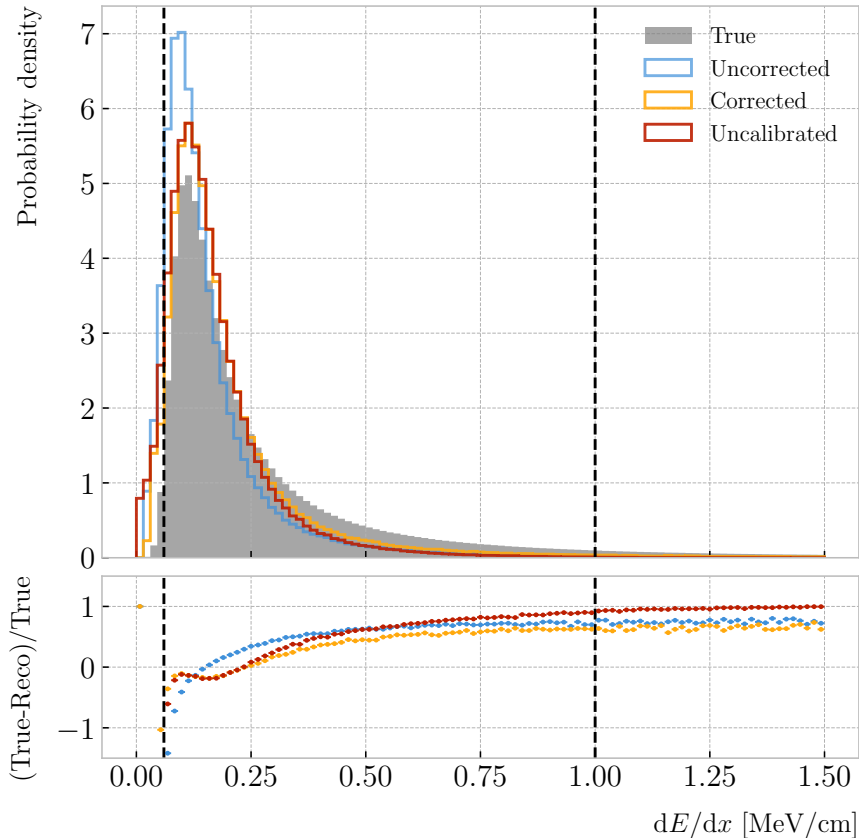


**Figure 6.6:** Top panel: area normalised  $dE/dx$  distributions for the true (solid grey) and the reconstructed energy deposits in the stopping proton sample, both after applying the calibration (blue) and the calibration and the normalisation correction (yellow). Also shown is the distribution obtained by applying a correction factor to the  $dQ/dx$  values but not the calibration (red). Bottom panel: fractional residuals for the uncorrected (blue), corrected (yellow) and uncalibrated (red) samples.

2803 Once the electrons reach the readout chambers, the pad response functions are applied,  
 2804 together with an electrons-to-ADC conversion and the ADC saturation limit.

2805 By default, GArSot applies a 12-bit ADC limit, which can be changed in the  
 2806 simulation configuration. However, it can only be increased up to 16-bit, as we represent  
 2807 the ADC collection as a `std::vector<short>`. This way, I tried to change the saturation  
 2808 parameter to see how it affects the relation between reconstructed charge and energy.  
 2809 Figure 6.5 shows a comparison between the most probable  $dQ/dx$  for 10, 12 and 16-  
 2810 bit ADC limits. As expected, the lower the limit is the sooner the charge saturates.  
 2811 For higher ADC limits the relation between energy and charge remains linear up to

## 6.2. $dE/dx$ measurement in the TPC

2812 higher  $dE/dx$  values, but even for the 16-bit limit the saturation is noticeable for values  
2813  $\gtrsim 0.5$  MeV/cm.

2814 Table 6.1 shows the results of fitting the samples with 10 and 16-bits ADC limits to  
2815 the calibration function from Eq. (6.5), using the weights based on their relative error  
2816 as described previously. One interesting feature to notice is how different the best fit  
2817 points look for the 10-bit ADC saturation when compared to the other two, which are  
2818 consistent with each other.

2819 At this point we can compare the  $dE/dx$  distribution one gets from Geant4, i.e. the  
2820 true energy loss distribution, and the distribution I found by applying the calibration  
2821 function to our collection of reconstructed  $dQ/dx$  values. Figure 6.6 (top panel) shows  
2822 the true (solid grey) and reconstructed (blue, labeled as uncorrected) distributions  
2823 together. The dashed vertical lines indicate the region of validity of the calibration fit, i.e.  
2824 the left and right edges of the first and last  $dE/dx$  bin respectively. Notice that these  
2825 histograms are area-normalised, as the total number of true energy deposits is much  
2826 higher than the number of reconstructed charge deposits. This is due to a combination  
2827 of effects, like the finite spatial resolution of the detector, the hit clustering used in the  
2828 track fitting and the reclustering we have applied here.

2829 The two distributions are significantly different. That can be seen clearly when  
2830 looking at the fractional residuals, shown in Fig. 6.6 (bottom panel). In particular,  
2831 the position of the peak is off, which could bias the mean energy loss predictions. It  
2832 seems like the difference between these may be due to an overall scaling factor. One  
2833 possibility is to scale the most probable value of the reconstructed distribution to  
2834 the most probable value predicted by Geant4. I do this by fitting both distributions  
2835 using a LanGauss function, obtaining  $dE/dx_{MPV, true} = 0.1145 \pm 0.0005$  MeV/cm and  
2836  $dE/dx_{MPV, reco} = 0.0928 \pm 0.0005$  MeV/cm for the true and reconstructed most probable  
2837 values respectively. These can be translated into an scaling factor  $S = 0.579 \pm 0.006$ .

2838 The result of applying the scaling correction can be seen in Fig. 6.6 (top panel).  
2839 The corrected  $dE/dx$  distribution (yellow, labeled as corrected) peaks around the same  
2840 value the true distribution does, as expected. Moreover, the high energy region is also

## Chapter 6. Particle ID in GArSoft

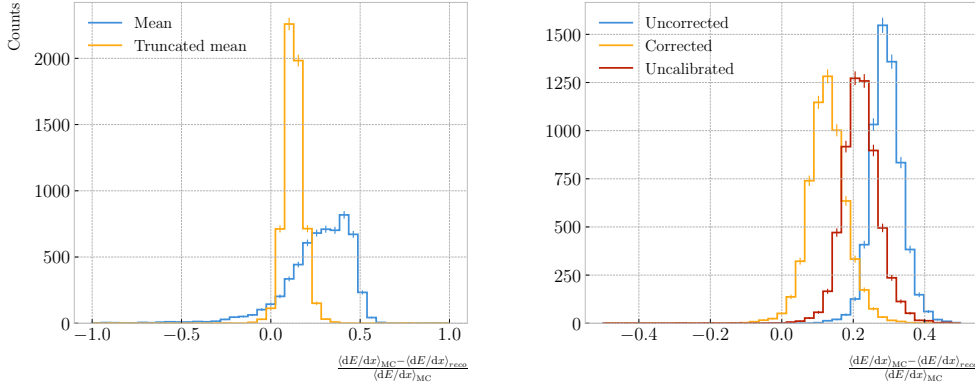


**Figure 6.7:** Left panel: fractional residuals between the true and the corrected  $dE/dx$  means (blue) and the 60% truncated means (yellow), for each event in the stopping proton sample. Right panel: fractional residuals between the true and the uncorrected (blue), corrected (yellow) and uncalibrated (red)  $dE/dx$  60% truncated means, for each event in the stopping proton sample.

slightly better described. For low ionisations, below the lower limit of the calibration fit, the differences between true and reconstructed are still significant. This low energy excess may be migration of some events from the peak region. The overall effect of the correction can be seen in the fractional residual plot in Fig. 6.6 (bottom panel).

One can also check what happens if instead of applying the logarithmic calibration we simply scale the  $dQ/dx$  distribution (post reclustering) to have the same most probable value as the true  $dE/dx$  distribution. In this case, following an analogous procedure to the one described earlier, I found the scaling factor  $S_{uncalibrated} = 0.414 \pm 0.002$  MeV/ADC<sup>5</sup>. The resulting distribution (red, labeled as uncalibrated) is also shown in Fig. 6.6 (top panel). The behaviour of the new distribution is similar to the corrected case at low energy losses, around the peak of the true distribution, but it is worse at describing the high energy tail. This is expected, it is in the high ionisation regime where saturation effects apply and therefore calibration is needed.

### 6.2.2 Truncated $dE/dx$ mean

Once we have a collection of  $dE/dx$  values for each reconstructed track, we can compute the corresponding most probable ionisation loss per unit length of the particle. This

<sup>5</sup>Notice that now the scaling factor is not dimensionless, as it acts more like a conversion factor here.

## 6.2. $dE/dx$ measurement in the TPC

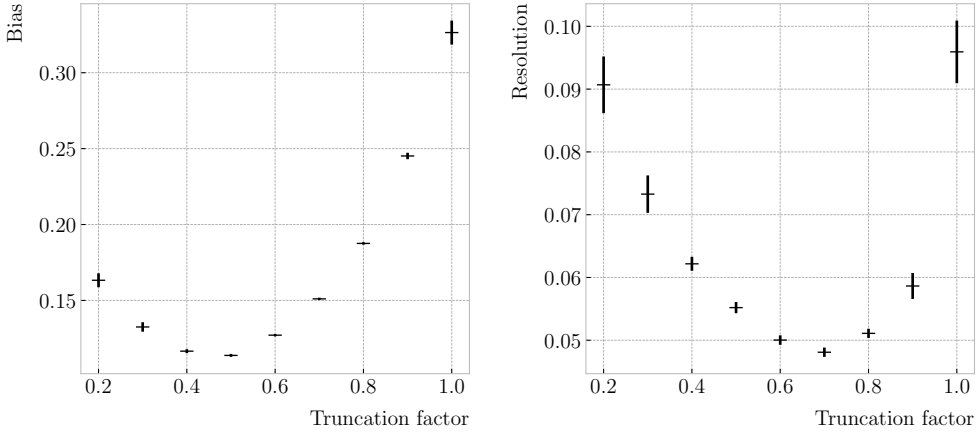


**Figure 6.8:** Estimated values of the mean  $dE/dx$  bias (left panel) and resolution (right panel) obtained using the corrected data from the stopping proton sample, for different values of the truncation factor.

2857 is the value predicted by the Bethe-Bloch or the PAI models, and together with a  
2858 measurement of the momentum it allows for particle identification.

2859 However, estimating the most probable  $dE/dx$  value for each reconstructed track  
2860 is not a trivial task. As mentioned before, the  $dE/dx$  distributions follow Landau-like  
2861 distributions. Therefore, one should perform e.g. a LanGauss fit to correctly estimate  
2862 the most probable values. Automating this kind of fits is often problematic, as they  
2863 usually incur in convergence problems. Moreover, the reconstructed  $dE/dx$  distributions  
2864 we obtain tend to have relatively small statistics, which may also produce poor fits. In  
2865 practice, doing these unsupervised fits may degrade our performance, and a more robust  
2866 method is preferred.

2867 A possibility could be taking the mean of the reconstructed  $dE/dx$  distribution for  
2868 each particle. The problem with this approach is that the high energy Landau tail,  
2869 combined with our limited statistics, can induce large fluctuations in the computation  
2870 of the mean. Imagine you have two protons with the same kinetic energy, but due to  
2871 reconstruction problems in one case you did not get as many charge deposits reconstructed  
2872 in its high ionisation loss region. If you do not remove the tails the computed  $dE/dx$   
2873 means will be significantly different.

2874 In order to avoid those fluctuations, one can compute the mean of a truncated  $dE/dx$

## Chapter 6. Particle ID in GArSoft

2875 distribution instead. By keeping only a given fraction of the lowest energy deposits  
2876 we obtain an estimate of the mean energy loss that is more resilient to reconstruction  
2877 inefficiencies and statistical effects. Figure 6.7 (left panel) shows a comparison between  
2878 the  $\langle dE/dx \rangle$  computed by taking the mean of the full distribution (blue line) and the  
2879 60% lowest energy clusters (yellow line), for the stopping proton sample. The fractional  
2880 residuals are computed for each proton, taking the corresponding means using their  
2881 collections of true and reconstructed energy deposits. One can see that using the simple  
2882 mean translates into a high bias and uncertainty in the  $\langle dE/dx \rangle$  estimation, whereas  
2883 applying the truncation reduces both significantly.

2884 Additionally, I performed a comparison between the 60% truncated mean  $dE/dx$   
2885 obtained using the different calibration methods discussed earlier, namely the uncorrected  
2886 (blue), corrected (yellow) and uncalibrated (red) distributions. The results are shown  
2887 in Fig. 6.7 (right panel). While the widths of these distributions are similar, the bias  
2888 obtained for the corrected sample, i.e. calibration function and correction factor applied,  
2889 is a factor of  $\sim 2$  lower than in the uncalibrated case and almost three times smaller  
2890 than for the uncorrected sample.

2891 The next step is to optimise the level of truncation we are going to apply to our  
2892 data. To do so, I used different truncation factors, i.e. the percentage of energy-ordered  
2893 reconstructed energy deposits we keep to compute the mean, on the corrected  $dE/dx$   
2894 sample of the stopping protons. Then, following the same procedure of computing the  
2895 fractional residuals as before, I fitted the resulting histograms using a double Gaussian  
2896 function. This is simply the sum of two Gaussian functions of the type:

$$g(x; \mu, \sigma, A) = A e^{-\frac{(x-\mu)^2}{2\sigma^2}}. \quad (6.6)$$

2897 I do not add the classical normalisation factor of the Gaussian,  $1/\sqrt{2\pi}\sigma$ , therefore  
2898 the amplitude  $A$  simply represents the maximum of the function. One of the two  
2899 Gaussian functions describes the core part of the distribution, while the other captures  
2900 the behaviour of the tails.

## 6.2. $dE/dx$ measurement in the TPC

2901 For each truncation factor, I look at the bias and the resolution I obtain. I define  
 2902 these as the weighted means of the corresponding parameters in the fits:

$$\bar{x} = \frac{A_{core} x_{core} + A_{tail} x_{tail}}{A_{core} + A_{tail}}, \quad (6.7)$$

2903 where  $A_{core}$  and  $A_{tail}$  are the amplitudes of the core and tail distributions respectively  
 2904 and  $x$  is either the mean  $\mu$  or the width  $\sigma$  of said distributions.

2905 Figure 6.8 shows the bias (left panel) and the resolution (right panel) I obtained  
 2906 for the stopping proton sample, using different values of the truncation. From these, it  
 2907 can be seen that a truncation factor of 50% minimises the bias in the estimation, while  
 2908 70% gives the best resolution. That way, I settled on the intermediate value of 60%  
 2909 truncation, which yields a  $\langle dE/dx \rangle$  resolution of  $5.00 \pm 0.08$  % for stopping protons.

### 2910 6.2.3 Mean $dE/dx$ parametrisation

2911 Now that we have a way to estimate the mean energy loss of a particle in the HPgTPC,  
 2912 we can determine the value of the free parameters in the ALEPH formula, Eq. (6.3).  
 2913 For this, I used a sample of  $10^5$  reconstructed FHC neutrino events inside ND-GAr. In  
 2914 this case I cannot use the stopping proton sample, as we need to cover the full kinematic  
 2915 range of interest for the neutrino interactions in our detector.

2916 The original data does not contain an estimation of the velocity of the tracks, instead  
 2917 the tracks have a value for the reconstructed momentum and the associated PDG code  
 2918 of the Geant4-level particle that created the track. Therefore, one can select some of the  
 2919 particles in the data, in this case I selected electrons, muons, pions and protons, and  
 2920 compute  $\beta$  and  $\gamma$  using the reconstructed momentum and their mass. In terms of  $\beta\gamma$   
 2921 the mean  $dE/dx$  does not depend on the particle species, so one can consider all the  
 2922 dataset as a whole. For this fit, I will express  $\beta$  in terms of the  $\beta\gamma$  product as:

$$\beta = \frac{\beta\gamma}{\sqrt{1 + (\beta\gamma)^2}}, \quad (6.8)$$

## Chapter 6. Particle ID in GArSoft

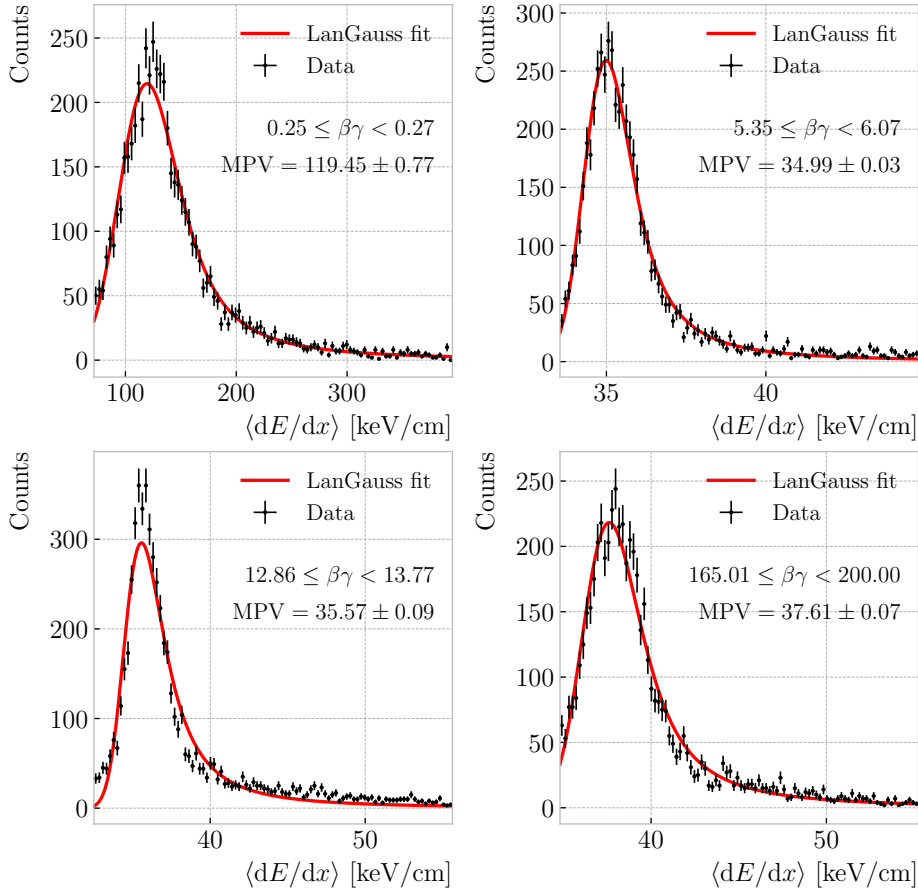


**Figure 6.9:** Examples of the truncated mean  $\langle dE/dx \rangle$  LanGauss fits for various  $\beta\gamma$  bins, from a simulated FHC neutrino sample.

2923 which can be easily proven from the definition of  $\gamma$ .

2924 Next, I bin the data in  $\beta\gamma$ . I chose a fine binning so as to capture the different  
 2925 features of the ionisation curve. Instead of fixing the bin width, I select them so each one  
 2926 has approximately the same statistics. Then, for each  $\beta\gamma$  slice, I compute the median  
 2927 and the interquartile range (IQR) of the  $\langle dE/dx \rangle$  distribution. Using these, I make a  
 2928 histogram in the range [median - IQR, median + 5 IQR], which I fit to a LanGauss  
 2929 function in order to extract the MPV. Using this range accounts for the asymmetric  
 2930 nature of the distributions, while also helps avoiding a second, lower maximum present  
 2931 at low  $\beta\gamma$ , probably a result of reconstruction failures.

2932 A few examples of these fits are shown in Fig. 6.9. The chosen values of  $\beta\gamma$  sit in  
 2933 very distinct points along the  $\langle dE/dx \rangle$  curve, going from the high ionisation region at

## 6.2. $dE/dx$ measurement in the TPC

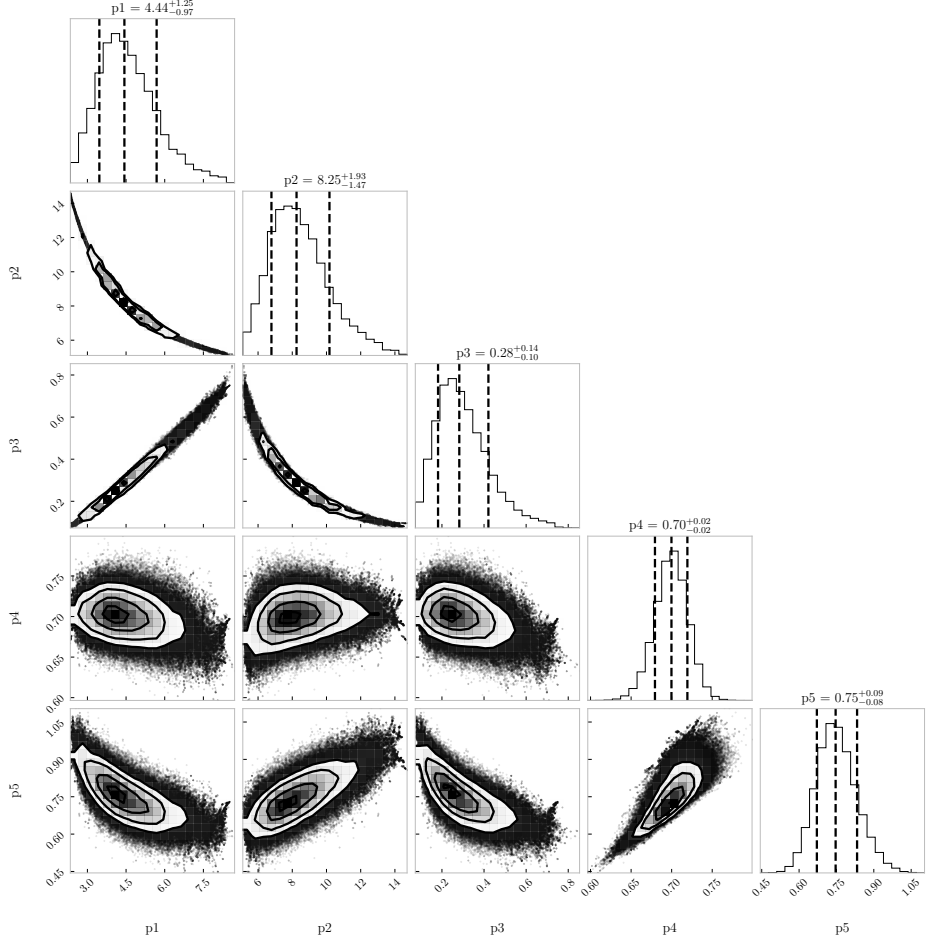


**Figure 6.10:** Resulting one and two dimensional projections of the posterior probability distributions of the ALEPH  $\langle dE/dx \rangle$  parameters obtained by fitting the 60% truncated mean  $dE/dx$  values from a FHC neutrino sample in ND-GAr. The vertical dashed lines in the 1D distributions represent the 16th, 50th and 84th percentiles.

2934 low velocities (top left panel), to the minimum point (top right panel), the beginning of  
 2935 the relativistic rise (bottom left panel), and the plateau produced by the density effect  
 2936 (bottom right panel).

2937 I used the resulting most probable  $\langle dE/dx \rangle$  values and the centres of the  $\beta\gamma$  bins as  
 2938 the points to fit to the ALEPH formula. For this particular fit I used the least-squares  
 2939 method to get a first estimation of the ALEPH parameters. Applying some uniform  
 2940 priors, I then used these values as the starting point of a 100000 steps MCMC. Figure 6.10  
 2941 shows the posterior probability distributions I obtain for each parameter. The reported  
 2942 best fit points are based on the 16th, 50th, and 84th percentiles in the marginalised

## Chapter 6. Particle ID in GArSoft

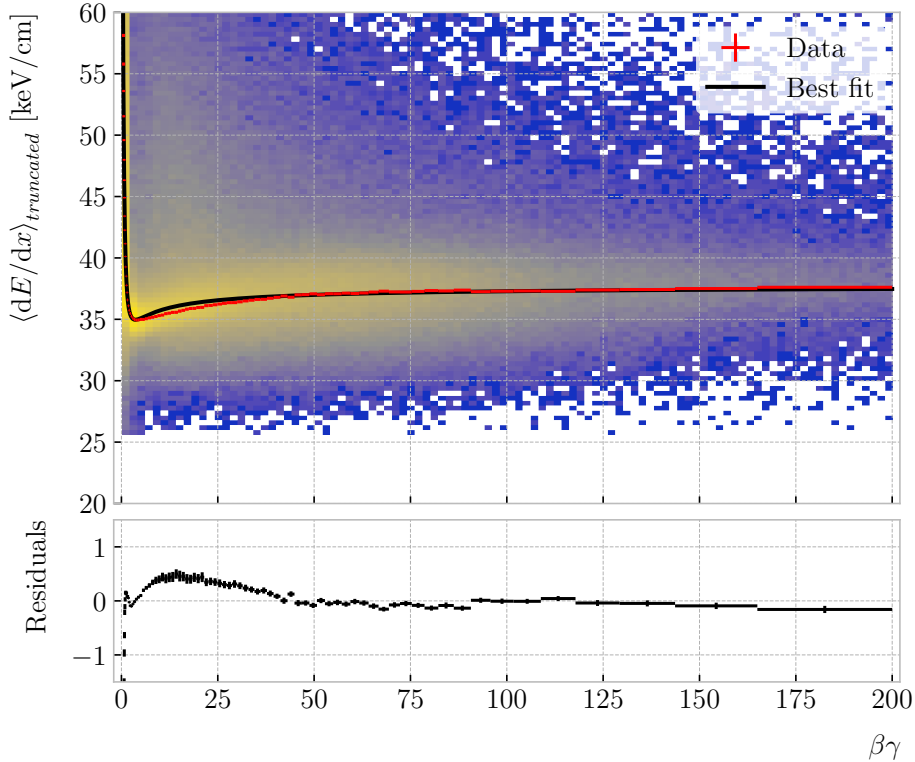


**Figure 6.11:** Truncated mean  $dE/dx$  obtained for the FHC neutrino sample as a function of the  $\beta\gamma$  product (upper panel). Also shown are the fitted most probable values for each  $\beta\gamma$  bin (red points) and the best fit obtained using the ALEPH parametrisation (black line). The residuals resulting from the fit are shown in the lower panel.

2943 distributions.

2944 The resulting fit (black line), compared to the data points (red points) and the  
 2945 underlying distribution is shown in Fig. 6.11 (top panel). The overall fit is good, with a  
 2946 reduced chi-squared of  $\chi^2/ndf = 1.02$ . However, there are some regions where the fit  
 2947 does not describe the data correctly, like the very low  $\beta\gamma$  regime, where the fit severely  
 2948 underestimates for energy losses  $\gtrsim 50$  keV/cm, and the start of the relativistic raise,  
 2949 where we have a slight overestimation. This is a result of those points having a larger  
 2950 uncertainty when compared to the ones around the dip or the plateau areas. These  
 2951 differences can be better seen in the residual plot, Fig. 6.11 (bottom panel).

### 6.3. Muon and pion separation in the ECal and MuID

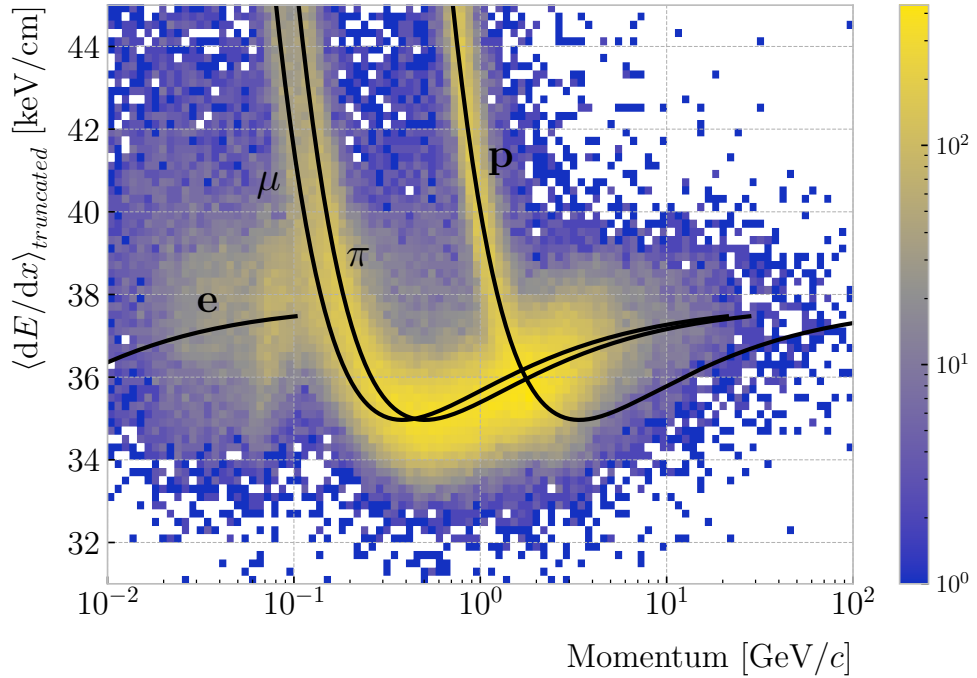


**Figure 6.12:** Distribution of the 60% truncated mean  $dE/dx$  versus reconstructed momentum for the FHC neutrino sample. The black lines indicate the predictions of the ALEPH parametrisation for electrons, muons, charged pions and protons.

2952    **6.2.4 Particle identification**

2953    **6.3 Muon and pion separation in the ECal and MuID**

2954    As it could be seen from Fig. 6.12, it is not possible to separate muons and charged pions  
 2955    in the HPgTPC using  $dE/dx$  for momenta  $\gtrsim 300$  MeV/c. In ND-GAr, approximately  
 2956    70% of the interactions in FHC mode will be  $\nu_\mu$  CC (compared to the 47% of  $\bar{\nu}_\mu$  CC  
 2957    interactions when operating in RHC mode), while 24% are neutral currents. Out of  
 2958    these, around 53% and 47% of them will produce at least one charged pion in the final  
 2959    state, respectively. Figure 6.14 shows a comparison between the spectra of the primary  
 2960    muons and the charged pions for  $\nu_\mu$  CC interactions in ND-GAr producing one or more  
 2961    charged pions. From this, one can see that (i) the majority of muons and charged pions  
 2962    are not going to be distinguishable with a  $\langle dE/dx \rangle$  measurement, and that (ii) particle  
 2963    identification is necessary both to classify correctly the  $\nu_\mu$  CC events and identify the

## Chapter 6. Particle ID in GArSoft

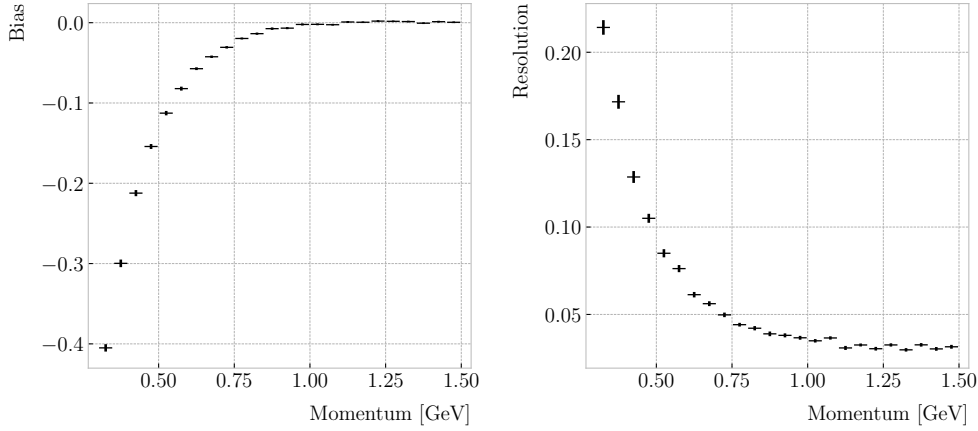


**Figure 6.13:** Estimated values of the mean  $dE/dx$  bias (left panel) and resolution (right panel) obtained for the true protons in a FHC neutrino sample.

2964 primary muon within them.

2965 ND-GAr features two other subdetectors which can provide additional information  
 2966 for this task, namely the ECal and MuID. The current ECal design, described in (ref  
 2967 section), consists of 42 layers, made of 5 mm of Pb, 7 mm of plastic scintillator and a  
 2968 1 mm PCB board. The total thickness of this calorimeter is 1.66 nuclear interaction  
 2969 lengths or 1.39 pion interaction lengths. The MuID design is in a more conceptual  
 2970 stage, however it is envisioned to feature layers with 10 cm of Fe and 2 cm of plastic  
 2971 scintillator<sup>6</sup>. With its three layers, it will have a thickness of 1.87 or 1.53 nuclear or pion  
 2972 interaction lengths, respectively.

2973 Because pion showers are dominated by inelastic nuclear interactions, the signatures  
 2974 of these particles in the calorimeter will look significantly different from those of muons.  
 2975 Although our ECal is not thick enough to fully contain the hadronic showers of the  
 2976 charged pions at their typical energies in FHC neutrino interactions, they can still be  
 2977 used to understand whether the original particle was more hadron-like or MIP-like. In  
 2978 Fig. 6.15 I show two examples of energy distributions created by a muon (left panel)  
 2979 and a charged pion (right panel) of similar momenta interacting in the ECal. These  
 2980 figures represent the transverse development of the interactions. For each of them, I

<sup>6</sup>It is not mentioned anywhere, but I assume that there should also be another layer of PCB board of 1 mm. However, in this case its contribution to the total thickness of the sampling calorimeter would be negligible.

### 6.3. Muon and pion separation in the ECal and MuID

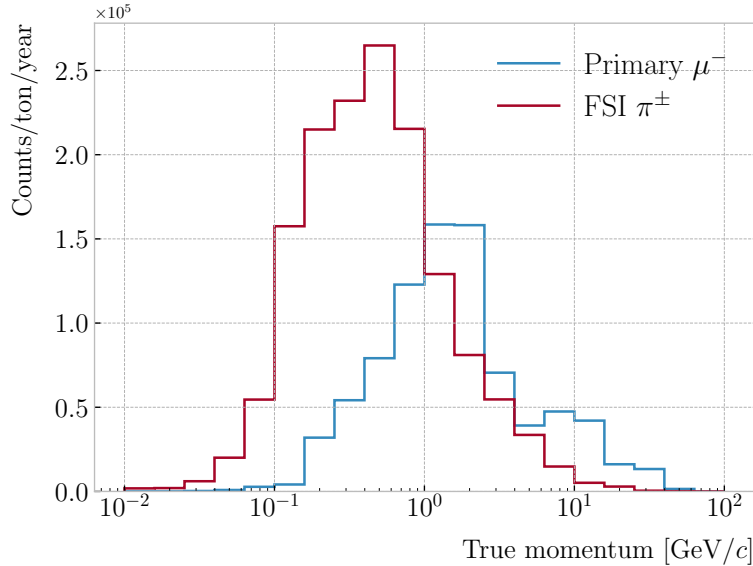


**Figure 6.14:** True momentum distribution for the primary muon in  $\nu_\mu$  CC  $N\pi^\pm$  interactions inside the fiducial volume of ND-GAr (blue line), compared to the post FSI charged pion spectrum (red line).

2981 computed the principal component and centre of mass of the interaction, projecting  
 2982 the position of the hits onto the plane perpendicular to that direction, and taking the  
 2983 distances relative to the centre. It can be seen that the muon follows an almost MIP-like  
 2984 behaviour, being the central bin in the histogram the one with the highest deposited  
 2985 energy. On the other hand, the pion not only deposits more energy overall, but also this  
 2986 energy is more spread-out among the different hits. It is this kind of information that  
 2987 would allow us to tell apart muons from pions.

2988 This way, I identify three main action points that need to be addressed if one wants  
 2989 to use these detectors to distinguish between muons and charged pions. These are:

- 2990 1. the way we make the associations between tracks in the HPgTPC to the activities  
 2991 (what in GArSoft we call clusters) in the ECal and the MuID,
- 2992 2. what variables or features one can extract from the calorimeters that encapsulate  
 2993 the information we are interested about,
- 2994 3. and how to carry out the classification problem.

## Chapter 6. Particle ID in GArSoft

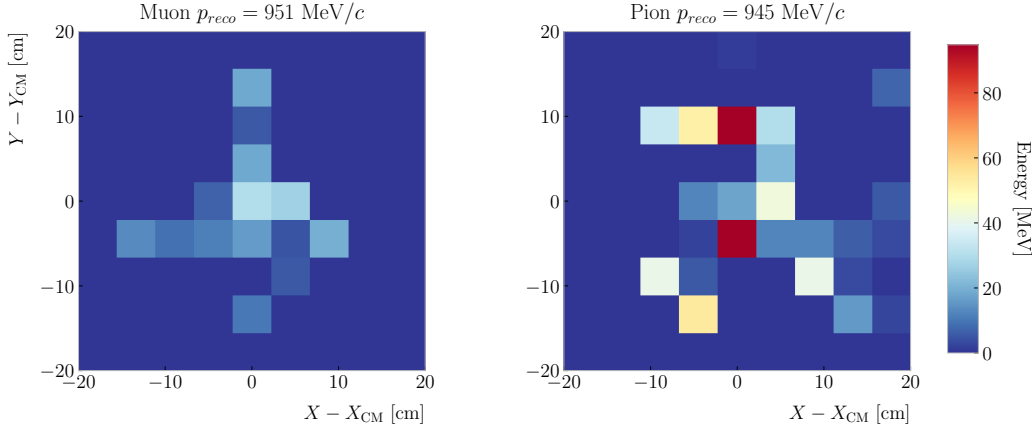


**Figure 6.15:** Distributions of energy deposits in the ECal for a muon (left panel) and a charged pion (right panel) with similar momenta. The energy is projected onto the plane perpendicular to the principal component of the hits, and the positions are relative to the center of the interaction.

### 2995 6.3.1 Track-ECal matching

2996 One of the main players in the muon and pion separation is the way we associate clusters  
 2997 in the ECal to reconstructed tracks in the TPC. Missing some associations or making  
 2998 wrong ones can bias the ECal quantities that we can use for classifying particles. The  
 2999 current algorithm in GArSoft provides precise associations, i.e. most of the associations  
 3000 that it produces are correct, but it appears to miss an important number of associations  
 3001 (at least when using the default configuration).

3002 The current TPC track-ECal cluster association algorithm is divided in four parts.  
 3003 It first checks whether the track end point fulfils certain conditions to be extrapolated.  
 3004 There are two cut values in this step, one for the drift direction and other radial.

3005 If the point can be extrapolated, the code computes the coordinates of the centre  
 3006 of curvature using the Kalman fit estimates at the track end ( $y$ ,  $z$ ,  $1/R$ ,  $\phi$ ,  $\tan\lambda$ ). It  
 3007 then compares the distance between this and the cluster in the  $(z, y)$  plane with  $R$ . This  
 3008 introduces another cut in the perpendicular direction.

3009 The next step is different for clusters in the barrel or in one of the end caps. If it  
 3010 is a barrel cluster the algorithm extrapolates the track up to the radial distance of the  
 3011 cluster. There are three possible outcomes, the extrapolated helix can cut the cylinder

### 6.3. Muon and pion separation in the ECal and MuID

3012 of radius  $r_{clus}$  two, one or zero times. I get the cut point that is closer to the cluster and  
3013 check that it is either in the barrel or the end caps. Computing the difference between  
3014 the  $x$  coordinates of the cluster and the extrapolated point, the module checks that this  
3015 is not greater than a certain cut. If the cluster is in an end cap, I propagate the track  
3016 up to the  $x$  position of the cluster. Then, the algorithm computes the angle in the  $(z, y)$   
3017 plane between the centre of curvature and the cluster,  $\alpha$ , and the centre of curvature  
3018 and the propagated point,  $\alpha'$ . A cut is applied to the quantity  $(\alpha - \alpha')R$ .

3019 If the cluster contains more than a certain number  $N$  of hits, I apply an extra cut to  
3020 the dot product of the direction of the track at the propagated  $x$  value and the cluster  
3021 direction.

3022 The code makes sure to only associate one end of the track (if any) to a cluster.  
3023 However, it can associate more than one track to the same cluster. This makes sense,  
3024 as different particles can contribute to the same cluster in the ECal, but it makes it  
3025 difficult to quantify the relative contributions of the tracks to a certain cluster.

3026 As a way of comparing the performance of this algorithm, a new, simpler association  
3027 module was written. The goal was to have a simple and robust algorithm, which depends  
3028 on as few parameters as possible and that can produce a one-to-one matching between  
3029 tracks and ECal clusters.

3030 For each reconstructed track, the new algorithms applies the same procedure to the  
3031 forward and the backward fits irrespective of their end point positions. It first gets the  
3032 Kalman fit parameters at the corresponding end point together with the  $X$  position,  $x_0$ ,  
3033 ( $y_0, z_0, 1/R, \phi_0, \tan\lambda$ ).

3034 For each ECal cluster, I compute the radial distance to the centre of the TPC and  
3035 find the  $\phi$  value in the range  $[\phi_0, \phi_0 + \text{sign}(R)\phi_{max}]$  that makes the propagated helix  
3036 intersect with the circle defined with such radius. The  $(x, y, z)$  position of the helix for  
3037 the  $\phi$  value found (if any) is then computed. In case there are two intersections, I keep  
3038 the one that minimises the distance between  $(y, z)$  and  $(y_c, z_c)$ .

3039 I then calculate  $\chi^2$  value based on the Euclidean distance between the propagated

## Chapter 6. Particle ID in GArSoft

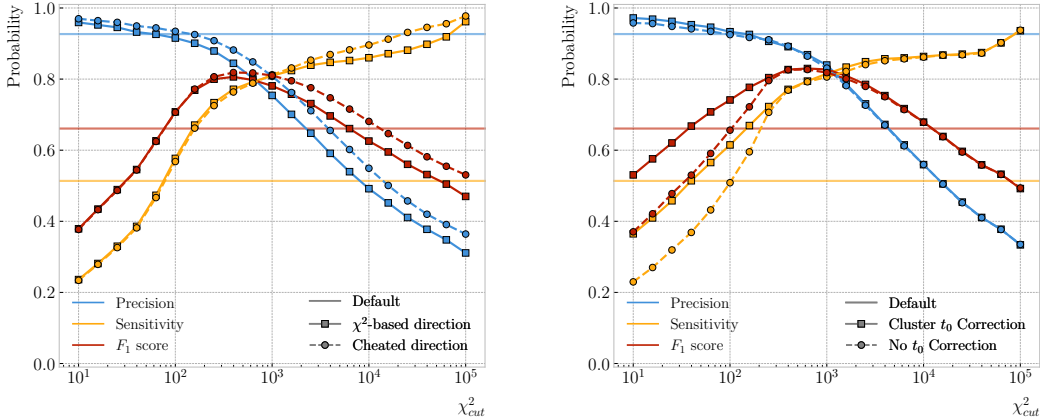


**Figure 6.16:** Left panel: comparison between the precision (blue), sensitivity (yellow) and  $F_1$  score (red) obtained for the default (horizontal lines) and new algorithms, both with the  $\chi^2$ -based direction estimator (squares) and cheating the directions (circles), for different values of the  $\chi^2$  cut. Right panel: comparison of the performance of the new algorithm when applying the cluster  $t_0$  correction (squares) and when (circles).

3040 point and the cluster:

$$\chi^2/ndf = \frac{\sum_{n=0}^2 (x^{(n)} - x_c^{(n)})^2}{3}. \quad (6.9)$$

3041 If there was no intersection I store a  $-1$  instead. In the end, for each reconstructed track  
3042 in the event one ends up with two collections of  $\chi^2$  values, one for each ECal cluster  
3043 and fit directions.

3044 The current code only supports having ECal clusters associated to one end of each  
3045 track. We have two options to decide what track end to keep. The first one tries to  
3046 cheat the selection, looking at the distance between the two track ends and the true  
3047 start position of the associated MC particle. The second one keeps the track end with  
3048 more  $\chi^2$  entries below the cut.

3049 This feature of only considering one track end limits the algorithm, making it not  
3050 suitable for reconstructing events with particles originating outside the TPC. However,  
3051 as for the moment the main concern of the group is the study of neutrino interactions  
3052 off the gaseous argon, this is an acceptable assumption.

3053 In order to associate a cluster to a track, I take all clusters with a  $\chi^2$  value in the  
3054 range  $[0, \chi^2_{cut}]$ . If a cluster has been assigned to more than one track we leave it with

### 6.3. Muon and pion separation in the ECal and MuID

3055 the one with the lowest  $\chi^2$ .

3056 This default behaviour of the algorithm can be modified to associate more than one  
3057 track to each cluster. Not only that, but the  $\chi^2$  values can be used to assign relative  
3058 weights to the different contributions.

3059 To evaluate the performance of the association method, I use a binary classification  
3060 approach. In this case, I check the leading MC Track IDs associated to the reconstructed  
3061 tracks and ECal clusters. I count an association as true positive (TP) if both Track  
3062 IDs coincide. An association is considered false positive (FP) when the Track IDs are  
3063 different. If a cluster has not been associated to any track but it shares the Track ID  
3064 with a reconstructed track it is counted as a false negative (FN).

3065 For the testing, I used a sample of 10000 FHC neutrino events inside the HPgTPC.  
3066 Figure 6.16 (left panel) shows the precision (blue line), sensitivity (yellow line), and  $F_1$   
3067 score (red line) I obtained for different values of  $\chi_{cut}^2$ . For comparison, the same metrics  
3068 computed for the default algorithm with the current configuration are also shown (dashed  
3069 lines). In the case of the new algorithm, I used both the  $\chi^2$ -based method to estimate  
3070 the track direction described earlier (square markers) and the cheated direction from the  
3071 Geant-level information (circle markers). For either of these we achieve similar values of  
3072 the precision compared to the old code, while having a considerably higher sensitivity.  
3073 It can be seen that cheating the direction of the tracks only makes a difference at high  
3074  $\chi_{cut}^2$ , past the optimal value of the cut around the  $F_1$  score maximum. Therefore, I set  
3075 the  $\chi^2$  method as the default.

3076 One of the possible weak points of this approach is that it relies on the position along  
3077 the drift direction to make the decisions. Within the current ND-GAr design implemented  
3078 in GArSoft, the timing information is provided by the ECal. That effectively means  
3079 that prior to make the track-ECal associations the reconstructed  $x$  positions of the track  
3080 trajectories differ from the simulated ones by an amount:

$$x_{reco}^{(n)} - x_{sim}^{(n)} = v_{drift} t_0, \quad (6.10)$$

## Chapter 6. Particle ID in GArSoft

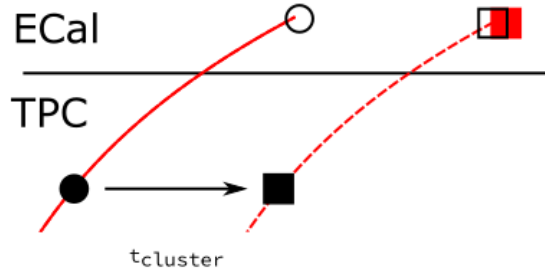


**Figure 6.17:** Schematics of a possible option to deal with track-ECal associations in non-zero  $t_0$  neutrino interaction events, trying to correct for the drift direction uncertainty in a cluster-by-cluster basis using the cluster time,  $t_{cluster}$ .

3081 where  $v_{drift}$  is the mean drift velocity in our medium and the initial time is in the range  
 3082  $t_0 \in [0, t_{spill}]$  where  $t_{spill}$  is the spill length. For a  $10 \mu\text{s}$  spill this translates into a  
 3083 maximum 30 cm uncertainty on the drift direction position.

3084 The current default in GArSoft sets  $t_0 = 0$ , but the functionality to randomly sample  
 3085 this within the spill time is in place. Therefore, we need to understand what is the impact  
 3086 of a non-zero  $t_0$  on the associations algorithm and foresee possible ways of minimising a  
 3087 loss in performance.

3088 Figure 6.17 represents a possible option to tackle the association problem when  
 3089 having events with a non-zero initial time  $t_0$ . The black and white circles represent the  
 3090 original points, whereas the squares indicate the corrected positions. The end points of  
 3091 the track and the propagated points up to the cluster radius are indicated using filled  
 3092 and unfilled markers respectively. The red square represents the position of the cluster.

3093 Here I try to correct for the drift coordinate position using the time associated to the  
 3094 cluster. Assuming that the drift time is much larger than the propagation time,  $t_{cluster}$   
 3095 could be used as a good estimation of the  $t_0$ . An alternative can be using the earliest  
 3096 time associated to a hit in said cluster. Doing this for each cluster before computing  
 3097 the  $\chi^2$  value could be used as an alternative to knowing the specific value of the  $t_0$ , as  
 3098 when the association is correct this will provide the right correction but its impact is  
 3099 small enough to not change the position significantly in the case the cluster does not  
 3100 correspond to a given track.

### 6.3. Muon and pion separation in the ECal and MuID

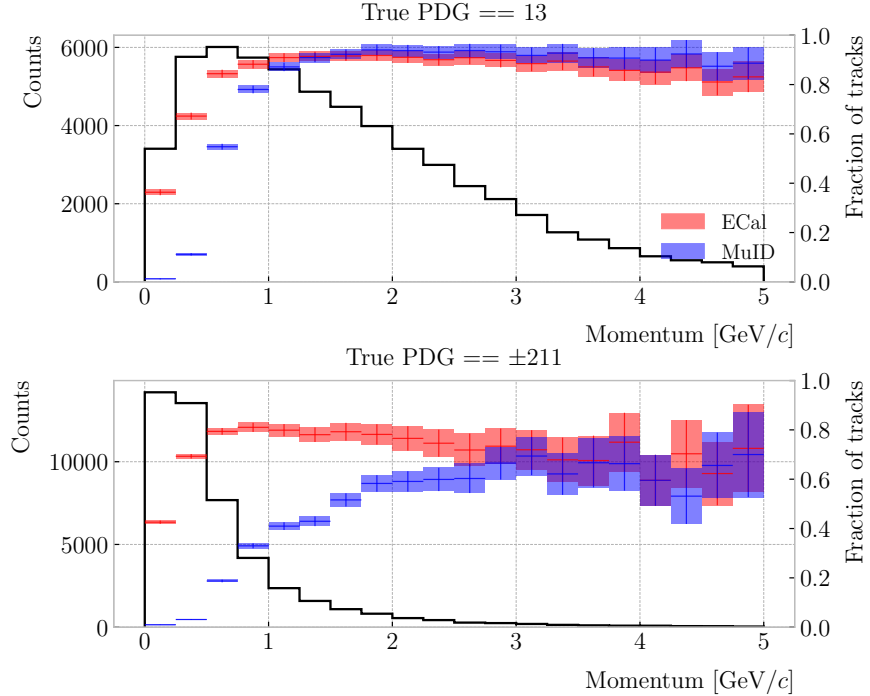


**Figure 6.18:** Momentum distribution for the reconstructed muons (top panel) and charged pions (bottom panel) in a FHC neutrino sample, together with the fraction of them reaching the ECal (red) and MuID (blue). Each entry corresponds to a reconstructed track, backtracked to a true muon or pion which has not produced any other reconstructed track.

3101 I tested the effect of this correction again using a sample of 10000 FHC neutrino  
 3102 events. Figure 6.16 (right panel) shows the precision (blue line), sensitivity (yellow line),  
 3103 and  $F_1$  score (red line) for the case the cluster  $t_0$  correction is applied (square markers)  
 3104 and for the no correction case (circle markers), as a function of  $\chi^2_{cut}$ . In this case, the  
 3105 differences are particularly notorious at low values of the cut. It makes sense, as the  $t_0$   
 3106 effect becomes subdominant when the distance we consider grows large. Overall, the  
 3107 correction increases the sensitivity while keeping the precision almost unchanged. As a  
 3108 result, I apply the  $t_0$  correction to the generated samples as the default.

#### 3109 6.3.2 Classification strategy

3110 The problem of the muon and charged pion separation has to be viewed in the broader  
 3111 context of the particle identification in our detector. Focusing on the beam neutrino

## Chapter 6. Particle ID in GArSoft

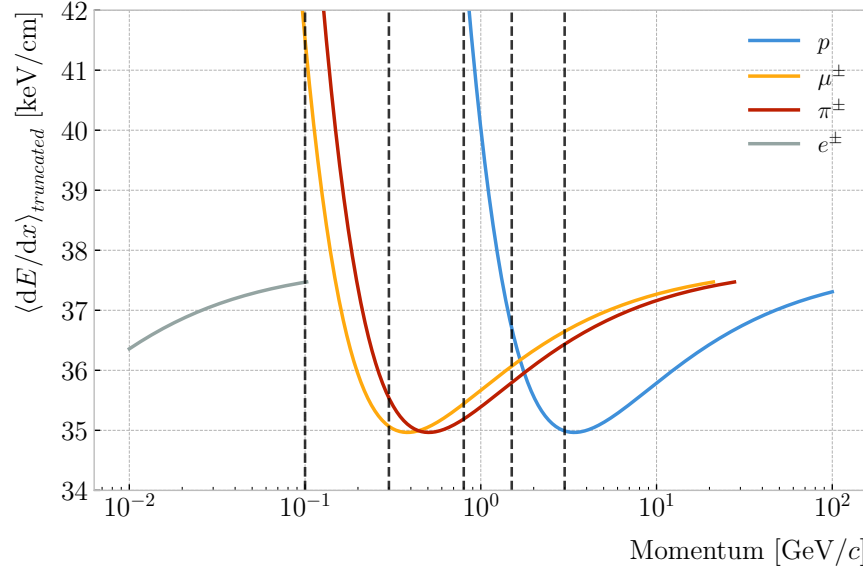


**Figure 6.19:** Predicted truncated mean  $dE/dx$  versus momentum, for electrons, muons, charged pions and protons, obtained using the ALEPH parametrisation. The vertical dashed lines represent the boundaries of the six regions used for the muon and pion classification training.

interactions, it is clear that we are going to have muons and pions spanning a broad momentum range. Not only that, but we will also have other particles with similar characteristics that will make the classification even more challenging. Therefore, we are presented with a task that will depend heavily on the kinematic range we are looking at each time, as both the available information and the possible impurities of other particle species vary.

For instance, distinguishing muons from pions could be difficult at low momenta, as a great number of them do not reach the ECal. Therefore, we could think of tailoring a version of the classification for that particular case, which could be complemented with a  $dE/dx$  measurement. Likewise, for momenta  $\gtrsim 1$  GeV muons and pions reach the calorimeters efficiently, but so do protons. Because of this, one can try to train another classifier for this energy range, and rely on other methods to remove as many of the protons as possible.

Figure 6.18 shows the momentum distribution of the reconstructed muons (top) and pions (bottom) in a FHC sample. It also contains the fraction of particles reaching the

### 6.3. Muon and pion separation in the ECal and MuID

**Table 6.2:** Momentum ranges and description of the PID approach assumed for the muon and pion classification task.

Momentum range	Description
< 0.1 GeV/c	All tracks can be separated with $dE/dx$
[0.1, 0.3) GeV/c	Use ECal for reaching muons and pions, $dE/dx$ for the rest
[0.3, 0.8) GeV/c	Use ECal for muons and pions, $dE/dx$ for protons
[0.8, 1.5) GeV/c	Use ECal and MuID for muons and pions, $dE/dx$ for protons
[1.5, 3.0) GeV/c	Use ECal and MuID for muons and pions, ToF for protons
$\geq 3.0$ GeV/c	Use ECal and MuID for muons and pions, $dE/dx$ and ToF for protons

3127    ECal (red) and MuID (blue), for the different momentum bins. In Fig. 6.19 I show the  
 3128    mean  $dE/dx$  of different particles as a function of the momentum, computed using the  
 3129    ALEPH parametrisation with the best fit parameters found in Subsec. 6.2.2.

3130    Using these two figures as references, I decided to approach the classification by  
 3131    dividing the problem into six different momentum regions. A summary of these can be  
 3132    found in Tab. 6.2. The basic idea is to exploit all the information that is available in  
 3133    each region and . For the problem at hand, I prepared separated samples of isotropic  
 3134    single muons and pions, with momenta uniformly distributed along the corresponding  
 3135    momentum range. Each sample contains 50000 events of the corresponding particle  
 3136    species. I did not generate samples for the first region, as it is assumed that the separation  
 3137    can be achieved using  $dE/dx$  only. For the last region, I generated particles up to a  
 3138    momentum of 10 GeV/c, as that is well above the typical energies of muons and pions  
 3139    from FHC neutrino interactions in ND-GAr.

3140    Additionally, I prepared another sample of 100000 FHC neutrino events. For each  
 3141    interaction, I select the reconstructed particles which were backtracked to true muons or  
 3142    charged pions. I use this dataset to perform validation checks, to see how the models  
 3143    trained with the single particle data generalise to a more realistic scenario.

3144    To tackle this classification problem, I make use of Boosted Decision Trees (BDT). A  
 3145    decision tree uses a flowchart-like structure to make decisions based on some input data.  
 3146    It starts from a root node, which represents the complete dataset, and then it splits

## Chapter 6. Particle ID in GArSoft

3147 this based on the variable or feature which gives the best separation between classes,  
3148 creating two new nodes. The process repeats for each node until it reaches a certain  
3149 limit, like a maximum number of splits or some tolerance criteria. The last set of nodes  
3150 are often called leave nodes, and represent the final prediction of the classifier.

3151 Boosting refers to a family of methods to combine the predictions from multiple  
3152 classifiers, following a sequential approach where each new model learns from the errors  
3153 of the previous one. The process starts with a simple decision tree, which is used to  
3154 make predictions on the training data. Then, the data points misclassified by the first  
3155 model are assigned higher weights, and another decision tree is trained on the data with  
3156 adjusted weights. The predictions of the two trees are then combined, and the cycle  
3157 repeats for a predefined number of iterations. Gradient boosting uses the direction of  
3158 the steepest error descent to guide the learning process and improve the accuracy with  
3159 each iteration.

### 3160 6.3.3 Feature selection and importance

3161 Using the reconstructed tracks as a starting point, I compute a number of ECal and  
3162 MuID variables for each of them. As there can be more than one cluster associated to a  
3163 track, what I do is collect all associated clusters and compute these variables from the  
3164 complete collection of associated hits. For the MuID, because it only features three layers  
3165 and typically there will be less hits, I also allow single hits to be associated with tracks<sup>7</sup>.  
3166 I can roughly divide the variables in three types: energy-related, geometry-related and  
3167 statistical. In the following, I briefly describe the variables related exclusively to the  
3168 ECal:

#### 3169 • Energy-related ECal

3170 – ECal total energy (ClusterTotalEnergy): sum of the energy of all the ECal  
3171 hits.

---

<sup>7</sup>At the reconstruction level what happens is that non-clustered hits are put into single hit clusters, instead of being thrown away. This is necessary to keep the consistency of the track-cluster association code.

### 6.3. Muon and pion separation in the ECal and MuID

- 3172     – Mean ECal hit energy (HitMeanEnergy): mean of the hit energy distribution.
- 3173     – Standard deviation ECal hit energy (HitStdEnergy): standard deviation of  
3174       the hit energy distribution.
- 3175     – Maximum ECal hit energy (HitMaxEnergy): maximum of the hit energy  
3176       distribution.

#### 3177     • Geometry-related ECal

- 3178     – Mean distance hit-to-cluster (DistHitClusterMean): mean of the distance  
3179       distribution between the hits and the corresponding cluster's main axis.
- 3180     – RMS distance hit-to-cluster (DistHitClusterRMS): root mean square of the  
3181       distance distribution between the hits and the corresponding cluster's main  
3182       axis.
- 3183     – Maximum distance hit-to-centre (DistHitCenterMax): maximum of the  
3184       distance distribution between the hits and the centre of the TPC.
- 3185     – Time-of-Flight velocity (TOFVelocity): slope obtained when fitting a straight  
3186       line to the hit time versus hit distance to the centre (i.e.  $d = v \times t$ ).

#### 3187     • Energy and geometry ECal

- 3188     – Radius 90% energy (Radius90E): distance in the hit-to-cluster distribution  
3189       for which 90% of the total energy is contained in the hits that are closer to  
3190       the axis (i.e. radius that contains 90% of the energy).

#### 3191     • Statistical ECal

- 3192     – Number of hits (NHits): total number of hits associated to the track.
- 3193     – Number of layers with hits (NLayers): not really a count of all layers with  
3194       hits but the difference between the last and the first layer with hits.

3195     Figure 6.20 shows the distributions of three different ECal variables, separating true  
3196       muons (blue) and charged pions (red), for the five momentum ranges considered. I chose

## Chapter 6. Particle ID in GArSoft

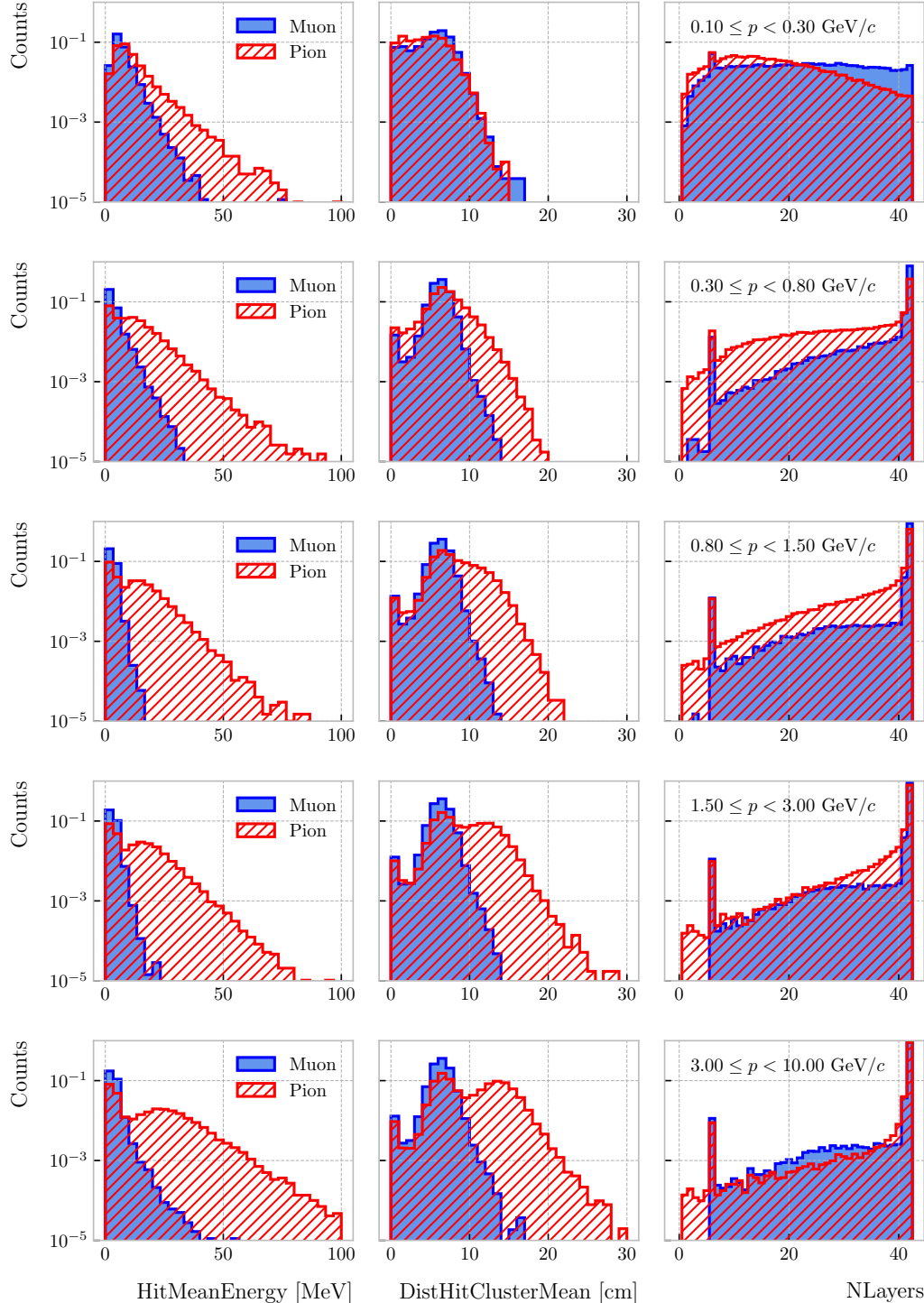


**Figure 6.20:** Example ECal feature distributions for muons (blue) and charged pions (red) in the five different momentum ranges considered (from top to bottom, in ascending momentum order). From left to right: mean hit energy, mean distance hit-to-cluster, and number of layers with hits.

### 6.3. Muon and pion separation in the ECal and MuID

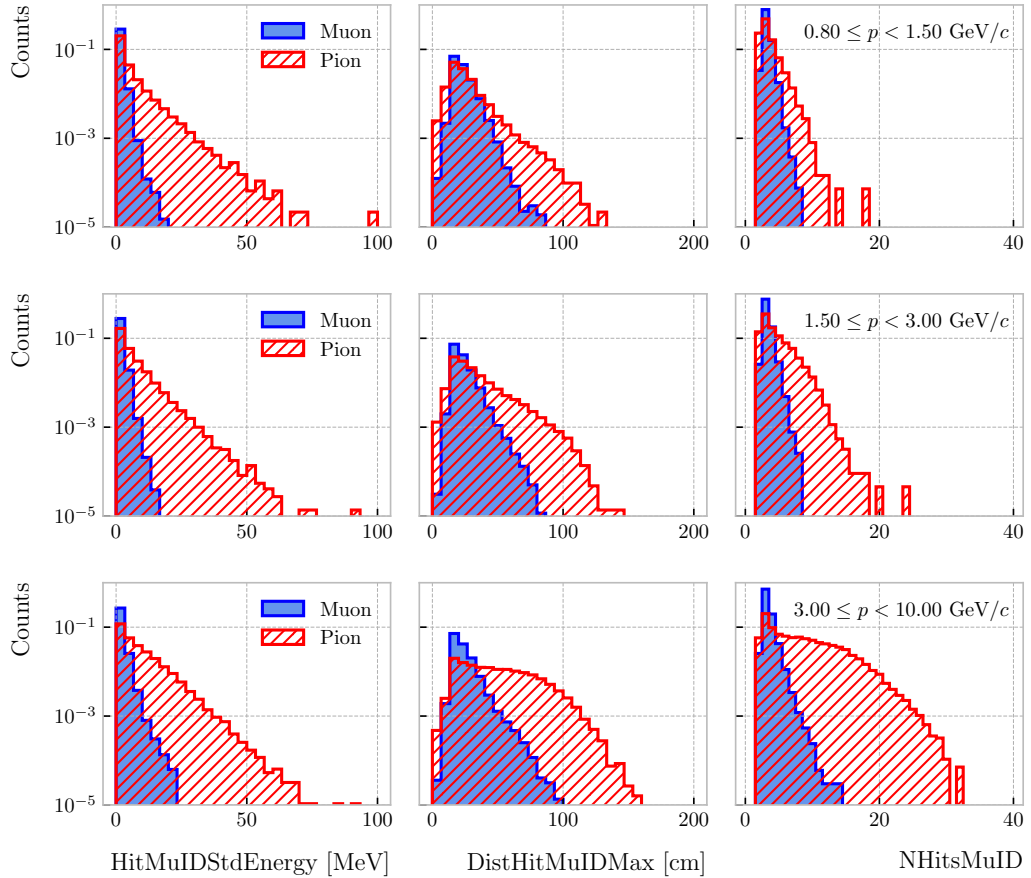


**Figure 6.21:** Example MuID feature distributions for muons (blue) and charged pions (red) in the three different momentum ranges considered (from top to bottom, in ascending momentum order). From left to right: standard deviation hit energy, maximum distance hit-to-hit, and number of hits.

3197 to show one feature from each category, namely the mean energy per hit (left column),  
 3198 the mean distance between the hits and the centre of the cluster (middle column), and  
 3199 the number of ECal layers with hits (right column). These give an idea of the separating  
 3200 power of the different features, and how it changes considerably with the energy. In  
 3201 the number of layers with hits distributions, the peak at 6 is due to the fact that the  
 3202 first six ECal layers sit inside the pressure vessel<sup>8</sup>. Therefore, some of the particles get  
 3203 stopped crossing it, never making it to the seventh layer.

3204 In the case of the MuID, because at low momenta a significant fraction of the particles

---

<sup>8</sup>Note to self: check this. I thought the ECal barrel had 8 layers of tiles, and that all of them were inside the pressure vessel.

## Chapter 6. Particle ID in GArSoft

3205 do not make it past the ECal, I only consider the information coming from this detector  
3206 for momenta  $\geq 0.8 \text{ GeV}/c$ , i.e. for the last three momentum regions. The variables I  
3207 extract from it are the following:

3208 • **Energy-related MuID**

- 3209 – MuID total energy (ClusterMuIDTotalEnergy): sum of the energy of all the  
3210 MuID hits.
- 3211 – Mean MuID hit energy (HitMuIDMeanEnergy): mean of the MuID hit energy  
3212 distribution.
- 3213 – Standard deviation MuID hit energy (HitMuIDStdEnergy): standard deviation  
3214 of the MuID hit energy distribution.
- 3215 – Maximum MuID hit energy (HitMuIDMaxEnergy): maximum of the MuID  
3216 hit energy distribution.

3217 • **Geometry-related MuID**

- 3218 – Maximum distance MuID hit-to-hit (DistHitMuIDMax): maximum distance  
3219 between pairs of MuID hits (not sure this is a good variable, distribution  
3220 looks nuts).
- 3221 – Maximum distance MuID hit-to-centre (DistHitCenterMuIDMax): maximum  
3222 of the distance distribution between the MuID hits and the centre of the  
3223 TPC.

3224 • **Statistical MuID**

- 3225 – Number of hits (NHitsMuID): total number of MuID hits associated to the  
3226 track.
- 3227 – Number of layers with hits (NLayersMuID): not really a count of all layers  
3228 with MuID hits but the difference between the last and the first layer with  
3229 MuIDhits.

### 6.3. Muon and pion separation in the ECal and MuID

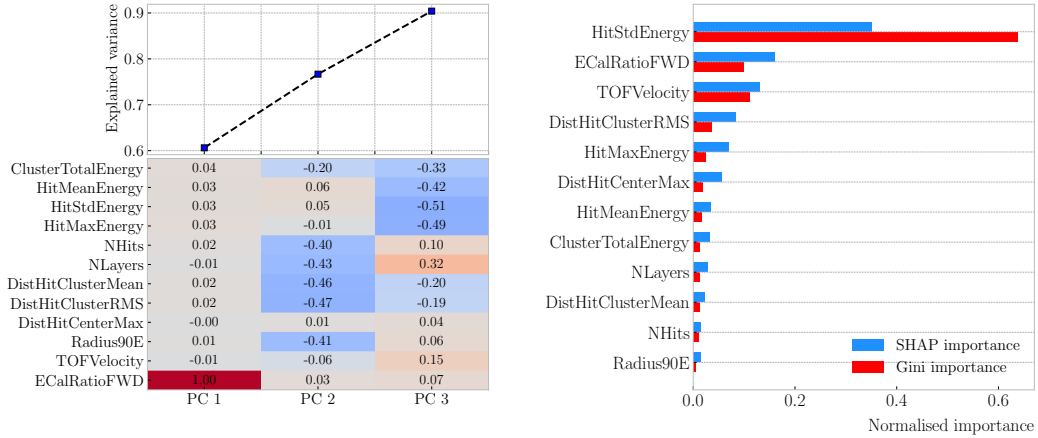


**Figure 6.22:** Left panel: cumulative explained variance for the first three principal components (top panel) and contribution of the different features to the principal axes in feature space (bottom panel). Right panel: Shapley (blue) and Gini (red) feature importances for the different input features. Both figures correspond to the samples in the momentum range  $0.3 \leq p < 0.8$  GeV/c.

3230     Figure 6.21 shows the distributions of three different MuID variables, separating true  
 3231     muons (blue) and charged pions (red), for the three momentum ranges which use the  
 3232     muon tagger information. In this case I decided to standard deviation of the MuID hit  
 3233     energy distribution (left column), the maximum distance between the MuID hit pairs  
 3234     (middle column), and the number of MuID hits (right column). These variables are used  
 3235     together with the ECal features at high momenta, providing additional disambiguation  
 3236     power.

3237     Once our features have been defined, one can do some exploratory analysis to  
 3238     understand how well the variables describe the target class, and avoid the black-box  
 3239     approach by what features are most relevant for the learning process. This way, I  
 3240     performed a feature analysis for each of the momentum ranges I divided this classification  
 3241     problem into. It follows three steps: first a principal component analysis (PCA), followed  
 3242     by a feature importance study using Gini and Shapley values, and finally a feature  
 3243     permutation importance analysis.

3244     The PCA is useful to understand the variance of the feature space. It is an  
 3245     unsupervised machine learning technique that allows the user to perform a dimensionality  
 3246     reduction. It uses a singular value decomposition of the input features to project them

## Chapter 6. Particle ID in GArSoft

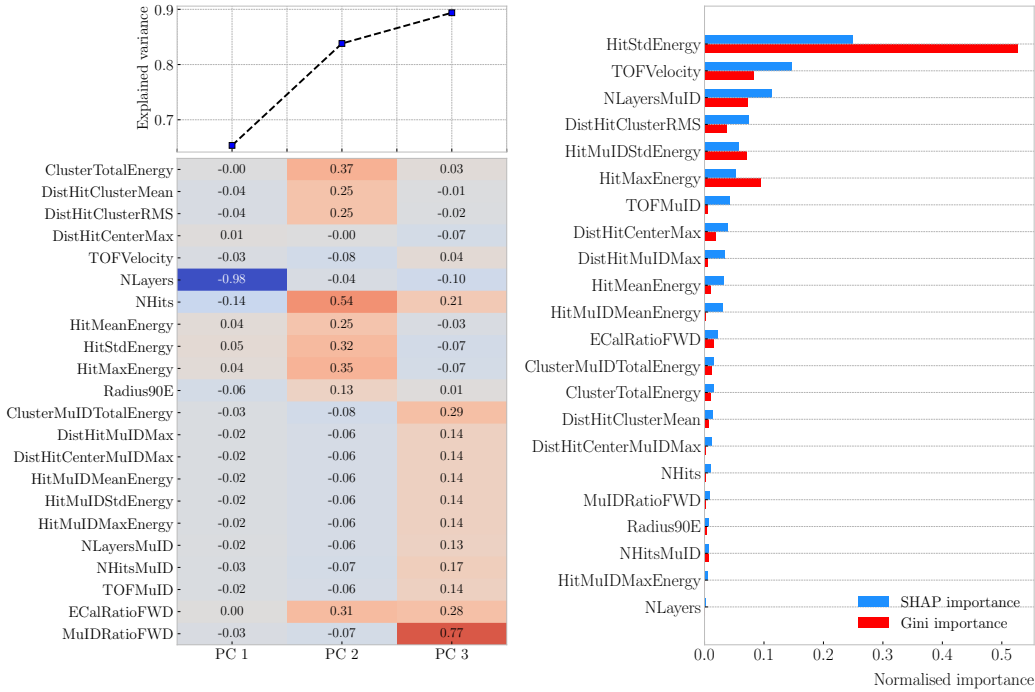


**Figure 6.23:** Left panel: cumulative explained variance for the first three principal components (top panel) and contribution of the different features to the principal axes in feature space (bottom panel). Right panel: Shapley (blue) and Gini (red) feature importances for the different input features. Both figures correspond to the samples in the momentum range  $0.8 \leq p < 1.5$  GeV/c.

3247 into a lower dimensional space. The idea is to find the matrix  $\mathbf{C}_m$ , whose columns are  
 3248 the first  $m$  orthonormal eigenvectors of the input covariance matrix. Consider the  $n \times p$   
 3249 real matrix of input data  $\mathbf{X}$ , where  $n$  is the number of samples and  $p$  the number of  
 3250 features. If  $\mathbf{X}$  is centred, i.e. the means of its columns are equal to zero, we can write the  
 3251 covariance matrix of  $\mathbf{X}$  as  $\mathbf{C} = \mathbf{X}^\top \mathbf{X} / (n - 1)$ . This matrix can be diagonalised, yielding:

$$\mathbf{C} = \mathbf{V} \mathbf{L} \mathbf{V}^\top, \quad (6.11)$$

3252 where  $\mathbf{V}$  is a matrix of eigenvectors and  $\mathbf{L}$  a diagonal matrix with eigenvalues  $\lambda_i$ . Then,  
 3253 performing SVD on  $\mathbf{X}$  gives us:

$$\mathbf{X} = \mathbf{U} \mathbf{S} \mathbf{V}^\top, \quad (6.12)$$

3254 where  $\mathbf{U}$  is a unitary matrix, whose columns are called left singular vectors,  $\mathbf{S}$  is a

### 6.3. Muon and pion separation in the ECal and MuID

3255 diagonal matrix of single values  $s_i$ , and  $\mathbf{W}$  is another unitary matrix, its columns known  
 3256 as right singular vectors. This way, we can write:

$$\mathbf{C} = \mathbf{WSU}^\top \mathbf{USW}^\top / (n - 1) = \mathbf{W} \frac{\mathbf{S}^2}{n - 1} \mathbf{W}^\top. \quad (6.13)$$

3257 meaning that the right singular vectors are also the eigenvectors of the covariance matrix.  
 3258 The SVD can be computed numerically following an iterative approach.  
 3259 This way, taking an input data vector  $X \in \mathbb{R}^n$ , the resulting feature vector  $Y \in \mathbb{R}^m$   
 3260 is given by:

$$Y = \mathbf{C}_m^\top X. \quad (6.14)$$

3261 The new features capture most of the variance of the original sample, while being lower  
 3262 dimensional, as  $m < n$ .

3263 Before applying the PCA reduction one needs to centre and scale the input data.  
 3264 Centring is necessary when using SVD to obtain the eigenvectors of the covariance  
 3265 matrix, as only in that case we can do the identification with the right singular vectors  
 3266 from the input data. Scaling is needed when variables are on different scales, as some  
 3267 can then dominate the PCA procedure.

3268 I used the PCA module of `scikit-learn`, together with the `RobustScaler`, which  
 3269 centres the data and scales it based on the interquartile range. In Fig. 6.22 (left panel)  
 3270 and Fig. 6.23 (left panel) I show the results I obtained from the PCA for the momentum  
 3271 ranges  $0.3 \leq p < 0.8 \text{ GeV}/c$  and  $0.8 \leq p < 1.5 \text{ GeV}/c$ , respectively. Notice that in  
 3272 the second case the number of features increases considerably, as this is the first region  
 3273 which uses the MuID variables. I found that, in all the cases, adding a fourth PC does  
 3274 not add additional information. As it can be seen in the top panels of the figures, the  
 3275 cumulative explained variance is already over 80% with three PCs.

3276 The bottom panels show the contribution of the variables to the principal axes. For  
 3277 the two first momentum regions, I observe a tendency of the energy-related and the  
 3278 geometry-related ECal variables to be clustered together. For the other ranges, when  
 3279 I include the MuID variables, there seems to be a division between ECal and MuID

## Chapter 6. Particle ID in GArSoft

variables. For these, it seems like the number of ECal layers with hits also plays an important role.

The next step in the analysis is to quantify the importance of the features based on two additional metrics, namely the Gini and the Shapley values. The Gini importance, often called mean decrease impurity, is based on how much a feature contributes to the purity improvement at the splits in each decision tree. The purity is measured in terms of the Gini impurity index, defined as:

$$I_G = 1 - \sum_i f_i, \quad (6.15)$$

where  $f_i$  is the fractional abundance of the  $i$ -th class. Then, for each split one can compute the weighted decrease in impurity as:

$$\Delta_G = \frac{N_t}{N} \left( I_G - \frac{N_t^R}{N_t} I_G^R - \frac{N_t^L}{N_t} I_G^L \right), \quad (6.16)$$

where  $N$  represents the total number of samples,  $N_t$  the number of samples at the current node,  $N_t^R$  and  $N_t^L$  the number of samples in the right and left children respectively,  $I_G$  is the Gini impurity at the current node, and  $I_G^R$  and  $I_G^L$  the Gini impurities of the resulting right and left children.

For each decision tree, one will have a normalised vector with the accumulated decrease in Gini impurity for each feature. In the case of a BDT, the feature importances are simply the mean for all the estimators in the ensemble<sup>9</sup>.

The concept of Shapley values originated in the context of game theory, and it measures the marginal contribution of a feature in enhancing the accuracy of a classifier. Take  $F$  to be the set of all features in a problem, and  $S \subseteq F$  the subset of features. To compute the Shapley value of the  $i$ -th feature, one has to train a model with that feature present,  $f_{S \cup \{i\}}$ , and another model trained without it,  $f_S$ . This has to be repeated for all possible combinations of subsets  $S \subset F \setminus \{i\}$ , and evaluating the models predictions

<sup>9</sup>Note to self: this appears not to be the case. If you get the `feature_importance` for each tree in the BDT and take the average, the result is not the same to be one reported in the `feature_importance` attribute of the BDT.

### 6.3. Muon and pion separation in the ECal and MuID

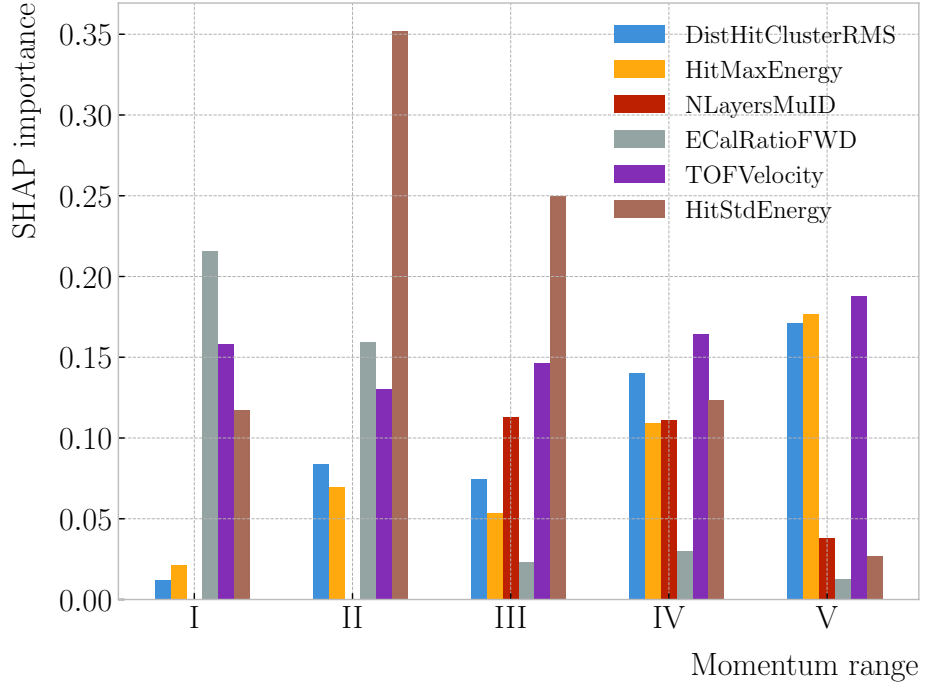


**Figure 6.24:** Evolution of the SHAP importance for the top six most important features across all five momentum ranges.

3302 on the appropriate sets of data  $x_S$ . This way, the Shapley value results:

$$\varphi_i = \sum_{S \subset F \setminus \{i\}} \frac{|S|! (|F| - |S| - 1)!}{|F|!} [f_{S \cup \{i\}}(x_{S \cup \{i\}}) - f_S(x_S)]. \quad (6.17)$$

3303 I trained the `GradientBoostingClassifier` from `scikit-learn` with the default  
 3304 configuration in order to evaluate both the Gini and Shapley importances. The Gini  
 3305 scores are automatically computed by `scikit-learn`, using the training data. For the  
 3306 Shapley importance, I used the implementation from the `SHAP` package, computing  
 3307 it using the test sample. The results can be seen in Fig. 6.22 (right panel) and  
 3308 Fig. 6.23 (right panel), again for the momentum ranges  $0.3 \leq p < 0.8 \text{ GeV}/c$  and  
 3309  $0.8 \leq p < 1.5 \text{ GeV}/c$ . The length of the bars denote either the SHAP (blue) or the Gini  
 3310 (red) importance of the feature. One interesting thing to notice is that, when looking at  
 3311 the Gini importance, there is always one feature that dominates over the rest. This is  
 3312 not the case for the SHAP importance, where importances tend to be more balanced.

## Chapter 6. Particle ID in GArSoft

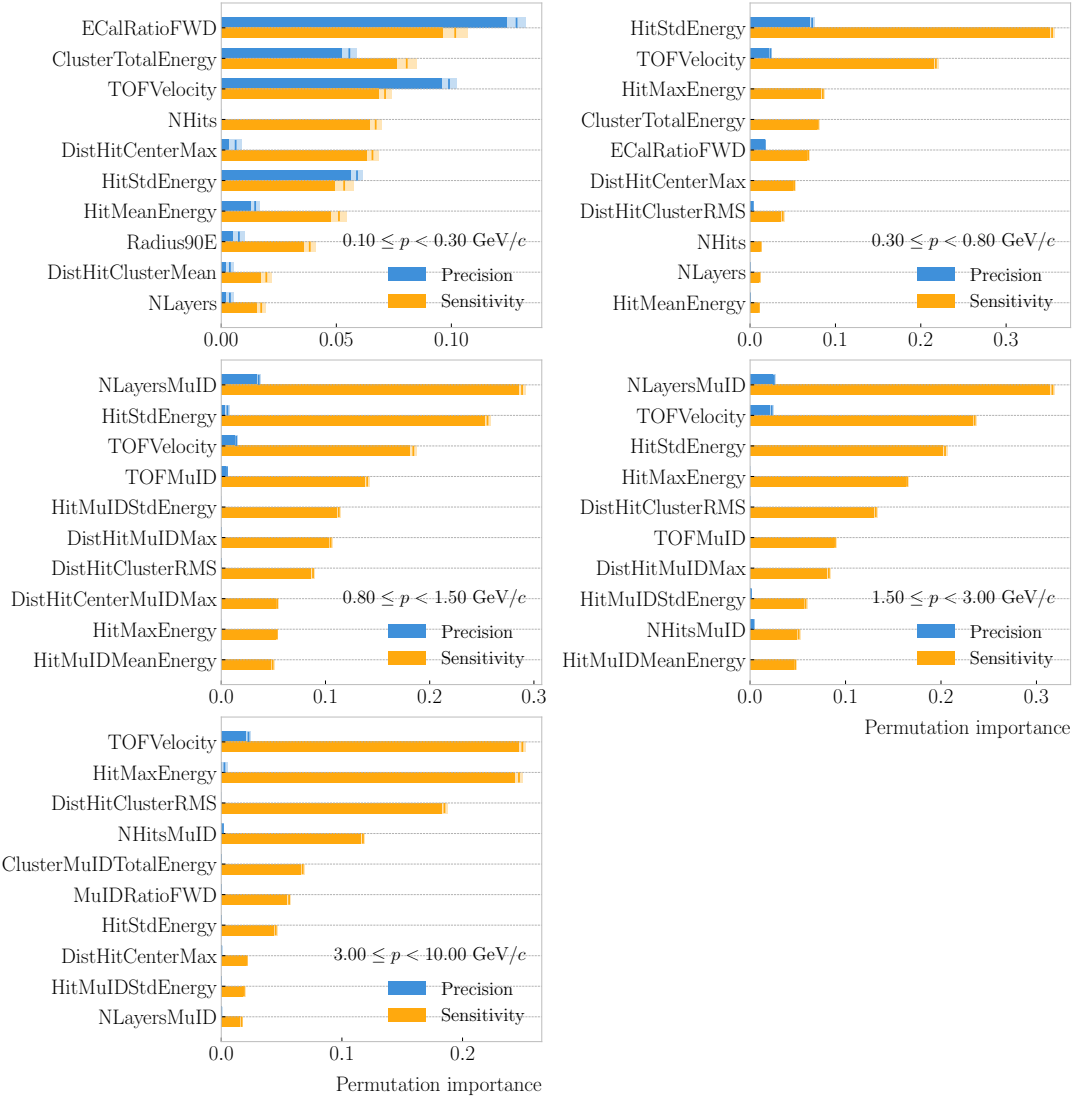


**Figure 6.25:** Permutation importances for the ten most important features in the different momentum ranges (from left to right, top to bottom, in increasing momentum order). The bars indicate the effect that permutations of each feature have on the purity (blue) and the sensitivity (yellow), the translucent regions representing one standard deviation around the central value.

### 6.3. Muon and pion separation in the ECal and MuID

3313 Across all momentum ranges, I observe that the most important features are. For  
3314 the five momentum ranges considered, only six variables sit in the top five at least once.  
3315 Figure 6.24 shows the evolution of the SHAP importance of these six features. It is  
3316 interesting to see that the time-of-flight variable keeps its importance almost unchanged  
3317 for all momenta. Also, it looks like the ECal energy ratio gets less relevant the higher the  
3318 momentum is, but the RMS of the hit-to-cluster distance distribution and the maximum  
3319 ECal hit energy become more important in the last momentum ranges.

3320 The last step in the feature selection analysis is the feature permutation. This  
3321 technique measures the contribution of each feature to the performance of a model by  
3322 randomly shuffling its values and checking how some scores degrade. For the present  
3323 case, I am interested in the precision or purity, and the sensitivity or efficiency, as these  
3324 two are the most relevant metrics from a physics point of view. The `scikit-learn`  
3325 module provides the user with a method to perform the permutation scans.

3326 The results of these are shown in Fig. 6.25. For the different momentum ranges  
3327 I show the permutation importances for the ten most important features. For each  
3328 of the variables I report the effect the permutations have on the precision (blue) and  
3329 sensitivity (yellow) of the models. The bars indicate the importance value, with the  
3330 lighter part representing one standard deviation around the mean (hinted as an additional  
3331 vertical line). Something to notice is that, in the first momentum region, the feature  
3332 permutations have an effect on both the precision and the sensitivity. However, for the  
3333 rest the precision is almost unaffected, while the sensitivity changes are considerably  
3334 larger.

3335 It is also interesting to see that most of the variables identified as important here  
3336 are the same I found when looking at the Shapley values. The behaviour of these across  
3337 the momentum ranges is also similar, with the same patterns of some features being  
3338 important at low momenta and then dropping in importance for the high momentum  
3339 ranges.

3340 Wit this, I conclude the study of the features. I have prepared the training and  
3341 testing datasets and understood what features are likely to have the largest impact on

## Chapter 6. Particle ID in GArSoft

3342 the performance of the classifiers.

### 3343 6.3.4 Hyperparameter optimisation

3344 Any BDT requires the user to specify a number of parameters that will dictate its  
3345 behaviour. They can be divided into two categories: (i) tree-specific parameters, which  
3346 affect each individual tree in the model, and (ii) boosting parameters, which control the  
3347 boosting operation in the model. The value of these so-called hyperparameters affect the  
3348 performance and predictive power of the models. Therefore, one needs to carefully select  
3349 their optimal values in order to extract as much information as possible from the data.

3350 From all the parameters used to define a tree in the `scikit-learn` implementation  
3351 of the BDT classifier, I only consider a subset of them. This is due to the fact that some  
3352 are mutually exclusive, but also because I noticed that others have little effect on the  
3353 problem at hand. Therefore, the parameters I investigate are the following:

3354 • `min_samples_split`: defines the minimum number of samples required in a node  
3355 to be considered for splitting. Higher values prevent a model from learning relations  
3356 which might be highly specific to the particular sample, but may lead to under-fitting  
3357 if the value is too low.

3358 • `min_samples_leaf`: defines the minimum samples required in a leaf node. For  
3359 imbalanced problems it should take a low value, as there will not be many cases  
3360 where the minority class dominates.

3361 • `max_depth`: maximum depth of a tree. Useful to prevent over-fitting, as higher  
3362 depth will allow a model to learn relations specific to the training sample.

3363 In the case of the boosting parameters, the ones I look at are:

3364 • `learning_rate`: determines the impact of each tree on the final outcome. Low  
3365 values make the model robust to the specific characteristics of a tree, and thus  
3366 allow it to generalise well. However, that usually requires a large number of trees  
3367 to model the data properly.

### 6.3. Muon and pion separation in the ECal and MuID

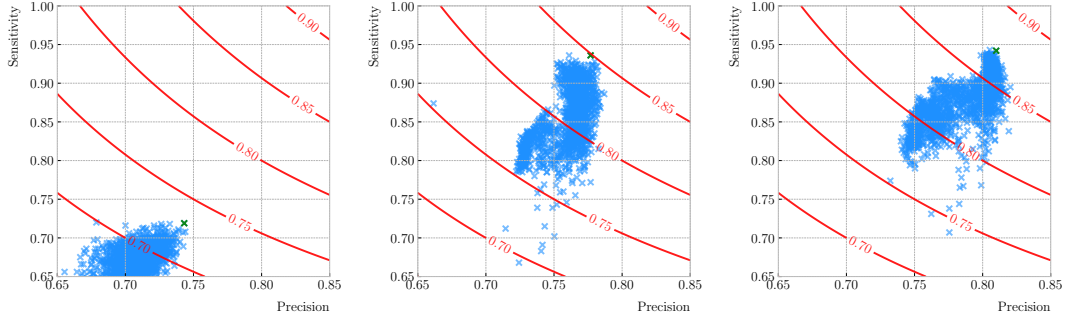


**Figure 6.26:** Values of the precision and sensitivity obtained for 10000 BDT hyperparameter configurations, for the momentum regions I, III and V. The red contours indicate the curves of equal  $F_1$ -score, while the green crosses are the selected configurations.

3368 • `n_estimators`: number of sequential trees to be trained. In general, BDTs are  
3369 fairly robust at higher number of trees but it can still overfit at a point.

3370 • `subsample`: fraction of observations to be selected for each tree. Values slightly  
3371 less than 1 make the model robust by reducing the variance.

3372 In general, hyperparameters depend on each other. Thus, it is not possible to  
3373 optimise them independently. In the literature, we find two main strategies to explore  
3374 the hyperparameter space. We could use a grid search, in which one discretises a  
3375 portion of the space of hyperparameters and evaluates the model at each point. Another  
3376 approach is the randomised search, where a certain number of random configurations of  
3377 hyperparameters are explored.

3378 In this case, I used the random search to scan the hyperparameter space. Also,  
3379 because it is not guaranteed that a set of hyperparameters can be efficiently applied  
3380 across different datasets, I perform the optimisation for each of the momentum ranges  
3381 considered. Table 6.3 shows the list of hyperparameters considered, and the range within  
3382 which I let them vary. I decided to fix the number of estimators to 400 in all cases, as  
3383 its value is correlated with that of the learning rate.

3384 I evaluate 10000 different hyperparameter configurations for each momentum range.  
3385 For the hyperparameter tuning, I used subsamples containing 10% of the full datasets,  
3386 keeping the original proportions between classes, in order to reduce the computational

## Chapter 6. Particle ID in GArSoft

**Table 6.3:** Optimal values of the hyperparameters used by the BDT, for each momentum range.

Hyperparameter	Range	Best value				
		I	II	III	IV	V
<code>min_samples_split</code>	[0.001, 1]	0.10	0.06	0.05	0.27	0.06
<code>min_samples_leaf</code>	[0.001, 1]	0.02	0.03	0.01	0.02	0.07
<code>max_depth</code>	{2, 3, ..., 8}	8	2	4	2	7
<code>learning_rate</code>	[0.05, 1]	0.10	0.23	0.07	0.13	0.09
<code>subsample</code>	[0.01, 1]	0.75	0.65	0.79	0.86	0.95

3387 load. The performance of the models was assessed using a stratified 3-fold cross-validation  
 3388 with replacement. Cross-validation involves dividing the data in a number of subsets,  
 3389 training the model using some of them, and testing it with the rest. In our case, I  
 3390 divide the data in 3 equal-sized subsets, maintaining the class proportions of the original  
 3391 dataset. Then, for 3 consecutive iterations, I train the models using 2 of the subsets  
 3392 while I compute the precision and sensitivity scores with the other. This approach  
 3393 provides a more robust estimate of the performance on unseen data.

3394 Figure 6.26 shows the results in the precision versus sensitivity plane, for the  
 3395 momentum regions I, III and V (from left to right). The contours represent the curves  
 3396 of equal  $F_1$ -score, i.e. the harmonic mean of the precision and the sensitivity. In order  
 3397 to select the optimal configurations (indicated in the plots with a green cross), I chose  
 3398 the point with the highest  $F_1$ -score.

3399 The results for the different momentum ranges are summarised in Tab. 6.3. One  
 3400 can see some consistency in hyperparameter choices, with models generally preferring  
 3401 small values for the tree-specific parameters, small learning rate, and relatively large  
 3402 subsample sizes.

3403 Now that I have obtained the optimal values of the hyperparameters, I can train  
 3404 the different BDTs. In this case I use the complete datasets, keeping 20% of the data  
 3405 for testing. Table 6.4 shows the values of the different performance metrics obtained  
 3406 using the selected hyperparameters and 5-fold cross-validation. The last row indicates

### 6.3. Muon and pion separation in the ECal and MuID

**Table 6.4:** Performance metrics of the BDTs with optimal hyperparameters, for the different momentum ranges.

Metric	Value $\pm 1\sigma$				
	I	II	III	IV	V
Accuracy	$0.779 \pm 0.003$	$0.812 \pm 0.003$	$0.846 \pm 0.002$	$0.861 \pm 0.003$	$0.874 \pm 0.002$
Precision	$0.769 \pm 0.003$	$0.752 \pm 0.005$	$0.788 \pm 0.002$	$0.805 \pm 0.003$	$0.815 \pm 0.003$
Sensitivity	$0.745 \pm 0.009$	$0.921 \pm 0.006$	$0.965 \pm 0.002$	$0.967 \pm 0.002$	$0.976 \pm 0.001$
$F_1$ -score	$0.757 \pm 0.004$	$0.828 \pm 0.003$	$0.867 \pm 0.002$	$0.879 \pm 0.002$	$0.889 \pm 0.002$
ROC AUC	$0.868 \pm 0.003$	$0.865 \pm 0.003$	$0.899 \pm 0.002$	$0.902 \pm 0.002$	$0.911 \pm 0.001$

3407 the value of the area under the receiver operating characteristic (ROC) curve. This  
3408 represents the sensitivity of a model as a function of the false positive rate. I have  
3409 included it here as it is a classic model metric used in the machine learning community.  
3410 Overall, there is a clear trend of models performing better at higher momentum.

#### 3411 6.3.5 Probability calibration

3412 So far, the trained BDTs are able to provide predictions of the class labels. Ideally,  
3413 one would like the output of a classifier to give a confidence level about the prediction.  
3414 However, it is not straightforward to interpret the outputs of our BDTs in terms of  
3415 probabilities.

3416 A way to visualise how well the predictions of a classifier are calibrated is using  
3417 reliability diagrams [138]. They represent the probability of the positive label versus the  
3418 probability predicted by the classifier. These can be obtained by binning the predicted  
3419 probabilities, and then compute the conditional probability  $P(y_{true} = 1 | y_i \leq y_{pred} <$   
3420  $y_{i+1})$  by checking the fraction of true positive instances in each bin. The reliability  
3421 diagram of a perfectly calibrated classifier would be a diagonal line.

3422 In this case, I try to correct the raw response of the classifiers by applying a sigmoid  
3423 function:

$$\sigma(x; A, B) = \frac{1}{1 + e^{Ax+B}}, \quad (6.18)$$

3424 where the parameters  $A$  and  $B$  are real numbers determined using the method of least

## Chapter 6. Particle ID in GArSoft

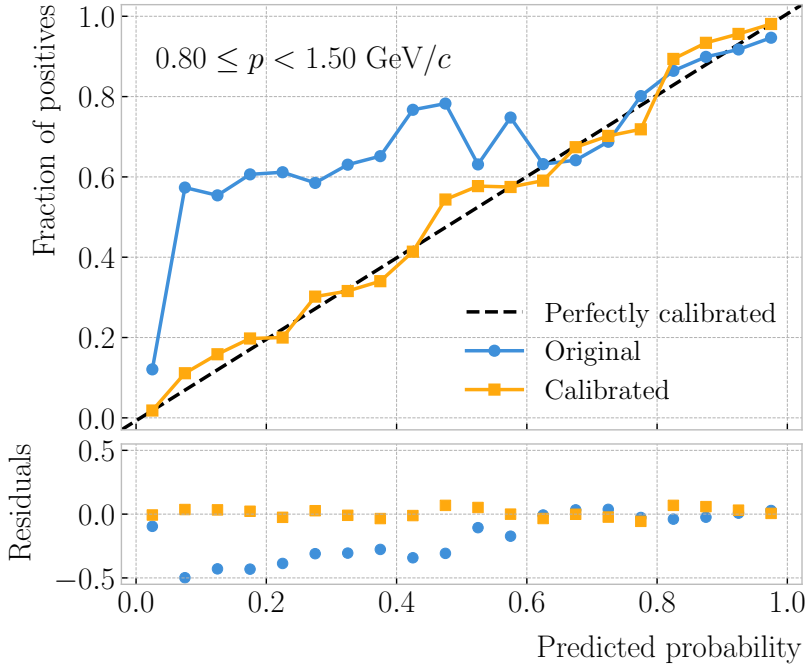


**Figure 6.27:** Reliability diagrams for the BDT classifier used in the momentum range  $0.3 \leq p < 0.8 \text{ GeV}/c$ , both for the original (blue circles) and calibrated (yellow squares) responses. For reference, the response of a perfectly calibrated classifier is also shown (black dashed line).

3425 squares.

3426 For each classifier, I perform a grid search to obtain the optimal values of  $A$  and  $B$ .  
 3427 For any pair, I compute the predicted probabilities as  $y_{pred} = \sigma(y_{raw}; A, B)$ , where  $y_{raw}$   
 3428 are the raw predictions of the classifier<sup>10</sup>. Then, I calculate the corresponding reliability  
 3429 curve, and take the sum of the squared residuals between it and the response of the  
 3430 perfectly calibrated classifier.

3431 Figure 6.27 shows the reliability diagrams for the original (blue) and calibrated  
 3432 (yellow) probability predictions of the classifier for the III momentum range,  $0.3 \leq p <$   
 3433  $0.8 \text{ GeV}/c$ . The original response of the classifier is given by  $y_{pred} = \sigma(y_{raw}; -2, 0)$ ,  
 3434 which is the transformation applied by `scikit-learn` to produce the probability estimate.  
 3435 Notice how the calibrated prediction matches the ideal response much better than the  
 3436 original, across all the probability range.

---

<sup>10</sup>In `scikit-learn` these correspond to the outputs of the `decision_function` method.

## 6.4. ECal time-of-flight

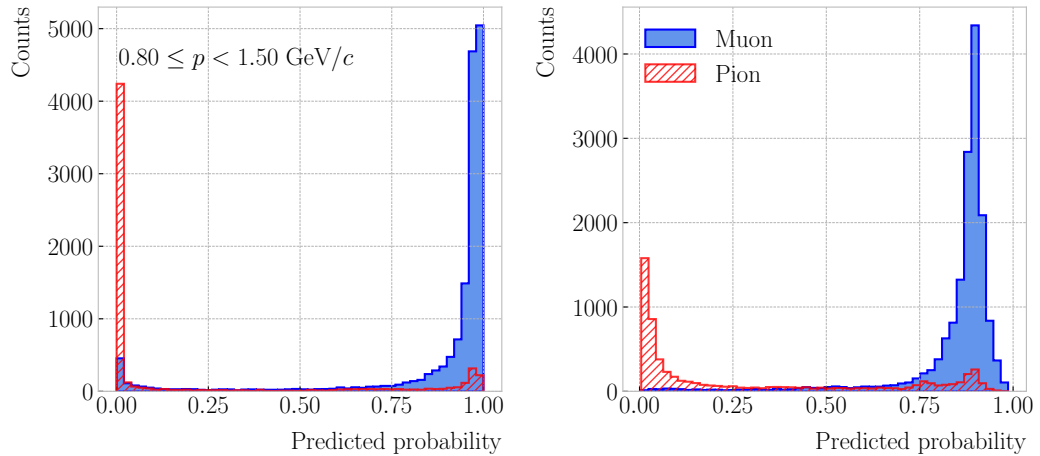


**Figure 6.28:** Uncalibrated (left panel) and calibrated (right panel) predicted probabilities assigned by the BDT classifiers for true muons (blue) and charged pions (red) in the momentum range  $0.3 \leq p < 0.8 \text{ GeV}/c$ .

3437 One can also compare the responses of the uncalibrated and calibrated classifiers  
 3438 broken down by true particle type, as shown in Fig. 6.28. It can be seen that the  
 3439 distributions for both muons (blue) and charged pions (red) smoothen after calibration,  
 3440 but still the separating power of the classifier remains unchanged.

3441 At this point, having the trained classifiers and the probability calibration parameters,  
 3442 I am able to assess the performance of the classification strategy in a physics-relevant  
 3443 case.

### 3444 6.3.6 Performance

## 3445 6.4 ECal time-of-flight

3446 Looking at Fig. 6.19, it is clear that for momentum values in the range  $1.0 - 3.0 \text{ GeV}/c$   
 3447 it is not possible to separate pions and protons using a  $\langle dE/dx \rangle$  measurement in the  
 3448 HPgTPC. However, in the previous section I assumed that protons at those energies  
 3449 could be identified by other means, and therefore were not an issue for the muon and  
 3450 pion discrimination.

3451 Some detectors, like ALICE [139] or the ILD concept [140], complement the PID  
 3452 capabilities of their gaseous trackers with time-of-flight measurements. The use of

## Chapter 6. Particle ID in GArSoft

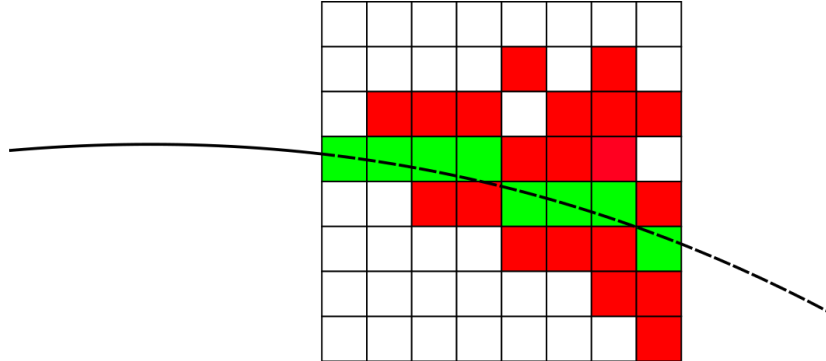


**Figure 6.29:** Schematic of the hit selection used for the ToF measurement. The grid represents the layers of the inner ECal, with coloured squares indicating the tiles with hits. Green squares indicate the selected hits.

3453 fast timing silicon sensors, with hit time resolutions under 100 ps, would allow for the  
 3454 identification of charged hadrons via a ToF measurement up to 5.0 GeV/c. In the case  
 3455 of ND-GAr, one could think of using the inner layers of the ECal, the ones consisting of  
 3456 high-granularity tiles, to obtain a ToF-based PID, with some inputs from the TPC.

3457 Measuring the momentum and the velocity of a charged particle allows for a  
 3458 determination of the mass through the relativistic momentum formula:

$$m = \frac{p}{\beta} \sqrt{1 - \beta^2}. \quad (6.19)$$

3459 In our case, the momentum is measured in the TPC, using the curvature and the dip  
 3460 angle of the helix inside the magnetic field. The velocity of the particle can be written  
 3461 as:

$$\beta = \frac{\ell_{track}}{c\tau}, \quad (6.20)$$

3462 where  $\ell_{track}$  is the length of the track, and  $\tau$  the arrival time to the ECal.

3463 In GArSoft, the track length is computed at the Kalman filter stage. It is simply the  
 3464 sum of the line segments along the track, either in the forward or backward fit. In this  
 3465 case, because we are only interested in the particles that make it to the ECal, I choose  
 3466 the fit direction based on the results of the track-cluster associations.

## 6.4. ECal time-of-flight

3467 Additionally, because the last 30 cm of the TPC radius are uninstrumented<sup>11</sup>, I need  
3468 to correct for the length of the tracks. Using the track fit parameters to propagate the  
3469 helix to its entry point in the ECal, one can write the total track length as:

$$\ell_{track} = \ell + \left| \frac{\phi_{EP} - \phi}{R^{-1}} \right| \sqrt{1 + \tan^2 \lambda}, \quad (6.21)$$

3470 where  $\phi_{EP}$  is the angle of rotation at the entry point to the calorimeter, and  $\ell$ ,  $\phi$ ,  $R$  and  
3471  $\lambda$  are the track length, angle of rotation, radius of curvature and dip angle at the last  
3472 point in the fit, respectively.

3473 To test the idea of performing a ToF measurement with the inner ECal, I generated  
3474 two data samples. Each consists of 10000 single particle events, either charged pions or  
3475 protons. Their momenta are uniformly distributed in the range  $0.5 - 5.0$  GeV/ $c$ , and  
3476 their directions are isotropic. I process each sample using different values of the time  
3477 resolution, from  $\Delta\tau = 0$ , the perfect time resolution case for comparison, to the current  
3478 nominal value of  $\Delta\tau = 0.7$  ns, and the worse scenario of  $\Delta\tau = 1.0$  ns.

### 3479 6.4.1 Arrival time estimations

3480 In the simulation, the limited time resolution of the ECal is taken into account by  
3481 applying a Gaussian smearing to the true hit times. Other effects, like the digitisation  
3482 of the signals, are not taken into account and fall beyond the scope of this study. After  
3483 the track-cluster, one ends up with a collection of ECal hits associated to each particle.  
3484 From these, the arrival time of the particle to the ECal can be extracted.

3485 The simplest possibilities are to either take the time of the earliest hit or the hit  
3486 closest to the entry point. Because these two coincide, in general, I focused only in  
3487 the earliest hit time. However, this needs to be corrected, to account for the distance  
3488 travelled from the entry point to the position of the hit:

$$\tau_{earliest} = \tau_{hit} - \frac{d_{EP-hit}}{c}, \quad (6.22)$$

---

<sup>11</sup>Note to self: check this number.

## Chapter 6. Particle ID in GArSoft

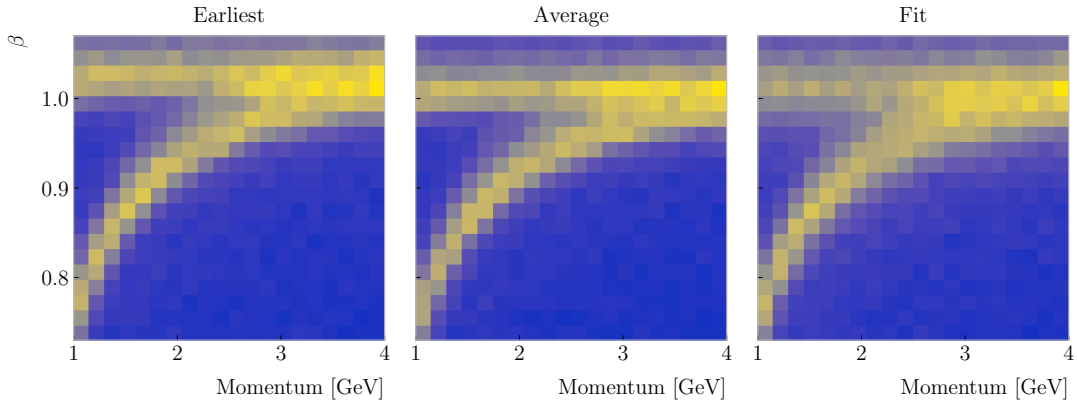


**Figure 6.30:** Particle velocity versus momentum measured with different ECal arrival time estimations. From left to right: earliest hit time, average hit time, and fitted hit time. In all cases the time resolution is  $\Delta\tau = 0.1$  ns.

3489 where  $\tau_{hit}$  is the time of the earliest hit, and  $d_{EP-hit}$  is the distance between that hit  
 3490 and the entry point of the particle to the ECal. This is computed as the arc length  
 3491 between the entry point and the point of the extrapolated helix up to the layer of the  
 3492 hit. This way of correcting the time assumes  $c$  for the propagation of the particle, which  
 3493 may lead to biased estimates.

3494 I also tried to estimate the arrival times using information from the rest of the hits.  
 3495 In order to do this, as a simplifying assumption, I approximate the hadronic shower  
 3496 considering only its MIP component. For each layer, I keep only the hit in the tile closest  
 3497 to the point of the extrapolated track up to that layer. Figure 6.29 shows an example of  
 3498 how this hit selection works. The dashed line represents the extrapolated track, while  
 3499 the coloured squares are the tiles containing hits. Green indicates the tiles closer to the  
 3500 track in each layer (in the sketch they correspond to the grid columns).

3501 Now, I can use these collections of hits to estimate the arrival times. A possibility  
 3502 is to take the average of the times of the selected hits, denoted  $\tau_{average}$ . For that to  
 3503 work, one needs to correct these times, in a similar way as in Eq. (6.22), before taking  
 3504 the average. However, as before, this correction assumes that the particle travels at the  
 3505 speed of light inside the ECal. Another option is to perform a linear fit to the hit times  
 3506 and the distances to the entry point. In that case, the arrival time would be the fitted

## 6.4. ECal time-of-flight

3507 value of the intercept,  $\tau_{fit}$ . This method would not assume a speed of light propagation.

3508 Figure 6.30 shows the velocity estimations as a function of the particle momentum,  
3509 for the earliest hit time (left panel), average hit time (middle panel), and fitted hit time  
3510 (right panel). The two bands correspond to the  $\pi^\pm$  and the  $p$  particles.  $\Delta\tau = 0.1$  ns.  
3511 Notice how, for the earliest hit time method, the velocities are significantly biased  
3512 towards larger values. For the multi-hit methods, the  $\tau_{fit}$  estimate appears to produce a  
3513 larger variance than when using the  $\tau_{average}$  method.

### 3514 6.4.2 Proton and pion separation

3515 Once we have the velocities of the particles, one can estimate their masses through  
3516 Eq. (6.19). The resulting mass spectra are shown in Fig. 6.31. I computed the masses  
3517 for the three arrival time estimates discussed above, and three different values of the  
3518 time resolution:  $\Delta\tau = 0.00$  (perfect time resolution),  $\Delta\tau = 0.10$  ns, and  $\Delta\tau = 0.70$  ns.  
3519 Although in all cases we have the same number of events, it appears as if the entries  
3520 in the histograms decrease as the time resolution increases. Sometimes, the particles  
3521 get unphysical values of  $\beta > 1$ , and in turn they do not contribute to the mass spectra.  
3522 This is more likely to happen for higher values of  $\Delta\tau$ .

3523 As noted before, the average hit time method produces the most robust estimates  
3524 when increasing  $\Delta\tau$ . Intuitively this makes sense, as by taking the mean one averages  
3525 out the effect of the Gaussian smearing. Going forward, I will use this arrival time  
3526 estimator, as it appears to be the best performing one.

3527 It is possible to use the velocity estimations to select a sample of protons. In this  
3528 case, I do so by dividing the relevant momentum range in bins of  $0.1$  GeV/ $c$ . For each  
3529 momentum bin, I compute the expected velocity for the protons via the inverse of Eq.  
3530 (6.19), and then take the fractional residuals of the measured velocities. Using that  
3531 distribution, I choose the cut that maximises the  $F_1$ -score of the proton selection.

3532 The results can be seen in Fig. 6.32, for the case  $\Delta\tau = 0.10$  ns. As expected from  
3533 Fig. 6.30, the performance of the selection degrades rapidly with increasing momentum.  
3534 However, the purity is still around 75% at 3.0 GeV/ $c$ . This is likely to be sufficient, as

## Chapter 6. Particle ID in GArSoft

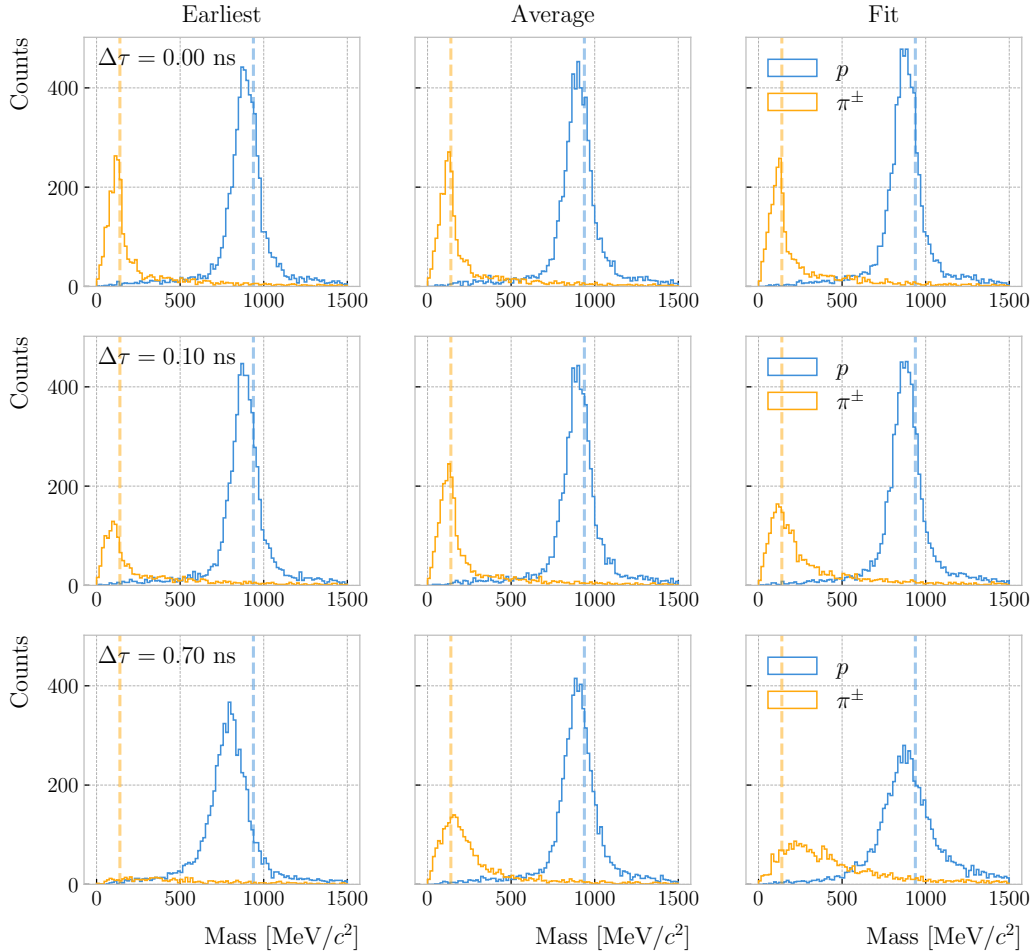


**Figure 6.31:** Mass spectra for  $p$  (blue) and  $\pi^\pm$  (yellow) particles, using different ECal time resolution values (from top to bottom, in ascending order), and arrival time estimates. From left to right: earliest hit time, average hit time, and fitted hit time. The dashed lines indicate the true masses of the particles.

3535 we do not expect protons or charged pions with higher energies from the beam neutrino

3536 interactions.

3537 Figure 6.33

## 3538 6.5 Charged pion decay in flight

3539 As discussed previously, in GArSoft the TPC tracks are formed after a pattern recognition

3540 algorithm and a Kalman filter are applied to the TPC clusters. These two steps can

3541 find discontinuities in the track candidates (e.g. due to a particle decay) when these

## 6.5. Charged pion decay in flight

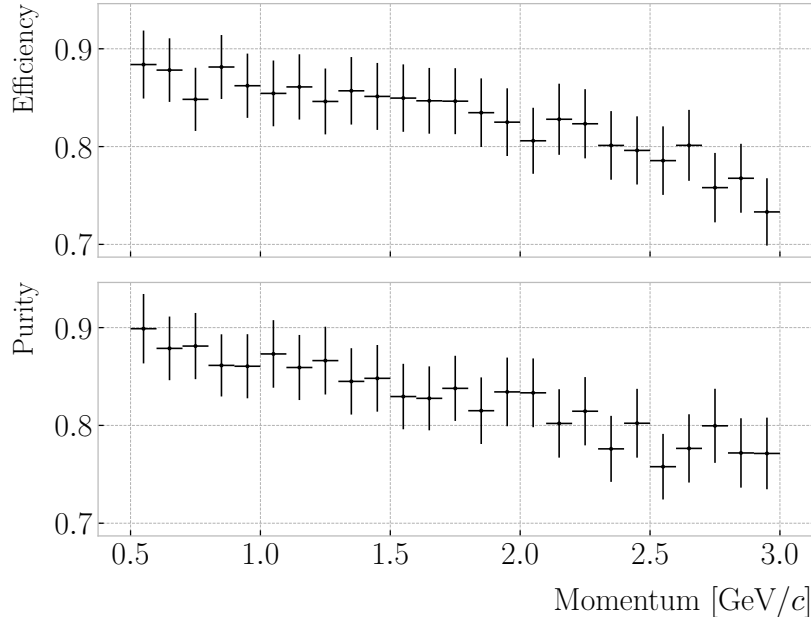


**Figure 6.32:** Efficiency (top panel) and purity (bottom panel) for the proton selection as a function of the momentum, for  $\Delta\tau = 0.10$  ns.

so-called breakpoints are large enough. However, for some, more subtle, cases they may miss them and form a single reconstructed track. It has been noted in the literature that Kalman filters offer, as a by-product, additional information to form test statistics to identify these breakpoints [141, 142].

Considering the mean life of the charged pion,  $\tau = (2.6033 \pm 0.0005) \times 10^{-8}$  s, one can estimate that about 12% of the pions with momentum  $p \sim \mathcal{O}(500 \text{ MeV}/c)$  (roughly the peak of the pion momentum distribution in  $\nu_\mu$  CC interactions off argon) decay inside the TPC. Figure 6.34 (left panel) shows the amount of charged pions decaying in the full TPC and fiducial volumes from an isotropic, monoenergetic sample of 100000 negatively charged pions with  $p = 500 \text{ MeV}/c$ . We see that about 10% of those decayed, with more than half of them decaying inside the TPC fiducial volume.

Figure 6.34 (right panel) shows an example event display of a charged pion (magenta line) decays in flight inside the TPC, but because the angle of the muon (blue line) is small both were reconstructed as one single track (black line). In this case, the composite track reaches the ECal, where it undergoes a muon-like interaction, thus being classified

## Chapter 6. Particle ID in GArSoft

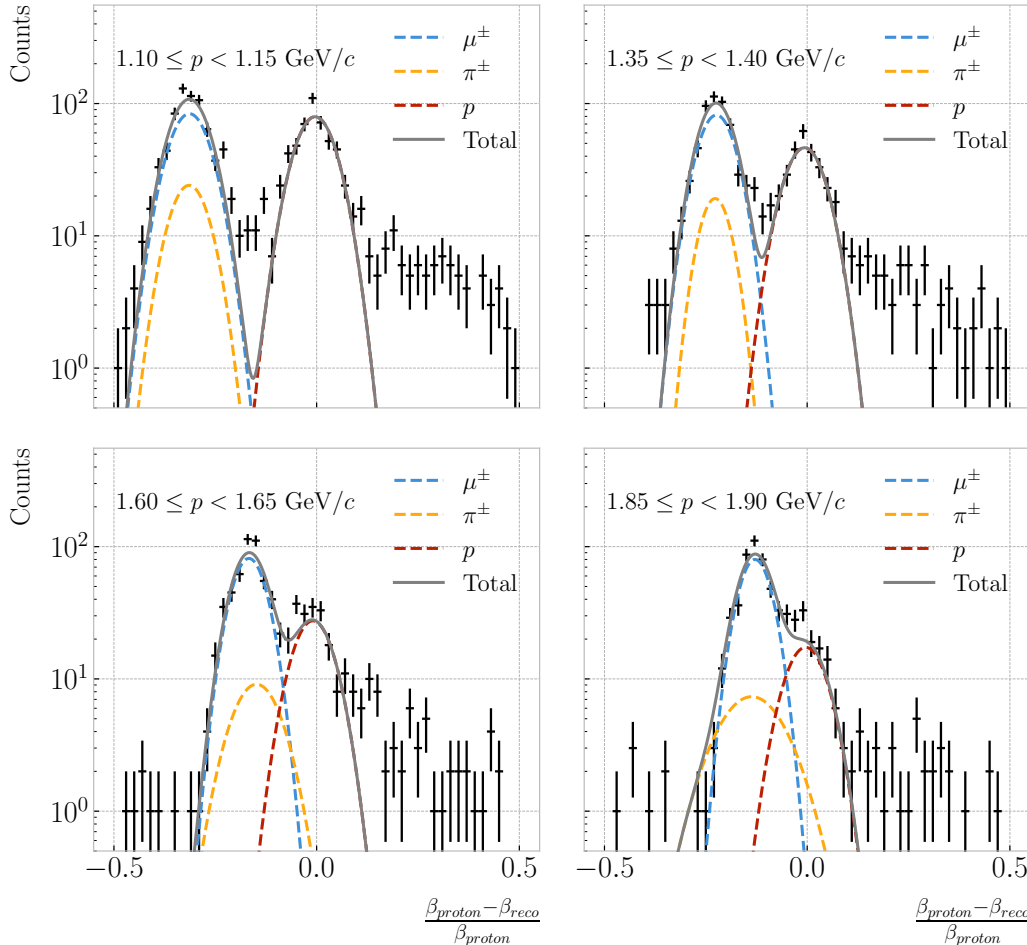


**Figure 6.33:** Distributions of the velocities measured by ToF with the inner ECal, for different momentum bins, in a FHC neutrino interaction sample. The Gaussian fits are performed around the maxima for each particle species.

3557 as a muon.

3558 A way to understand what decaying pion tracks were totally or partially reconstructed  
 3559 together with the daughter muon is looking at the relative energy contributions to the  
 3560 reconstructed track. In order to select a sample of such events, I require that a minimum  
 3561 50% of the total energy comes from the pion and at least 20% from the muon.

### 3562 6.5.1 Track breakpoints

3563 To identify potential decays we can use the information we obtain from the Kalman  
 3564 filter at each step of the fitted track. The simplest test we can think about is computing

## 6.5. Charged pion decay in flight

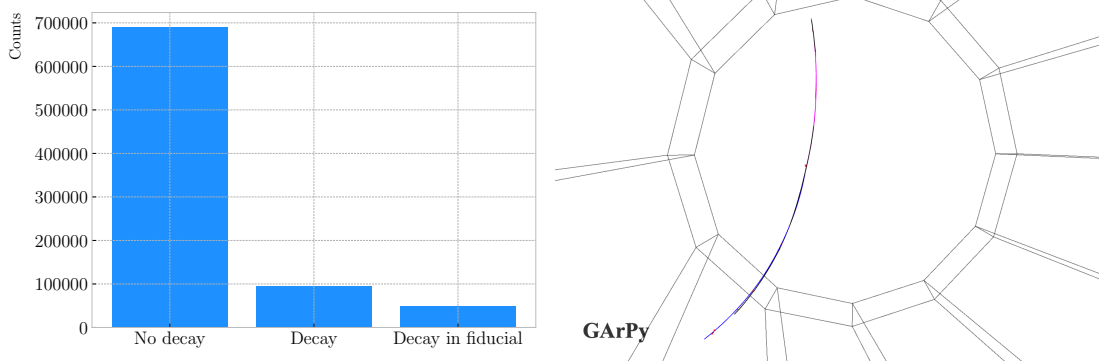


**Figure 6.34:** Left panel: number of non-decaying, decaying and decaying in the fiducial volume pions for a MC sample of 100000,  $p = 500$  MeV/c isotropic positively charged pions inside the TPC. Right panel: event display for a positive pion decaying inside the fiducial volume, with a single reconstructed track for the pion and muon system.

3565 the  $\chi^2$  of the mismatch between all the parameters in the forward and the backward fits:

$$\chi_k^{2(FB)} = (\hat{x}_k^B - \hat{x}_k^F)^T [V^{(\hat{x}_k, B)} + V^{(\hat{x}_k, F)}]^{-1} (\hat{x}_k^B - \hat{x}_k^F), \quad (6.23)$$

3566 where  $\hat{x}_k^F$ ,  $\hat{x}_k^B$  are the Kalman filter state vector estimates at step  $k$  in the forward and  
3567 backward fits and  $V^{(\hat{x}_k, F)}$ ,  $V^{(\hat{x}_k, B)}$  the covariance matrices of  $\hat{x}_k^F$  and  $\hat{x}_k^B$  respectively.

3568 Using the values of the  $\chi^2$  at measurement  $k$  for the forward and backward fits we can  
3569 compute another  $\chi^2$  value that characterises the overall track fit:

$$\chi_{track}^2 = \chi_k^{2(F)} + \chi_k^{2(B)} + \chi_k^{2(FB)}, \quad (6.24)$$

3570 which remains approximately constant for all  $k$ .

3571 An alternative approach proposed in the context of the NOMAD experiment was  
3572 using a fit with a more elaborate breakpoint hypothesis, so we can perform a comparison  
3573 of the  $\chi^2$  with and without breakpoints. This can be achieved by using some alternative  
3574 parametrisation with extra parameters, which allows some of the track parameters to  
3575 be discontinuous at certain points. A decay changes the momentum magnitude and  
3576 direction, so we can use the new state vector:

$$\alpha = (y, z, 1/R_F, 1/R_B, \phi_F, \phi_B, \tan\lambda_F, \tan\lambda_B)^T. \quad (6.25)$$

## Chapter 6. Particle ID in GArSoft

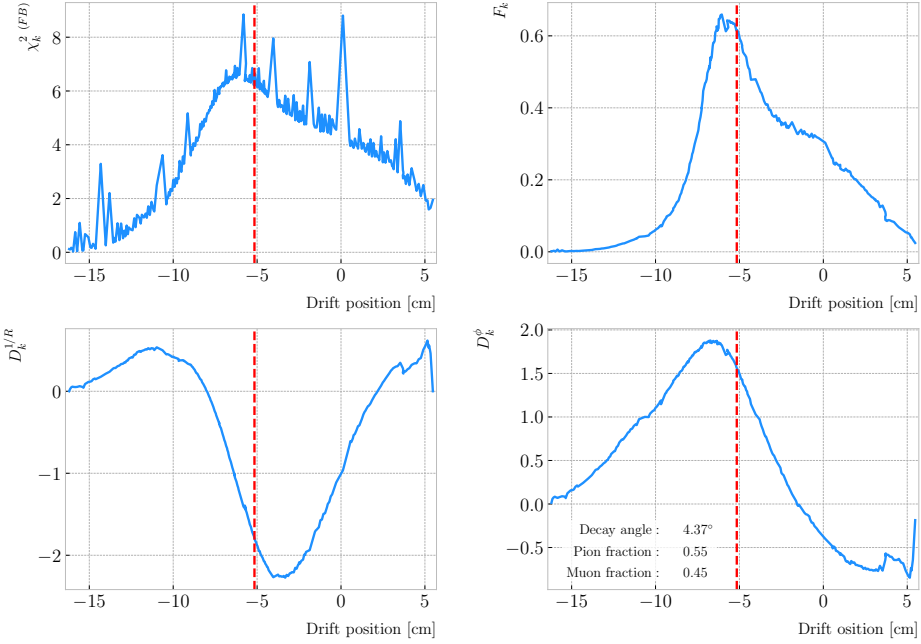


**Figure 6.35:** Values of  $\chi_k^2(FB)$  (top left panel),  $F_k$  (top right panel),  $D_k^{1/R}$  (bottom left panel) and  $D_k^\phi$  (bottom right panel) versus position along the drift direction for a reconstructed track in a positive pion decay event. The vertical red dashed line indicates the true location of the decay point.

3577 As we already have the estimates from the standard Kalman filter and their  
 3578 covariance matrices at each point, we do not need to repeat the Kalman fit for the new  
 3579 parametrisation. Instead, I can compute the values of  $\alpha$  at each point  $k$  that minimise  
 3580 the  $\chi^2$  resulting from comparing them to  $\{\hat{x}_k^B, \hat{x}_k^F\}$ . Introducing the two  $5 \times 8$  matrices:

$$H^F = \begin{pmatrix} 1 & 0 & 0 & 0 & 0 & 0 & 0 & 0 \\ 0 & 1 & 0 & 0 & 0 & 0 & 0 & 0 \\ 0 & 0 & 1 & 0 & 0 & 0 & 0 & 0 \\ 0 & 0 & 0 & 0 & 1 & 0 & 0 & 0 \\ 0 & 0 & 0 & 0 & 0 & 0 & 1 & 0 \end{pmatrix}, \quad H^B = \begin{pmatrix} 1 & 0 & 0 & 0 & 0 & 0 & 0 & 0 \\ 0 & 1 & 0 & 0 & 0 & 0 & 0 & 0 \\ 0 & 0 & 0 & 1 & 0 & 0 & 0 & 0 \\ 0 & 0 & 0 & 0 & 0 & 1 & 0 & 0 \\ 0 & 0 & 0 & 0 & 0 & 0 & 0 & 1 \end{pmatrix}, \quad (6.26)$$

3581 we can write this as:

$$\begin{aligned} \chi_k^2(FB)(\alpha) &= (\hat{x}_k^F - H^F \alpha)^T \left[ V^{(\hat{x}_k, F)} \right]^{-1} (\hat{x}_k^F - H^F \alpha) \\ &\quad + (\hat{x}_k^B - H^B \alpha)^T \left[ V^{(\hat{x}_k, B)} \right]^{-1} (\hat{x}_k^B - H^B \alpha). \end{aligned} \quad (6.27)$$

3582 The minimum of  $\chi_k^2(FB)(\alpha)$  is found when the measured new state vector takes the

## 6.5. Charged pion decay in flight

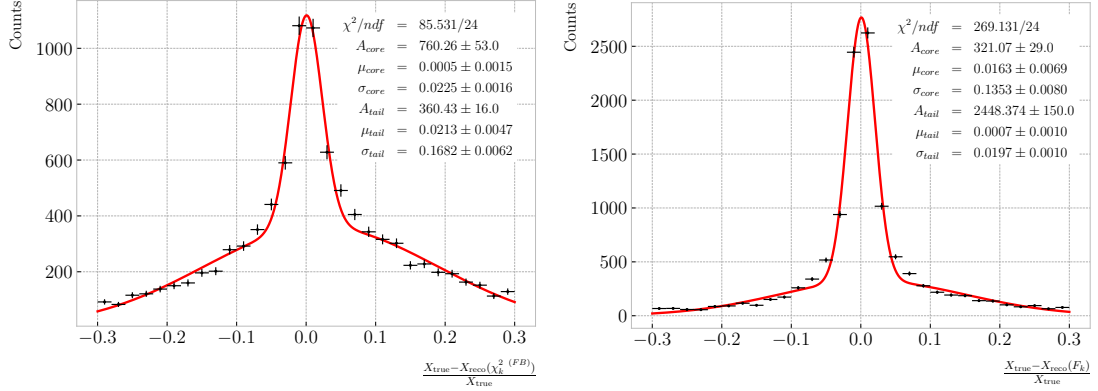


**Figure 6.36:** Fractional residual distributions of the true and reconstructed decay position along the drift coordinate, using the position of the maximum of  $\chi_k^2(FB)$  (left panel) and  $F_k$  (right panel) as estimates of the decay position. Also shown are double Gaussian fits to these points (red lines).

3583 value:

$$\hat{\alpha}_k = V^{(\hat{\alpha}_k)} H^T (V^{(\hat{x}_k)})^{-1} \hat{X}, \quad (6.28)$$

3584 where  $\hat{X} = \{\hat{x}_k^B, \hat{x}_k^F\}$ ,  $V^{(\hat{x}_k)}$  is the block diagonal matrix formed by  $V^{(\hat{x}_k, F)}$  and  $V^{(\hat{x}_k, B)}$   
3585 and  $V^{(\hat{\alpha}_k)}$  is the covariance matrix of  $\hat{\alpha}_k$ , given by:

$$V^{(\hat{\alpha}_k)} = \left( H^T (V^{(\hat{x}_k)})^{-1} H \right)^{-1}. \quad (6.29)$$

3586 From these new fit estimates we can compute the  $F$  statistic, which tells us whether  
3587 the model with breakpoint provides a statistically significant better fit:

$$F_k = \left( \frac{\chi_{track,k}^2 - \chi_{full,k}^2}{8 - 5} \right) / \left( \frac{\chi_{full,k}^2}{N - 8} \right). \quad (6.30)$$

3588 One can also compute the signed difference of the duplicated variables divided by  
3589 their standard deviation at each point. These represent how significant the discontinuity  
3590 in each variable is. For any variable  $\eta$  we can write it as:

$$D_k^\eta = \frac{\hat{\eta}_k^B - \hat{\eta}_k^F}{\sqrt{\text{Var}[\hat{\eta}_k^F] + \text{Var}[\hat{\eta}_k^B] - 2\text{Cov}[\hat{\eta}_k^F, \hat{\eta}_k^B]}}. \quad (6.31)$$

## Chapter 6. Particle ID in GArSoft

3591 In our case, the relevant ones to look at are  $D_k^{1/R}$  and  $D_k^\phi$ .

3592 Figure 6.35 shows the values of  $\chi_k^2(FB)$ ,  $F_k$ ,  $D_k^{1/R}$  and  $D_k^\phi$  as functions of the position  
 3593 along the drift direction, for an example reconstructed track with 55.5% of the energy  
 3594 coming from the charged pion and 45.5% from the daughter muon. The true position of  
 3595 the decay is indicated (dashed red lines). Notice how  $\chi_k^2(FB)$  and  $F_k$ ,  $D_k^{1/R}$  reach their  
 3596 maxima near the decay point. In the former case this indicates a large forward-backward  
 3597 difference in the track fit. In the later it represents that the extended state vector  
 3598 improves the fit particularly around that point.

3599 I can estimate the decay position finding resolution by computing the difference  
 3600 between the  $X$  position of the maxima of  $\chi_k^2(FB)$  and  $F_k$  and the  $X$  position of the  
 3601 true decay. Figure 6.36 represent the the fractional residual distributions for both  
 3602 cases, from the sample of tracks containing pion decays. Fitting a double Gaussian to  
 3603 the distributions (red lines) I find a resolution of  $(3.31 \pm 0.15)\%$  and  $(6.94 \pm 0.31)\%$   
 3604 respectively.

3605 In principle, the  $F$ -statistic should follow a Fisher distribution with  $(8 - 5)$  and  
 3606  $(N - 8)$  degrees of freedom under the null hypothesis. In most of our cases  $N \sim \mathcal{O}(100)$ ,  
 3607 so the probability density functions will look very similar. In this case, it is safe to take  
 3608 the limit  $N \rightarrow \infty$  in the Fisher PDF:

$$\begin{aligned}\tilde{f}(x; a - b) &= \lim_{N \rightarrow \infty} f(x; a - b, N - a) \\ &= \frac{2^{-\frac{a-b}{2}}}{\Gamma(\frac{a-b}{2})} (a - b)^{\frac{a-b}{2}} x^{\frac{a-b}{2}-1} e^{-\frac{a-b}{2}x}.\end{aligned}\tag{6.32}$$

3609 In our case  $a - b = 8 - 5 = 3$ , so we would obtain a p-value of 0.05 at  $x = 2.60$ .

3610 Figure 6.37 contains the distributions of the maxima of  $\chi_k^2(FB)$ ,  $F_k$  and  $D_k^\phi$  and the  
 3611 minima of  $D_k^{1/R}$  for a sample of non-decaying pion tracks (blue) and another sample of  
 3612 reconstructed tracks containing part of the pion and the daughter muon from a decay  
 3613 inside the fiducial volume (red). Notice that, even though the values of  $F_k^{(max)}$  for the  
 3614 decay sample are typically larger than for the non-decaying one, just a small fraction of  
 3615 the events go beyond the aforementioned value of  $F = 2.60$ . Therefore, from a practical

## 6.5. Charged pion decay in flight

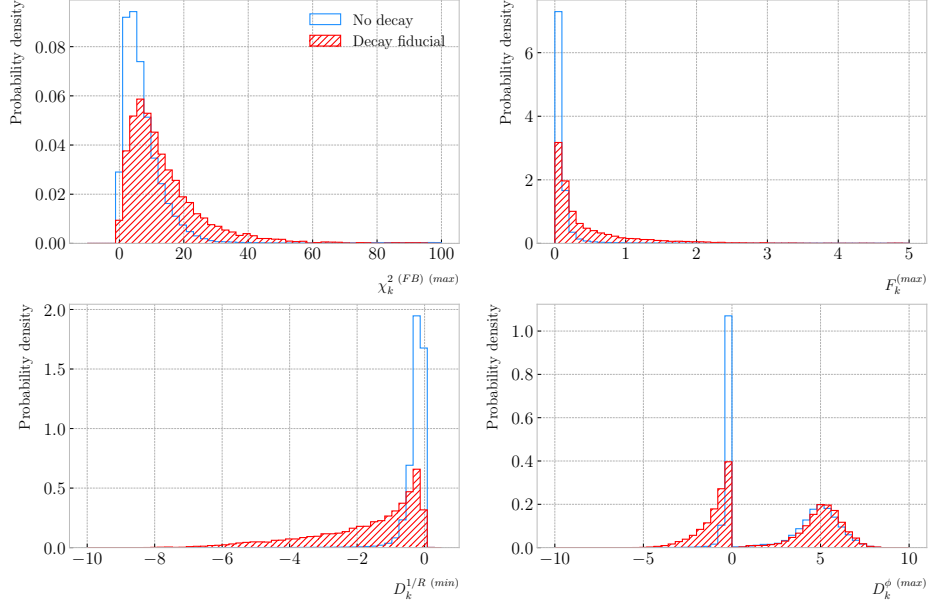


**Figure 6.37:** Distributions of the extreme values of  $\chi_k^2(FB)$  (top left panel),  $F_k$  (top right panel),  $D_k^{1/R}$  (bottom left panel) and  $D_k^\phi$  (bottom right panel) for non-decaying reconstructed pion tracks (blue) and tracks which include the decay inside the fiducial volume (red).

3616 point of view, it is not the most efficient variable to use for selecting the decay events.

3617 However, looking at the  $D_k^{1/R}(\min)$  distribution we can see there is a big difference  
 3618 between non-decaying and decaying events in this variable. One can use a combination  
 3619 of these four variables to distinguish between the pion decay events (signal) and the  
 3620 non-decaying pions (background).

3621 An approach to this classification could be using a boosted decision tree (BDT). One  
 3622 of the advantages of BDTs is that they are easy to interpret and identify the relative  
 3623 importance of the different input variables. Training a BDT with 400 estimators and a  
 3624 maximum depth of 4 I can obtain an efficient classification without overtraining. Figure  
 3625 6.38 (left panel) shows the distribution of probabilities predicted by the BDT for a test  
 3626 sample. The signal efficiency as a function of background acceptance, the so-called ROC  
 3627 curve, is shown in Fig. 6.38 (right panel). With a relative importance of 0.83, the most  
 3628 important variable turned out to be  $D_k^{1/R}(\min)$ .

3629 One thing we can check is how the resolution to the decay and the signal efficiency in

## Chapter 6. Particle ID in GArSoft

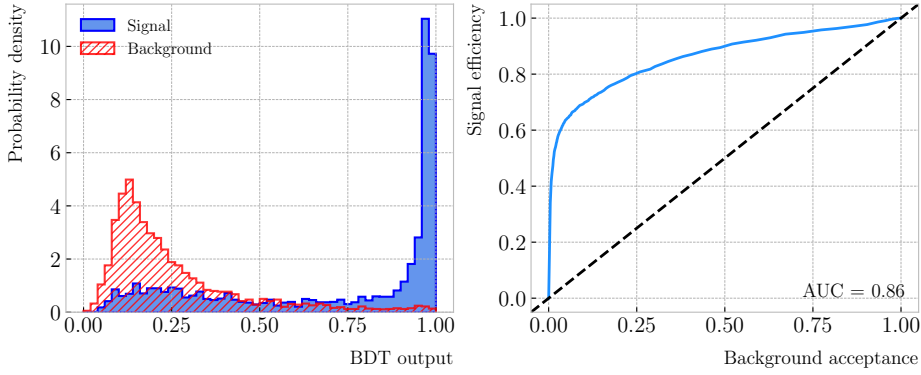


**Figure 6.38:** Left panel: distributions of the predicted probabilities assigned by the BDT classifier to a test sample of decaying pion+muon tracks (blue) and non-decaying pion tracks (red). Left: signal efficiency versus background acceptance (ROC curve) obtained from the BDT for the test sample.

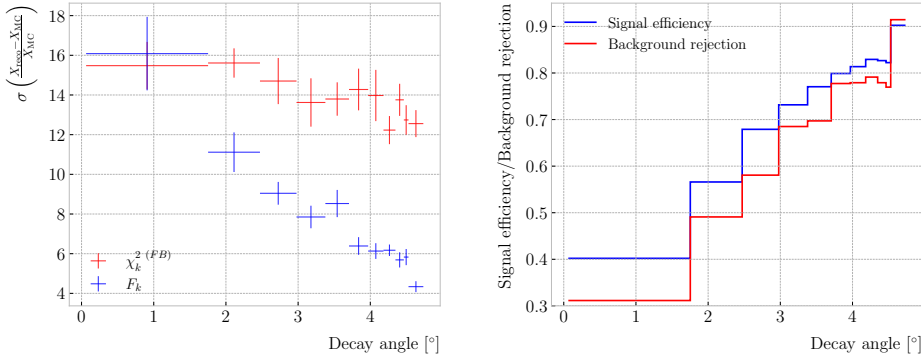


**Figure 6.39:** Left panel: dependence of the decay position finding resolution on the true value of the decay angle for the  $\chi_k^2(FB)$  (red) and  $F_k$  (blue) methods. Right panel: signal efficiency (blue line) and background rejection (red line) from the BDT classifier versus true decay angle.

3630 the classification changes with the true decay angle. Using an equal-frequency binning  
3631 for the decay angles, we can repeat the previous steps for each bin.

3632 Figure 6.39 (left panel) shows the dependence on the decay angle of the decay finding  
3633 resolution. We can see that for the  $\chi_k^2(FB)$  maximum location method the resolution  
3634 consistently lies between 12 to 16%. However, the  $F_k^{(max)}$  approach gives a significantly  
3635 better resolution for high angle values, reaching the 4 – 6% range for decay angles  $\geq 4^\circ$ .

3636 For the classification dependence on the angle, I use the same classifier I trained  
3637 before but evaluating the test sample for each individual angular bin. I compute the  
3638 signal efficiency in each bin for a fixed value of the background rejection, in this case

## 6.6. Neutral particle identification

3639 90%. Similarly, for the background rejection estimation I use a fixed signal efficiency  
3640 value of 90%. Figure 6.39 (right panel) represents the change in signal efficiency (blue)  
3641 and background rejection (red) with the value of the true decay angles.

## 3642 6.6 Neutral particle identification

### 3643 6.6.1 ECal clustering

3644 Another important reconstruction item is the clustering algorithm of ECal hits in  
3645 GArSoft. The default module features a NN algorithm that treats all hits in the same  
3646 way, independently of the layer each hit comes from. However, the current ECal design  
3647 of ND-GAr has two very different types of scintillator layers. The inner layers are made  
3648 out of tiles, which provide excellent angular and timing resolutions. On the other hand,  
3649 the outer layers are cross scintillator strips. That way, an algorithm that treats hits  
3650 from both kinds of layers differently may be able to improve the current performance.

3651 Inspired by the reconstruction of T2K’s ND280 downstream ECal [143], the idea  
3652 was to put together a clustering module that first builds clusters for the different ECal  
3653 views (tiles, strips segmented in the  $X$  direction and strips segmented in  $Y$  direction),  
3654 and then tries to match them together to form the final clusters.

3655 Working on a module-by-module basis, the algorithm first separates the hits depending  
3656 on the layer type they come from. Then, it performs a NN clustering for the 3 sets of  
3657 hits separately. For the tile hits it clusters together all the hits which are in nearest-  
3658 neighbouring tiles and nearest-neighbouring layers, for strip hits it looks at nearest-  
3659 neighbouring strips and next-to-nearest-neighbouring layers (as the layers with strips  
3660 along the two directions are alternated). For strip clusters an additional cut in the  
3661 direction along the strip length is needed.

3662 After this first clustering I then apply a recursive re-clustering for each collection  
3663 of strip clusters based on a PCA method. In each case, we loop over the clusters with  
3664  $N_{hits} \geq 2$ , computing the centre of mass and three principal components. Propagating  
3665 these axes up to the layers of the rest of the clusters, we check if the propagated point

## Chapter 6. Particle ID in GArSoft

3666 and the centre of mass of the second cluster are within next-to-nearest-neighbouring  
3667 strips. An additional cut in the direction along the strip length is also needed. Moreover,  
3668 I require that the two closest hits across the two clusters are at most in next-to-nearest-  
3669 neighbouring strips. I merge the clusters if these three conditions are satisfied. The  
3670 re-clustering is repeated until no more cluster pairs pass the cuts.

3671 The clusters in each strip view are combined if their centres of mass are close enough  
3672 and they point in the same direction. An alternative approach for the strip cluster  
3673 merging could be to compute the overlap between the ellipsoids defined by the principal  
3674 axes of the clusters, and then merge the pair if the overlap exceeds some threshold.  
3675 Further study is needed to understand if this change would have an impact in the overall  
3676 clustering performance.

3677 To merge the tile clusters to the combined strip clusters I propagate the principal  
3678 axis of the strip cluster towards the inner layers, up to the centre of mass layer of the  
3679 tile cluster. I merge the clusters if the distance between the propagated point and the  
3680 centre of mass is below a certain cut.

3681 The last step is to check if clusters in neighbouring modules should be merged  
3682 together, both across two barrel modules, across end cap modules and between barrel  
3683 end cap modules. I check the distance between the two closest hits in the pair of clusters  
3684 and merge them if it passes this and an additional direction cut.

3685 Figure ?? presents an example of the clustering steps relevant for strip layer hits, from  
3686 the input hits (top left panel) to the NN clustering (top right panel) and re-clustering  
3687 (bottom left panel) for each strip view and the final merging strip clusters (bottom  
3688 right panel). It shows the hits from a single ECal barrel module in a  $\nu_\mu$  CC interaction  
3689 event with a neutral pion and a proton in the final state. The two clusters on the left  
3690 correspond to the photon pair from the  $\pi^0$  decay and the one on the upper right corner  
3691 is associated to the proton.

3692 This algorithm has a total number of eight free parameters that need to be optimised.  
3693 I used a sample of 1000  $\nu_\mu$  CC interactions in order to obtain the optimal configuration of  
3694 clustering parameters. This sample was generated up to the default ECal hit clustering

## 6.6. Neutral particle identification

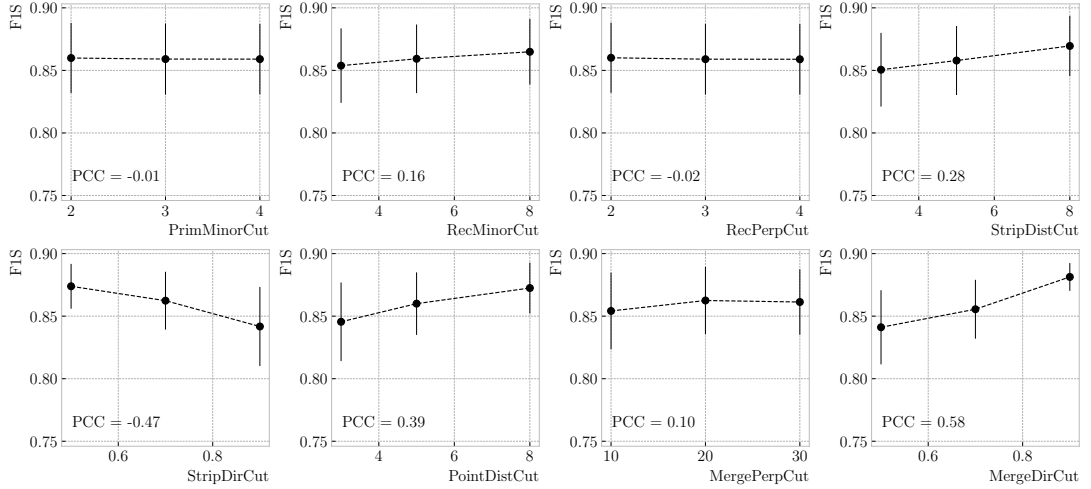


**Figure 6.40:** Mean values of the  $F_1$ -score marginal distributions for the different free parameters of the new clustering algorithm, with the error bars representing one standard deviation around the mean. The  $F_1$ -score values were computed for the 6561 possible parameter configurations using 1000  $\nu_\mu$  CC interaction events.

**Table 6.5:** Summary of parameters and sampled values used in the optimisation of the clustering algorithm.

Name	Units	Sampled values	Description
PrimMinorCut	strips	2, 3, 4	Distance along strip length in NN clustering
RecMinorCut	strips	3, 5, 8	Distance between propagated point and CM along strip length in re-clustering
RecPerpCut	strips	2, 3, 4	Closest hit pair distance in re-clustering
StripDistCut	strips	3, 5, 8	Distance between CMs in strip cluster merging
StripDirCut	cos	0.5, 0.7, 0.9	Main axes direction cut in strip cluster merging
PointDistCut	tiles	3, 5, 8	Distance between propagated point and CM in strip-tile matching
MergePerpCut	cm	10, 20, 30	Closest hit pair distance in module merging
MergeDirCut	cos	0.5, 0.7, 0.9	Main axes direction cut in module merging

3695 level, so then I could run the new clustering algorithm each time with a different  
 3696 configuration of parameters. As the number of parameters is relatively large, I only  
 3697 performed a coarse-grained scan of the parameter space. Sampling each of the eight  
 3698 parameters at three different points each I obtain 6561 different configurations. These  
 3699 parameters, together with the used values, are summarised in Tab. 6.5.

3700 In order to measure the performance of the clustering, I use a binary classification  
 3701 approach. For each formed cluster, I identify the Geant4 Track ID of the matching MC

## Chapter 6. Particle ID in GArSoft

3702 particle and the energy fraction of each hit. Then, I assign to each cluster the Track ID  
3703 with the highest total energy fraction. For each of the different Track IDs associated to  
3704 the clusters, I select the cluster with the highest energy (only from the hits with the  
3705 same Track ID). I identify such a cluster as the main cluster for that Track ID. I count  
3706 as true positives (TPs) the hits with the correct Track ID in each main cluster. False  
3707 positives (FPs) are the hits with the incorrect Track ID for the cluster they are in, not  
3708 only main clusters. The false negatives (FNs) are the hits with the correct Track ID in  
3709 clusters other than the main.

3710 Figure 6.40 shows the computed  $F_1$ -score values for the different cuts. In each case,  
3711 the central value represents the mean of the  $F_1$ -score distribution for the specified value  
3712 of the corresponding variable and the vertical error bar represents one standard deviation  
3713 around the mean. Also shown are the Pearson correlation coefficients of these central  
3714 values. We can see that five of the variables have a sizeable effect on the  $F_1$ -score, with  
3715 an absolute difference between the last and first values as big as 4%.

3716 The working configuration is obtained as follows. I first select all configurations  
3717 with purity  $\geq 90\%$ . Among those, I choose the combinations that yield the maximum  
3718  $F_1$ -score. If more than one configuration remains I select the one with the highest  
3719 sensitivity. Doing so, I end up with a parameter configuration with an efficiency of 88%  
3720 and a 90% purity. Compared with the default algorithm, which gives an efficiency of  
3721 76% and a purity of 91% for the same sample, I have managed to improve the efficiency  
3722 by a factor of 1.16.

### 3723 6.6.2 $\pi^0$ reconstruction

3724 One of the potential applications of the new ECal hit clustering is the reconstruction of  
3725 neutral particles, in particular pions. Neutral pions decay promptly after being produced,  
3726 through the  $\pi^0 \rightarrow \gamma\gamma$  channel ( $98.823 \pm 0.034\%$ ) of the time. The photon pair does  
3727 not leave any traces in the HPgTPC (unless one or both of them converts into an  
3728 electron-positron pair), but each of them will produce an electromagnetic shower in  
3729 the ECal.

## 6.6. Neutral particle identification

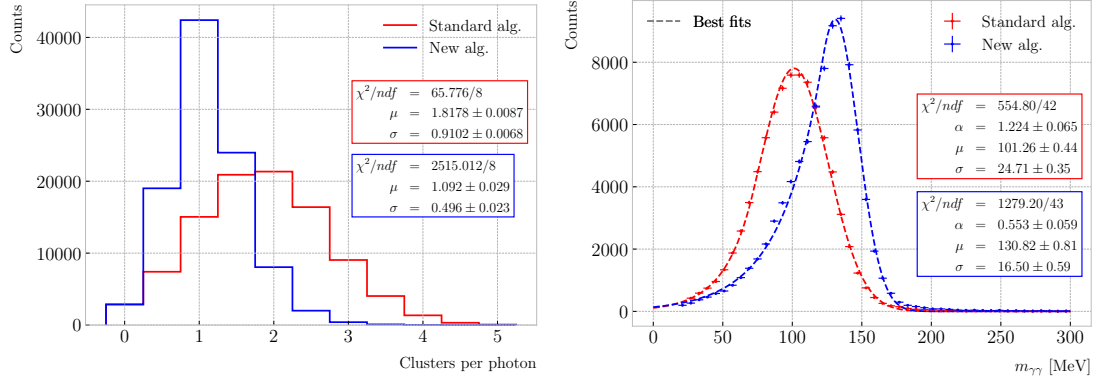


**Figure 6.41:** Left panel: distributions of the number of ECal clusters per photon from  $\pi^0$  decays for the standard (red) and new (blue) clustering algorithms. Right panel: reconstructed invariant mass distributions for photon pairs from single  $\pi^0$  events using the standard (red) and new (blue) ECal clustering algorithms.

3730 To test the potential impact of the new algorithm in  $\pi^0$  reconstruction, I generated  
 3731 a MC sample of single, isotropic neutral pions inside the HPgTPC. All pions were  
 3732 generated with a momentum  $p = 500$  MeV and their initial positions were uniformly  
 3733 sampled inside a  $2 \times 2 \times 2$  m box aligned with the centre of the TPC. I ran both the  
 3734 default and the new clustering algorithms, using for the latter the optimised configuration  
 3735 discussed above.

3736 The first thing to notice is that the number of clusters produced per photon has  
 3737 decreased. Figure 6.41 (left panel) shows these distributions for the default (red) and  
 3738 new (blue) algorithms. Using a simple Gaussian fit, we see that the mean number of  
 3739 ECal clusters per photon went from  $1.82 \pm 0.01$  to  $1.09 \pm 0.03$ . This effectively means that  
 3740 with the new algorithm the ECal activity of one true particle is typically reconstructed  
 3741 as a single object. From the reconstruction point of view this can be an advantage. As  
 3742 now most of the photon energy ends up in a single ECal cluster, I can simply use cluster  
 3743 pairs to identify the  $\pi^0$  decay.

3744 In general, one calculates the invariant mass of the photon pair as:

$$m_{\gamma\gamma} = \sqrt{2E_1E_2(1 - \cos \theta)}, \quad (6.33)$$

3745 where  $E_i$  are the energies of the photons and  $\theta$  the opening angle between them. In this

## Chapter 6. Particle ID in GArSoft

3746 case I can use the energies deposited in the ECal and their incident directions. This  
 3747 quantity is computed for all possible pairs of clusters, using their position together with  
 3748 the true decay point. In a more realistic scenario, e.g.  $\nu_\mu$  CC interaction, one could use  
 3749 the position of the reconstructed primary vertex instead. I also tried to use the principal  
 3750 direction of the clusters, but that approach gave considerably worse results. For each  
 3751 event I only keep the pair with an invariant mass closer to the true  $\pi^0$  mass value.

3752 Figure 6.41 (right panel) shows the invariant mass distributions for the photon pairs  
 3753 we get using the default (red) and the new (blue) ECal clustering algorithms. For the fit  
 3754 I used a modified version of the Crystal Ball function [144], obtained by taking the limit  
 3755 where the parameter controlling the power-law tail goes to infinity:

$$f(x; N, \mu, \sigma, \alpha) = N \cdot \begin{cases} e^{\frac{\alpha(2x-2\mu+\alpha\sigma)}{2\sigma}}; & x \leq \mu - \alpha\sigma, \\ e^{-\frac{(x-\mu)^2}{2\sigma^2}}; & x > \mu - \alpha\sigma. \end{cases} \quad (6.34)$$

3756 Comparing the fitted mean and standard deviation values for the Gaussian cores, we  
 3757 see that the distribution for the new algorithm is a 67% narrower and also peaks much  
 3758 closer to the true  $m_{\pi^0}$  value, going from  $101.3 \pm 0.4$  MeV to  $130.8 \pm 0.6$  MeV.

3759 Chapter 7

3760 Event selection in ND-GAr

3761 7.1 CAFs and CAFAna

3762 7.2 Event selection

3763 7.2.1  $\nu_\mu$  CC selection

3764 7.2.2 Charged pion multiplicity



<sup>3765</sup> Chapter 8

<sup>3766</sup> Conclusions



<sup>3767</sup> Appendix A

<sup>3768</sup> An appendix



<sup>3769</sup>

# Bibliography

- <sup>3770</sup> [1] J.N. Bahcall, A.M. Serenelli and S. Basu, *New solar opacities, abundances,*  
<sup>3771</sup> *helioseismology, and neutrino fluxes, Astrophys. J. Lett.* **621** (2005) L85  
<sup>3772</sup> [[astro-ph/0412440](#)]. 22, 42, 123, 125
- <sup>3773</sup> [2] R. Garani and S. Palomares-Ruiz, *Dark matter in the Sun: scattering off electrons*  
<sup>3774</sup> *vs nucleons, JCAP* **05** (2017) 007 [[1702.02768](#)]. 22, 121, 122, 124, 125, 126, 149
- <sup>3775</sup> [3] M. Honda, M. Sajjad Athar, T. Kajita, K. Kasahara and S. Midorikawa,  
<sup>3776</sup> *Atmospheric neutrino flux calculation using the NRLMSISE-00 atmospheric model,*  
<sup>3777</sup> *Phys. Rev. D* **92** (2015) 023004 [[1502.03916](#)]. 22, 129, 130
- <sup>3778</sup> [4] M. Colom i Bernadich and C. Pérez de los Heros, *Limits on Kaluza-Klein dark*  
<sup>3779</sup> *matter annihilation in the Sun from recent IceCube results, Eur. Phys. J. C,* **80** 2  
<sup>3780</sup> (2020) 129 **80** (2019) [[1912.04585](#)]. 23, 134
- <sup>3781</sup> [5] ANTARES collaboration, *Search for Dark Matter in the Sun with the ANTARES*  
<sup>3782</sup> *Neutrino Telescope in the CMSSM and mUED frameworks, Nucl. Instrum. Meth.*  
<sup>3783</sup> *A* **725** (2013) 76 [[1204.5290](#)]. 23, 134
- <sup>3784</sup> [6] N. Deutschmann, T. Flacke and J.S. Kim, *Current LHC Constraints on Minimal*  
<sup>3785</sup> *Universal Extra Dimensions, Phys. Lett. B* **771** (2017) 515 [[1702.00410](#)]. 23, 134,  
<sup>3786</sup> 135
- <sup>3787</sup> [7] ICECUBE collaboration, *Search for GeV-scale dark matter annihilation in the Sun*  
<sup>3788</sup> *with IceCube DeepCore, Phys. Rev. D* **105** (2022) 062004 [[2111.09970](#)]. 24, 146,  
<sup>3789</sup> 147

## BIBLIOGRAPHY

- 3790 [8] C.-S. Chen, F.-F. Lee, G.-L. Lin and Y.-H. Lin, *Probing Dark Matter*  
3791 *Self-Interaction in the Sun with IceCube-PINGU*, *JCAP* **10** (2014) 049  
3792 [1408.5471]. 24, 146, 147
- 3793 [9] N.F. Bell, M.J. Dolan and S. Robles, *Searching for dark matter in the Sun using*  
3794 *Hyper-Kamiokande*, *JCAP* **11** (2021) 004 [2107.04216]. 24, 146, 147
- 3795 [10] E. Behnke et al., *Final Results of the PICASSO Dark Matter Search Experiment*,  
3796 *Astropart. Phys.* **90** (2017) 85 [1611.01499]. 24, 146, 147
- 3797 [11] PICO collaboration, *Dark Matter Search Results from the Complete Exposure of*  
3798 *the PICO-60 C<sub>3</sub>F<sub>8</sub> Bubble Chamber*, *Phys. Rev. D* **100** (2019) 022001  
3799 [1902.04031]. 24, 146, 147
- 3800 [12] DARKSIDE collaboration, *Constraints on Sub-GeV Dark-Matter–Electron*  
3801 *Scattering from the DarkSide-50 Experiment*, *Phys. Rev. Lett.* **121** (2018) 111303  
3802 [1802.06998]. 24, 150, 151
- 3803 [13] XENON collaboration, *Light Dark Matter Search with Ionization Signals in*  
3804 *XENON1T*, *Phys. Rev. Lett.* **123** (2019) 251801 [1907.11485]. 24, 150, 151
- 3805 [14] P.F. de Salas, D.V. Forero, S. Gariazzo, P. Martínez-Miravé, O. Mena,  
3806 C.A. Ternes et al., *2020 global reassessment of the neutrino oscillation picture*,  
3807 *JHEP* **02** (2021) 071 [2006.11237]. 31, 56, 61
- 3808 [15] W. Pauli, *Dear radioactive ladies and gentlemen*, *Phys. Today* **31N9** (1978) 27. 37
- 3809 [16] F. Reines and C.L. Cowan, *Detection of the free neutrino*, *Phys. Rev.* **92** (1953)  
3810 830. 37
- 3811 [17] S.L. Glashow, *Partial-symmetries of weak interactions*, *Nuclear Physics* **22** 579. 37
- 3812 [18] S. Weinberg, *A model of leptons*, *Physical Review Letters* **19** 1264. 37
- 3813 [19] A. Salam, *Weak and Electromagnetic Interactions*, *Conf. Proc. C* **680519** (1968)  
3814 367. 37

## BIBLIOGRAPHY

- 3815 [20] A. Pich, *The Standard Model of Electroweak Interactions*, in *2010 European  
3816 School of High Energy Physics*, pp. 1–50, 1, 2012 [[1201.0537](#)]. 38
- 3817 [21] ALEPH, DELPHI, L3, OPAL, SLD, LEP ELECTROWEAK WORKING GROUP,  
3818 SLD ELECTROWEAK GROUP, SLD HEAVY FLAVOUR GROUP collaboration,  
3819 *Precision electroweak measurements on the Z resonance*, *Phys. Rept.* **427** (2006)  
3820 257 [[hep-ex/0509008](#)]. 41
- 3821 [22] R. Davis, D.S. Harmer and K.C. Hoffman, *Search for neutrinos from the sun*,  
3822 *Physical Review Letters* **20** 1205. 42
- 3823 [23] J.N. Bahcall, N.A. Bahcall and G. Shaviv, *Present Status of the Theoretical  
3824 Predictions for the  $^{37}\text{Cl}$  Solar-Neutrino Experiment*, . 43
- 3825 [24] B.T. Cleveland, T. Daily, R. Davis, Jr., J.R. Distel, K. Lande, C.K. Lee et al.,  
3826 *Measurement of the solar electron neutrino flux with the Homestake chlorine  
3827 detector*, *Astrophys. J.* **496** (1998) 505. 43
- 3828 [25] SAGE collaboration, *Measurement of the solar neutrino capture rate with gallium  
3829 metal. III: Results for the 2002–2007 data-taking period*, *Phys. Rev. C* **80** (2009)  
3830 015807 [[0901.2200](#)]. 43, 55
- 3831 [26] F. Kaether, W. Hampel, G. Heusser, J. Kiko and T. Kirsten, *Reanalysis of the  
3832 GALLEX solar neutrino flux and source experiments*, *Phys. Lett. B* **685** (2010) 47  
3833 [[1001.2731](#)]. 43, 55
- 3834 [27] Q.R. Ahmad, R.C. Allen, T.C. Andersen, J.D. Anglin, G. Bühler, J.C. Barton  
3835 et al., *Measurement of the Rate of  $\nu_e + d \rightarrow p + p + e^-$  Interactions Produced by  
3836  $^8\text{B}$  Solar Neutrinos at the Sudbury Neutrino Observatory*, . 43
- 3837 [28] Q.R. Ahmad, R.C. Allen, T.C. Andersen, J. D. Anglin, J.C. Barton, E.W. Beier  
3838 et al., *Direct Evidence for Neutrino Flavor Transformation from Neutral-Current  
3839 Interactions in the Sudbury Neutrino Observatory*, . 43
- 3840 [29] T.K. Gaisser and M. Honda, *Flux of atmospheric neutrinos*, . 44

## BIBLIOGRAPHY

- 3841 [30] K. Hirata, T. Kajita, M. Koshiba, M. Nakahata, S. Ohara, Y. Oyama et al.,  
3842 *Experimental study of the atmospheric neutrino flux*, . 44
- 3843 [31] D. Casper, R. Becker-Szendy, C.B. Bratton, D.R. Cady, R. Claus, S.T. Dye et al.,  
3844 *Measurement of atmospheric neutrino composition with the imb-3 detector*, . 44
- 3845 [32] M. Ambrosio, R. Antolini, C. Aramo, G. Auriemma, A. Baldini, G. C. Barbarino  
3846 et al., *Measurement of the atmospheric neutrino-induced upgoing muon flux using*  
3847 *macro*, . 44
- 3848 [33] W. Allison, G. Alner, D. Ayres, W. Barrett, C. Bode, P. Border et al.,  
3849 *Measurement of the atmospheric neutrino flavour composition in soudan 2*, . 44
- 3850 [34] SUPER-KAMIOKANDE collaboration, *Evidence for oscillation of atmospheric*  
3851 *neutrinos*, *Phys. Rev. Lett.* **81** (1998) 1562 [[hep-ex/9807003](#)]. 44
- 3852 [35] P. Minkowski,  $\mu \rightarrow e\gamma$  at a Rate of One Out of  $10^9$  Muon Decays?, *Phys. Lett. B*  
3853 **67** (1977) 421. 47
- 3854 [36] M. Gell-Mann, P. Ramond and R. Slansky, *Complex Spinors and Unified Theories*,  
3855 *Conf. Proc. C* **790927** (1979) 315 [[1306.4669](#)]. 47
- 3856 [37] T. Yanagida, *Horizontal gauge symmetry and masses of neutrinos*, *Conf. Proc. C*  
3857 **7902131** (1979) 95. 47
- 3858 [38] R.N. Mohapatra and G. Senjanovic, *Neutrino Mass and Spontaneous Parity*  
3859 *Nonconservation*, *Phys. Rev. Lett.* **44** (1980) 912. 47
- 3860 [39] J. Schechter and J.W.F. Valle, *Neutrino Masses in  $SU(2) \times U(1)$  Theories*, *Phys.*  
3861 *Rev. D* **22** (1980) 2227. 47
- 3862 [40] B. Pontecorvo, *Mesonium and anti-mesonium*, *Sov. Phys. JETP* **6** (1957) 429. 48
- 3863 [41] M. Gell-Mann and A. Pais, *Behavior of neutral particles under charge conjugation*,  
3864 . 48

## BIBLIOGRAPHY

- 3865 [42] B. Pontecorvo, *Neutrino Experiments and the Problem of Conservation of*  
3866 *Leptonic Charge*, *Zh. Eksp. Teor. Fiz.* **53** (1967) 1717. 48
- 3867 [43] B. Pontecorvo, *Inverse beta processes and nonconservation of lepton charge*, *Zh.*  
3868 *Eksp. Teor. Fiz.* **34** (1957) 247. 49
- 3869 [44] Z. Maki, M. Nakagawa and S. Sakata, *Remarks on the unified model of elementary*  
3870 *particles*, *Prog. Theor. Phys.* **28** (1962) 870. 49
- 3871 [45] PARTICLE DATA GROUP collaboration, *Review of particle physics*, *Phys. Rev. D*  
3872 **110** (2024) 030001. 52
- 3873 [46] L. Wolfenstein, *Neutrino Oscillations in Matter*, *Phys. Rev. D* **17** (1978) 2369. 52
- 3874 [47] B.T. Cleveland, T. Daily, R. Davis, Jr., J.R. Distel, K. Lande, C.K. Lee et al.,  
3875 *Measurement of the solar electron neutrino flux with the Homestake chlorine*  
3876 *detector*, *Astrophys. J.* **496** (1998) 505. 55
- 3877 [48] G. Bellini et al., *Precision measurement of the  $^{7}\text{Be}$  solar neutrino interaction rate*  
3878 *in Borexino*, *Phys. Rev. Lett.* **107** (2011) 141302 [[1104.1816](#)]. 55
- 3879 [49] SUPER-KAMIOKANDE collaboration, *Solar neutrino measurements in*  
3880 *super-Kamiokande-I*, *Phys. Rev. D* **73** (2006) 112001 [[hep-ex/0508053](#)]. 55
- 3881 [50] SNO collaboration, *Combined Analysis of all Three Phases of Solar Neutrino*  
3882 *Data from the Sudbury Neutrino Observatory*, *Phys. Rev. C* **88** (2013) 025501  
3883 [[1109.0763](#)]. 55
- 3884 [51] SUPER-KAMIOKANDE collaboration, *Atmospheric neutrino oscillation analysis*  
3885 *with external constraints in Super-Kamiokande I-IV*, *Phys. Rev. D* **97** (2018)  
3886 072001 [[1710.09126](#)]. 55
- 3887 [52] ICECUBE collaboration, *Measurement of Atmospheric Neutrino Oscillations at*  
3888 *6–56 GeV with IceCube DeepCore*, *Phys. Rev. Lett.* **120** (2018) 071801  
3889 [[1707.07081](#)]. 55

## BIBLIOGRAPHY

- 3890 [53] KamLAND collaboration, *Reactor On-Off Antineutrino Measurement with  
KamLAND*, *Phys. Rev. D* **88** (2013) 033001 [[1303.4667](#)]. 55
- 3891
- 3892 [54] RENO collaboration, *Measurement of Reactor Antineutrino Oscillation Amplitude  
and Frequency at RENO*, *Phys. Rev. Lett.* **121** (2018) 201801 [[1806.00248](#)]. 55
- 3893
- 3894 [55] DAYA BAY collaboration, *Measurement of the Electron Antineutrino Oscillation  
with 1958 Days of Operation at Daya Bay*, *Phys. Rev. Lett.* **121** (2018) 241805  
3895 [[1809.02261](#)]. 55
- 3896
- 3897 [56] K.J. Kelly, P.A.N. Machado, S.J. Parke, Y.F. Perez-Gonzalez and R.Z. Funchal,  
*Neutrino mass ordering in light of recent data*, *Phys. Rev. D* **103** (2021) 013004.  
3898
- 3899 55
- 3900 [57] P. Dunne, “Latest Neutrino Oscillation Results from T2K.” Jul, 2020. 55
- 3901
- 3902 [58] MINOS collaboration, *Combined analysis of  $\nu_\mu$  disappearance and  $\nu_\mu \rightarrow \nu_e$   
appearance in MINOS using accelerator and atmospheric neutrinos*, *Phys. Rev. Lett.* **112** (2014) 191801 [[1403.0867](#)]. 55
- 3903
- 3904 [59] OPERA collaboration, *Final Results of the OPERA Experiment on  $\nu_\tau$   
Appearance in the CNGS Neutrino Beam*, *Phys. Rev. Lett.* **120** (2018) 211801  
3905
- 3906 [[1804.04912](#)]. 55
- 3907 [60] K2K collaboration, *Measurement of Neutrino Oscillation by the K2K Experiment*,  
*Phys. Rev. D* **74** (2006) 072003 [[hep-ex/0606032](#)]. 55
- 3908
- 3909 [61] DUNE collaboration, *Long-baseline neutrino oscillation physics potential of the  
DUNE experiment*, *Eur. Phys. J. C* **80** (2020) 978 [[2006.16043](#)]. 55
- 3910
- 3911 [62] HYPER-KAMIOKANDE collaboration, *Physics potential of Hyper-Kamiokande for  
neutrino oscillation measurements*, *PoS NuFact2019* (2019) 040. 55
- 3912
- 3913 [63] SUPERNEMO collaboration, *Probing New Physics Models of Neutrinoless Double  
Beta Decay with SuperNEMO*, *Eur. Phys. J. C* **70** (2010) 927 [[1005.1241](#)]. 57
- 3914

## BIBLIOGRAPHY

- 3915 [64] SNO+ collaboration, *Current Status and Future Prospects of the SNO+*  
3916 *Experiment, Adv. High Energy Phys.* **2016** (2016) 6194250 [[1508.05759](#)]. 57
- 3917 [65] NEXT collaboration, *Sensitivity of a tonne-scale NEXT detector for neutrinoless*  
3918 *double beta decay searches, JHEP* **2021** (2021) 164 [[2005.06467](#)]. 57
- 3919 [66] L. Bathe-Peters, S. Gardiner and R. Guenette, *Comparing generator predictions*  
3920 *of transverse kinematic imbalance in neutrino-argon scattering,* [2201.04664](#). 58
- 3921 [67] DUNE collaboration, *Deep Underground Neutrino Experiment (DUNE), Far*  
3922 *Detector Technical Design Report, Volume I Introduction to DUNE, JINST* **15**  
3923 (2020) T08008 [[2002.02967](#)]. 59, 60, 61, 66, 67, 77, 78, 79, 80
- 3924 [68] DUNE collaboration, *Snowmass Neutrino Frontier: DUNE Physics Summary,*  
3925 [2203.06100](#). 61, 62
- 3926 [69] DUNE collaboration, *Deep Underground Neutrino Experiment (DUNE), Far*  
3927 *Detector Technical Design Report, Volume II: DUNE Physics,* [2002.03005](#). 61, 63,  
3928 64, 71, 129, 138, 142
- 3929 [70] SUPER-KAMIOKANDE collaboration, *Search for Proton Decay via  $p \rightarrow e^+ \pi_0$  and*  
3930  *$p \rightarrow \mu^+ \pi_0$  in a Large Water Cherenkov Detector, Phys. Rev. Lett.* **102** (2009)  
3931 141801 [[0903.0676](#)]. 62
- 3932 [71] S. Raby, *Grand Unified Theories*, in *2nd World Summit: Physics Beyond the*  
3933 *Standard Model*, 8, 2006 [[hep-ph/0608183](#)]. 62
- 3934 [72] KAMIOKANDE-II collaboration, *Observation of a Neutrino Burst from the*  
3935 *Supernova SN 1987a, Phys. Rev. Lett.* **58** (1987) 1490. 63
- 3936 [73] R.M. Bionta et al., *Observation of a Neutrino Burst in Coincidence with*  
3937 *Supernova SN 1987a in the Large Magellanic Cloud, Phys. Rev. Lett.* **58** (1987)  
3938 1494. 63

## BIBLIOGRAPHY

- 3939 [74] J. Strait, E. McCluskey, T. Lundin, J. Willhite, T. Hamernik, V. Papadimitriou  
3940 et al., *Long-baseline neutrino facility (lbnf) and deep underground neutrino*  
3941 *experiment (dune) conceptual design report volume 3: Long-baseline neutrino*  
3942 *facility for dune june 24, 2015*, 1601.05823. 63, 64
- 3943 [75] DUNE collaboration, *Deep Underground Neutrino Experiment (DUNE) Near*  
3944 *Detector Conceptual Design Report, Instruments* **5** (2021) 31 [2103.13910]. 65,  
3945 67, 69, 70, 72, 73, 153
- 3946 [76] DUNE collaboration, *DUNE Phase II: Scientific Opportunities, Detector*  
3947 *Concepts, Technological Solutions*, 2408.12725. 68, 74
- 3948 [77] DUNE collaboration, *A Gaseous Argon-Based Near Detector to Enhance the*  
3949 *Physics Capabilities of DUNE*, 2203.06281. 70
- 3950 [78] F. Sauli, *Gem: A new concept for electron amplification in gas detectors*, . 72, 76
- 3951 [79] A. Ritchie-Yates et al., *First operation of an ALICE OROC operated in high*  
3952 *pressure Ar-CO<sub>2</sub> and Ar-CH<sub>4</sub>*, *Eur. Phys. J. C* **83** (2023) 1139 [2305.08822]. 75
- 3953 [80] ALICE TPC collaboration, *The upgrade of the ALICE TPC with GEMs and*  
3954 *continuous readout*, *JINST* **16** (2021) P03022 [2012.09518]. 75
- 3955 [81] F. Sauli, *The gas electron multiplier (gem): Operating principles and applications*,  
3956 . 76
- 3957 [82] C. Lippmann, *A continuous read-out tpc for the alice upgrade*, . 76
- 3958 [83] C. Calabria, *Large-size triple gem detectors for the cms forward muon upgrade*, .  
3959 76
- 3960 [84] DUNE collaboration, *The DUNE Far Detector Vertical Drift Technology*,  
3961 *Technical Design Report*, 2312.03130. 81, 82

## BIBLIOGRAPHY

- 3962 [85] DUNE collaboration, *Deep Underground Neutrino Experiment (DUNE), Far*  
3963 *Detector Technical Design Report, Volume IV: Far Detector Single-phase*  
3964 *Technology, JINST* **15** (2020) T08010 [2002.03010]. 83
- 3965 [86] DUNE DAQ, “dtp-firmware.”  
3966 <https://gitlab.cern.ch/dune-daq/readout/dtp-firmware>, 2020. 85
- 3967 [87] DUNE DAQ, “dtp-simulation.”  
3968 <https://gitlab.cern.ch/dune-daq/readout/dtp-simulation>, 2020. 88
- 3969 [88] DUNE DAQ, “dtpemulator.”  
3970 [https://github.com/DUNE-DAQ/dtpemulator/tree/fmlopez/filter\\_ana](https://github.com/DUNE-DAQ/dtpemulator/tree/fmlopez/filter_ana),  
3971 2022. 88
- 3972 [89] J. McClellan and T. Parks, *A personal history of the Parks-McClellan algorithm*,  
3973 *IEEE Signal Processing Magazine* **22** (2005) 82. 89
- 3974 [90] G. Turin, *An introduction to matched filters*, *IEEE Transactions on Information*  
3975 *Theory* **6** (1960) 311. 92
- 3976 [91] J.W. Goodman, *Statistical Optics*, Wiley (1985). 94
- 3977 [92] B. Dwork, *Detection of a pulse superimposed on fluctuation noise*, *Proceedings of*  
3978 *the IRE* **38** (1950) 771. 95
- 3979 [93] L. Wainstein and V. Zubakov, *Extraction of Signals from Noise*, Prentice-Hall  
3980 (1962). 95
- 3981 [94] E.D. Church, *Larsoft: A software package for liquid argon time projection drift*  
3982 *chambers*, **1311.6774**. 98, 99
- 3983 [95] S.V. Stehman, *Selecting and interpreting measures of thematic classification*  
3984 *accuracy*, *Remote Sensing of Environment* **62** (1997) 77. 112
- 3985 [96] A.A. Taha and A. Hanbury, *Metrics for evaluating 3d medical image*  
3986 *segmentation: analysis, selection, and tool*, *BMC Medical Imaging* **15** (2015) . 113

## BIBLIOGRAPHY

- 3987 [97] J. Silk, K.A. Olive and M. Srednicki, *The Photino, the Sun and High-Energy*  
3988 *Neutrinos*, *Phys. Rev. Lett.* **55** (1985) 257. 119
- 3989 [98] M. Srednicki, K.A. Olive and J. Silk, *High-Energy Neutrinos from the Sun and*  
3990 *Cold Dark Matter*, *Nucl. Phys. B* **279** (1987) 804. 119
- 3991 [99] J.S. Hagelin, K.W. Ng and K.A. Olive, *A High-energy Neutrino Signature From*  
3992 *Supersymmetric Relics*, *Phys. Lett. B* **180** (1986) 375. 119
- 3993 [100] T.K. Gaisser, G. Steigman and S. Tilav, *Limits on Cold Dark Matter Candidates*  
3994 *from Deep Underground Detectors*, *Phys. Rev. D* **34** (1986) 2206. 119
- 3995 [101] N. Bernal, J. Martín-Albo and S. Palomares-Ruiz, *A novel way of constraining*  
3996 *WIMPs annihilations in the Sun: MeV neutrinos*, *JCAP* **08** (2013) 011  
3997 [1208.0834]. 119, 120, 121, 127
- 3998 [102] C. Rott, J. Siegal-Gaskins and J.F. Beacom, *New Sensitivity to Solar WIMP*  
3999 *Annihilation using Low-Energy Neutrinos*, *Phys. Rev. D* **88** (2013) 055005  
4000 [1208.0827]. 119, 126
- 4001 [103] C. Rott, S. In, J. Kumar and D. Yaylali, *Dark Matter Searches for Monoenergetic*  
4002 *Neutrinos Arising from Stopped Meson Decay in the Sun*, *JCAP* **11** (2015) 039  
4003 [1510.00170]. 119
- 4004 [104] DUNE collaboration, *Searching for solar KDAR with DUNE*, *JCAP* **10** (2021)  
4005 065 [2107.09109]. 119
- 4006 [105] G. Busoni, A. De Simone and W.-C. Huang, *On the Minimum Dark Matter Mass*  
4007 *Testable by Neutrinos from the Sun*, *JCAP* **07** (2013) 010 [1305.1817]. 120
- 4008 [106] V.A. Bednyakov and F. Simkovic, *Nuclear spin structure in dark matter search:*  
4009 *The Zero momentum transfer limit*, *Phys. Part. Nucl.* **36** (2005) 131  
4010 [hep-ph/0406218]. 121

## BIBLIOGRAPHY

- 4011 [107] A. Gould, *WIMP Distribution in and Evaporation From the Sun*, *Astrophys. J.*  
 4012 **321** (1987) 560. 122
- 4013 [108] J.N. Bahcall, M.H. Pinsonneault and S. Basu, *Solar models: Current epoch and*  
 4014 *time dependences, neutrinos, and helioseismological properties*, *Astrophys. J.* **555**  
 4015 (2001) 990 [[astro-ph/0010346](#)]. 124
- 4016 [109] T. Golan, J.T. Sobczyk and J. Zmuda, *NuWro: the Wroclaw Monte Carlo*  
 4017 *Generator of Neutrino Interactions*, *Nucl. Phys. B Proc. Suppl.* **229-232** (2012)  
 4018 499. 128
- 4019 [110] G. Cowan, K. Cranmer, E. Gross and O. Vitells, *Asymptotic formulae for*  
 4020 *likelihood-based tests of new physics*, *Eur. Phys. J. C* **71** (2011) 1554 [[1007.1727](#)].  
 4021 129
- 4022 [111] T. Kaluza, *Zum Unitätsproblem der Physik, Sitzungsber. Preuss. Akad. Wiss.*  
 4023 *Berlin (Math. Phys.)* **1921** (1921) 966 [[1803.08616](#)]. 131
- 4024 [112] O. Klein, *Quantum Theory and Five-Dimensional Theory of Relativity. (In*  
 4025 *German and English)*, *Z. Phys.* **37** (1926) 895. 131
- 4026 [113] T. Appelquist, H.-C. Cheng and B.A. Dobrescu, *Bounds on universal extra*  
 4027 *dimensions*, *Phys. Rev. D* **64** (2001) 035002 [[hep-ph/0012100](#)]. 131
- 4028 [114] N. Arkani-Hamed, S. Dimopoulos and G.R. Dvali, *The Hierarchy problem and new*  
 4029 *dimensions at a millimeter*, *Phys. Lett. B* **429** (1998) 263 [[hep-ph/9803315](#)]. 131
- 4030 [115] L. Randall and R. Sundrum, *A Large mass hierarchy from a small extra*  
 4031 *dimension*, *Phys. Rev. Lett.* **83** (1999) 3370 [[hep-ph/9905221](#)]. 131
- 4032 [116] G. Servant and T.M.P. Tait, *Is the lightest Kaluza-Klein particle a viable dark*  
 4033 *matter candidate?*, *Nucl. Phys. B* **650** (2003) 391 [[hep-ph/0206071](#)]. 131
- 4034 [117] H.-C. Cheng, K.T. Matchev and M. Schmaltz, *Radiative corrections to*  
 4035 *Kaluza-Klein masses*, *Phys. Rev. D* **66** (2002) 036005 [[hep-ph/0204342](#)]. 133

## BIBLIOGRAPHY

- 4036 [118] M. Blennow, J. Edsjö and T. Ohlsson, *Neutrinos from WIMP annihilations using*  
4037 *a full three-flavor Monte Carlo*, *JCAP* **01** (2008) 021 [[0709.3898](#)]. 133, 136
- 4038 [119] J. Edsjö, J. Elevant and C. Niblaeus, *WimpSim Neutrino Monte Carlo*. 133, 136
- 4039 [120] U. Haisch and A. Weiler, *Bound on minimal universal extra dimensions from*  
4040 *anti-B —> X(s)gamma*, *Phys. Rev. D* **76** (2007) 034014 [[hep-ph/0703064](#)]. 135
- 4041 [121] A. Freitas and U. Haisch, *Anti-B —> X(s) gamma in two universal extra*  
4042 *dimensions*, *Phys. Rev. D* **77** (2008) 093008 [[0801.4346](#)]. 135
- 4043 [122] C. Rott, D. Jeong, J. Kumar and D. Yaylali, *Neutrino Topology Reconstruction at*  
4044 *DUNE and Applications to Searches for Dark Matter Annihilation in the Sun*,  
4045 *JCAP* **07** (2019) 006 [[1903.04175](#)]. 138
- 4046 [123] F. Pedregosa, G. Varoquaux, A. Gramfort, V. Michel, B. Thirion, O. Grisel et al.,  
4047 *Scikit-learn: Machine learning in Python*, *Journal of Machine Learning Research*  
4048 **12** (2011) 2825. 144
- 4049 [124] J. Kopp, V. Niro, T. Schwetz and J. Zupan, *DAMA/LIBRA and leptonically*  
4050 *interacting Dark Matter*, *Phys. Rev. D* **80** (2009) 083502 [[0907.3159](#)]. 148
- 4051 [125] PARTICLE DATA GROUP collaboration, *Review of Particle Physics*, *PTEP* **2020**  
4052 (2020) 083C01. 149
- 4053 [126] M. Beltran, D. Hooper, E.W. Kolb and Z.C. Krusberg, *Deducing the nature of*  
4054 *dark matter from direct and indirect detection experiments in the absence of*  
4055 *collider signatures of new physics*, *Phys. Rev. D* **80** (2009) 043509 [[0808.3384](#)].  
4056 149
- 4057 [127] PLANCK collaboration, *Planck 2018 results. VI. Cosmological parameters*, *Astron.*  
4058 *Astrophys.* **641** (2020) A6 [[1807.06209](#)]. 150
- 4059 [128] C. Green, J. Kowalkowski, M. Paterno, M. Fischler, L. Garren and Q. Lu, *The*  
4060 *Art Framework*, *J. Phys. Conf. Ser.* **396** (2012) 022020. 154

## BIBLIOGRAPHY

- 4061 [129] H. Bethe, *Zur theorie des durchgangs schneller korpuskularstrahlen durch materie,*  
 4062 *Annalen der Physik* **397** (1930) 325. 159
- 4063 [130] E. Fermi, *The ionization loss of energy in gases and in condensed materials,*  
 4064 *Physical Review* **57** (1940) 485. 159
- 4065 [131] R. Sternheimer, M. Berger and S. Seltzer, *Density effect for the ionization loss of*  
 4066 *charged particles in various substances, Atomic Data and Nuclear Data Tables* **30**  
 4067 (1984) 261. 159
- 4068 [132] W.W.M. Allison and J.H. Cobb, *Relativistic Charged Particle Identification by*  
 4069 *Energy Loss, Ann. Rev. Nucl. Part. Sci.* **30** (1980) 253. 160
- 4070 [133] W. Blum, L. Rolandi and W. Riegler, *Particle detection with drift chambers,*  
 4071 *Particle Acceleration and Detection* (2008), 10.1007/978-3-540-76684-1. 160
- 4072 [134] ALICE TPC collaboration, *Particle identification of the ALICE TPC via dE/dx,*  
 4073 *Nucl. Instrum. Meth. A* **706** (2013) 55. 160
- 4074 [135] L. Landau, *On the energy loss of fast particles by ionization, J. Phys. (USSR)* **8**  
 4075 (1944) 201. 163
- 4076 [136] W. Ulmer and E. Matsinos, *Theoretical methods for the calculation of Bragg*  
 4077 *curves and 3D distributions of proton beams, The European Physical Journal*  
 4078 *Special Topics* **190** (2010) 1. 165
- 4079 [137] E. Aprile, A.E. Bolotnikov, A.L. Bolozdynya and T. Doke, *Noble Gas Detectors,*  
 4080 Wiley (Oct., 2008), 10.1002/9783527610020. 166
- 4081 [138] D.S. Wilks, *Statistical Methods in the Atmospheric Sciences*, Academic Press. 203
- 4082 [139] ALICE collaboration, *Production of pions, kaons and protons in pp collisions at*  
 4083  $\sqrt{s} = 900 \text{ gev with alice at the lhc}$ , **1101.4110**. 205
- 4084 [140] U. Einhaus, *Charged hadron identification with de/dx and time-of-flight at future*  
 4085 *higgs factories*, **2110.15115**. 205

## BIBLIOGRAPHY

- 4086 [141] R. Frühwirth, *Application of filter methods to the reconstruction of tracks and*  
4087 *vertices in events of experimental high energy physics*, Ph.D. thesis, Technischen  
4088 Universität Wien, 1988. 211
- 4089 [142] P. Astier, A. Cardini, R.D. Cousins, A. Letessier-Selvon, B.A. Popov and  
4090 T. Vinogradova, *Kalman filter track fits and track breakpoint analysis*, *Nuclear*  
4091 *Instruments and Methods in Physics Research Section A: Accelerators,*  
4092 *Spectrometers, Detectors and Associated Equipment* **450** (2000) 138. 211
- 4093 [143] T2K UK collaboration, *The Electromagnetic Calorimeter for the T2K Near*  
4094 *Detector ND280*, *JINST* **8** (2013) P10019 [1308.3445]. 219
- 4095 [144] J.E. Gaiser, *Charmonium Spectroscopy From Radiative Decays of the  $J/\psi$  and  $\psi'$* ,  
4096 Ph.D. thesis, Stanford University, 1982. 224